



National Library
of Canada

Bibliothèque nationale
du Canada

Canadian Theses Service

Service des thèses canadiennes

Ottawa, Canada
K1A 0N4

NOTICE

The quality of this microform is heavily dependent upon the quality of the original thesis submitted for microfilming. Every effort has been made to ensure the highest quality of reproduction possible.

If pages are missing, contact the university which granted the degree.

Some pages may have indistinct print especially if the original pages were typed with a poor typewriter ribbon or if the university sent us an inferior photocopy.

Reproduction in full or in part of this microform is governed by the Canadian Copyright Act, R.S.C. 1970, c. C-30, and subsequent amendments.

AVIS

La qualité de cette microforme dépend grandement de la qualité de la thèse soumise au microfilmage. Nous avons tout fait pour assurer une qualité supérieure de reproduction.

S'il manque des pages, veuillez communiquer avec l'université qui a conféré le grade.

La qualité d'impression de certaines pages peut laisser à désirer, surtout si les pages originales ont été dactylographiées à l'aide d'un ruban usé ou si l'université nous a fait parvenir une photocopie de qualité inférieure.

La reproduction, même partielle, de cette microforme est soumise à la Loi canadienne sur le droit d'auteur, SRC 1970, c. C-30, et ses amendements subséquents.

Reflectivity of Highly Deformed Terranes Based on
Laboratory and In Situ Velocity Measurements
from the Grenville Front Tectonic Zone,
Central Ontario, Canada

By

Margaret Mary Burke

©

Submitted in Partial Fulfillment of the requirements
for the Degree of Doctor of Philosophy

at

Dalhousie University
Halifax, Nova Scotia
May, 1991

© Copyright by Margaret Mary Burke, 1991



National Library
of Canada

Bibliothèque nationale
du Canada

Canadian Theses Service Service des thèses canadiennes

Ottawa, Canada
K1A 0N4

The author has granted an irrevocable non-exclusive licence allowing the National Library of Canada to reproduce, loan, distribute or sell copies of his/her thesis by any means and in any form or format, making this thesis available to interested persons.

The author retains ownership of the copyright in his/her thesis. Neither the thesis nor substantial extracts from it may be printed or otherwise reproduced without his/her permission.

L'auteur a accordé une licence irrévocable et non exclusive permettant à la Bibliothèque nationale du Canada de reproduire, prêter, distribuer ou vendre des copies de sa thèse de quelque manière et sous quelque forme que ce soit pour mettre des exemplaires de cette thèse à la disposition des personnes intéressées.

L'auteur conserve la propriété du droit d'auteur qui protège sa thèse. Ni la thèse ni des extraits substantiels de celle-ci ne doivent être imprimés ou autrement reproduits sans son autorisation.

ISBN 0-315-64529-6

Canada

Dedication

This thesis is dedicated to Bap the Wonder Dog
who is always glad to see me and
who has been present for every phase of this work.

Table of Contents

Dedication	iv
Table of Contents	v
List of Figures	viii
List of Tables	xi
Abstract	xii
Acknowledgements	xiii
 CHAPTER ONE - INTRODUCTION	 1
Crustal Reflectivity	1
Origin of Deep Crustal Reflections	2
GLIMPCE Profile J	3
Purpose and Extent of Study	5
 Geology of the Grenville Front	 9
Southern Province and Plutonic Suites	12
Huronian Supergroup	12
Nipissing Diabase	14
Killarney Complex	14
Bell Lake Granite and Annie Lake Complex	15
GFTZ Boundary Faults	16
GFTZ Rocks	17
Collins Inlet Area	17
Tyson Lake Area	20
 CHAPTER TWO - LABORATORY VELOCITY MEASUREMENTS	 23
Sample Descriptions	23
Orthogneiss	32
Paragneiss	36
Mafic Rocks	37
Metamorphosed Mafic Dikes	37
Plagioclase-Hornblende Gneiss	38
Diabase Dikes	39
 Experimental Method	 40
Experimental Results	51
Velocity-Pressure Relationships	51
Velocity-Density Relationships	56
Seismic Anisotropy	63
 Summary	 74
 CHAPTER THREE - <u>IN SITU</u> VELOCITY MEASUREMENTS	 78
On-going Great Lakes Experiments	78

Experimental Method	81
Data Acquisition	81
Data Processing	85
RAYAMP Raytracing	86
Experimental Results	89
Boundary Fault Profiles	89
Line 3 Velocities	90
Line 4 Velocities	96
Anisotropy of the GFTZ Boundary Fault	101
Beaverstone Bay Profiles	101
Line 5 Velocities	102
Line 6 Velocities	104
Mill Lake Profile	111
Line 1 Velocities	112
Velocities from Line 1 and Line 6	119
Summary	120
CHAPTER FOUR - DATA INTERPRETATION	122
Mylonitic Orthogneiss	123
Velocities	123
Anisotropy	130
Paragneiss	131
Velocities	131
Constraints on Reflection Coefficients	141
Pressure Dependence	141
Effect of Seismic Anisotropy	143
Variable Angles of Incidence	144
Summary	147
CHAPTER FIVE - SYNTHETIC MODELS	149
Introduction	149
Thin Mafic Dikes	150
Resolution of Thin Beds	150
Modelling Technique	153
Collins Inlet	154
Detailed Models of Mafic Dikes	162
Generalized Model of Mafic Dikes	167
Thin Layer Implications	177
Lithologic Variation	178
Modelling Technique	179
Simplified Model	182
Synthetic Sections	184
Lithologic Variation Implications	191
Summary	194

CHAPTER SIX - CONCLUSIONS	196
Laboratory Velocity Measurements	196
Granitic Orthogneiss	196
Paragneiss	197
Mafic Gneiss	197
OGLE Refraction Velocities	198
Orthogneiss Profiles	198
Paragneiss Profiles	199
Deep Crustal Reflections Revisited	200
Synthetic Models	203
Further Work	207
Appendix One - OGLE Mid-Line Refraction Profiles	209
References Cited	228

List of Figures

1.1	Line Drawing of part of GLIMPCE Profile J	4
1.2	Magnetic Map of Georgian Bay	6
1.3	Sub-Provinces of the Grenville Province	10
1.4	Geologic Map of the GFTZ	13
1.5	Geologic Map of Collins Inlet	18
1.6	Geologic Map of Tyson Lake	21
2.1	Outline of Collins Inlet and Tyson Lake Regions	24
2.2	Location of Samples Along Collins Inlet	25
2.3	Location of GFTZ Boundary Fault Samples	26
2.4	Location of Collins Inlet Thin Section Samples	29
2.5	Ternary Diagram for Orthogneiss Velocity Samples	34
2.6	Ternary Diagram for Orthogneiss Thin Section Samples	35
2.7	Core Orientation Convention	41
2.8	Sample Assembly Diagram	43
2.9	Pulse Waveform	45
2.10	Velocity-Pressure Plot for GFTZ-47A	52
2.11	Velocity-Pressure Plot for two runs of GFTZ-47B	54
2.12	Velocity-Density Plot for all GFTZ Samples	57
2.13	Velocity Density diagram for Lithologic Units	59
2.14	Velocity-Density Plot for Paragneiss Samples	61
2.15	Velocity-Density Plot for Mafic Samples	64
2.16	Anisotropy-Pressure Plot for GFTZ-7	67
2.17	Anisotropy-Total Mica Plot for Slow Paragneiss	70
2.18	Anisotropy-Total Mica Plot for Fast Paragneiss	72
2.19	Anisotropy-Hornblende Plot for Mafic Rocks	73

3.1	Location of OGLE Refraction Profiles	80
3.2	Near Field Signature of GI Airgun	83
3.3	Near Field Frequency Response of GI Airgun	84
3.4	Section and picked break for GB 3-1	91
3.5	Section and picked break for GB 3-3	93
3.6	Superposition of GB 3-1 and 3-3 breaks	95
3.7	Section and picked break for GB 4-1	97
3.8	Section and picked break for GB 4-4	99
3.9	Section for BB 5-1	103
3.10	Section and picked break for BB 6-1	105
3.11	Section and picked break for BB 6-4	107
3.12	Superposition of BB 6-1 and BB 6-4 breaks	110
3.13	Section and picked break for ML 1-1	113
3.14	Section and picked break for ML 1-6	114
3.15	Section and picked break for ML 1-7	117
4.1	Refraction Models for OGLE Lines 3 and 4	124
4.2	Average Vp versus confining pressure for mylonitized orthogneiss	128
4.3	Refraction Models for Mill Lake	132
4.4	Refraction Models for Beaverstone Bay	136
4.5	C-direction Vp versus confining pressure for paragneiss	138
4.6	Angles of incidence for a variably dipping boundary	145
5.1	Vertical Resolution of a Thin Bed (Widess, 1973)	152
5.2	Thin Mafic Dike Distribution Along Collins Inlet	155
5.3	Detailed Dike Synthetic Traces	163
5.4	Detailed Dike Synthetic Traces with Hurich's (1988) Velocities	166

5.5	Detailed Dike Synthetic Traces, $R_c = 0.03$	168
5.6	Detailed Dike Synthetic Traces, $R_c = 0.04$	169
5.7	Detailed Dike Synthetic Traces, $R_c = 0.05$	170
5.8	Detailed Dike Synthetic Traces, $R_c = 0.06$	171
5.9	Detailed Dike Synthetic Traces, $R_c = 0.07$	172
5.10	Detailed Dike Synthetic Traces, $R_c = 0.08$	173
5.11	Generalized Cluster Synthetic Traces	176
5.12	Velocity Depth Model of Tyson Lake	183
5.13	Milkereit et al.(1990) Model of the GFTZ	185
5.14	Synthetic CDP Profile, No Noise	186
5.15	Synthetic CDP Profile, Five Per Cent Noise	189
6.1	Possible Reflectors on Profile J	206
A.1	Section and picked break for GB 3-2	210
A.2	Section and picked break for GB 4-2	212
A.3	Section and picked break for GB 4-3	214
A.4	Section and picked break for BB 6-2	216
A.5	Section and picked break for BB 6-3	218
A.6	Section and picked break for ML 1-2	220
A.7	Section and picked break for ML 1-3	222
A.8	Section and picked break for ML 1-4	224
A.9	Section and picked break for ML 1-5	226

List of Tables

2.1	Mineralogy of GFTZ Velocity Samples	27
2.2	Mineralogy of Collins Inlet Thin Section Samples	30
2.3	Compressional Wave Velocities of GFTZ Rocks	46
2.4	Velocity Hysteresis of GFTZ Rocks	55
2.5	Seismic Anisotropy of GFTZ Rocks	65
2.6	Average Velocities for GFTZ Rocks	75
3.1	Site Information for OGLE Refraction Profiles	82
3.2	Compressional Wave Velocities and Errors of OGLE Refraction Profiles	87
3.3	Shear Wave Velocities and Errors for OGLE Refraction Profiles	88
4.1	Possible Reflection Coefficients for GFTZ Rocks	142
5.1	Detailed Distribution of Dikes Along Collins Inlet	156
5.2	Dike Cluster Distribution and Averaged Physical Properties	174

Abstract

The Grenville Front Tectonic Zone (GFTZ) is a pronounced geological and geophysical discontinuity which extends from northern Labrador to the southern United States. A deep seismic reflection profile (GLIMPCE Profile J) across the GFTZ in Lake Huron shows a series of high amplitude, multicyclic, dipping reflections. This work addresses the origin of these reflections based on laboratory and in situ measurements of compressional wave velocities in GFTZ rocks.

Forty-one samples of three main lithologic groups were used for laboratory velocity studies. Orthogneiss samples, including highly deformed mylonitic rocks from the boundary fault of the GFTZ, have an average velocity of 6.29 km/s at 600 MPa and seismic anisotropy ranging from 1-6%. Paragneiss samples have an average velocity of 6.31 km/s at 600 MPa and seismic anisotropy ranging from 2-15%. Mafic gneisses exhibit anisotropy from 4-16% and an average velocity of 6.88 km/s at 600 MPa.

In situ profiles show very shallow (ca. 300 m) level alteration (fracturing, weathering, etc.) indicated by very low compressional wave velocities for both orthogneiss and paragneiss assemblages. However, in situ measurements of compressional wave velocities at slightly deeper levels show good agreement with low pressure laboratory velocities. Data from orthogonal profiles across the boundary fault rocks also indicate minimal seismic anisotropy for the mylonitic rocks exposed.

Detailed one-dimensional models, based on mapped dikes along Collins Inlet, show that very thin layers (ca. 30 cm thick) can produce reflections, if clustered in some fashion so as to resemble units with intermediate velocity that have thicknesses on the order of seismic wavelengths. A more general, two-dimensional model shows that contacts between mafic gneisses and other lithologies are the most likely contributors to reflectivity in this area of the GFTZ.

Acknowledgements

This work was enormously helped by a large number of people from Dalhousie University, the Geologic Survey of Canada, the United States Geologic Survey and the University of Wyoming. However, first my parents Walter and Nancy Burke deserve my utmost thanks for their continued support of my education, and for giving me the self confidence that made my various degrees possible. They are the best parents ever.

I would also like to thank my fiance, Ray Donelick, who has given me the day-to-day support that kept me plugging away at this work. He has also provided much needed critical reviews of each chapter, and his constant questions have kept me on my toes

Isa Asudeh at the GSC and Debbie Hutchinson at the USGS provided not only the necessary equipment for the OGLE surveys, but also tremendous advice and expertise. The OGLE surveys were truly collaborative research, and Isa and Debbie have my continued thanks for all their help.

OGLE had the help of many others who laid out and maintained the instruments, and ran Neecho and the airguns. They are; Rebecca Irving, Malcolm Argyle, Alan Marincheck, Tim Cartwright, Dave Nichols, Dave Mason, Barry Irwin and Alan Stark. Carl Spencer and Bernd Milkereit were helpful in detecting and solving problems with processing these data in Ottawa. The people at Seismic Services Inc. very generously provided their brand new bubble-free airgun, which worked like a charm. Alan Green gave me many helpful hints while I

was writing the grants which funded OGLE, and I am grateful to him.

The first season of fieldwork was helped by the presence of Melanie Haggart and Geoff Gallant. Bap kept us entertained. The Killarney Provincial Park authorities allowed us to work within their boundaries, and we thank them. Kathy Bethune and Tony Davidson provided us a good introduction to the geology of the Grenville Front.

The laboratory velocity measurements would have been impossible if not for Bob Iuliucci, the technician for the High Pressure Laboratory at Dalhousie. Gordon Brown milled my velocity samples and made many of my thin sections. Sandy Grist provided much needed help during the final stages of preparation of this document.

The synthetic models were run at the Department of Geology and Geophysics at the University of Wyoming. I thank Scott Smithson, who allowed me to return to Laramie to do this work, and Brian Fuller, who gave me access to his programs and his expertise and whose help is very much appreciated. All synthetic models were run on the VAX 11/780 computer in the Program for Crustal Studies at the University of Wyoming.

Becky Jamieson, Keith Loudon and Nick Culshaw served on my supervisory committee, and Peter Reynolds and Ron Clowes served on my examining committee and I thank them for their time and suggestions. My supervisor was Matt Salisbury.

CHAPTER 1

INTRODUCTION

Crustal Reflectivity

The increased use of high resolution reflection and refraction profiling has provided increasingly sophisticated models of continental structure and composition. In particular, deep reflection profiles reveal crustal geometries to higher resolution than other geophysical methods (Smithson, 1986) and in many instances provide apparent visual cross-sections of the crust. Reflections from the deep (ca. >15 km) continental crust have been observed in many areas including: the western United States (Potter et al., 1987), northwestern Britain (Brewer et al., 1984), France (Bois et al., 1987; Choukroune, 1989) and Australia (Mathur, 1983).

Translating these reflection geometries into a geologic framework is quite difficult, primarily because seismic reflectivity and compressional wave velocities usually cannot be interpreted uniquely in terms of lithology (e.g. Kern and Schenk, 1985; Burke and Fountain, 1990), and because surface geologic structures cannot usually be extrapolated to great depths. Deep crustal reflections are commonly horizontal to sub-horizontal with

high amplitudes and complex, multicyclic waveforms (Fuchs, 1969; Meissner, 1986). It is therefore not uncommon to propose a number of possible geologic interpretations for any given set of deep crustal reflections (e.g., Green et al., 1988; Klemperer et al., 1985) and without additional data, it is impossible to eliminate some of these ambiguities.

Origin of Deep Crustal Reflections

The origin of deep crustal reflectors is a subject of much debate (e.g. Baranzangi and Brown, 1986; Matthews and Smith, 1987). Green et al. (1990) have outlined the five most commonly cited causes for crustal reflectivity: (1) primary depositional layering, (2) primary intrusive layering, (3) tectonically imposed layering, including shear zones, (4) metamorphic layering and (5) fluid related phenomena. The contributions of most of these reflection sources are not mutually exclusive, and it seems likely that many of these factors act together in the continental crust. Constructive interference of thin layers can boost the effect of any of these possible reflections to produce the high amplitudes commonly seen in crustal profiles (Hurich et al., 1987). However, discerning the relative effect each of these causes may have on a seismic profile is usually not possible without additional data.

Additional constraints on deep seismic profiling can be provided by detailed examination of the seismic properties and spatial relationships of rocks that once resided in the deep continental crust (Fountain, 1986; Fountain et al., 1990). Exposures of such deep crustal terranes can allow direct observation of critical parameters such as the composition, thickness and lateral extent of lithologic units. Detailed models of the crust can then be constructed from field geologic relationships and the compressional wave velocity behavior of representative lithologic units. Studies of such regions may be complicated by retrogression of original mineral assemblages or by tectonic complications associated with uplift, but nonetheless can provide actualistic models of the deep continental crust (Fountain et al., 1987).

GLIMPCE Profile J

The Great Lakes International Multidisciplinary Project on Crustal Evolution (GLIMPCE) acquired over 300 km of deep seismic reflection and refraction data across Lake Huron and Georgian Bay (Figure 1.1). The deep reflection line, Profile J, displayed a spectacular series of strong, multicyclic events associated with the Grenville Front Tectonic Zone (GFTZ) (Green et al., 1988). A distinctive magnetic anomaly pattern coincident with the GFTZ (Figure

Profile J Across the GFTZ

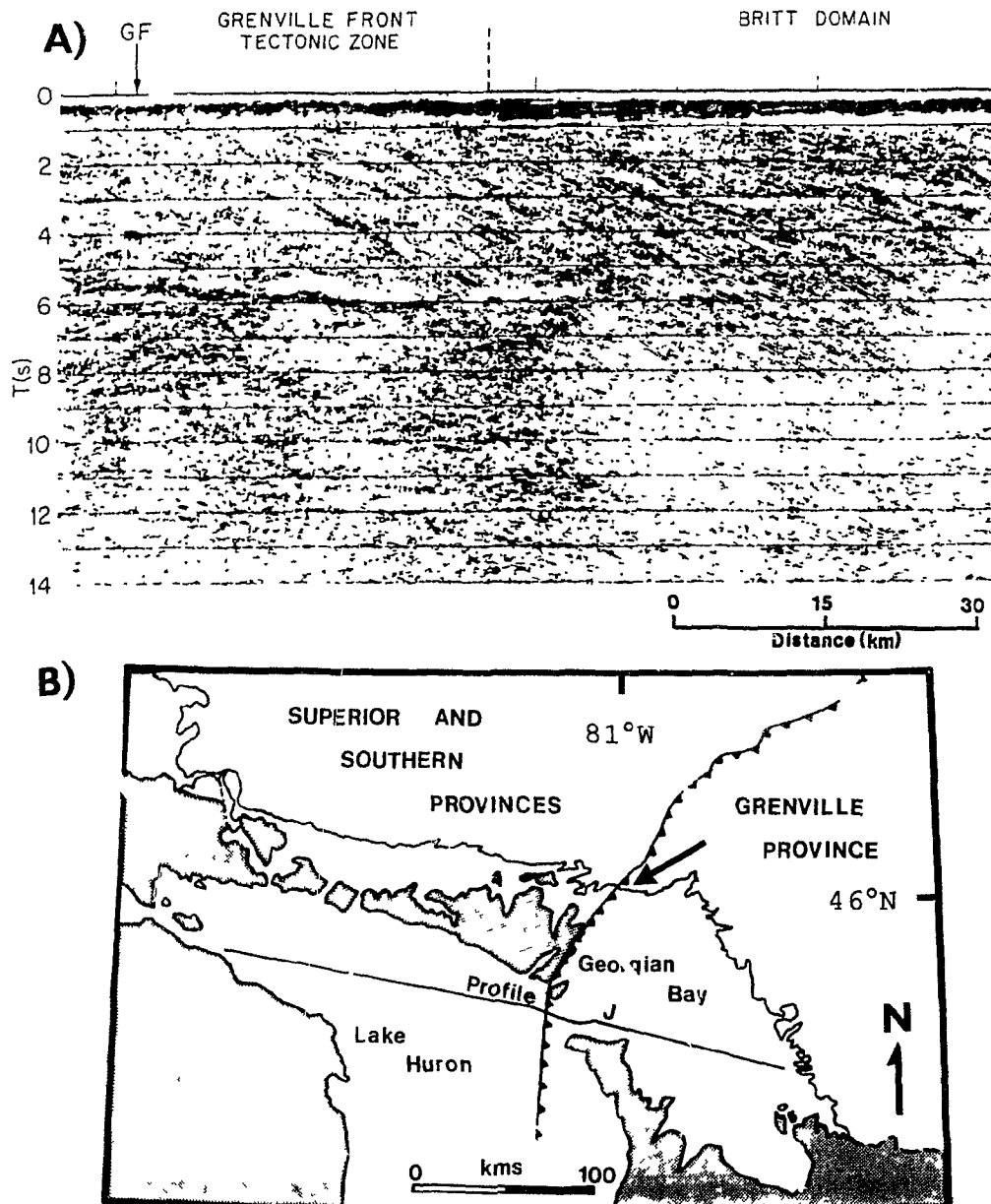


Figure 1.1. A) Seismic section of the portion of GLIMPCE Profile J that crosses the Grenville Front Tectonic Zone from Green et al. (1988). The vertical axis is two-way travel time and the horizontal axis is distance. B) Location map of Profile J, showing position of the Grenville Front. The large arrow points to the part of the GFTZ examined in this study, the small arrows to the portion of Profile J shown in the line drawing. The shaded area is covered by Paleozoic sedimentary rocks.

1.2) links this reflective portion of Profile J to the shore of Georgian Bay, 80 km north, where rocks of the GFTZ are well exposed (GSC, 1987). Based on the outcrop patterns mapped by Davidson and Bethune (1988) and Frarey (1985), Green et al. (1988) attributed the high reflectivity across the GFTZ either to velocity contrasts across highly strained and attenuated lithologic contacts, or to anisotropic effects associated with major mylonite zones.

Reflections attributed to the GFTZ in Profile J have apparent dips that systematically decrease to the southeast from 35 to 25 degrees. This pattern is mimicked by structures and fabrics in the rocks on the north shore of Georgian Bay (Davidson and Bethune, 1988). These strong, dipping reflections were recorded to 9 seconds two way travel time (ca. 30 km depth) and weaker, more ambiguous reflections were observed to times as great as 14 seconds (ca. 45 km depth). Profile J shows evidence of high strain that is pervasive throughout the entire thickness of the continental crust (Green et al., 1988).

Purpose and Extent of Study

This study focuses on the laboratory and in situ compressional wave velocities of rocks from the southernmost exposures of the Grenville Front Tectonic Zone (GFTZ) and endeavors to explain the origin of the unusually

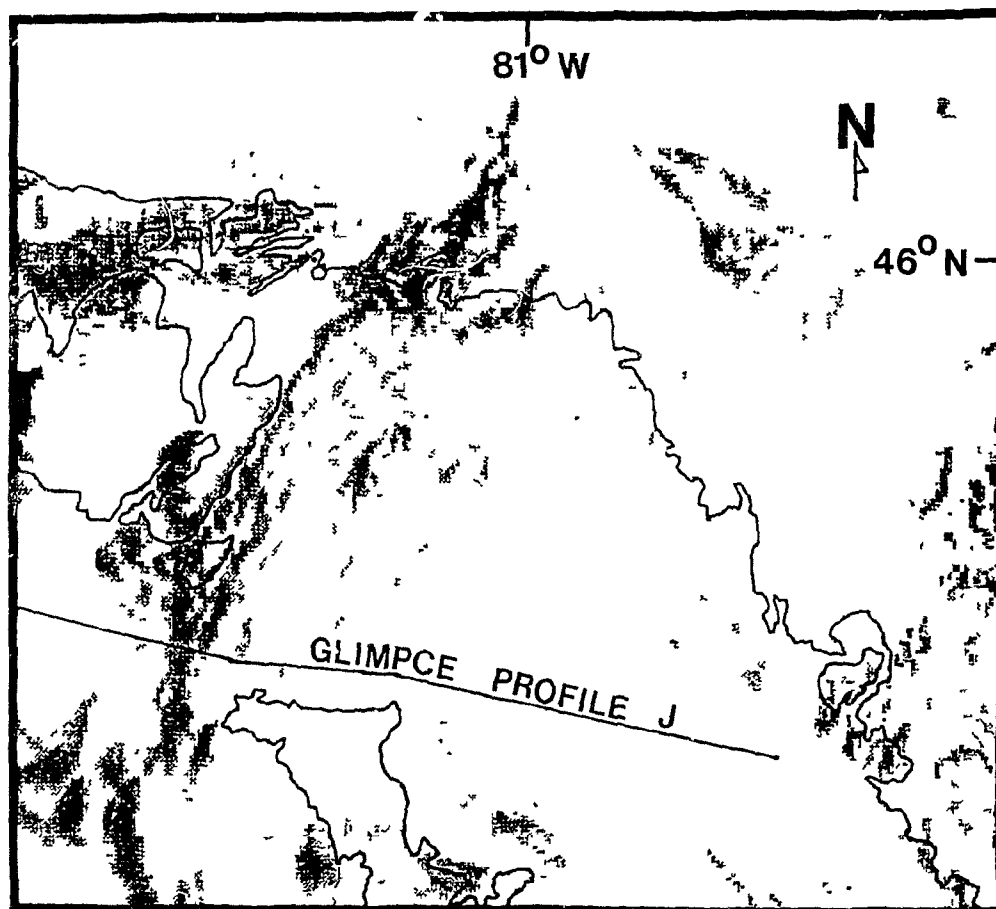


Figure 1.2. Aeromagnetic map of Georgian Bay (GSC, 1987). The strong magnetic signature correlates the reflective portion of Profile J to the rocks exposed on the north shore of Georgian Bay.

high amplitude dipping reflectors underlying this major geological and geophysical discontinuity. These data will add to the current understanding of what causes seismic reflectivity in highly deformed regions.

This work includes laboratory studies of the effect on compressional wave velocity of (1) varying mineralogy in and between different lithologic groups, (2) different degrees of deformation within a single lithologic group and (3) different wave propagation directions within a single rock sample. The results of a series of high resolution refraction profiles provide in situ compressional and shear wave velocities for the uppermost crust in the same area. The combination of a laboratory study of compressional wave velocity at elevated pressures and a series of in situ velocity experiments over the same rocks is uncommon, and provides considerable insight into the seismic response of highly deformed rocks throughout the entire thickness of the continental crust. This dual approach of laboratory and in situ velocity determinations also allows an assessment of the effect of fractures on shallow velocity structure in crystalline rocks, and in addition, addresses the issue of the suitability of laboratory derived velocities for realistic crustal modelling.

Construction of synthetic models based on geologic relationships and laboratory derived velocities is also an

effective way of assessing the seismic response of geologic structures. This work includes a series of highly detailed, one-dimensional models to assess the effect of very thin, irregularly spaced layers on crustal reflectivity. More general, two-dimensional models help constrain the effects of lithologic variability on crustal reflection response. Used together, the modeling results help explain the high reflectivity of GLIMPCE Profile J, and have broader implications for understanding the origin of reflective lower crust throughout the world.

The lower continental crust is often, although not always, highly reflective (Meissner, 1986; Wever et al., 1990). When reflective lower crust coincides with high velocities (>7.0 km/s), large volumes of mafic rocks are commonly invoked to explain the reflective character (Holbrook et al., 1988; Mueller et al., 1987; Burke and Fountain, 1990). However, not all occurrences of reflective lower crust coincide with high velocity regions (e.g. the GFTZ (Green et al., 1988; Mereu et al., 1989), the Georgina Basin (Finlayson, 1982; Mathur, 1983) and Scotland (Brewer et al., 1983; Jones et al., 1984)). Explaining the origins of the lower crustal reflections in these areas is often difficult. This work provides a model that can be used to explain both the presence and absence of lower crustal reflections in average velocity crust.

Geology of the Grenville Front

Wynne-Edwards (1972) divided the Grenville Province into a number of sub-provinces, based on differences in metamorphism and structural style. In the southernmost area of the Grenville Province he identified three sub-provinces (Figure 1.3); (1) the Central Gneiss Belt (CGB), (2) the Central Metasedimentary Belt (CMB) and (3) the Grenville Front Tectonic Zone (GFTZ). The CGB comprises gneissic rocks, many of which are migmatized, and a number of large scale ductile shear zones, many of which show northwest- directed thrusting (Davidson, 1985). The CMB comprises highly deformed amphibolite to granulite facies metasedimentary rocks (Davidson, 1985). The GFTZ, correlated with the reflective portion of Profile J by its distinctive magnetic anomaly (GSC, 1987), is a thin zone of very highly deformed rocks with amphibolite grade metamorphism and front-parallel foliation (Davidson, 1985; Davidson and Bethune, 1988). The GFTZ is exposed for almost 2000 km from Georgian Bay to Labrador. The southernmost GFTZ (the Beaverstone Terrane of Rivers et al., 1989) and the adjacent Southern Province region are described in more detail below.

Figure 1.3. Divisions of the southern Grenville Province from Wynne-Edwards (1972). The darkly shaded region is the GFTZ and Paleozoic sedimentary rocks are shown as the stippled pattern. The inset in the upper right shows the extent of the exposed Grenville Province from Georgian Bay to Labrador. The location of Figure 1.4 is shown by the small box on the north shore of Georgian Bay.

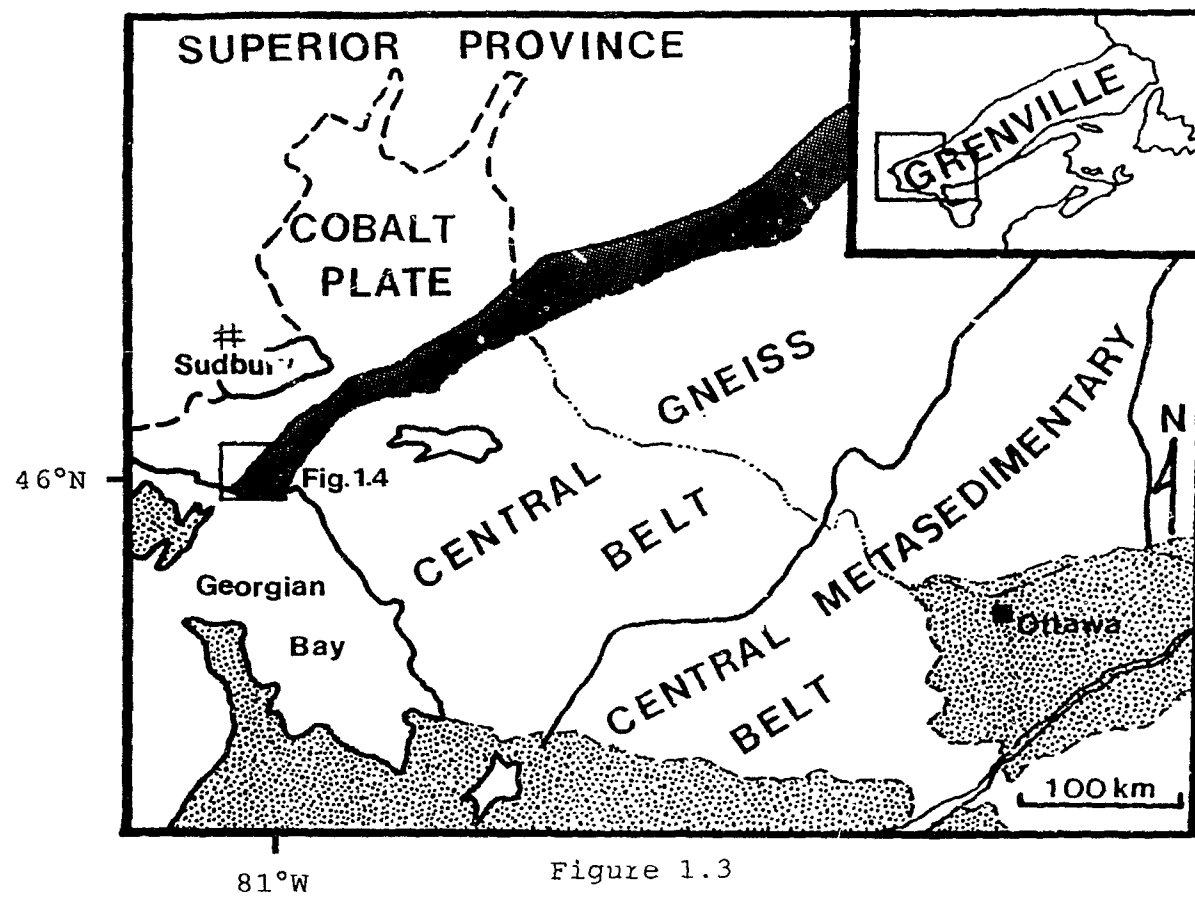


Figure 1.3

Southern Province and Plutonic Suites

Between Killarney and Sudbury (Figure 1.4) the GFTZ is juxtaposed against rocks of the Southern Province, the Killarney Complex and other mid-Proterozoic plutonic rocks (Card and Lumbers, 1978). The Southern Province consists of a sequence of Archean passive-margin deposits (Huronian Supergroup) intruded by diabasic sills (Nipissing Diabase). These rocks were folded about east-west axes during the equivalent to the Penokean Orogeny at 2.33 Ga (Zolnai, et al., 1984).

The southeast part of this region was deformed during the intrusion of the Killarney Complex at 1.74 Ga (Davidson, 1986; van Breemen and Davidson, 1988). Later anorogenic granites (including the Bell Lake Granite and Annie Lake Complex) were emplaced at 1.45-1.5 Ga (Krogh and Davis, 1971; Stockwell, 1982). Both of these granite suites are similar to rocks found in the midcontinent region of the United States (Bickford et al., 1986) and gravity and magnetic data support their southward continuation to that area (O'Hara and Hinze, 1980; GSC, 1987).

Huronian Supergroup

The Huronian Supergroup in the area adjacent to the Grenville Front Tectonic Zone consists of 10 formations (Bar River, Gordon Lake, Lorrain, Gowganda, Serpent,

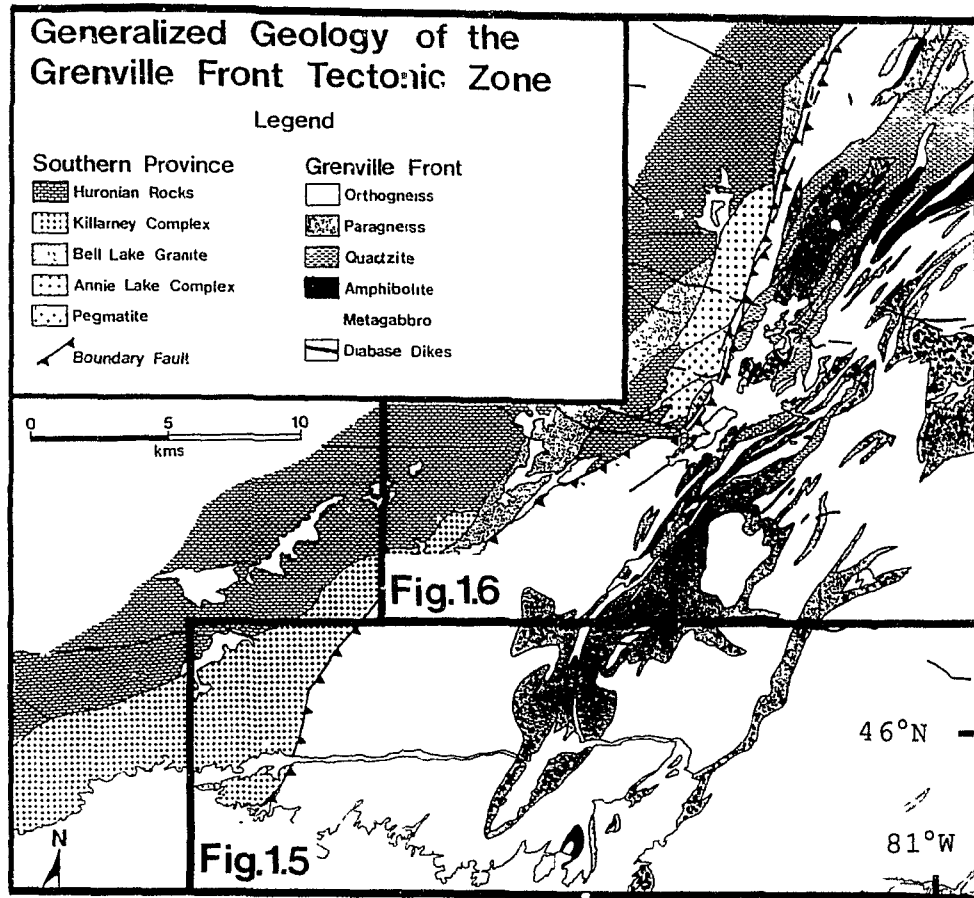


Figure 1.4. Generalized geology of the southernmost exposures of the GFTZ (modified from Frarey, 1985). The position of the GFTZ boundary fault as defined by Davidson (1986) is shown as the heavy, barbed line. Note the increase in complexity of rock distributions within the GFTZ from southwest to northeast.

Espanola, Bruce, Mississagi, Pecors and Ramsey Lake Fms.). Virtually all rocks in the Huronian are clastic, with an estimated total thickness of 9200 meters (Frarey, 1985). Paleocurrent data (Young, 1968) and sediment thickening patterns (Card et al., 1972) suggest these units were carried from their source by southward directed currents. Card et al. (1984) suggest that the Huronian succession was deposited on a south-facing passive continental margin.

Nipissing Diabase

The Huronian rocks were intruded by sheet-like metagabbro masses up to 500 meters thick and 15 km in length (Frarey, 1985). These diabasic rocks have plagioclase and hornblende or actinolite-tremolite as the major minerals and minor amounts of quartz, epidote, apatite, sphene, ilmenite, sulphides and carbonate (Frarey, 1985).

Killarney Complex

The volcanic and plutonic rocks of the Killarney Complex have been dated at 1740 Ma (van Breemen and Davidson, 1988) and show a weak planar fabric dipping steeply to the north or to the northeast (Davidson, 1986). The Killarney Complex consists of two members: (1) massive, pink, leucocratic granite that in places, especially along the northwest boundary, has xenoliths or screens of exotic material (Davidson, 1986), and (2) a composite member which

consists of foliated granite, the Lighthouse Porphyry, a fine grained felsite of the same composition as the main granite (Quirke and Collins, 1930) and equigranular rhyolite and felsic volcanoclastic rocks (Davidson, 1986). The metamorphic grade of the Killarney rocks is no greater than greenschist facies, with albite, muscovite, chlorite, green biotite, epidote and titanite as common, fine-grained metamorphic minerals (Davidson, 1986).

Bell Lake Granite and Annie Lake Complex

The Bell Lake Granite and Annie Lake Complex were originally included as parts of the Killarney Batholith (Quirke and Collins, 1930). However, recent mapping (Davidson, 1986) and isotopic dating (Krogh et al., 1971; Stockwell, 1982; van Breemen and Davidson, 1988) show that a significant time interval passed between the intrusion of the Killarney Granite at 1740 Ma and that of the Bell Lake-Annie Lake suites at 1535-1470 Ma. The Bell Lake Granite is a coarse, porphyritic granite with up to 15 per cent biotite. The Annie Lake Complex consists of three texturally distinct granites (Frarey, 1985): (1) an equigranular, fine- to medium-grained granite, (2) an equigranular to sub-porphyritic medium-grained granite and (3) a highly porphyritic, coarse-grained granite resembling the Bell Lake Granite.

GFTZ Boundary Faults

The northwest limit of the Grenville Province in Ontario is defined by the system of GFTZ boundary faults (Card and Lumbers, 1977). The boundary fault system of the Grenville Front is commonly expressed as a topographic low, with Archean or Mid-Proterozoic plutonic rocks on the northwest side, and highly deformed gneissic rocks of uncertain origin on the southeast side (Davidson, 1986). In its southernmost exposures it represents an abrupt break in structural style, degree of metamorphism and geologic age (Davidson and Bethune, 1988).

Davidson (1986) located the boundary fault of the GFTZ southeast of the Mid-Proterozoic granitic rocks (Figure 1.4). On the islands off the southern shore of Philip Edward Island the boundary fault is a zone of protomylonite, mylonite and ultramylonite that is tens of meters thick, always dipping moderately to the southeast (Davidson, 1986; Davidson and Bethune, 1988). These rocks have very well developed shear fabrics, including C-S fabric, shear band foliation, and rotated feldspar augen, with all kinematic indicators showing northwest-directed thrusting (Davidson, 1986). Narrow bogs or valleys mark the trace of the boundary fault between Collins Inlet and Tyson Lake. In the Tyson Lake region there are a number of

splays of the mylonite zone (Frarey and Cannon, 1969), but similar structural features are observed.

GFTZ Rocks

Southeast of the boundary faults lies a region of highly deformed rocks with a strong foliation generally parallel to the boundary fault system (Frarey and Cannon, 1969). Quirke and Collins (1930) attempted to relate the deformed and metamorphosed rocks in the GFTZ to metamorphic equivalents of rocks of the neighboring Southern Province, but such correlations cannot be substantiated (Frarey, 1985). The distribution of rock types (Figure 1.4) is not uniform along the length of the front (Frarey and Cannon, 1969). The region surrounding Collins Inlet is dominated by orthogneiss outcrops, but the area around Tyson Lake has a greater variety of rock types including paragneiss, amphibolite gneisses and quartzite gneisses. Therefore the rock types and distribution patterns in these regions will be discussed in separate sections.

Collins Inlet Area

Along Collins Inlet and eastward to the main entrance to French River (Figure 1.5) the GFTZ comprises a variety of variably deformed orthogneiss assemblages, with minor amounts of other rock types (Davidson and Bethune, 1988). The orthogneiss units are dominantly granitic along Collins

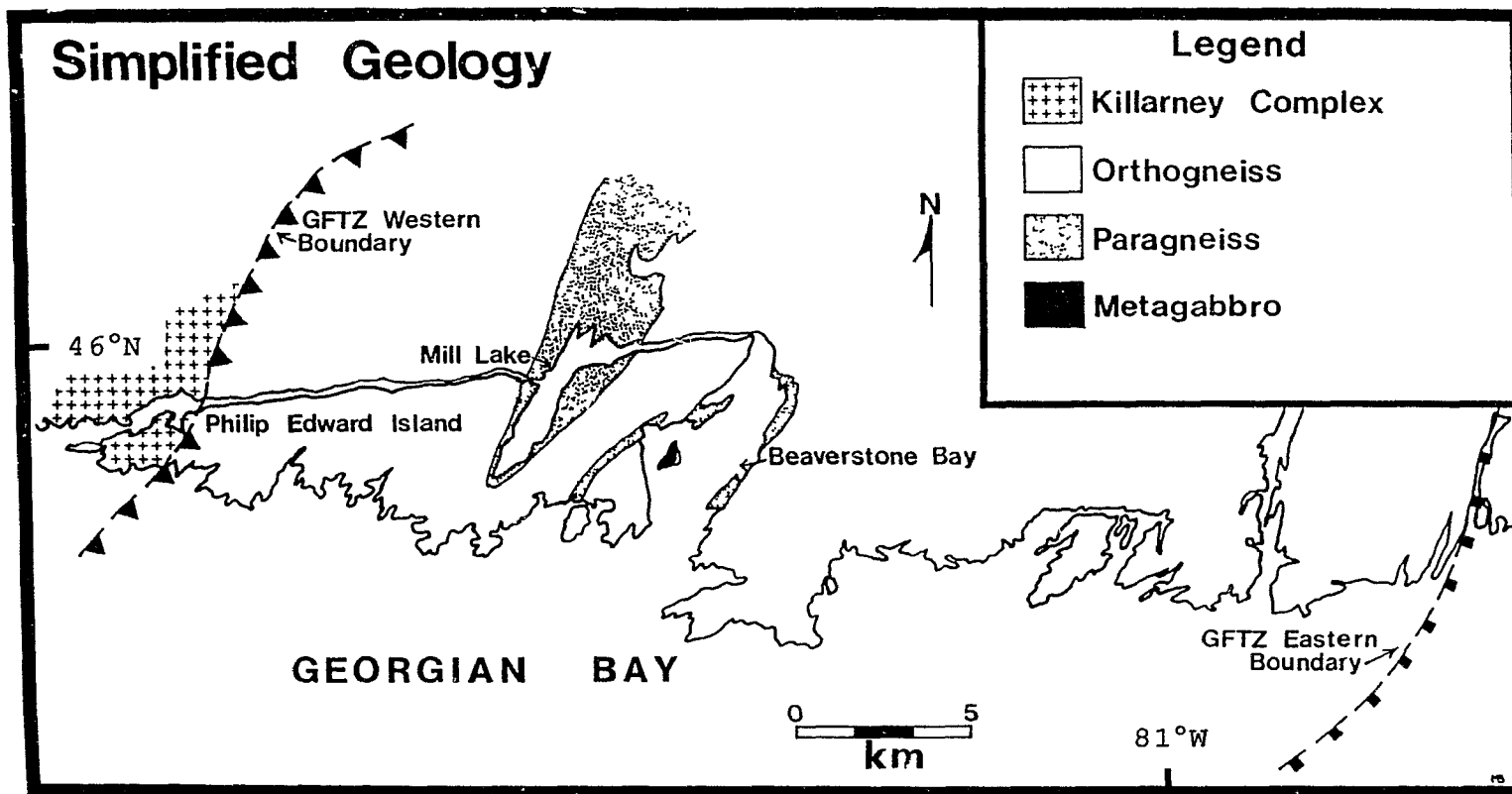


Figure 1.5. Generalized geologic map from Collins Inlet to French River (modified from Davidson and Bethune, 1988). The variations in orthogneiss assemblages mapped by Davidson and Bethune are consolidated into a single lithology in this figure (see text for explanation).

Inlet (see Chapter 2), but other compositions (i.e. granodiorite, tonalite, quartz syenite and quartz monzonite) occur locally (Frarey, 1985; Davidson and Bethune, 1988). Commonly these units are bounded by high strain zones that expose mylonitic equivalents of the adjacent rocks and commonly have well developed stretching lineations (Davidson and Bethune, 1988). Kinematic indicators in these mylonite zones show the same sense of displacement as seen in the boundary fault of the GFTZ. Davidson (1986) suggested that the granitic orthogneiss units along Collins Inlet may be deformed or reworked equivalents of the Killarney Complex, a suggestion substantiated by isotopic ages from van Breemen and Davidson (1988).

Mill Lake and Beaverstone Bay (Figure 1.5) are notable as the only areas in these southernmost exposures of the GFTZ to have paragneiss outcrops. At Mill Lake three types of paragneiss are common (Davidson and Bethune, 1988; Frarey, 1985): (1) pelitic schist with garnet, sillimanite, biotite, quartz and plagioclase; (2) semi-pelitic schist with garnet, biotite, quartz, plagioclase and potassium feldspar; and (3) quartzite with minor muscovite. Calcareous gneiss occurs in small amounts in this region. The rocks at Beaverstone Bay resemble those at Mill Lake,

with minor textural variations (Davidson and Bethune, 1988).

Tyson Lake Area

Unlike the geology of Collins Inlet, a wide variety of rocks with different compositions is exposed in the vicinity of Tyson Lake (Figure 1.6). Most of the mapped units are composite due to the complex intercalation of different units. The interlayering of units occurs on a variety of scales from centimeters to tens of meters. Orthogneiss units account for approximately one third of all outcrops in this area, and are similar to those exposed along Collins Inlet, with the same compositional range and structural features (Frarey, 1985). Paragneiss units at Tyson Lake are similar to the assemblages at Mill Lake and Beaverstone Bay, but account for a higher proportion of outcrop and occur as elongate masses approximately 1 km wide and up to 10 km in length.

In addition to the paragneiss and orthogneiss assemblages, amphibolite gneisses, metagabbro bodies, quartzite and quartzitic gneisses occur in this area. These units form elongate, lens-shaped masses 1-2 km in width and up to 15 km in length. Different lithologic units are often separated by mylonitic shear zones.

The amphibolite gneisses are composed almost entirely of equal proportions of plagioclase and hornblende. The

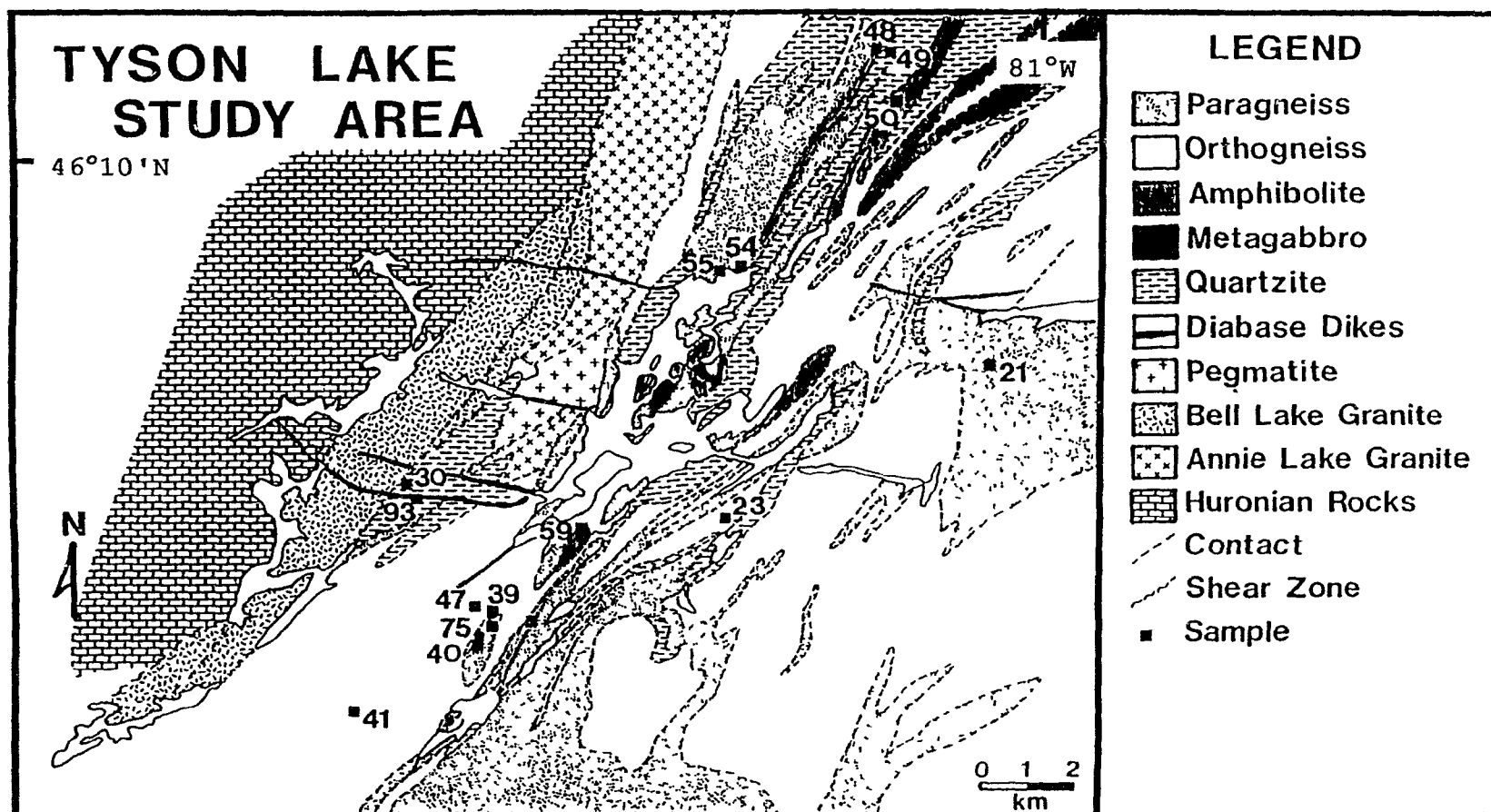


Figure 1.6. Generalized geologic map of the Tyson Lake region (modified from Frarey, 1985). Sample locations of samples for velocity measurement (GFTZ sample suite) are shown.

protoliths may have been sedimentary or igneous rocks, but the origins are unclear due to their deformation and pervasive recrystallization (Frarey, 1985). Relict igneous textures are preserved in metagabbros, and their origins are less equivocal. The metagabbros are mineralogically equivalent to the amphibolite gneisses, with plagioclase, hornblende and biotite as the common mineral assemblage.

The quartzite gneisses around Tyson Lake have been divided into three types (Frarey and Cannon, 1969). The first is a vitreous, recrystallized quartzite with thin mica partings that occurs in small lenses. Volumetrically more important is feldspathic quartzite gneiss that has up to 30 per cent plagioclase and potassium feldspar and minor amounts of biotite, garnet and sillimanite. Between Tyson Lake and outcrops of the Bell Lake Granite is the third type of quartzite, which has been successfully correlated with the Lorrain Formation of the Huronian Supergroup (Frarey, 1985). The Lorrain enclave may have been engulfed during intrusion of the Bell Lake Granite and subsequently deformed by Grenvillian deformation (Frarey, 1985).

CHAPTER 2

LABORATORY VELOCITY MEASUREMENTS

Sample Descriptions

Samples for physical properties measurement were collected from two areas, Collins Inlet and Tyson Lake, in the southernmost part of the GFTZ (Figure 2.1). The sampling in Collins Inlet included a densely spaced traverse of the GFTZ boundary fault. These areas were chosen because each offers relatively easy access to representative suites of rocks. Sample localities are shown in Figures 2.2, 2.3 and 1.6. Rocks that lacked secondary mineral alteration and intense visible fractures were preferentially chosen for the laboratory study. Some samples were not used for velocity measurement because of small size, extensive small fractures or extreme difficulty in coring.

Thin sections were prepared for all samples and modal mineralogies determined by the point-counting technique, with at least 1000 points counted on each slide. Plagioclase compositions were determined, where possible, by the Michel-Levy method. However, many of the strained rocks had plagioclase grains which showed strong undulatory extinction, which prevented the measurement of plagioclase

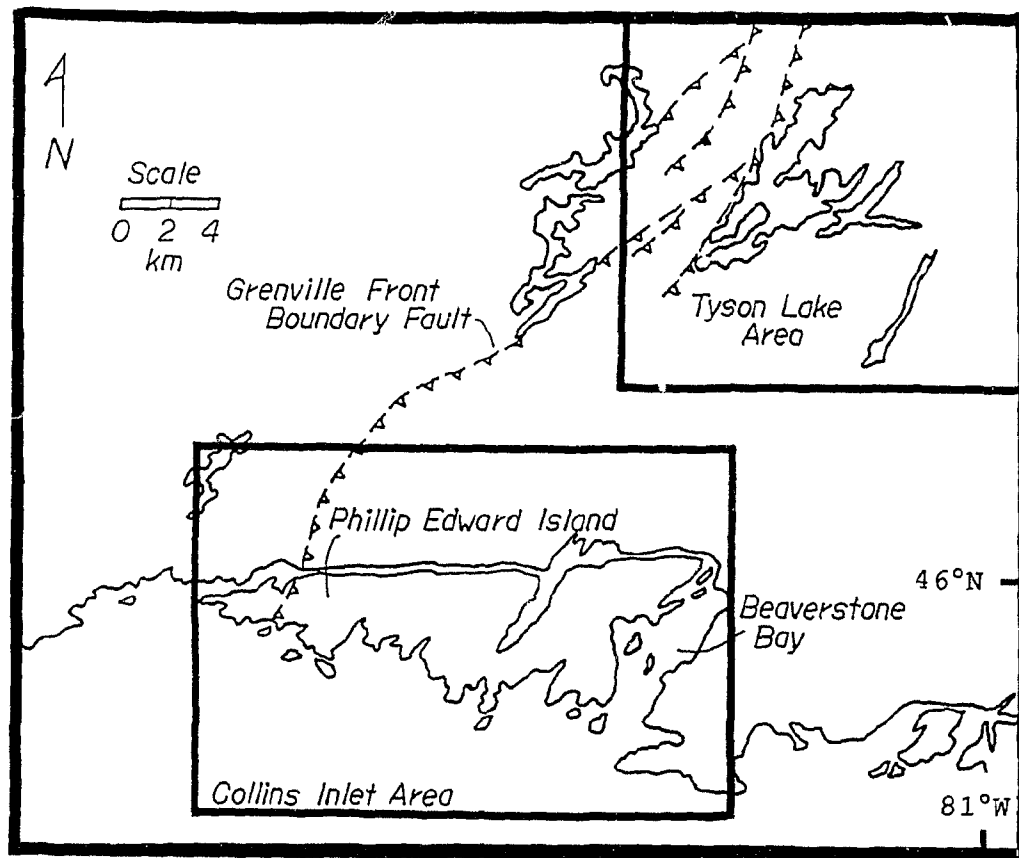


Figure 2.1. Geologic map modified from Frarey (1985) showing the location of the Collins Inlet (Figure 2.2) and the Tyson Lake (Figure 2.4) regions.

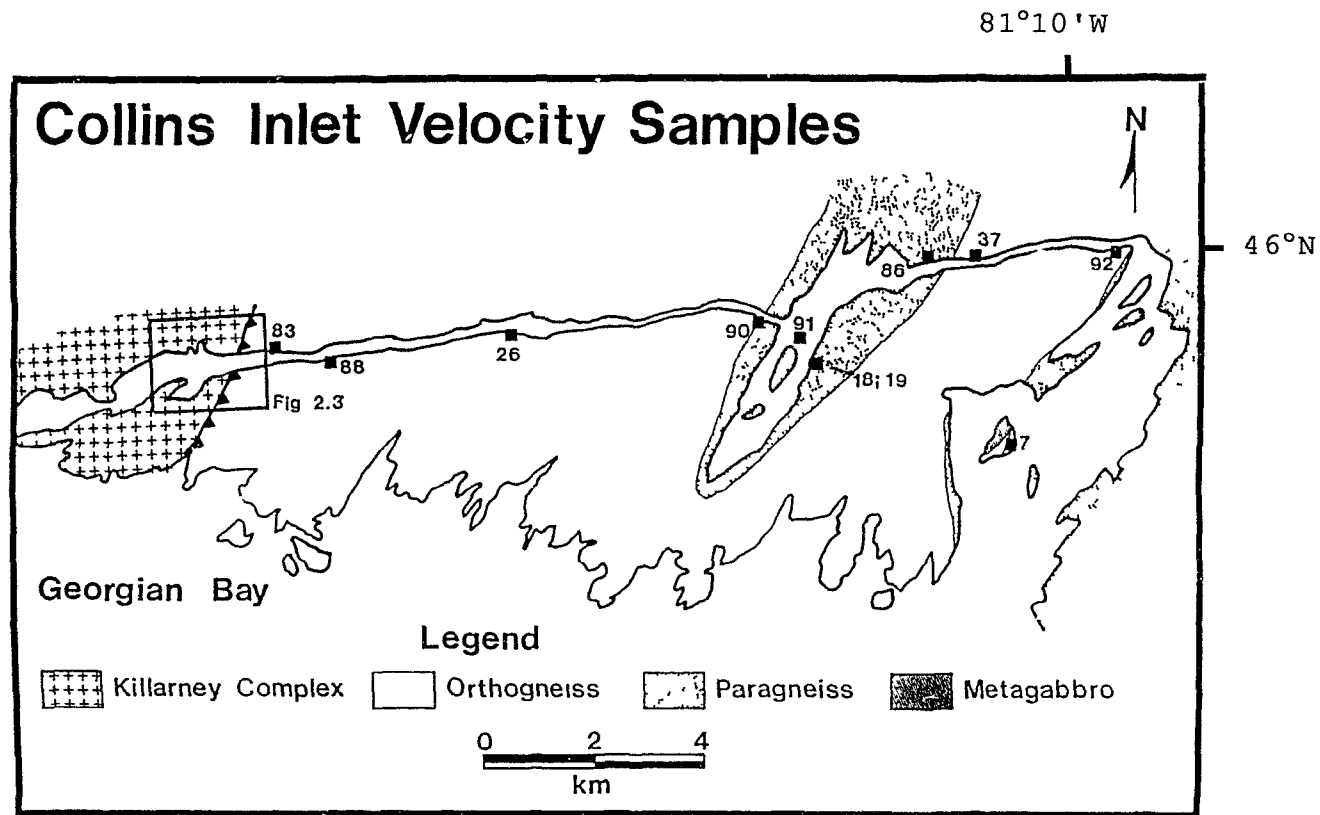


Figure 2.2. Location of velocity samples from Collins Inlet (GFTZ sample suite). The location of Figure 2.3 is also indicated.

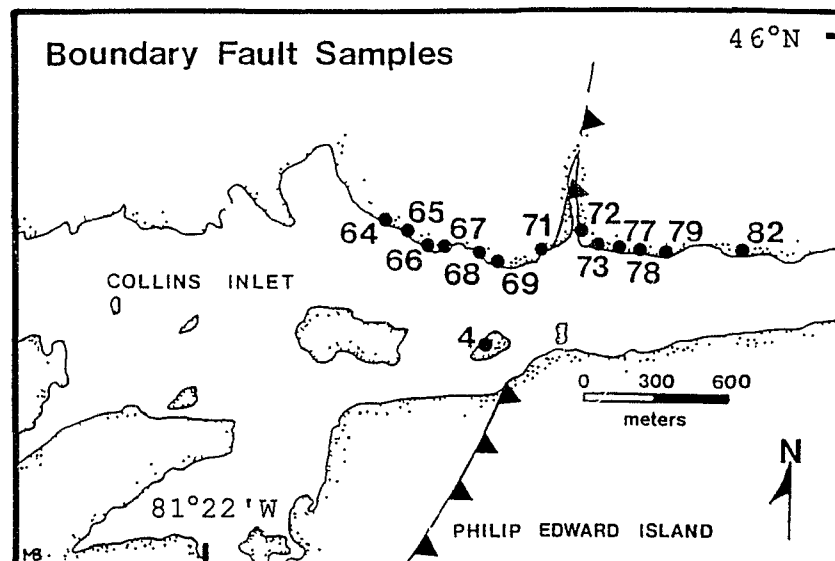


Figure 2.3. Location of velocity samples from the GFTZ boundary fault traverse (GFTZ sample suite). All of the samples collected from the north shore of Collins Inlet are granitic, with varying degrees of deformation. Sample GFTZ-4 is a metamorphosed mafic dike.

Table 2.1 Modal mineralogies (in %) of GFTZ samples determined by point-count analysis.

Sample	Otz	Plag	Kspr	Bi	Hb	Opq	Gar	Ap	Chl	Musc	Sil	Opx	Cpx	Zir	Sph	Oli
GFTZ- 4	6.9	11.9	0.0	0.0	56.1	2.8	0.0	5.9	0.4	0.0	0.0	0.0	0.0	0.0	16.0	0.0
GFTZ- 7	23.8	50.8	2.6	13.1	7.0	1.7	0.0	1.0	0.0	0.0	0.0	0.0	0.0	0.0	0.0	0.0
GFTZ-18	26.9	37.3	10.6	18.8	0.0	3.0	5.4	0.0	0.0	0.0	0.7	0.0	0.0	0.0	0.0	0.0
GFTZ-19	2.3	19.3	0.0	23.3	50.7	2.3	0.5	0.0	0.7	0.0	0.0	0.0	0.0	0.4	0.0	0.0
GFTZ-21	15.2	44.6	8.7	20.2	2.0	2.0	2.8	1.3	1.0	0.0	2.2	0.0	0.0	0.0	0.0	0.0
GFTZ-23	43.8	18.7	13.2	14.6	0.0	0.1	8.6	0.4	0.0	0.5	0.0	0.0	0.0	0.0	0.1	0.0
GFTZ-26	20.0	35.7	31.5	10.9	0.0	1.2	0.1	0.6	0.0	0.0	0.0	0.0	0.0	0.1	0.0	0.0
GFTZ-30	30.1	30.1	2.5	15.4	0.2	1.8	0.0	0.2	0.0	19.7	0.1	0.0	0.0	0.0	0.0	0.0
GFTZ-37	3.2	38.2	0.0	5.7	37.0	1.0	0.0	0.0	0.0	0.0	0.0	10.0	4.9	0.0	0.0	0.0
GFTZ-39	0.6	36.9	0.0	14.9	46.5	0.2	0.0	0.9	0.0	0.0	0.0	0.0	0.0	0.0	0.0	0.0
GFTZ-40	10.9	31.1	0.5	14.7	37.2	2.2	0.0	1.0	2.2	0.0	0.0	0.0	0.0	0.0	0.0	0.0
GFTZ-41	31.1	38.3	2.4	22.7	0.0	2.1	0.0	1.6	0.2	0.0	0.0	0.0	0.0	0.4	0.0	0.0
GFTZ-47	18.3	27.1	11.3	20.7	18.6	1.3	1.5	1.2	0.0	0.0	0.0	0.0	0.0	0.0	0.0	0.0
GFTZ-48	5.4	51.6	0.0	32.6	0.0	2.1	1.0	0.4	1.5	0.0	0.0	5.4	0.0	0.0	0.0	0.0
GFTZ-49	65.8	14.1	10.0	8.0	0.0	0.9	0.0	0.0	0.0	1.2	0.0	0.0	0.0	0.0	0.0	0.0
GFTZ-50	21.8	35.1	0.2	30.6	0.0	0.4	11.8	0.0	0.1	0.0	0.0	0.0	0.0	0.0	0.0	0.0
GFTZ-54	0.0	41.5	0.0	3.6	44.6	1.3	0.0	0.3	0.4	0.0	0.0	0.0	0.0	0.0	0.0	0.0
GFTZ-55	23.9	23.6	13.9	36.7	0.0	0.5	0.2	0.6	0.0	0.0	0.0	0.0	0.0	0.6	0.0	0.0
GFTZ-59	0.0	54.2	0.0	0.1	36.6	8.4	0.0	0.6	0.0	0.0	0.0	0.0	0.0	0.1	0.0	0.0
GFTZ-64	28.1	33.0	29.9	1.6	1.4	1.7	0.0	0.3	0.0	0.7	0.0	0.0	0.0	1.3	0.0	0.0
GFTZ-65	29.0	32.4	28.2	2.7	2.2	3.0	0.0	0.3	1.6	0.0	0.0	0.0	0.0	0.2	0.4	0.0
GFTZ-66	27.7	39.1	21.0	5.2	0.0	1.5	0.0	0.0	1.5	0.0	0.0	0.0	0.0	0.0	0.9	0.0
GFTZ-67	29.2	30.0	28.4	0.4	0.0	3.2	0.0	0.7	5.6	0.0	0.0	0.0	0.0	0.1	2.4	0.0
GFTZ-68	n.a.															
GFTZ-69	28.7	31.2	28.6	1.4	0.0	2.9	0.0	1.0	5.0	0.0	0.0	0.0	0.0	0.2	2.0	0.0

Table 2.1 (cont)

Sample	Otz	Plag	Kspr	Bi	Hb	Opx	Gar	Ap	Chl	Musc	Sil	Opx	Cpx	Zir	Sph	Oli
GFTZ-71	n.a.															
GFTZ-72	25.4	36.0	23.5	5.9	4.1	2.8	0.0	1.0	0.7	0.0	0.0	0.0	0.0	0.0	0.6	0.0
GFTZ-73	29.4	34.0	32.4	0.9	0.0	0.8	0.0	0.7	1.5	0.0	0.0	0.0	0.0	0.0	0.3	0.0
GFTZ-75	3.2	40.3	0.0	5.8	47.8	0.3	0.0	1.3	0.1	0.0	0.0	1.0	0.0	0.2	0.0	0.0
GFTZ-77	28.7	32.8	29.8	6.0	0.0	1.9	0.0	0.0	0.2	0.0	0.0	0.0	0.0	0.0	0.2	0.0
GFTZ-78	25.1	34.1	31.9	3.2	2.0	2.9	0.3	0.1	0.3	0.0	0.0	0.0	0.0	0.0	0.1	0.0
GFTZ-79	30.0	32.8	32.8	5.0	2.5	3.3	0.2	0.0	0.6	0.0	0.0	0.0	0.0	0.0	0.1	0.0
GFTZ-82	30.0	29.1	26.3	8.6	0.9	2.6	0.0	0.6	0.0	0.0	0.0	0.0	0.0	0.0	1.9	0.0
GFTZ-83	33.5	30.3	23.4	6.2	3.1	1.4	0.0	0.4	0.1	0.0	0.0	0.0	0.0	0.0	1.6	0.0
GFTZ-86	9.7	24.2	0.0	8.5	34.5	0.8	0.0	0.0	2.3	0.0	0.0	9.2	0.0	0.0	0.0	0.0
GFTZ-87	0.0	25.0	0.0	3.1	62.7	9.2	0.0	0.0	0.0	0.0	0.0	0.0	0.0	0.0	0.0	0.0
GFTZ-88	21.8	36.6	22.1	5.7	9.0	2.8	0.0	0.1	0.0	0.0	0.0	0.0	0.0	0.1	1.8	0.0
GFTZ-90	25.3	54.1	3.0	5.9	4.4	3.1	0.0	0.6	3.5	0.0	0.0	0.0	0.0	0.0	0.0	0.0
GFTZ-91	26.7	26.7	15.8	21.0	0.0	1.3	0.6	0.4	0.6	2.7	0.0	0.0	0.0	0.1	0.0	0.0
GFTZ-92	0.0	45.9	0.0	0.0	11.8	13.8	0.0	0.0	0.0	0.0	0.0	0.0	0.0	0.1	0.0	0.0
GFTZ-93	0.0	62.9	0.0	4.5	0.3	6.1	0.0	0.0	0.0	0.0	0.0	0.0	0.0	0.0	0.0	13.2

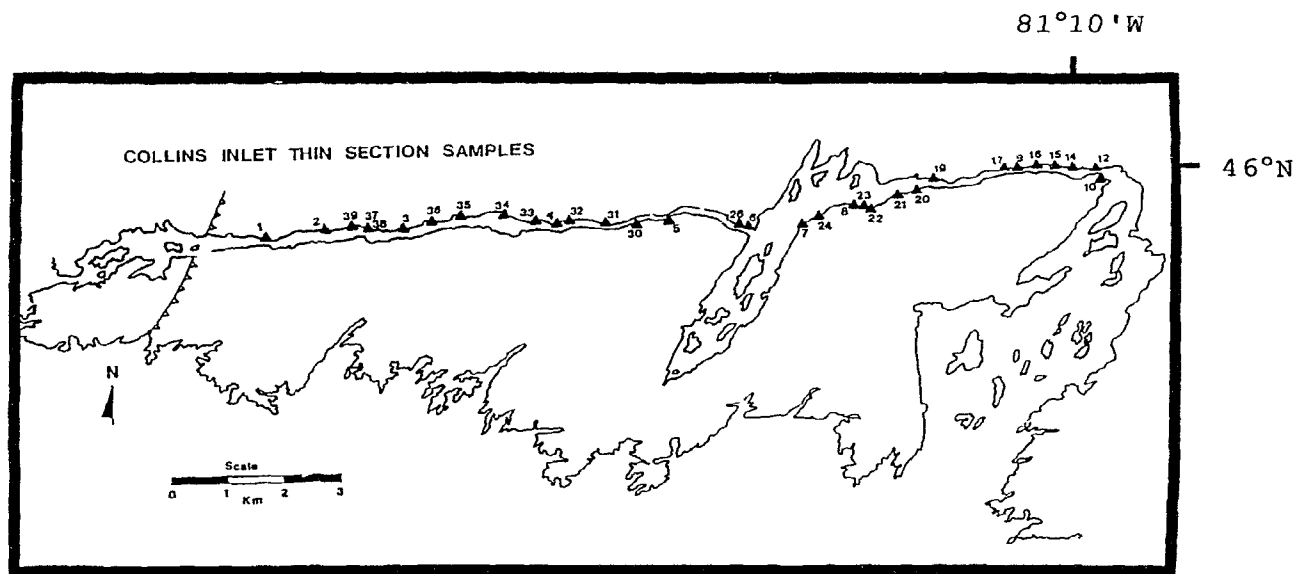


Figure 2.4. Location of thin section samples along Collins Inlet (CI sample suite). These samples were obtained to determine the mineralogy of the orthogneiss assemblages mapped by Davidson and Bethune (1988).

Table 2.2 Modal mineralogies (in %) of Collins Inlet thin section samples determined by point-count analysis.

Sample	Otz	Plag	Kspr	Bi	Hb	Opq	Gar	Ap	Chl	Musc	Sil	Cpx
CI- 1	31.1	19.5	36.8	7.8	0.1	0.8	0.0	0.0	0.0	0.0	0.0	0.0
CI- 2	42.3	34.6	13.9	7.4	0.0	1.7	0.0	0.0	0.0	0.0	0.0	0.0
CI- 3	28.9	17.1	37.5	8.8	0.0	0.6	0.0	0.0	0.0	0.0	2.0	0.0
CI- 4	35.6	26.1	30.3	5.8	0.0	0.9	0.0	0.0	0.2	0.0	0.5	0.0
CI- 5	6.6	45.3	0.0	2.9	28.5	12.0	0.0	0.0	0.0	0.0	0.0	0.0
CI- 6	37.8	19.4	25.7	13.8	2.5	0.8	0.0	0.0	0.0	0.0	0.0	0.0
CI- 7	36.7	11.1	22.3	16.6	0.0	0.2	11.9	0.0	0.0	0.0	0.2	0.0
CI- 8	53.0	13.1	15.7	17.1	0.0	0.8	0.0	0.0	0.0	0.0	0.3	0.0
CI- 9	19.5	31.9	22.3	8.7	8.7	3.4	0.0	0.0	0.2	4.3	0.2	0.0
CI-10	11.4	50.7	0.0	4.5	23.2	4.5	0.0	0.0	0.0	5.2	0.0	0.0
CI-12	21.1	34.5	29.7	2.2	0.1	4.3	0.0	0.0	0.2	0.2	0.0	0.0
CI-14	39.9	27.2	9.4	7.1	12.2	1.1	0.0	0.0	0.0	0.0	0.0	0.0
CI-15	31.2	40.1	9.1	7.3	10.6	1.7	0.0	0.0	0.0	0.0	0.0	0.0
CI-17	35.3	37.5	6.4	7.9	5.4	3.0	0.0	0.5	0.0	2.4	1.0	0.0
CI-19	1.0	41.7	0.0	1.0	33.8	1.0	0.0	1.0	0.0	0.0	0.0	8.7
CI-20	22.0	41.0	17.0	12.1	5.3	2.0	0.0	0.0	0.1	0.0	0.0	0.0
CI-21	26.2	25.9	8.9	31.7	0.7	1.5	5.1	0.0	0.0	0.0	0.0	0.0
CI-22	56.9	20.2	12.9	8.4	0.0	1.6	0.0	0.0	0.0	0.0	0.0	0.0
CI-23	35.5	29.1	2.9	24.9	0.0	0.5	7.0	0.0	0.0	0.0	0.0	0.0
CI-24	8.8	18.9	22.9	36.0	0.0	0.4	2.2	0.0	0.0	3.0	0.0	0.0
CI-26	27.9	25.1	26.8	14.9	1.2	4.1	0.0	0.0	0.0	0.0	0.0	0.0
CI-30	0.0	26.2	0.0	18.0	43.6	2.2	0.0	0.0	0.0	0.0	0.0	0.0
CI-31	28.9	35.5	26.9	6.2	0.9	1.1	0.1	0.1	0.0	0.0	0.1	0.0
CI-32	26.8	42.7	16.8	8.1	4.2	0.2	0.0	0.1	0.0	0.0	0.1	0.0
CI-33	31.1	36.5	22.9	5.5	0.0	0.4	0.0	0.0	0.0	0.0	1.4	0.0

Table 2.2 (cont)

Sample	Otz	Plag	Kspr	Bi	Hb	Opg	Gar	Ap	Chl	Musc	Sil	Cpx
CI-34	33.6	32.5	20.4	10.4	0.0	0.9	0.0	0.1	0.0	0.0	0.0	0.0
CI-35	47.3	27.8	19.6	4.3	0.0	0.8	0.0	0.0	0.2	0.0	0.0	0.0
CI-36	35.8	25.9	22.4	13.1	1.4	1.4	0.0	0.0	0.0	0.0	0.0	0.0
CI-37	0.9	29.5	0.0	6.8	54.6	8.2	0.0	0.0	0.0	0.0	0.0	0.0
CI-38	30.2	22.8	35.3	9.0	0.0	2.4	0.0	0.0	0.2	0.0	0.0	0.0
CI-39	27.6	37.7	22.0	4.9	3.5	1.1	0.0	0.0	0.3	0.0	1.3	0.0

composition by this method. Potassium feldspars were stained with sodium-cobaltinitrate to aid in identification.

Mineralogical data for velocity samples are summarized in Table 2.1. Samples GFTZ-68 and GFTZ-71 are too fine-grained to point count, and no analysis for them are reported. Additional thin section samples were prepared for rocks collected along Collins Inlet (Figure 2.4) to help constrain mineralogic variation in the grossly similar orthogneiss assemblages observed there. These data are summarized in Table 2.2. The petrography of the lithologic units based on both of these thin section studies is described below.

Orthogneiss

Eighteen samples of orthogneiss (GFTZ-7, -26, -64, -65, -66, -67, -68, -69, -71, -72, -73, -77, -78, -79, -82, -83, -88, and -90) were collected for velocity measurement along Collins Inlet. Orthogneiss packages range in thickness from 0.2 to 2.6 km in outcrop and have lens-shaped or oval outcrop patterns (Davidson and Bethune, 1988). The samples collected included those taken along a closely spaced traverse (GFTZ-64 to GFTZ-79) of the GFTZ Boundary Fault (Figure 2.3), and many of these rocks display strong mylonitic fabrics (especially samples GFTZ-

68, -71, and -79). Typical features of these rocks include S-C fabrics, feldspar porphyroclasts (commonly rotated and with undulatory extinction) and quartz ribbons; all are commonly associated with mylonites (Lister and Snoke, 1984).

All orthogneiss samples except GFTZ-7 and GFTZ-90 can be classified as granites (Figure 2.5) using the I.U.G.S. classification scheme (Streckeisen, 1979). Accessory minerals include biotite, hornblende, opaque oxides, sphene, apatite, zircon and chlorite. Plagioclase compositions were not measured in most samples due to the strong undulatory extinction in the plagioclase grains but where measured range from An₂₂ to An₃₄. The thin section study along Collins Inlet confirms the mineralogic similarity (Figure 2.6) of the various orthogneiss units of Davidson and Bethune (1988).

Sample GFTZ-7, from the eastern edge of Philip Edward Island, is a tonalite. It is equigranular with biotite and hornblende defining a weak foliation. Quartz displays strong undulatory extinction and the plagioclase composition is An₂₇. Sample GFTZ-90, also a tonalite, was taken near the gradational contact (Davidson and Bethune, 1988) between the paragneiss unit at Mill Lake and the orthogneiss to the west (see Figure 2.2). It has a well developed fabric, including quartz ribbons, and a foliation

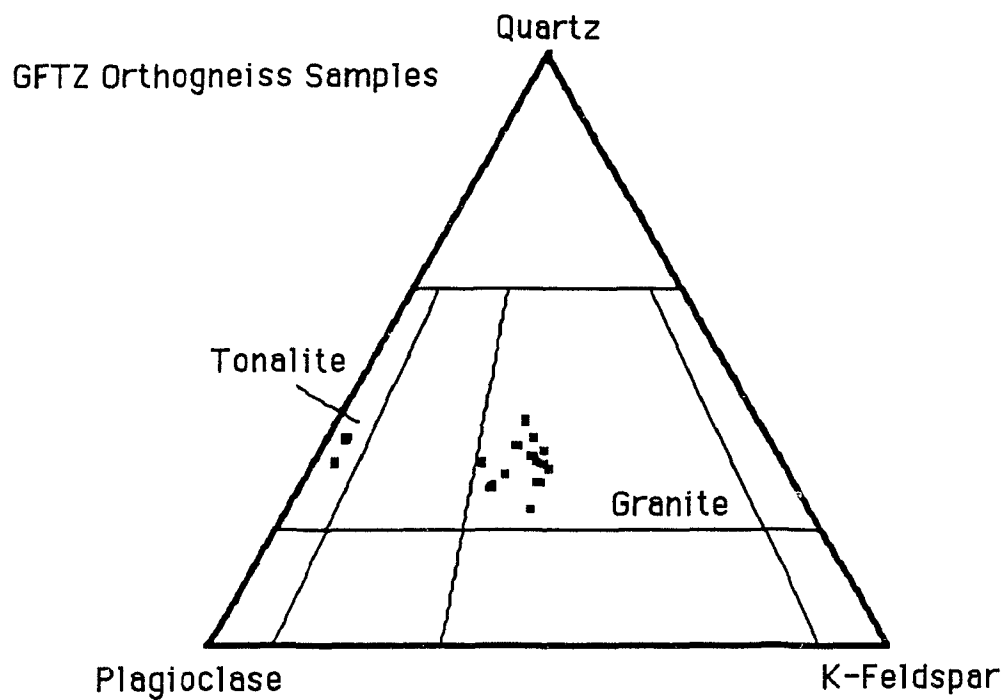


Figure 2.5 . Ternary diagram for the GFTZ orthogneiss samples. Note the tight clustering of most of the data in the granite field. Samples are discussed in more detail in the text.

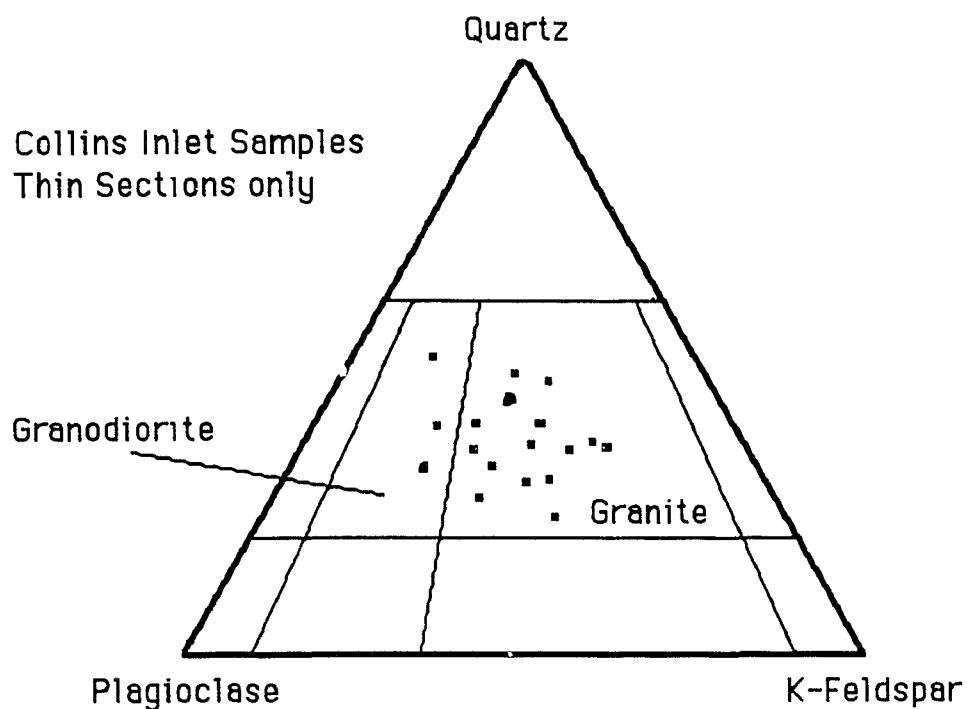


Figure 2.6. Ternary diagram for thin section samples of orthogneiss rocks collected along Collins Inlet. Velocities were not measured on these samples.

defined by different sized grains. The micas are lepidoblastic, and the plagioclase grains commonly have bent twins.

Paragneiss

A mica + garnet content greater than 15 % is used as the criterion to distinguish paragneiss from orthogneiss. Eleven samples of paragneiss (GFTZ-18, -21, -23, -30, -41, -47, -48, -49, -50, -55, and -91) were collected from Collins Inlet and Tyson Lake. Paragneiss outcrops along Collins Inlet are restricted to Mill Lake and Beaverstone Bay, but they occur over a wider region in the Tyson Lake area (see Figures 2.2 and 1.6). Paragneiss outcrops are generally lens-shaped with outcrop thicknesses of ca. 1.5 km and varying lengths up to 15 km.

The paragneiss samples are well foliated, usually with lepidoblastic micas. Samples GFTZ-41, GFTZ-47 and GFTZ-55 have mylonitic fabrics, including shear-band foliations. Garnets are highly embayed and poikiloblastic in all samples except GFTZ-50 where they are idiomorphic and slightly elongated in the foliation plane.

The mineralogy of the paragneiss samples is more varied than that of the orthogneisses. Plagioclase, quartz, potassium feldspar and biotite occur in all samples, except GFTZ-48 which has no potassium feldspar but

does have hypersthene. Measured plagioclase compositions range from An₂₇ to An₄₈. Muscovite, garnet, hornblende and sillimanite are locally present in significant amounts. Common accessory minerals include opaque oxides, apatite, chlorite and zircon. GFTZ-49 is notable for its very high quartz content (65.8%).

Mafic Rocks

Three distinct types of mafic rocks occur in this part of the GFTZ. They include: (1) metamorphosed mafic dikes or sills probably intruded well before the deformation in the GFTZ (Frarey, 1985), (2) large amphibolite and metagabbro bodies of uncertain origin that were involved in the GFTZ deformation and are now predominantly plagioclase-hornblende gneisses (Frarey, 1985), and (3) diabase dikes intruded during (?) and after the principal deformation in the GFTZ (Bethune and Davidson, 1988). Characteristics of each of these groups are described below.

Metamorphosed Mafic Dikes

Four samples of metamorphosed mafic dikes or boudins were collected along Collins Inlet. The dikes are thin (average thickness is 30 cm) and are parallel to the strong GFTZ fabric. Frarey (1985) suggested that these dikes may be Nipissing Diabase equivalents. Two of these samples are from the limbs of large isoclinal folds (GFTZ-4 and

GFTZ-86), one was taken from a boudin (GFTZ-19) and one was taken from the hinge region of a small complex fold (GFTZ-37). The samples from the fold limbs and the boudin are strongly foliated with lepidoblastic biotite, elongate hornblende crystals and mafic-felsic mineral segregations. The sample from the hinge region has generally equant grains and no obvious foliation or preferred mineral orientation, even in thin section.

All of these rocks consist predominantly of plagioclase (An₄₆-An₆₈) and hornblende. Biotite occurs in all samples, and overgrows hornblende in sample GFTZ-19. All samples have minor amounts of chlorite, generally overgrowing biotite. GFTZ-4 has an anomalously large percentage of sphene (16.0%) and apatite (5.9%).

Plagioclase-Hornblende Gneiss

Six samples of plagioclase-hornblende gneiss (GFTZ-39, -40, -54, -59, -75, and -87) were collected from the Tyson Lake region. These units occur as lens-shaped masses, similar in form to the paragneiss outcrops, although usually smaller. This lithology also occurs as a small metagabbro body on Burnt Island in Beaverstone Bay in the Collins Inlet region.

The plagioclase-hornblende gneisses are commonly well foliated with lepidoblastic biotite and segregations of mafic and felsic phases. Hornblende is strongly lineated

in samples GFTZ-39 and GFTZ-59. In addition, the plagioclase has bent twin lamellae in samples GFTZ-39 and GFTZ-40. All of the rocks are equigranular.

These rocks have mineralogies similar to the metamorphosed mafic dikes, dominated by plagioclase and hornblende. The main difference between the mafic dikes and the plagioclase-hornblende gneisses is their outcrop pattern. The plagioclase-hornblende gneisses are much larger units, usually without clearly defined boundaries. In contrast, the thin mafic dikes along Collins Inlet have sharply defined boundaries and are not part of larger units.

Diabase Dikes

One sample of Sudbury Diabase (GFTZ-93) and one of Grenville Diabase (GFTZ-92) were collected. Both dikes occur as units less than 50 m thick which cross-cut the GFTZ fabrics, although in places the Sudbury Dikes are involved in the GFTZ deformation (Bethune and Davidson, 1988). Both samples collected show original ophitic textures and no clear evidence of the GFTZ deformation. The distinction between these two dike swarms is described in some detail by Bethune and Davidson (1988).

The sample of Sudbury Dike has plagioclase (An₆₉), olivine and clinopyroxene as its major minerals and minor amounts of opaque oxides, biotite and baddeleyite. It was

taken from the "relatively undeformed" zone described by Bethune and Davidson (1988). The Grenville Dike sample consists of plagioclase (An₅₆), clinopyroxene, and minor serpentine, opaque oxides and accessory zircon. It was taken from the eastern end of Collins Inlet, where the Grenville Dike outcrops in vuggy exposures.

Experimental Method

Three mutually perpendicular cores approximately 2.5 cm in diameter and 3.8 cm long were obtained for velocity measurement from each field sample (Figure 2.7). One core was taken normal to the foliation plane of the rock ("A" direction) and two within the foliation plane: one parallel to the lineation ("B" direction) and one normal to the lineation ("C" direction). If the rock was foliated, but not lineated, the "B" and "C" direction cores were arbitrarily placed in the foliation plane. All but one of the samples measured had at least a weakly defined foliation. This type of analysis requires rocks of a relatively fine grain size (no grains greater than 0.5 cm in diameter) for cores to be representative of the bulk rock.

The cores were machine lapped to produce smooth, parallel core ends before the dimensions and mass were

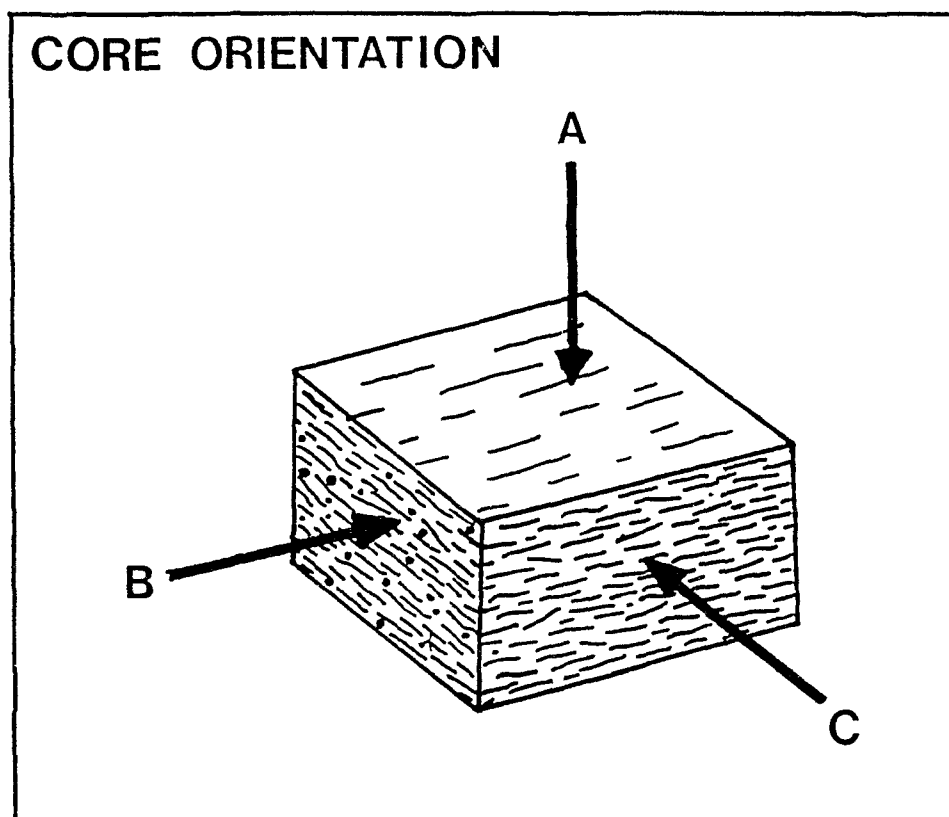


Figure 2.7. Schematic diagram showing core orientation conventions. The "A" direction is normal to the foliation, "B" is parallel to the lineation, if present, and "C" is normal to the lineation.

measured. Bulk density for each core was calculated using the mass of the sample and the volume calculated from the core dimensions. This technique only provides an estimate of the bulk density because deviation of the core shape from a perfect cylinder and the effect of core irregularities are not taken into account. Following these measurements, the cores were jacketed in copper foil, and thin (0.0005 cm) brass foil was placed on the core ends, to ensure electrical conductivity between the ends of the samples. The jacketed samples were placed between lead zirconate piezoelectric crystals with a resonant frequency of 1 MHz. The crystals were backed with brass electrodes in a manner similar to that described by Birch (1960). The sample assembly was placed in tight gum-rubber tubing to hold the assembly together (Figure 2.8) and to prevent saturation by the pressure medium. Samples (up to five at a time) were placed in a large high pressure vessel in which hydrostatic confining pressures up to 600 MPa were generated using an air-driven fluid pump in conjunction with a multi-stage fluid intensifier system. A low viscosity oil (ESSO MONOPLEX) was used as the pressure medium. Pressures above 600 MPa were not attainable due to increasing viscosity of the oil at very high confining pressures. Pressure was monitored by a strain gauge on the

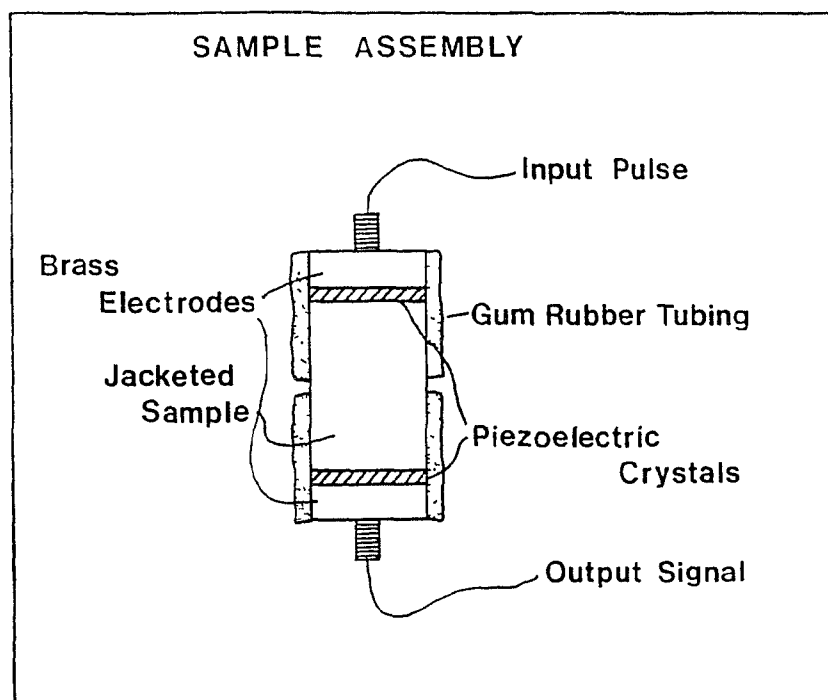


Figure 2.8. Schematic diagram of the sample assembly showing the jacketed sample placed between pulse-generating crystals and electrodes. The tubing holds the assembly in tight contact and prevents saturation of the sample with the pressure medium.

high pressure side of the intensifier and recorded digitally.

Waveforms generated by the pulse-transmission technique (Birch, 1960) were displayed on a Nicolet digital oscilloscope and stacked over at least four pulse repetitions to increase the signal to noise ratio. A typical waveform is shown in Figure 2.9. The first breaks of the waveforms were manually picked in order to determine the pulse transmission time through the sample while increasing and decreasing pressure in a series of graduated steps. Velocities were calculated at each pressure from the pulse transmission time and the length of the core.

Compressional wave velocities from smoothed velocity-pressure curves for each sample are summarized in Table 2.3. Only descending pressure measurements are used because of low pressure hysteresis effects (see below). Velocities are not corrected for changes in sample length at elevated confining pressure because this is significant only in the calculation of elastic constants and pressure derivatives (e.g. Brace, 1965). Other sources of error in velocity measurement arise from errors in measuring sample length and errors in travel time determination. Core lengths are precise to 0.05 cm and travel times to 2.5 nanoseconds. This results in a velocity measurement precision of 0.4 per cent for standard length cores. The

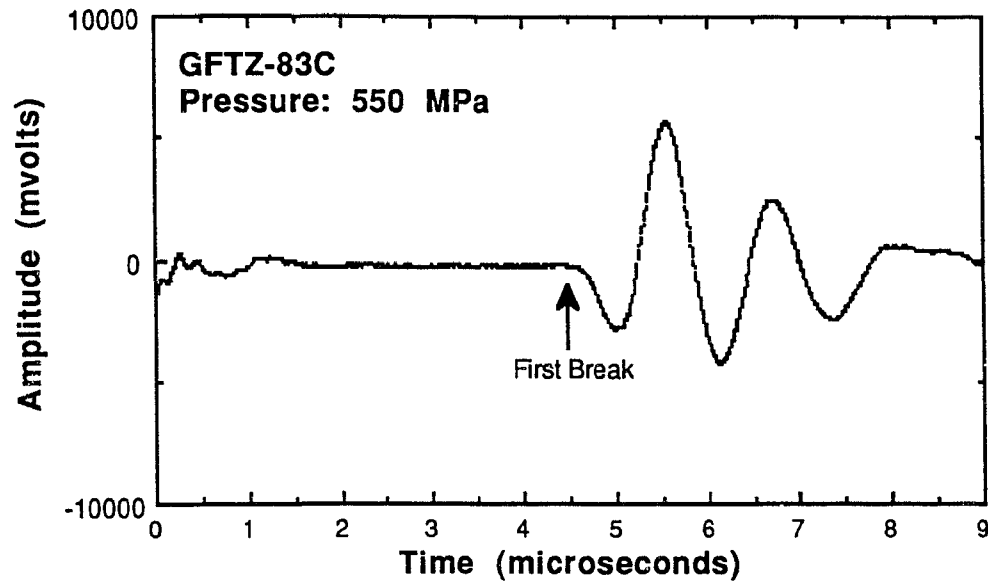


Figure 2.9. Pulse waveform at 550 MPa for sample GFTZ-83C. A total of 20 microseconds are recorded, but the information of interest (the first break) generally occurs between 3 and 6 microseconds for the lengths used in this study.

Table 2.3 Densities and compressional wave velocities of GFTZ samples at various confining pressures.

Sample	Lithology	Density (g/cc)	Velocity at Confining Pressure						
			50	100	200	300	400	500	600
			MPa	MPa	MPa	MPa	MPa	MPa	MPa
			(km/s)						
GFTZ- 4A	mafic dk.	3.00	6.26	6.31	6.35	6.37	6.38	6.39	6.39
GFTZ- 4B		2.99	7.03	7.06	7.09	7.11	7.12	7.13	7.13
GFTZ- 4C		2.99	7.02	7.07	7.09	7.10	7.11	7.11	7.12
AVERAGE		2.99	6.77	6.81	6.84	6.86	6.87	6.88	6.88
GFTZ- 7A	orthogn.	2.70	5.49	5.81	6.02	6.10	6.15	6.18	6.20
GFTZ- 7B		2.70	5.96	6.13	6.25	6.30	6.33	6.34	6.35
GFTZ- 7C		2.70	5.90	6.03	6.17	6.22	6.25	6.26	6.27
AVERAGE		2.70	5.78	5.99	6.15	6.21	6.24	6.26	6.27
GFTZ-18A	paragn.	2.72	5.97	6.09	6.14	6.16	6.19	6.21	6.23
GFTZ-18B		2.73	6.23	6.34	6.42	6.46	6.47	6.49	6.50
GFTZ-18C		2.73	6.17	6.30	6.42	6.48	6.51	6.53	6.55
AVERAGE		2.73	6.12	6.24	6.33	6.37	6.39	6.41	6.43
GFTZ-19A	mafic dk.	3.02	6.09	6.16	6.23	6.27	6.28	6.29	6.30
GFTZ-19B		2.96	7.05	7.12	7.17	7.19	7.20	7.21	7.21
GFTZ-19C		3.02	6.85	6.91	6.97	7.00	7.01	7.02	7.02
AVERAGE		3.00	6.16	6.73	6.79	6.82	6.83	6.84	6.84
GFTZ-21A	paragn.	2.71	5.87	5.95	6.02	6.05	6.07	6.08	6.09
GFTZ-21B		2.74	6.28	6.37	6.46	6.49	6.51	6.52	6.53
GFTZ-21C		2.73	6.35	6.44	6.48	6.50	6.51	6.52	6.53
AVERAGE		2.73	6.17	6.25	6.32	6.35	6.36	6.37	6.38
GFTZ-23A	paragn.	2.66	5.89	5.99	6.04	6.06	6.07	6.08	6.09
GFTZ-23B		2.67	5.86	6.02	6.10	6.13	6.14	6.15	6.16
GFTZ-23C		2.72	5.95	6.08	6.17	6.19	6.20	6.21	6.22
AVERAGE		2.68	5.90	6.03	6.10	6.13	6.14	6.15	6.16
GFTZ-26A	orthogn.	2.66	5.50	5.86	6.05	6.13	6.17	6.18	6.19
GFTZ-26B		2.65	5.87	6.13	6.32	6.39	6.43	6.45	6.46
GFTZ-26C		2.67	5.72	6.02	6.22	6.27	6.30	6.32	6.33
AVERAGE		2.66	5.70	6.00	6.20	6.26	6.30	6.32	6.33
GFTZ-30A	paragn.	2.72	5.72	5.78	5.83	5.85	5.86	5.86	5.87
GFTZ-30B		2.69	6.47	6.58	6.67	6.73	6.77	6.79	6.80
GFTZ-30C		2.70	6.11	6.26	6.36	6.41	6.44	6.45	6.46
AVERAGE		2.70	6.10	6.21	6.29	6.33	6.36	6.37	6.38
GFTZ-37A	mafic dk.	2.93	6.84	6.90	6.97	7.00	7.01	7.02	7.03
GFTZ-37B		2.92	6.88	6.97	7.06	7.10	7.01	7.13	7.14
GFTZ-37C		2.91	6.65	6.75	6.84	6.89	6.92	6.93	6.94
AVERAGE		2.92	6.79	6.87	6.96	7.00	6.98	7.03	7.04

Table 2.3 (cont)

Sample	Lithology	Density (g/cc)	Velocity at Confining Pressure						
			50	100	200	300	400	500	600
			MPa	MPa	MPa	MPa	MPa	MPa	MPa
			(km/s)						
GFTZ-39A	mafic gn.	2.96	6.20	6.26	6.31	6.32	6.33	6.34	6.34
GFTZ-39B		2.96	7.18	7.25	7.33	7.37	7.39	7.40	7.41
GFTZ-39C		2.94	6.75	6.81	6.86	6.89	6.91	6.92	6.94
AVERAGE		2.95	6.71	6.77	6.83	6.86	6.88	6.89	6.90
GFTZ-40A	mafic gn.	2.89	6.23	6.34	6.44	6.48	6.51	6.52	6.52
GFTZ-40B		2.90	6.63	6.71	6.75	6.77	6.78	6.79	6.79
GFTZ-40C		2.90	6.59	6.69	6.74	6.76	6.77	6.78	6.78
AVERAGE		2.90	6.48	6.58	6.64	6.67	6.69	6.70	6.70
GFTZ-41A	paragn.	2.63	n.a.	6.02	6.06	6.07	6.07	6.08	6.09
GFTZ-41B		2.71	6.24	6.32	6.39	6.43	6.45	6.46	6.47
GFTZ-41C		2.70	6.19	6.27	6.33	6.37	6.39	6.40	6.41
AVERAGE		2.68	6.22	6.20	6.26	6.29	6.30	6.31	6.32
GFTZ-47A	paragn.	2.79	5.75	5.94	6.06	6.08	6.12	6.13	6.14
GFTZ-47B		2.84	6.29	6.43	6.53	6.58	6.59	6.60	6.61
GFTZ-47C		2.85	6.00	6.09	6.18	6.23	6.25	6.27	6.28
AVERAGE		2.83	6.01	6.15	6.26	6.30	6.32	6.33	6.34
GFTZ-47B2		2.84	6.30	6.50	6.54	6.57	6.58	6.59	6.60
GFTZ-48A	paragn.	2.75	5.82	5.90	5.96	6.00	6.02	6.03	6.03
GFTZ-48B		2.76	6.44	6.53	6.58	6.60	6.62	6.63	6.63
GFTZ-48C		2.76	5.91	6.02	6.12	6.15	6.17	6.18	6.19
AVERAGE		2.78	6.12	6.24	6.30	6.33	6.35	6.36	6.36
GFTZ-49A	paragn.	2.58	5.74	5.89	5.97	6.01	6.03	6.04	6.05
GFTZ-49B		2.62	5.72	5.88	6.01	6.06	6.07	6.08	6.08
GFTZ-49C		2.63	6.08	6.20	6.30	6.34	6.35	6.36	6.36
AVERAGE		2.61	5.85	5.99	6.09	6.14	6.15	6.16	6.16
GFTZ-50A	paragn.	2.78	5.44	5.65	5.84	5.90	5.94	5.96	5.98
GFTZ-50B		2.78	6.20	6.37	6.47	6.52	6.55	6.58	6.60
GFTZ-50C		2.78	6.46	6.53	6.56	6.58	6.59	6.60	6.61
AVERAGE		2.78	6.03	6.18	6.29	6.33	6.36	6.38	6.40
GFTZ-54A	mafic gn.	2.88	5.99	6.24	6.37	6.40	6.42	6.44	6.45
GFTZ-54B		2.88	6.72	6.80	6.88	6.92	6.94	6.95	6.96
GFTZ-54C		2.89	6.72	6.78	6.85	6.88	6.90	6.92	6.93
AVERAGE		2.88	6.48	6.61	6.70	6.73	6.75	6.77	6.78
GFTZ-55A	paragn.	2.72	5.91	5.97	6.00	6.02	6.03	6.04	6.04
GFTZ-55B		2.70	5.70	5.83	5.96	6.02	6.05	6.08	6.09
GFTZ-55C		2.73	5.98	6.07	6.20	6.23	6.25	6.27	6.28
AVERAGE		2.72	5.86	5.96	6.05	6.09	6.11	6.13	6.14

Table 2.3 (cont)

Sample	Lithology	Density (g/cc)	Velocity at Confining Pressure						
			50	100	200	300	400	500	600
			MPa	MPa	MPa	MPa	MPa	MPa	MPa
			(km/s)						
GFTZ-59A	mafic gn.	2.93	6.72	6.87	6.93	6.95	6.96	6.96	6.96
GFTZ-59B		2.98	7.03	7.15	7.23	7.25	7.26	7.27	7.27
GFTZ-59C		3.05	7.30	7.46	7.58	7.62	7.64	7.64	7.64
AVERAGE		2.99	7.02	7.16	7.25	7.27	7.29	7.29	7.29
GFTZ-64A	orthogn./	2.67	5.88	6.02	6.14	6.19	6.21	6.23	6.24
GFTZ-64B	mylonite	2.67	5.91	5.99	5.67	6.13	6.17	6.19	6.21
GFTZ-64C		2.68	6.07	6.15	6.24	6.28	6.29	6.30	6.31
AVERAGE		2.67	5.95	6.05	6.02	6.20	6.22	6.24	6.25
GFTZ-65A	orthogn./	2.68	6.01	6.13	6.23	6.29	6.30	6.31	6.31
GFTZ-65B	mylonite	2.68	6.03	6.11	6.17	6.21	6.23	6.25	6.26
GFTZ-65C		2.68	5.87	5.95	6.04	6.08	6.10	6.11	6.11
AVERAGE		2.68	5.97	6.06	6.15	6.19	6.21	6.22	6.23
GFTZ-66A	orthogn./	2.68	5.92	6.05	6.08	6.11	6.14	6.17	6.18
GFTZ-66B	mylonite	2.68	6.14	6.20	6.28	6.33	6.36	6.38	6.39
GFTZ-66C		2.69	6.09	6.19	6.25	6.28	6.29	6.30	6.31
AVERAGE		2.68	6.05	6.15	6.20	6.24	6.26	6.28	6.29
GFTZ-67A	orthogn./	2.65	6.16	6.26	6.35	6.40	6.43	6.45	6.46
GFTZ-67B	mylonite	2.66	6.16	6.21	6.25	6.27	6.28	6.29	6.30
GFTZ-67C		2.66	6.18	6.28	6.37	6.39	6.42	6.43	6.44
AVERAGE		2.66	6.17	6.25	6.32	6.35	6.38	6.39	6.40
GFTZ-68A	orthogn./	2.66	5.96	6.00	6.05	6.08	6.11	6.12	6.12
GFTZ-68B	mylonite	n.a.	n.a.	n.a.	n.a.	n.a.	n.a.	n.a.	n.a.
GFTZ-68C		2.66	6.13	6.17	6.22	6.24	6.25	6.26	6.27
AVERAGE		2.66	6.05	6.09	6.14	6.16	6.18	6.19	6.19
GFTZ-69A	orthogn./	2.62	6.37	6.49	6.57	6.60	6.62	6.63	6.63
GFTZ-69B	mylonite	2.65	6.08	6.14	6.20	6.23	6.24	6.25	6.26
GFTZ-69C		2.64	6.14	6.21	6.27	6.30	6.31	6.32	6.33
AVERAGE		2.64	6.20	6.28	6.35	6.38	6.39	6.40	6.41
GFTZ-71A	orthogn./	2.65	6.06	6.14	6.18	6.20	6.22	6.24	6.25
GFTZ-71B	mylonite	2.64	6.03	6.09	6.14	6.18	6.20	6.21	6.22
GFTZ-71C		2.66	6.10	6.16	6.21	6.23	6.25	6.27	6.28
AVERAGE		2.65	6.06	6.13	6.18	6.20	6.22	6.24	6.25
GFTZ-72A	orthogn./	2.64	5.66	5.92	6.05	6.10	6.12	6.13	6.14
GFTZ-72B	mylonite	2.65	5.93	6.07	6.20	6.27	6.32	6.34	6.35
GFTZ-72C		2.63	6.00	6.18	6.26	6.29	6.31	6.32	6.32
AVERAGE		2.64	5.86	6.06	6.17	6.22	6.25	6.26	6.27

Table 2.3 (cont)

Sample	Lithology	Density (g/cc)	Velocity at Confining Pressure						
			50 MPa	100 MPa	200 MPa	300 MPa	400 MPa	500 MPa	600 MPa
			(km/s)						
GFTZ-73A	orthogn./	2.60	5.94	6.03	6.14	6.19	6.21	6.22	6.23
GFTZ-73B	mylonite	2.59	5.91	6.10	6.23	6.30	6.33	6.35	6.36
GFTZ-73C		2.61	5.93	6.01	6.09	6.11	6.11	6.11	6.12
AVERAGE		2.60	5.93	6.05	6.15	6.20	6.22	6.23	6.24
GFTZ-75A	mafic gn.	2.91	6.47	6.53	6.58	6.61	6.63	6.64	6.64
GFTZ-75B		2.92	6.87	6.99	7.08	7.12	7.15	7.17	7.18
GFTZ-75C		2.91	6.45	6.56	6.65	6.60	6.72	6.74	6.75
AVERAGE		2.91	6.60	6.69	6.77	6.78	6.83	6.85	6.86
GFTZ-77A	orthogn./	2.61	5.99	6.15	6.24	6.28	6.30	6.31	6.32
GFTZ-77B	mylonite	2.62	6.11	6.18	6.26	6.29	6.31	6.32	6.33
GFTZ-77C		2.60	6.13	6.24	6.33	6.36	6.37	6.38	6.38
AVERAGE		2.61	6.08	6.19	6.28	6.31	6.33	6.34	6.34
GFTZ-78A	orthogn./	2.62	5.80	5.95	6.06	6.10	6.12	6.13	6.13
GFTZ-78B		n.a.	n.a.	n.a.	n.a.	n.a.	n.a.	n.a.	n.a.
GFTZ-78C		2.62	6.00	6.09	6.21	6.28	6.32	6.33	6.34
AVERAGE		2.62	5.90	6.02	6.14	6.19	6.22	6.23	6.24
GFTZ-79A	orthogn./	2.62	6.16	6.24	6.30	6.33	6.34	6.36	6.37
GFTZ-79B	mylonite	2.65	6.08	6.16	6.25	6.29	6.31	6.32	6.33
GFTZ-79C		2.62	6.09	6.19	6.24	6.27	6.28	6.29	6.30
AVERAGE		2.63	6.11	6.20	6.26	6.30	6.31	6.32	6.33
GFTZ-82A	orthogn.	2.64	6.05	6.13	6.20	6.24	6.27	6.38	6.29
GFTZ-82B		2.65	6.14	6.21	6.29	6.34	6.37	6.38	6.39
GFTZ-82C		2.65	6.16	6.27	6.36	6.39	6.41	6.42	6.43
AVERAGE		2.65	6.12	6.20	6.28	6.32	6.35	6.39	6.37
GFTZ-83A	orthogn.	2.66	6.06	6.23	6.34	6.37	6.39	6.40	6.41
GFTZ-83B		2.67	6.06	6.17	6.25	6.27	6.28	6.29	6.30
GFTZ-83C		2.64	6.18	6.27	6.36	6.40	6.43	6.44	6.45
AVERAGE		2.66	6.10	6.22	6.32	6.35	6.37	6.38	6.39
GFTZ-86A	mafic dk.	2.88	5.99	6.04	6.09	6.13	6.15	6.17	6.18
GFTZ-86B		2.94	6.84	6.92	6.97	6.99	7.00	7.01	7.01
GFTZ-86C		2.92	6.85	6.92	6.97	6.99	7.01	7.02	7.03
AVERAGE		2.91	6.56	6.63	6.68	6.70	6.72	6.73	6.74
GFTZ-87A	mafic gn.	3.19	n.a.	6.07	6.30	6.39	6.43	6.45	6.46
GFTZ-87B		3.19	6.48	6.65	6.81	6.88	6.92	6.93	6.94
GFTZ-87C		3.19	6.26	6.53	6.67	6.73	6.76	6.78	6.80
AVERAGE		3.19	6.37	6.42	6.59	6.67	6.70	6.72	6.73

Table 2.3 (cont)

Sample	Lithology	Density (g/cc)	Velocity at Confining Pressure						
			50	100	200	300	400	500	600
			MPa	MPa	MPa	MPa	MPa	MPa	MPa
			(km/s)						
GFTZ-88A	orthogn.	2.69	5.72	5.88	5.99	6.05	6.08	6.10	6.11
GFTZ-88B		n.a.	n.a.	n.a.	n.a.	n.a.	n.a.	n.a.	n.a.
GFTZ-88C		2.65	6.16	6.24	6.32	6.36	6.39	6.40	6.41
AVERAGE		2.67	5.94	6.06	6.15	6.21	6.23	6.25	6.26
GFTZ-90A	orthogn.	2.65	5.92	6.02	6.60	6.08	6.09	6.10	6.11
GFTZ-90B		2.65	n.a.	5.87	6.03	6.10	6.13	6.14	6.15
GFTZ-90C		2.66	6.09	6.17	6.24	6.28	6.30	6.32	6.32
AVERAGE		2.65	6.01	6.02	6.29	6.15	6.17	6.19	6.19
GFTZ-91A	paragn.	2.66	5.91	6.01	6.11	6.16	6.19	6.21	6.21
GFTZ-91B		2.65	6.21	6.41	6.51	6.54	6.56	6.56	6.57
GFTZ-91C		2.66	5.94	6.16	6.27	6.31	6.33	6.34	6.35
AVERAGE		2.66	6.02	6.19	6.30	6.34	6.36	6.37	6.38
GFTZ-92A	Grenville	2.97	6.42	6.51	6.56	6.58	6.60	6.60	6.60
GFTZ-92B	Diabase	2.99	6.47	6.51	6.53	6.54	6.55	6.55	6.56
GFTZ-92C		2.97	6.40	6.47	6.52	6.54	6.55	6.56	6.57
AVERAGE		2.98	6.43	6.50	6.54	6.55	6.57	6.57	6.58
GFTZ-93A	Sudbury	3.00	6.84	6.89	6.93	6.95	6.97	6.98	6.98
GFTZ-93B	Diabase	3.06	6.85	6.92	6.96	6.97	6.98	6.98	6.99
GFTZ-93C		3.03	6.87	6.93	6.97	6.98	7.00	7.01	7.01
AVERAGE		3.03	6.85	6.91	6.95	6.97	6.98	6.99	6.99

Notes: n.a. indicates not available
 orthogn.=orthogneiss
 paragn.=paragneiss
 mafic gn.=mafic gneiss
 mafic dk.=mafic dike

absolute error associated with the pulse transmission technique is generally regarded to be less than 2 per cent (Christensen and Shaw, 1970).

Experimental Results

Velocity-Pressure Relationships

All samples show the initial increase of compressional wave velocity with increasing pressure (Figure 2.10) that has been related to the closure of microcracks (Birch, 1960; 1961; Christensen, 1965; Walsh, 1965). The magnitude of this velocity increase is nearly constant for orthogonal cores within a single rock.

For all samples, the velocity-pressure curves become nearly linear following the initial abrupt velocity increase. Some samples, especially mafic rocks, exhibit linear behavior at pressures as low as 150 MPa, but more commonly the linear behavior is apparent at pressures above 200 MPa. Once this linear behavior is observed, all microcracks are assumed closed, and the effects of preferred mineral orientation and mineral composition can be assessed (Christensen, 1965; Walsh, 1965).

Velocity hysteresis is observed in some of the pressure runs. The velocity measured during initial pressurization is commonly lower than the velocity measured

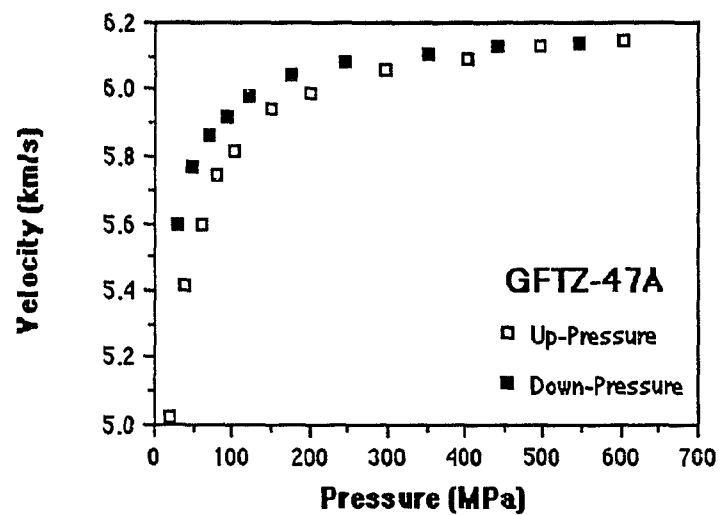


Figure 2.10. Compressional wave velocity as a function of confining pressure for sample GFTZ-47A, showing the typical sharp increase in velocity with increasing confining pressure. Velocity measured during initial pressurization is lower than the velocity measured as pressure is decreased.

as pressure is decreased (Figure 2.10). This velocity hysteresis is believed to be related to microcracks because it is not observed in either single crystals (McSkimin and Andreatch, 1962) or in fused quartz samples with air bubbles (Peselnick and Wilson, 1968). Hysteresis is related to the sealing of microcracks at high confining pressures (Birch, 1961; Gardner et al., 1965) and is common in rocks at pressures below 200 MPa (Burke and Fountain, 1990). Re-pressurization results in velocities intermediate between the up and down pressure curves of the first cycle, but the down pressure measurements of the first run can be reproduced during the second decompression (Figure 2.11). Because of this slight effect, curves are fit only through the down pressure measurements, because they are the only reproducible data. Following the convention of Burke (1987), hysteresis (H) at a single pressure is quantified as

$$H = (V_{\text{down}} - V_{\text{up}}) / V_{\text{mean}} \quad (1)$$

where V_{down} is the velocity measured during depressurization, V_{up} is the velocity measured during initial pressurization and V_{mean} is their average.

Hysteresis values at 50 and 100 MPa are given in Table 2.4 for all samples that displayed significant hysteresis.

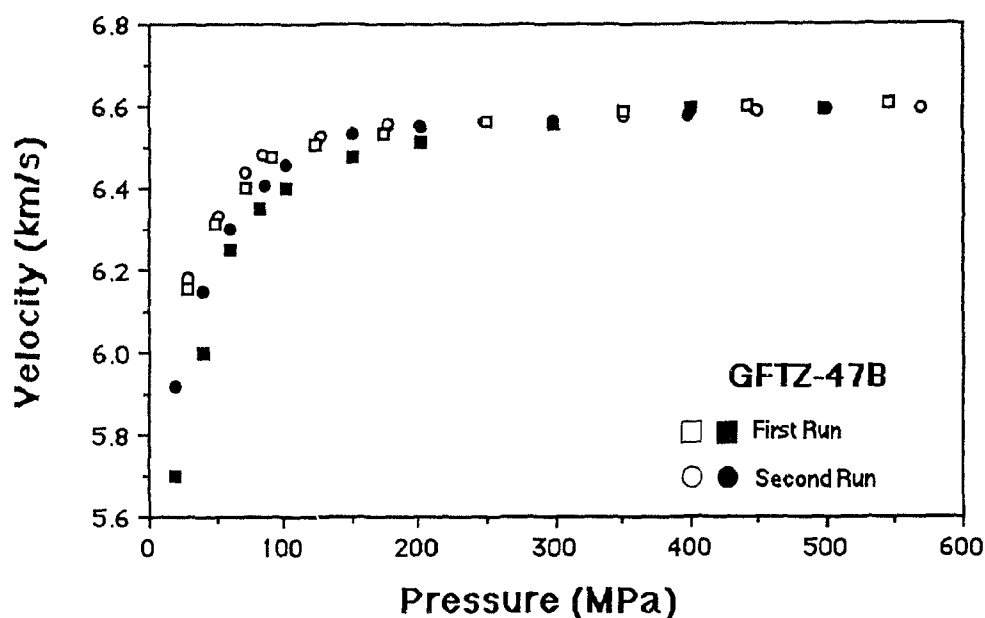


Figure 2.11. Compressional wave velocities measured for sample GFTZ-47B subjected to back-to-back experimental runs. The square and circular symbols correspond to the first and second runs respectively. The closed symbols represent up-pressure velocity measurements; the open symbols represent down-pressure velocities. Note that the up-pressure velocities for the second run (closed circular symbols) are systematically higher than those of the first run at similar confining pressures. In contrast, the velocities determined for each run during decompression are similar at similar confining pressures.

Table 2.4. Velocity hysteresis at 50 and 100 MPa of GFTZ rocks.

Sample	H at 50 MPa	H at 100 MPa
GFTZ-18A	3.9	1.5
GFTZ-18B	2.8	1.3
GFTZ-18C	1.1	0.5
GFTZ-21A	1.4	1.0
GFTZ-21B	3.4	1.4
GFTZ-23A	1.5	0.0
GFTZ-23B	2.8	1.7
GFTZ-26A	2.3	2.6
GFTZ-26C	4.8	1.7
GFTZ-39B	2.8	0.0
GFTZ-41B	1.5	0.8
GFTZ-47A	5.3	4.0
GFTZ-47B	3.3	0.2
GFTZ-48C	3.9	1.1
GFTZ-49B	0.2	1.2
GFTZ-49C	1.3	0.0
GFTZ-50A	2.2	1.4
GFTZ-50B	2.4	1.4
GFTZ-55B	1.8	0.7
GFTZ-59A	1.2	0.0
GFTZ-69A	1.5	0.5
GFTZ-72A	3.9	2.1
GFTZ-72B	3.5	1.3
GFTZ-77C	1.7	0.6
GFTZ-78B	4.4	1.6
GFTZ-78C	4.9	1.7
GFTZ-91A	2.1	0.5

Hysteresis in the GFTZ rocks is a relatively minor effect and never exceeded 6 per cent in the cores measured. Hysteresis disappears once the velocity-pressure curves approach linearity, and displays no obvious trends with propagation direction, lithology or mineralogy.

Velocity-Density Relationships

Average compressional wave velocity is proportional to density for rocks of the same mean atomic weight (Birch, 1961). Most rocks of the continental crust have mean atomic weights between 20 and 22 g/mol (Birch, 1961).

The average compressional wave velocity at 600 MPa is plotted against bulk density in Figure 2.12. Also shown are the $m=21$ and $m=22$ lines of constant mean atomic weight of Birch (1961). All of the data in this study fall between the $m=21$ and $m=22$ lines, except samples GFTZ-87 and GFTZ-92. These rocks have high percentages of opaque minerals (9.2 and 13.8 per cent, respectively), which tends to increase the mean atomic weight. Thus these samples have relatively low velocity for high density, and plot on or below the $m=22$ line. None of the other samples had opaque minerals accounting for more than 9 per cent of the total.

The result of a linear least-squares fit to these data, excluding the values of samples GFTZ-87 and -92, is

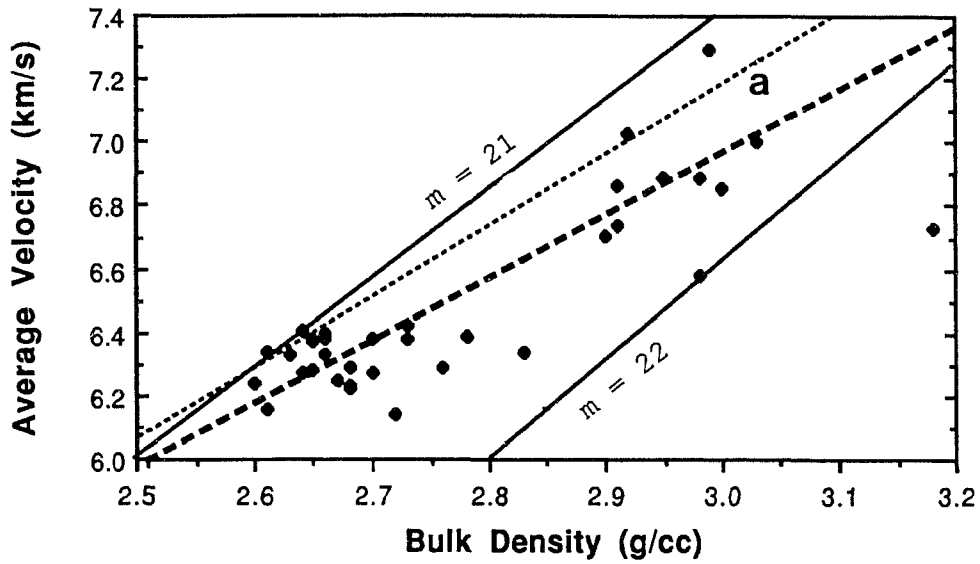


Figure 2.12. Average velocity plotted against bulk density for all GFTZ samples measured. Lines of constant mean atomic weight ($m=21$ and $m=22$) are from Birch, 1960. The heavy dashed line is the result of a linear fit to the data, excluding samples GFTZ-82 and GFTZ-92 (see text). Line **a** (dotted) is the relationship of Christensen and Fountain (1975) for granulite facies rocks.

shown as a heavy dashed line on Figure 2.12. The equation of this line is:

$$V_p = 1.097 + 1.953\rho_b \quad (2)$$

and the correlation coefficient is 0.89. This line is nearly parallel to the fit of Christensen and Fountain (1975) for granulite facies rocks, but is offset by 0.2 km/s toward lower velocities. This is expected as the rocks in the GFTZ are representative of the amphibolite, not granulite facies. Compressional wave velocity increases in a regular manner with increasing metamorphic grade from amphibolite to granulite facies in the Ivrea zone as garnet progressively replaces biotite (Burke and Fountain, 1990).

Velocity-density diagrams may be used to discern the controls of lithology on compressional wave velocity and bulk density. Figure 2.13 shows the fields of different lithologic groups as a function of velocity at 600 MPa and bulk density. All of the data from individual cores (including those from samples GFTZ-87 and GFTZ-92) are used to define these fields. Orthogneiss samples form the most tightly constrained field on this diagram, with density ranging from 2.60 to 2.70 g/cc, and velocity from 6.11 to 6.46 km/s. One core (GFTZ-69A) acted as a "fast" outlier,

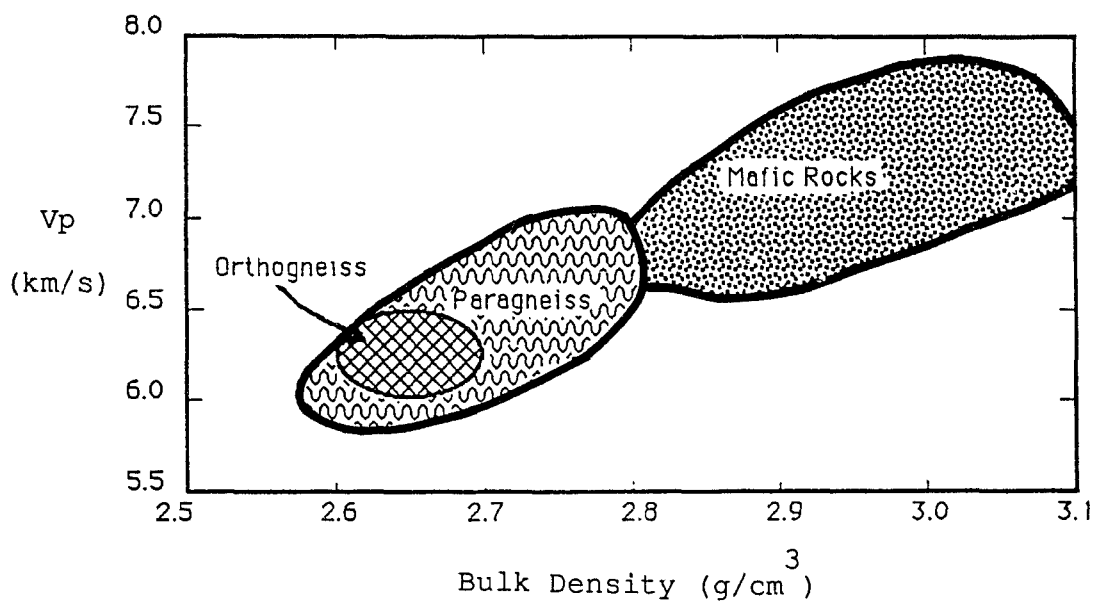


Figure 2.13. Schematic diagram of velocity-bulk density fields of rocks of the GFTZ. These fields envelop all data measured regardless of core orientation.

but this core had a large plagioclase porphyroclast, and is not representative of the sample as a whole. The tight clustering of these data is due to the mineralogic similarity of the samples, and in part to their lack of significant seismic anisotropy. These data essentially duplicate other laboratory measurements of compressional wave velocity for granitic rocks found throughout the world (Birch, 1960; Christensen, 1965; Burke and Fountain, 1990; Fountain et al., 1990).

It is important to stress that the orthogneiss lithologic group contains samples of mylonitized orthogneiss from the GFTZ boundary fault. These rocks show varying degrees of strain, manifested as grain size variations in both groundmass and porphyroclasts. Although the strain in these samples varies considerably, the ultrasonic seismic velocities are virtually uniform for all samples and wave propagation directions. Thus the high strain displayed by these samples seemingly has no effect on either the bulk velocity or the seismic anisotropy of these rocks.

The field of the paragneiss samples overlies the orthogneiss field, and in addition covers an area with higher velocity (5.87 to 6.80 km/s) and density (2.58 to 2.85 g/cc). A closer examination of the paragneiss data (Figure 2.14) reveals that there are two distinct sub-

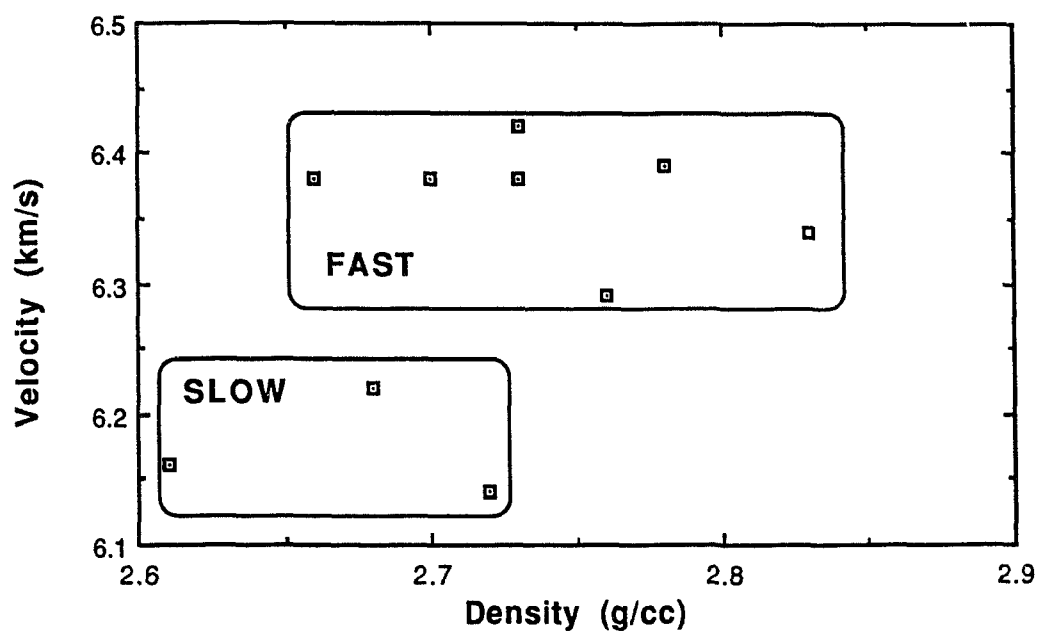


Figure 2.14. Average compressional wave velocity plotted against bulk density for paragneiss samples. The "slow" paragneiss samples have abundant quartz and potassium feldspar, while the "fast" rocks have relatively less quartz and potassium feldspar.

fields distinguished on the basis of velocity. The "slow" velocity field encompasses three samples (GFTZ-23, -49, and -55) and has an average velocity below 6.20 km/s. The "fast" field includes the remaining samples and has an average velocity greater than 6.30 km/s and a wider range of densities. The rocks with lower average velocity have higher proportions of quartz and potassium feldspar (see Table 2.1). These minerals are notable for low Voight-Reuss-Hill aggregate velocities of 6.05 km/s (McSkimin and Andreatch, 1962) and 6.01 km/s (Alexandrov and Ryzhova, 1962; 1965), respectively. These rocks also have minimal seismic anisotropy, with values never exceeding 5 per cent at 600 MPa.

The paragneiss samples in the higher velocity field have higher proportions of minerals with high Voight-Reuss-Hill aggregate velocities such as plagioclase and garnet. Anisotropy in these paragneiss samples ranges from 5 to 15 per cent. Higher values of anisotropy tend to increase the amount of scatter in these data. Sample GFTZ-30 had the highest seismic anisotropy, with the velocity of individual cores ranging from 5.87 to 6.80 km/s despite negligible density variation. This type of anisotropic effect introduces considerable ambiguity into simple interpretations of velocity-density relationships.

The mafic samples do not show very consistent velocity-density behavior and cover a large area in Figure 2.13. These rocks have higher density (2.88-3.19 g/cc) than the previously discussed groups, due to greater proportions of mafic minerals, especially hornblende. Velocities of individual cores range from 6.18 to 7.64 km/s (Figure 2.15) and are a function of the amount of hornblende, its degree of preferred orientation and the presence of relatively calcic plagioclase (average An₄₅). The samples furthest from the relationship of Birch (1961) are GFTZ-87 and GFTZ-92, due to their high opaque mineral content; and GFTZ-59 which has a more calcic plagioclase than other samples (An₆₈) and a significant amount of strongly aligned hornblende. Compressional wave velocity in the plagioclase feldspar series is strongly related to composition, with the more calcic members displaying higher velocities (Ryzhova, 1964). The alignment of hornblende in GFTZ-59 introduces significant seismic anisotropy (9.3%).

Seismic Anisotropy

Compressional wave anisotropy is commonly observed in many of the samples, and is of considerable magnitude in many (Table 2.5). Anisotropy is calculated as the per cent difference between the maximum and minimum velocity with respect to the mean velocity (Birch, 1961). In many rocks

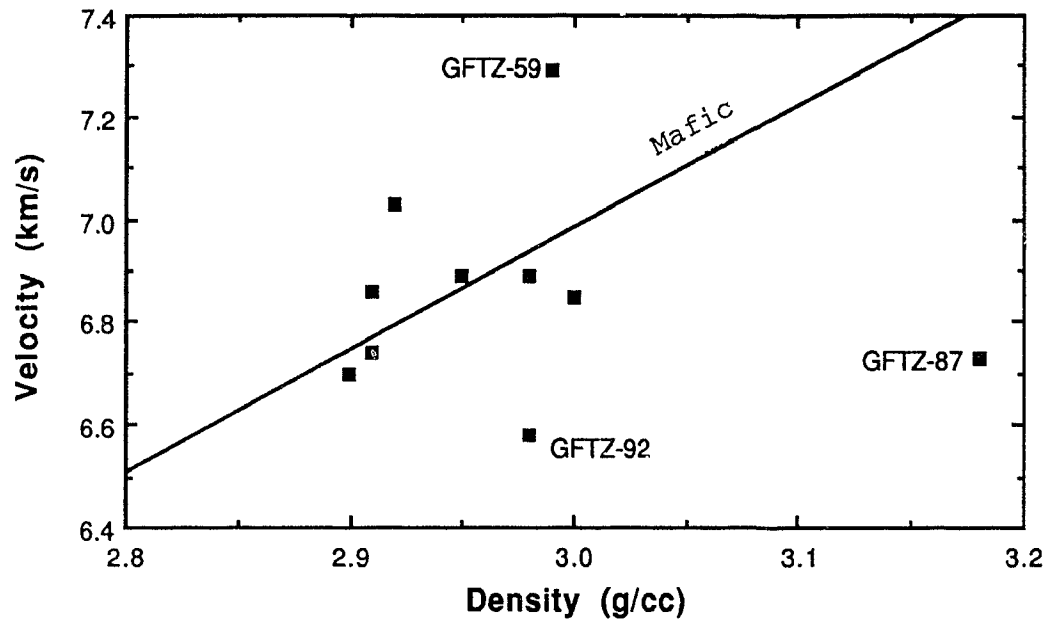


Figure 2.15. Average compressional wave velocity plotted against bulk density for all mafic samples. The line labelled "mafic" is from Birch's (1961) fit for mafic rocks. Samples GFTZ-87 and -92 fall well below this line because of their high opaque mineral contents, GFTZ-59 is above this relationship because of the high anisotropy related to alignment of hornblende crystals in this rock.

Table 2.5 Compressional wave velocity anisotropy of GFTZ samples at various confining pressures.

Sample	Lithology	Anisotropy at Confining Pressure						
		50	100	200	300	400	500	600
		MPa	MPa	MPa	MPa	MPa	MPa	MPa
(%)								
GFTZ-4	mafic dike	11.4	11.2	10.8	10.8	10.8	10.8	10.8
GFTZ-7	orthogneiss	8.1	5.3	3.7	3.2	2.9	2.6	2.4
GFTZ-18	paragneiss	4.3	4.0	4.4	5.0	5.0	5.0	5.0
GFTZ-19	mafic dike	14.4	14.3	13.8	13.5	13.5	13.5	13.3
GFTZ-21	paragneiss	7.8	7.8	7.3	7.1	6.9	6.9	6.9
GFTZ-23	paragneiss	1.5	1.5	2.1	2.1	2.1	2.1	2.1
GFTZ-26	orthogneiss	6.5	4.5	4.4	4.2	4.1	4.3	4.3
GFTZ-30	paragneiss	12.3	12.9	13.4	13.9	14.3	14.6	14.6
GFTZ-37	mafic dike	3.4	3.2	3.2	3.0	1.3	2.9	2.8
GFTZ-39	mafic gneiss	14.6	14.6	14.9	15.3	15.4	15.4	15.5
GFTZ-40	mafic gneiss	6.2	5.6	4.7	4.4	4.0	4.0	4.0
GFTZ-41	paragneiss	0.8	4.8	5.3	5.7	6.0	6.0	6.0
GFTZ-47	paragneiss	9.0	8.0	7.5	7.9	7.4	7.4	7.4
GFTZ-48	paragneiss	10.1	10.1	9.8	9.5	9.5	9.4	9.4
GFTZ-49	paragneiss	6.2	5.3	5.4	5.4	5.2	5.2	5.0
GFTZ-50	paragneiss	16.9	14.2	11.5	10.7	10.2	10.0	9.9
GFTZ-54	mafic gneiss	11.3	8.5	7.6	7.7	7.7	7.5	7.5
GFTZ-55	paragneiss	4.8	4.0	4.0	3.5	3.6	3.8	3.9
GFTZ-59	mafic gneiss	8.3	8.2	9.0	9.2	9.3	9.3	9.3
GFTZ-64	orthogn./myl.	3.2	2.6	9.5	2.4	1.9	1.8	1.6
GFTZ-65	orthogn./myl.	2.7	3.0	3.1	3.4	3.2	3.2	3.2
GFTZ-66	orthogn./myl.	3.6	2.4	3.2	3.5	3.5	3.3	3.3
GFTZ-67	orthogn./myl.	0.3	1.1	1.9	2.1	2.4	2.5	2.5
GFTZ-68	orthogn./myl.	2.8	2.8	2.8	2.6	2.3	2.3	2.4
GFTZ-69	orthogn./myl.	4.7	5.6	5.8	5.8	6.0	5.9	5.8
GFTZ-71	orthogn./myl.	1.2	1.1	1.1	0.8	0.8	1.0	1.0
GFTZ-72	orthogn./myl.	5.8	4.3	3.4	3.1	3.2	3.4	3.4
GFTZ-73	orthogn./myl.	0.5	1.5	2.3	3.1	3.5	3.9	3.9
GFTZ-75	mafic gneiss	6.4	6.9	7.4	7.7	7.6	7.7	7.9
GFTZ-77	orthogn./myl.	2.3	1.5	1.4	1.3	1.1	1.1	1.0
GFTZ-78	orthogn./myl.	3.4	2.3	2.4	2.9	3.2	3.2	3.4
GFTZ-79	orthogn./myl.	1.3	1.3	1.0	1.0	1.0	1.1	1.1
GFTZ-82	orthogneiss	1.8	2.3	2.6	2.4	2.2	0.6	2.2
GFTZ-83	orthogneiss	2.0	1.6	1.7	2.1	2.4	2.4	2.4
GFTZ-86	mafic dike	13.1	13.3	13.2	12.8	12.8	12.6	12.6
GFTZ-87	mafic gneiss	3.5	9.0	7.7	7.4	7.3	7.1	7.1
GFTZ-88	orthogneiss	7.4	5.9	5.4	5.0	5.0	4.8	4.8
GFTZ-90	orthogneiss	2.8	5.0	9.1	3.3	3.4	3.6	3.4
GFTZ-91	paragneiss	5.0	6.5	6.4	6.0	5.8	5.5	5.7
GFTZ-92	Grenville Dia.	1.1	0.6	0.6	0.6	0.8	0.8	0.6
GFTZ-93	Sudbury Dia.	0.4	0.6	0.6	0.4	0.4	0.4	0.4

Note: orthogn./myl.=mylonitic orthogneiss

anisotropy decreases sharply with increasing pressure (Figure 2.16) until a stable value is reached. Extreme anisotropy at low confining pressures is most probably related to oriented fractures and microcracks in a rock, and may be sympathetic to or opposed to anisotropy related to the preferred orientation of anisotropic minerals (Christensen, 1965). As these microcracks close with increasing confining pressure, the anisotropy related to microcracks decreases, and anisotropy related to mineralogic orientation becomes apparent.

The two samples of diabase dikes (GFTZ-92 and -93) are virtually isotropic to compressional waves (anisotropy generally less than 1%). This is clearly a result of the preservation of original ophitic igneous textures in these samples. Even though these rocks contain high proportions of highly anisotropic minerals, the minerals are randomly oriented, and thus the bulk rocks are isotropic. Similar extremely low anisotropies for diabasic rocks are reported by Birch (1961).

The orthogneiss samples (including mylonitized orthogneiss) also show remarkably similar compressional wave velocities, regardless of wave propagation direction. An exception to this is GFTZ-69A, which has a much higher velocity than any other orthogneiss core measured (see Table 2.3). Closer examination of this core shows the

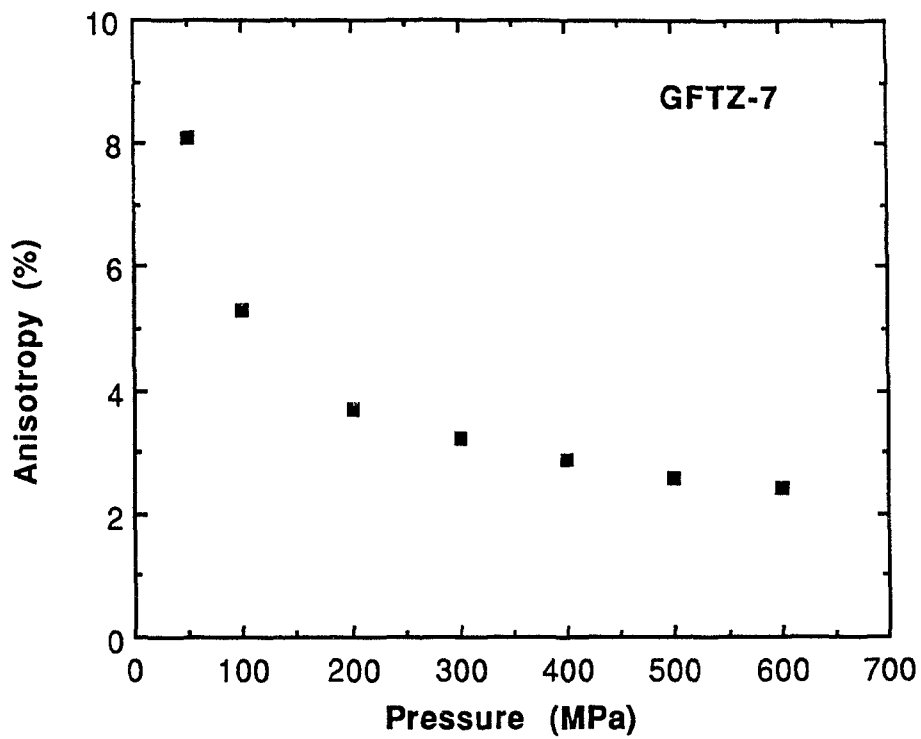


Figure 2.16. Seismic anisotropy in GFTZ-7 plotted against confining pressure. This sample shows the typical decrease in anisotropy that is related to microcrack closure.

presence of a large plagioclase porphyroclast (1.5 cm diameter) in the core, and therefore this core is not representative of the rock as a whole. Population statistics for velocity at 50 and 600 MPa in the orthogneiss samples (excluding GFTZ-69A) show average velocities of 6.00 and 6.29 km/s respectively. Even more informative, however, are the standard deviations from these mean values. At 50 MPa the standard deviation is 0.13 km/s, and it decreases to 0.07 km/s at 600 MPa. This tight clustering of velocity data is another indication that these rocks have low seismic anisotropy (generally less than 4%) throughout the measured pressure range.

The low anisotropy values for orthogneisses are related to the high proportions of feldspar and quartz, and the relative lack of mica in these rocks (see Table 2.1). Mylonitic fabrics in rocks with low percentages of mica are not capable of generating strong alignment of the c-axes of the mica grains, especially if S-C fabrics are developed (Jones and Nur, 1984; McDonough and Fountain, 1988). In addition, feldspar grains in mylonitic rocks generally show little or no preferred orientation, and thus generate no seismic anisotropy (Jones and Nur, 1984). Preferred orientation of feldspar grains is not observed in any of the GFTZ mylonitic samples.

Anisotropy in the paragneiss samples ranges from 1 to 17 per cent at 50 MPa, and from 2 to 15 per cent at 600 MPa. In these rocks the slow wave propagation direction is normal to the foliation (A) and the velocities for propagation directions in the foliation plane are often nearly equal, and faster (see Table 2.3). This pattern of transverse isotropy is most commonly related to preferred orientation of the c-axes of micas (Christensen, 1965). Alexandrov and Ryzhova (1961) showed that the compositional variations between biotite, muscovite and phlogopite have little effect on their respective velocities, but that micas in general are strongly anisotropic. They found that the slow direction in single crystals is along the c-axis (4.3 km/s); within the cleavage plane, velocities are fast and nearly equal (7.9 km/s).

Anisotropy in the "slow" paragneiss samples (GFTZ-23, -49 and -55) is uniformly low (less than or equal to 5% at 600 MPa) and shows no clear trend with per cent total mica (Figure 2.17). In samples GFTZ-23 and -49 the low anisotropy can be related to low amounts of mica, but GFTZ-55 has considerable mica. GFTZ-55 is a mylonitized paragneiss, with a strongly developed S-C fabric. As mentioned previously, this type of fabric development hinders the alignment of c-axes in micas, and thus this sample has a low anisotropy despite a high mica content.

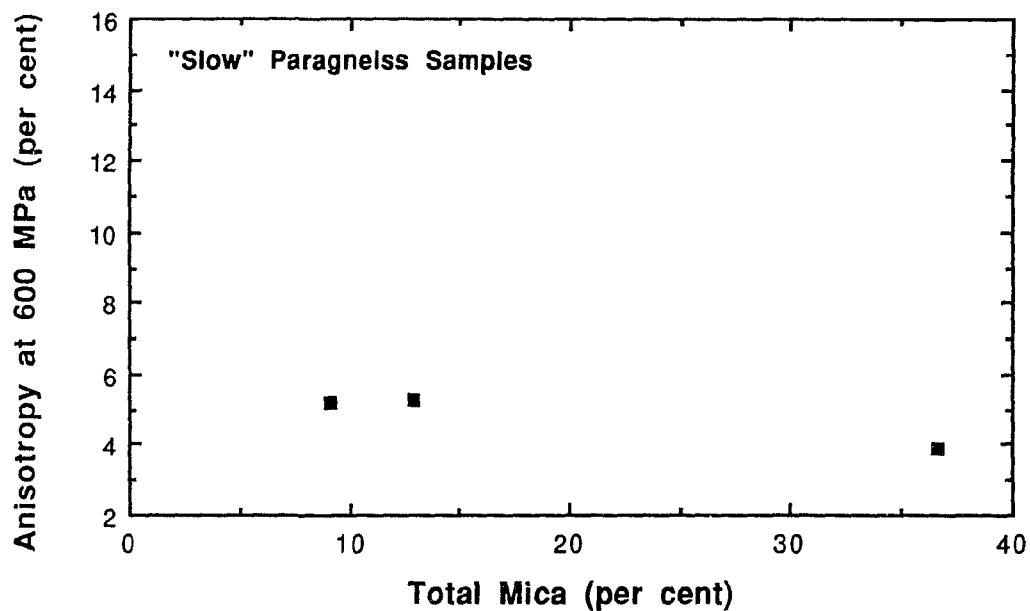


Figure 2.17. Anisotropy versus per cent mica for the "slow" paragneiss samples, which have uniformly low anisotropy. These data are in contrast to those in Figure 2.18, where the "fast" paragneisses have variable anisotropy that is dependent on per cent mica.

The mica content of the paragneiss samples with high average velocities is plotted against per cent anisotropy in Figure 2.18. The dashed line in this figure is for 100 per cent parallel orientation of the c-axes of micas from Christensen (1965). The present data form a linear trend, with a correlation coefficient of 0.86 that falls below the relationship for perfect alignment of micas. In these rocks the anisotropy is strongly controlled by mica content and its preferred orientation.

Anisotropy in mafic rocks is dominated by hornblende because of its tendency toward strong preferred orientation, and because of the strong anisotropy of single crystals (Siegesmund et al., 1988). The anisotropy of hornblende is pronounced (Alexandrov and Ryzhova, 1961) with the fast wave propagation direction along the c-axis (7.85 km/s) and the slowest propagation direction along the crystallographic a-axis (6.10 km/s). Anisotropy in the mafic samples from the GFTZ, excluding the diabase rocks, is generally high but shows no consistent trends with mineralogy, including modal hornblende (Figure 2.19). GFTZ-37 and GFTZ-40 are exceptions in that they show low anisotropy at 600 MPa (less than or equal to 4%). GFTZ-37 is taken from the hinge region of a complexly folded mafic dike, and preferred orientation of hornblende is not observed in either of the arbitrarily oriented B or C

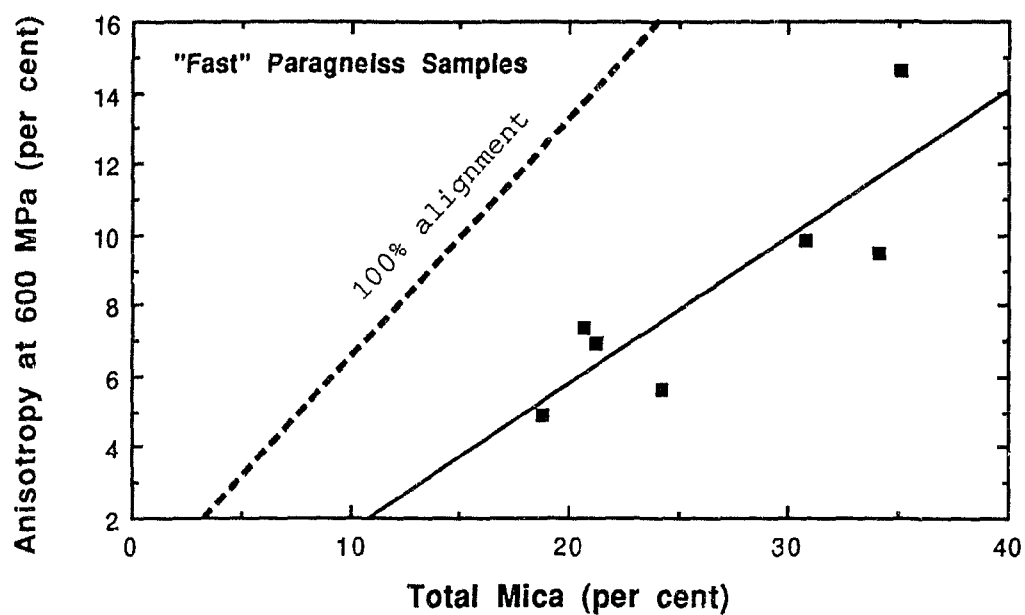


Figure 2.18. Anisotropy as a function of mica content for the faster paragneiss samples. The 100% alignment relationship (dashed line) is from Christensen (1965). The solid line fits the GFTZ data, and is discussed in the text.

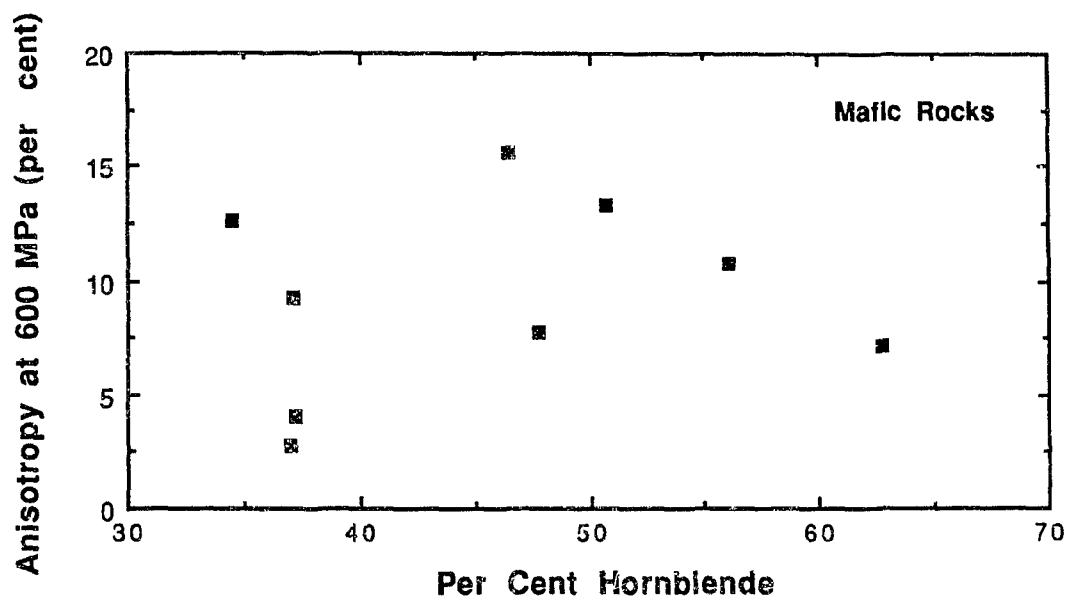


Figure 2.19. Anisotropy at 600 MPa plotted against per cent hornblende for the mafic rocks. Anisotropy ranges from 6 to 16 per cent in these samples (which exclude the diabase samples) but shows no consistent trend with the amount of hornblende. Some of these rocks show strong hornblende orientation (those with high anisotropy) but others show little to no alignment.

direction cores. GFTZ-40 is a sample of metagabbro, and lacked an obvious preferred orientation of hornblende.

There is no systematic variation with modal hornblende for the mafic samples with high anisotropy (see Figure 2.19). This is a consequence of the strong alignment of hornblende in some samples (especially GFTZ-39 and -59) and lesser degrees of preferred orientation in others.

Comparisons between per cent anisotropy and the relative abundances of other anisotropic minerals also revealed no systematic variation for the samples of mafic rocks. This is likely a complication of the variation in modal mineralogy for these rocks, and the wide variation in apparent preferred orientations. It is interesting to note however, that among the metamorphosed mafic dikes along Collins Inlet the amount of seismic anisotropy in individual rocks is fairly uniform (10.8 to 13.3%), except for the one sample that was taken from a fold hinge.

Summary

The compressional wave velocities through representative lithologies of the GFTZ in central Ontario are reported in Table 2.6 for different propagation directions at 50, 200 and 600 MPa. All samples show marked increases in compressional wave velocity through the

Table 2.6 Mean densities and compressional wave velocities of GFTZ lithologies at various confining pressures. One standard deviation of each value is given immediately below in *italics*.

Lithology	Number of Analyses	Density (g/cc)	50 MPa	100 MPa	200 MPa	300 MPa	400 MPa	500 MPa	600 MPa
Average Properties									
orthogneiss	18	2.65 <i>0.03</i>	6.00 <i>0.13</i>	6.11 <i>0.09</i>	6.21 <i>0.09</i>	6.25 <i>0.07</i>	6.27 <i>0.07</i>	6.29 <i>0.07</i>	6.29 <i>0.07</i>
orthogn./myl.	12	2.65 <i>0.03</i>	6.03 <i>0.11</i>	6.13 <i>0.09</i>	6.20 <i>0.09</i>	6.25 <i>0.07</i>	6.27 <i>0.07</i>	6.28 <i>0.07</i>	6.29 <i>0.07</i>
paragneiss	11	2.72 <i>0.06</i>	6.04 <i>0.12</i>	6.15 <i>0.11</i>	6.24 <i>0.10</i>	6.27 <i>0.10</i>	6.29 <i>0.10</i>	6.30 <i>0.10</i>	6.31 <i>0.11</i>
mafic gneiss	6	2.97 <i>0.11</i>	6.61 <i>0.23</i>	6.71 <i>0.25</i>	6.80 <i>0.24</i>	6.83 <i>0.23</i>	6.86 <i>0.22</i>	6.87 <i>0.22</i>	6.88 <i>0.22</i>
mafic dike	6	2.97 <i>0.05</i>	6.68 <i>0.16</i>	6.74 <i>0.16</i>	6.79 <i>0.16</i>	6.82 <i>0.17</i>	6.83 <i>0.16</i>	6.84 <i>0.17</i>	6.85 <i>0.17</i>
A Direction									
orthogneiss	18	2.65 <i>0.03</i>	5.93 <i>0.23</i>	6.07 <i>0.17</i>	6.20 <i>0.18</i>	6.21 <i>0.14</i>	6.24 <i>0.14</i>	6.26 <i>0.14</i>	6.26 <i>0.14</i>
orthogn./myl.	12	2.64 <i>0.03</i>	5.99 <i>0.18</i>	6.12 <i>0.16</i>	6.20 <i>0.15</i>	6.24 <i>0.15</i>	6.26 <i>0.15</i>	6.28 <i>0.15</i>	6.28 <i>0.15</i>
paragneiss	11	2.70 <i>0.06</i>	5.80 <i>0.15</i>	5.93 <i>0.12</i>	6.00 <i>0.10</i>	6.03 <i>0.09</i>	6.05 <i>0.10</i>	6.07 <i>0.10</i>	6.07 <i>0.10</i>
mafic gneiss	5	2.96 <i>0.12</i>	6.32 <i>0.28</i>	6.39 <i>0.28</i>	6.49 <i>0.24</i>	6.53 <i>0.23</i>	6.55 <i>0.23</i>	6.56 <i>0.22</i>	6.56 <i>0.22</i>
mafic dike	6	2.97 <i>0.05</i>	6.41 <i>0.37</i>	6.47 <i>0.37</i>	6.52 <i>0.37</i>	6.55 <i>0.36</i>	6.57 <i>0.36</i>	6.58 <i>0.36</i>	6.58 <i>0.36</i>

Table 2.6 (cont)

Lithology	Number of Analyses	Density (g/cc)	50 MPa	100 MPa	200 MPa	300 MPa	400 MPa	500 MPa	600 MPa
(km/s)									
B Direction									
orthogneiss	15	2.65 0.03	6.03 0.10	6.12 0.09	6.19 0.16	6.26 0.08	6.29 0.08	6.30 0.08	6.31 0.08
orthogn./myl.	10	2.65 0.03	6.04 0.09	6.12 0.07	6.17 0.18	6.25 0.06	6.28 0.06	6.29 0.06	6.30 0.06
paragneiss	11	2.72 0.06	6.15 0.27	6.28 0.25	6.37 0.24	6.41 0.24	6.43 0.24	6.45 0.24	6.46 0.24
mafic gneiss	6	2.97 0.11	6.82 0.26	6.93 0.24	7.01 0.24	7.05 0.23	7.07 0.23	7.09 0.23	7.09 0.23
mafic dike	6	2.98 0.05	6.85 0.21	6.92 0.21	6.96 0.23	6.98 0.23	6.98 0.23	7.00 0.24	7.01 0.23
C Direction									
orthogneiss	18	2.65 0.03	6.05 0.13	6.16 0.10	6.24 0.09	6.28 0.09	6.30 0.09	6.31 0.09	6.32 0.09
orthogn./myl.	12	2.65 0.03	6.06 0.09	6.15 0.09	6.23 0.09	6.26 0.09	6.28 0.09	6.29 0.09	6.29 0.09
paragneiss	11	2.73 0.06	6.10 0.18	6.22 0.16	6.31 0.14	6.34 0.14	6.36 0.14	6.38 0.14	6.39 0.14
mafic gneiss	6	2.98 0.12	6.68 0.35	6.81 0.34	6.89 0.35	6.91 0.36	6.95 0.35	6.96 0.34	6.97 0.34
mafic dike	6	2.97 0.05	6.77 0.22	6.84 0.21	6.89 0.20	6.92 0.20	6.93 0.20	6.94 0.20	6.95 0.19

Note: orthogn./myl.=mylonitic orthogneiss

confining pressure range 50-200 MPa. Above 200 MPa, the velocity-pressure curves approach linearity and intrinsic velocities related to mineral content and preferred orientations are apparent.

Granitic orthogneiss samples form a tightly clustered field in velocity-density space, with an average velocity of 6.29 km/s at 600 MPa. Paragneiss samples are subdivided into two groups, based on modal quartz+potassium feldspar. Samples with high modal quartz+potassium feldspar have a low average velocity (6.20 km/s), while those with low modal quartz + potassium feldspar have relatively higher velocities (6.30 km/s). Mafic rocks display a high average velocity of 6.96 km/s at 600 MPa.

Anisotropy decreases in most rocks with confining pressure. Mylonite and orthogneiss samples always have low anisotropy values (less than 4%), primarily because of the low modal mica in these rocks. Paragneiss and mafic rocks have generally higher and more variable anisotropy values (5 to 15%), related to the percentage and degree of orientation of anisotropic minerals in these rocks.

CHAPTER 3

IN SITU VELOCITY MEASUREMENTS

On-going Great Lakes Experiments

The laboratory velocity data presented in the previous chapter highlight some important features of compressional wave velocities in the rocks of the GFTZ, most notably (1) strain variation in mylonitic orthogneiss does not introduce seismic velocity variation or significant seismic anisotropy, (2) average paragneiss velocities are nearly equal to average orthogneiss velocities, although paragneiss velocities can be directionally dependent and (3) seismic anisotropy in paragneiss and amphibolite gneiss units is higher than anisotropy in the orthogneiss assemblages. However, it is unclear if these results are a function of the 'true' seismic response of the rocks of the GFTZ, or if they were biased by the sampling requirements for laboratory velocity measurements (no fractures, minimal alteration, and the small size of the cores). Large scale fractures or lithologic variation within a single unit can have a significant effect on in situ velocity behavior (e.g. Moos and Zoback, 1983; Pyrak-Nolte et al., 1990), but the importance of these factors cannot be assessed in a simple laboratory study.

On-going Great Lakes Experiments (OGLE) a small consortium of scientists from Dalhousie University, the Geological Survey of Canada (GSC) and the United States Geological Survey (USGS), was formed to determine the in situ physical properties of the rocks of the GFTZ (Burke et al., 1989).

The OGLE group conducted five shallow, high resolution refraction profiles in the southernmost GFTZ (Figure 3.1). Two of these profiles (Lines 3 and 4) crossed the GFTZ boundary fault region south of Philip Edward Island in order to evaluate the effect of visible, large scale fractures on the in situ velocity and anisotropy of the mylonites. The boundary fault mylonite zone is often a topographic low, posing an additional challenge for unbiased sampling.

Davidson (personal communication, 1988) postulates that Beaverstone Bay and Mill Lake may overlie an easily eroded, mica-rich paragneiss unlike those that outcrop along the shorelines of the lakes. Lines 5 and 6 were run in Beaverstone Bay to assess the in situ seismic velocity of the paragneisses. Line 1 in Mill Lake serves as a control for Line 6. Line 2 (indicated by a dashed line in Figure 3.1) was proposed as a cross-strike profile in Mill Lake, but the water in Mill Lake was too shallow for seismic acquisition in that location. Individual site

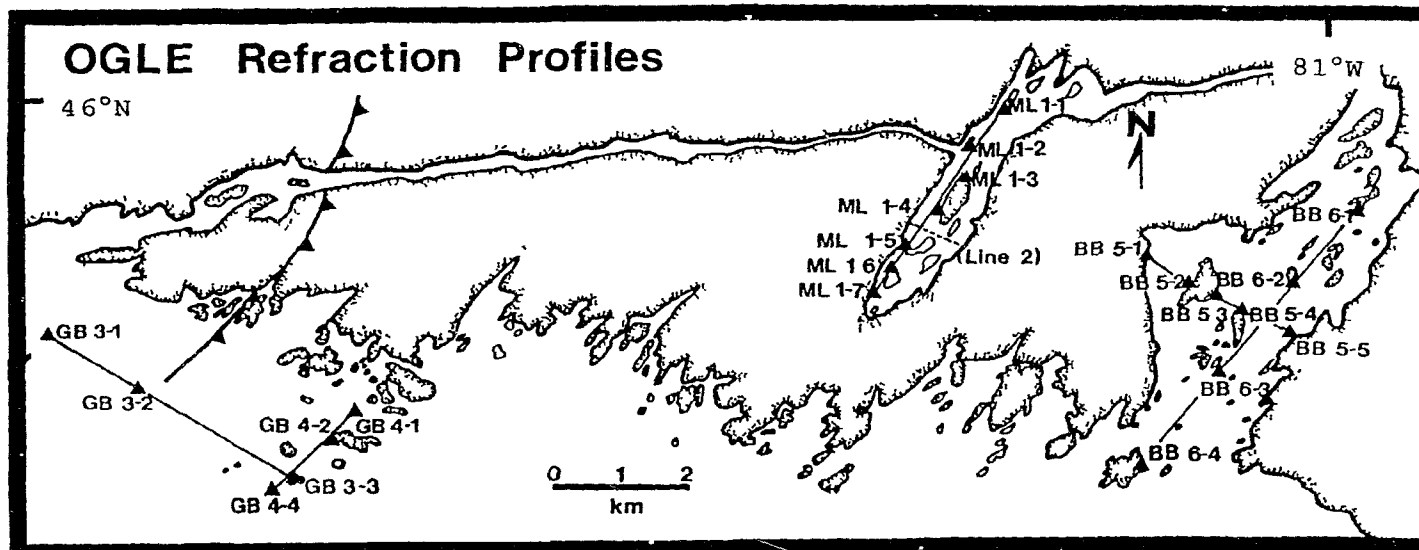


Figure 3.1 Location of OGLE refraction profiles. Lines 3 and 4 cross the boundary fault region south of Philip Edward Island, Lines 1 (in Mill Lake) and 6 (in Beaverstone Bay) were shot to determine velocity parallel to foliation in paragneiss. The location for proposed Line 2 is indicated by the dashed line.

information on each of the OGLE refraction profiles is summarized in Table 3.1

Experimental Method

Data Acquisition

The seismic source for all profiles was a new, bubble-free airgun towed one meter below the water surface behind the USGS boat *Neecho*. The maximum volume of the gun when operated in the bubble-free mode is 2.5 liters (150 cubic inches), and it operates at a pressure of 70 bars (1000 psi). The airgun signature (Figure 3.2) and frequency response (Figure 3.3) were especially desirable for the OGLE profiles as they lack the "ringiness" commonly associated with the use of airguns. Because of the sharp signal of this airgun, minimal post-acquisition processing of the data was required in order to display pertinent features on the final sections. Shots were automatically fired every 30 seconds (ca. 15-25 meters apart) and were located using a Mini RangerTM network.

Land-based digital seismometer locations were precisely determined to 0.05 m using a Wild Electronic Distance MeterTM to measure distances (horizontal and vertical) and angles to the Mini RangerTM antennae. Shots were recorded on PRS-1 "lunchbox" seismographs located on

Table 3.1. Site geometry information for OGLE profiles.

Site Number	Elevation (m)	Site Geometry	Closest Offset (km)	Farthest Offset (km)
ML 1-1	8.200	End-on	0.152	3.255
ML 1-2	1.514	Split	0.049	2.520
ML 1-3	1.081	Split	0.165	2.005
ML 1-4	1.703	Split	0.120	1.770
ML 1-5	2.664	Split	0.011	2.561
ML 1-6	1.339	End-on	0.018	3.001
ML 1-7	7.250	End-on	0.450	3.529
GB 3-1	0.821	End-on	0.029	4.163
GB 3-2	1.190	Split	0.097	2.554
GB 3-3	6.626	End-on	0.284	4.417
GB 4-1	2.030	End-on	0.199	1.416
GB 4-2	1.870	Split	0.092	0.750
GB 4-3	6.626	End-on	0.092	1.248
GB 4-4	2.260	End-on	0.598	1.801
BB 5-1	4.180	End-on	0.047	2.384
BB 5-2	0.841	Split	0.140	1.634
BB 5-3	6.750	Split	0.048	1.237
BB 5-4	3.120	Split	0.055	1.624
BB 5-5	0.900	End-on	0.088	2.400
BB 6-1	1.440	End-on	0.138	5.147
BB 6-2	8.250	Split	0.086	3.628
BB 6-3	2.650	Split	0.101	3.200
BB 6-4	2.680	End-on	0.116	5.133

Note: Sites GB 3-3 and GB 4-3 are the same location. Prefix GB denotes sites on Georgian Bay, BB denotes Beaverstone Bay sites, and ML denotes Mill Lake sites.

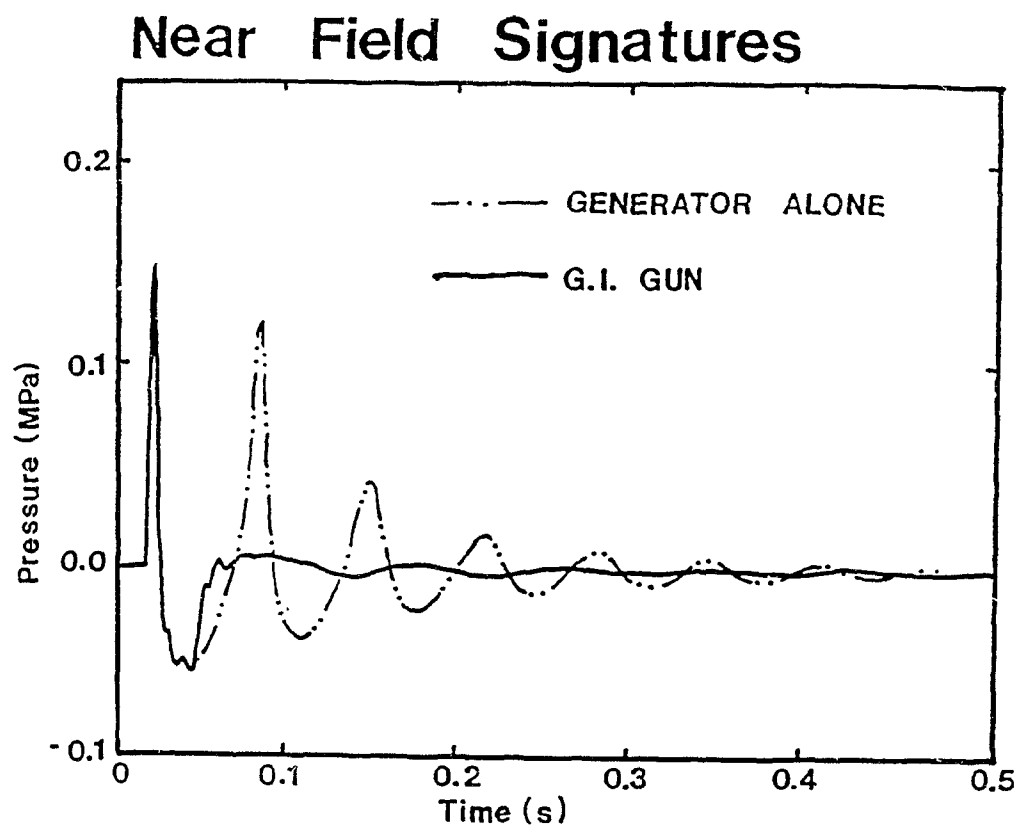


Figure 3.2 Signature of the G.I. (Generator-Injector) "bubble-free" airgun (heavy curve). For comparison, the output of the generator alone (comparable to a standard airgun) is shown as the light, dashed curve.

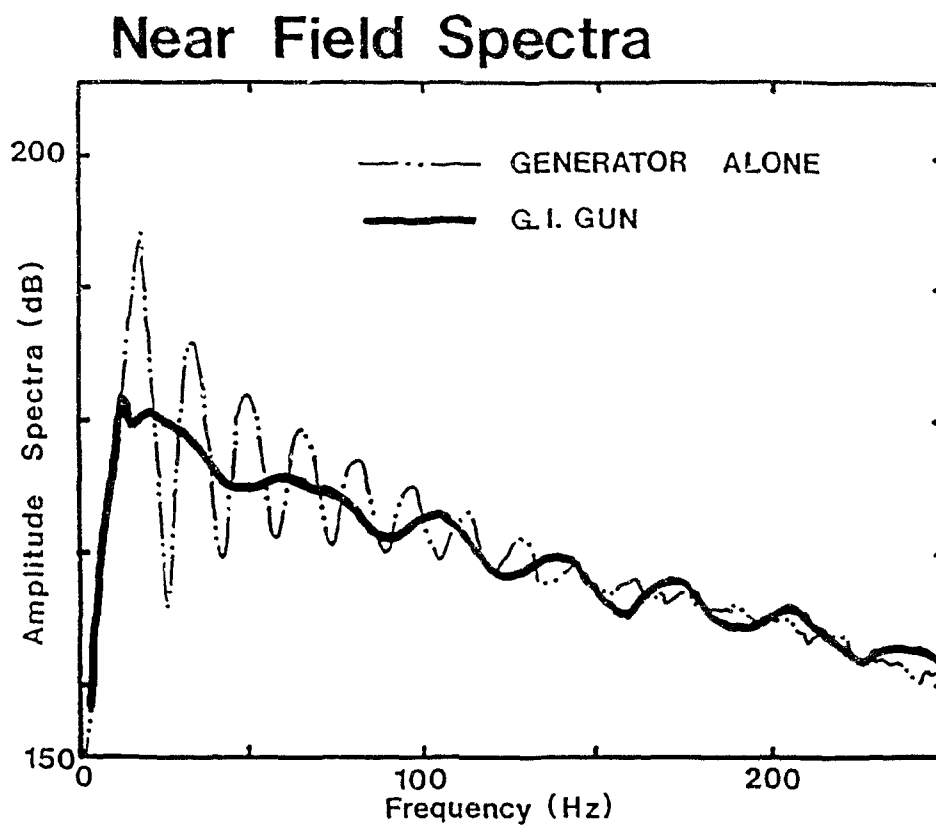


Figure 3.3 The frequency response of the G.I. airgun (heavy curve). The lighter, dashed curve is the frequency response of the generator cylinder alone, and shows the "ringiness" commonly associated with airguns.

small islands in the lakes surveyed. Both the shot clock and the clocks used to time each seismograph were based on the GOES east satellite clock. Data were collected only when tracking of the east satellite resulted in a precision of 10 microseconds or better.

The sampling rate of the seismographs was 120 samples/microsecond, and the frequency response was 5-30 Hz (Mereu et al., 1989). Seismometers were plastered onto the smooth rock outcrops to reduce shaking and extraneous movement. In addition, the seismometers were covered with pails or boxes to lessen wind generated noise.

Data Processing

Following the data acquisition, the data from each recorder were downloaded onto minicassettes. Field sections were displayed from these tapes to check data quality. The data were converted to standard SEG-Y format, including the integration of the navigation data, using the LithoSeisTM processing package developed at the GSC.

The data presented in this work have only been corrected for true shot offset and recorder time drift: no further processing of the sections was done. The clarity and the simplicity of most of the sections does not require a more sophisticated processing sequence. Problems associated with Line 5 will be discussed below.

Travel time picks of the various arrivals were made using the VISTA 6TM processing package. Simple linear regression (Press et al., 1986) was performed on segments of each set of arrivals to derive the velocity and the error associated with the slope estimates. The linear regression results for compressional wave velocities are given in Table 3.2 for each site. Slope fits from the linear regression analyses for shear wave arrivals are given in Table 3.3.

RAYAMP Raytracing

The adequacy of the linear regression results was tested using the RAYAMP raytracing package, which is based on the WKBJ algorithm (Whittall and Clowes, 1979). RAYAMP modelling showed that no rays in the model reached the surface unless either velocity discontinuities or extremely high velocity gradients were incorporated into the input parameters (details in Chapter 4). The WKBJ method is noted for its failure to calculate rays correctly at caustics (Fuchs and Muller, 1971). Therefore, layers with very large velocity discontinuities are not appropriate input parameters for the RAYAMP modelling package.

Several features of the seismic sections, including uniform amplitudes and lack of distinct slope segments, suggest the presence of velocity gradients. The high

Table 3.2. Slope fits, errors and correlation coefficients (R) for OGLE compressional wave velocity data.

Site Name	Offsets (km)	Velocity (km/s)	Error (km/s)	R
ML 1-1	0.15-0.64	4.03	0.23	0.97
ML 1-1	0.70-2.84	6.10	0.05	0.99
ML 1-2	0.05-0.48	4.42	0.31	0.96
ML 1-2	0.43-1.93	5.96	0.05	0.99
ML 1-3	0.16-0.60	4.34	0.20	0.97
ML 1-3	0.63-1.08	6.00	0.28	0.97
ML 1-4	0.12-0.29	3.78	0.30	0.96
ML 1-4	0.32-1.35	5.89	0.10	0.98
ML 1-5	0.03-0.34	4.37	0.21	0.98
ML 1-5	0.36-1.67	6.21	0.10	0.99
ML 1-6	0.04-0.39	4.06	0.25	0.96
ML 1-6	0.41-2.31	6.02	0.09	0.99
ML 1-7	0.57-2.77	5.99	0.05	0.99
GB 3-1	0.29-1.25	5.34	0.04	0.99
GB 3-1	1.27-4.35	5.88	0.04	0.99
GB 3-2	0.24-1.21	5.31	0.03	0.99
GB 3-2	1.23-2.75	5.86	0.03	0.99
GB 3-3	0.21-1.22	5.33	0.04	0.99
GB 3-3	1.25-4.42	5.89	0.04	0.99
GB 4-1	0.19-1.42	5.73	0.06	0.99
GB 4-2	0.23-0.74	5.75	0.05	0.98
GB 4-3	0.10-1.18	5.81	0.03	0.99
GB 4-4	0.61-1.80	5.80	0.03	0.99
BB 6-1	0.14-0.77	4.49	0.10	0.98
BB 6-1	0.81-4.37	6.34	0.09	0.98
BB 6-2	0.09-0.80	4.60	0.21	0.95
BB 6-2	0.82-2.95	6.22	0.08	0.99
BB 6-3	0.10-0.89	4.51	0.14	0.98
BB 6-3	0.91-3.20	6.32	0.08	0.99
BB 6-4	0.12-0.73	3.95	0.16	0.97
BB 6-4	0.81-4.04	6.31	0.04	0.99

Table 3.3. Slope fits, errors and correlation coefficients (R) for OGLE shear wave velocity data.

Site Name	Offsets (km)	Velocity (km/s)	Error (km/s)	R
ML 1-1	0.23-0.98	2.70	0.04	0.99
ML 1-1	1.01-2.63	3.26	0.09	0.97
ML 1-2	0.58-1.02	2.69	0.05	0.98
ML 1-2	1.05-2.27	3.20	0.04	0.99
ML 1-3	0.35-0.98	2.71	0.06	0.98
ML 1-3	1.02-1.36	3.09	0.07	0.97
ML 1-4	0.17-1.10	2.78	0.03	0.99
ML 1-4	1.14-1.78	3.14	0.04	0.99
ML 1-5	0.23-0.98	2.68	0.07	0.98
ML 1-5	1.00-1.67	3.16	0.03	0.99
ML 1-6	0.14-1.13	2.62	0.03	0.99
ML 1-6	1.16-2.25	3.12	0.07	0.98
ML 1-7	0.65-3.27	3.17	0.02	0.99
GB 3-1	0.03-0.84	2.80	0.01	0.99
GB 3-1	0.86-4.28	3.24	0.02	0.99
GB 3-2	0.24-0.78	2.69	0.05	0.99
GB 3-2	0.82-2.74	3.27	0.04	0.99
GB 3-3	0.09-0.80	2.67	0.05	0.99
GB 3-3	0.82-4.38	3.20	0.02	0.99
GB 4-1	0.19-1.37	2.77	0.03	0.99
GB 4-2	0.25-0.74	2.79	0.05	0.98
GB 4-3	0.23-1.20	2.64	0.02	0.99
GB 4-4	0.65-1.78	2.81	0.03	0.99
BB 6-1	0.44-1.30	2.65	0.06	0.98
BB 6-1	1.33-3.97	3.42	0.05	0.98
BB 6-2	0.13-1.23	2.69	0.06	0.99
BB 6-2	1.26-2.36	3.35	0.09	0.98
BB 6-3	0.25-1.23	2.61	0.06	0.98
BB 6-3	1.25-1.78	3.21	0.10	0.98
BB 6-4	0.19-1.22	2.59	0.06	0.98
BB 6-4	1.26-3.96	3.39	0.04	0.99

velocity gradients necessary to trace rays through the RAYAMP model (in excess of 4 km/s/km; see Chapter 4) greatly exceed the laboratory-derived values (0.1 km/s/MPa or 0.3 km/s/km). While these velocity gradients seem high, they are consistent with other results in the Shield (D. White, personal communication, 1991) and with the plane layer solutions in the following sections. This strongly suggests that the near-surface velocity gradients are dominated by the presence of open fractures.

Experimental Results

Boundary Fault Profiles

OGLE Lines 3 and 4 were designed to determine the in situ velocity and anisotropy behavior at shallow levels across the mylonitic orthogneisses of the GFTZ boundary fault just south of Philip Edward Island. Line 3 is 4.5 km long and is oriented normal to the mylonitic fabrics. Line 4 is 1.25 km long and parallels the strong mylonitic foliation. The length of Line 4 was limited by very shallow water and numerous islands in the region.

Three seismograph sites were located along the length of Line 3 (Figure 3.1). The seismic sections from the end-

of-line sites, along with the corresponding travel time picks of the first arrivals are shown in Figures 3.4 and 3.5.

Line 3 Velocities

The seismic sections from the endpoints of Line 3 (Figures 3.4 and 3.5) provide the farthest offsets and therefore velocity information on the deepest traveling rays. The slopes of these sections can be broken into two segments. Clear first breaks are apparent across the lengths of both sections, although there was more wind noise recorded at site GB 3-3, because of its higher elevation (6.62 meters) than at other locations (see Table 3.1). The first segment, at close offsets, has a V_p of 5.33 km/s; the second segment shows a velocity of 5.87 km/s.

Shear wave arrivals at sites GB 3-1 and GB 3-3 show a change in slope similar to that of the first arrivals. The second arrivals result in shear wave velocities of 2.80 km/s for offsets less than 0.84 km, and 3.21 km/s for greater offsets.

Superposition of the first breaks on these end-of-line sections (Figure 3.6) emphasizes the similarity in travel times for up-dip shooting (site GB 3-1) and down-dip shooting (site GB 3-3). This similarity requires that the dip of velocity features is negligible, and thus the

Figure 3.4. A) Seismic section and B) picked P and S wave arrivals at site GB 3-1.

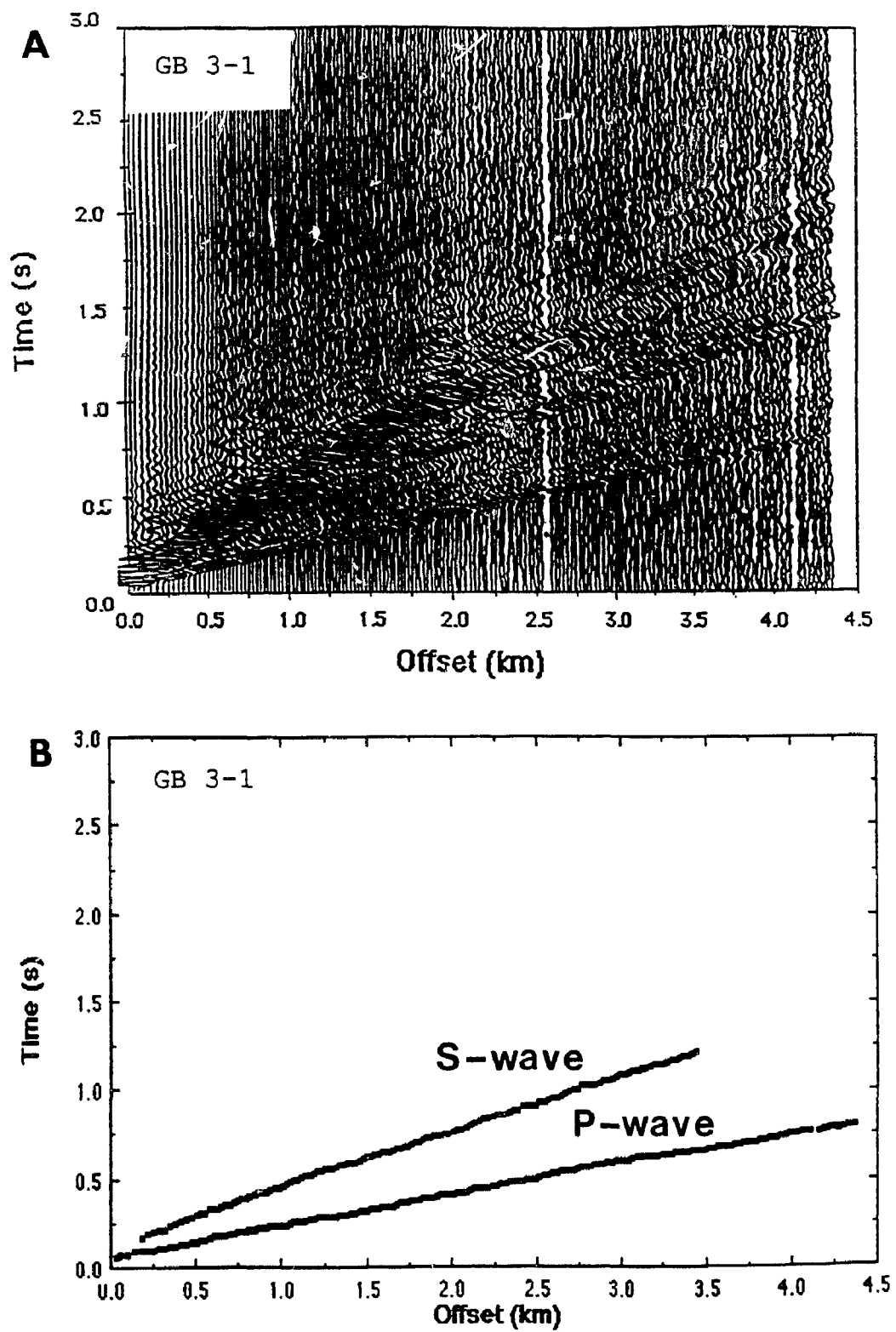


Figure 3.4

Figure 3.5. A) Seismic section and B) picked arrivals at site GB 3-3.

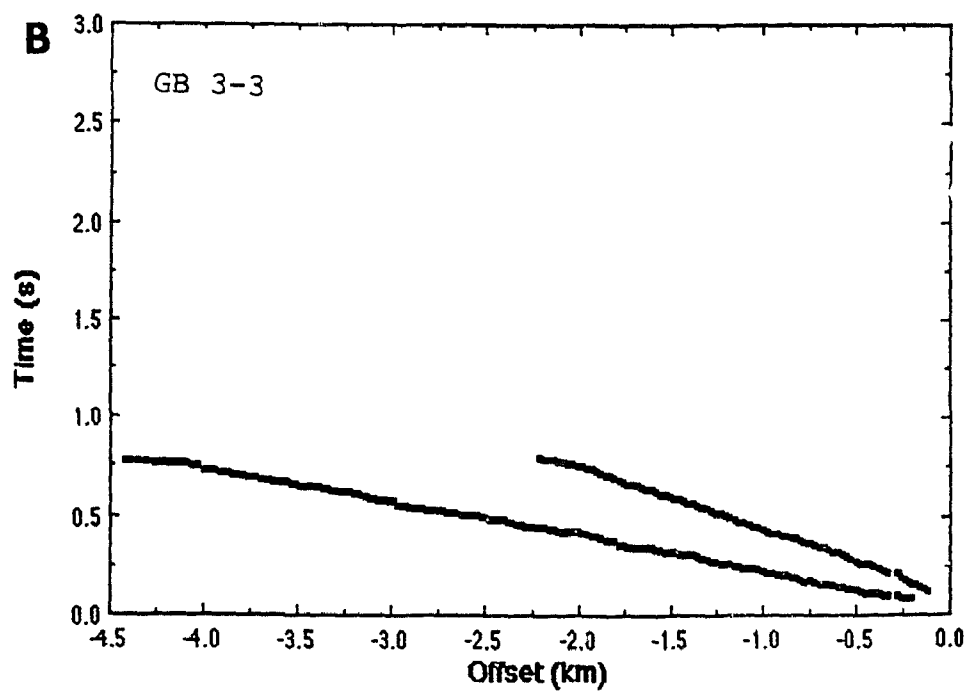
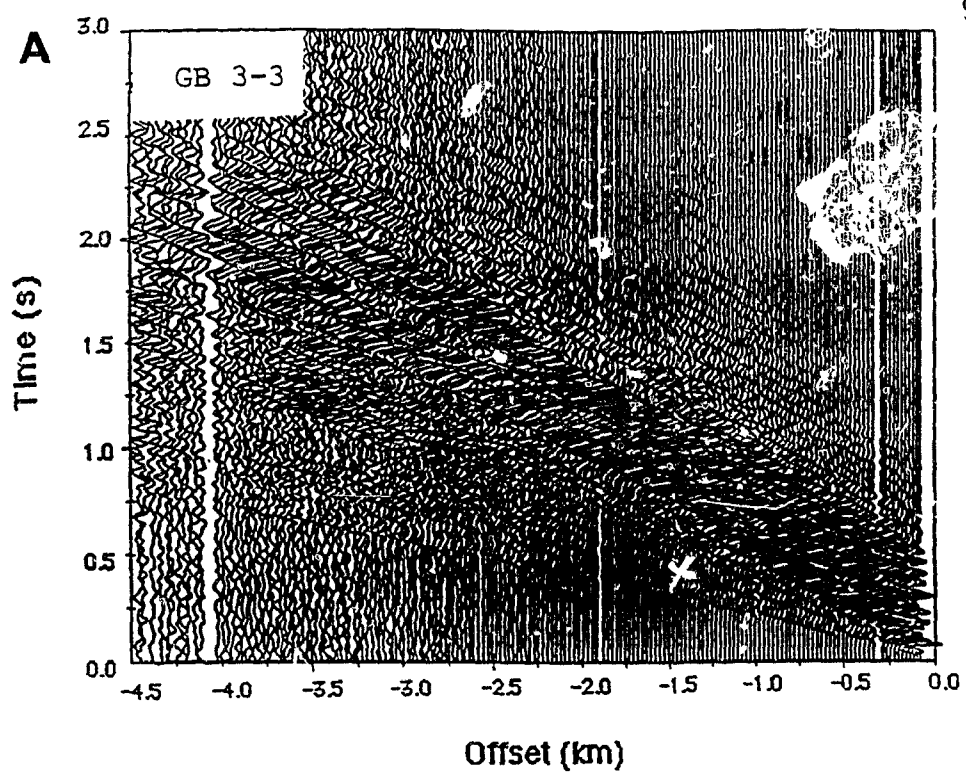


Figure 3.5

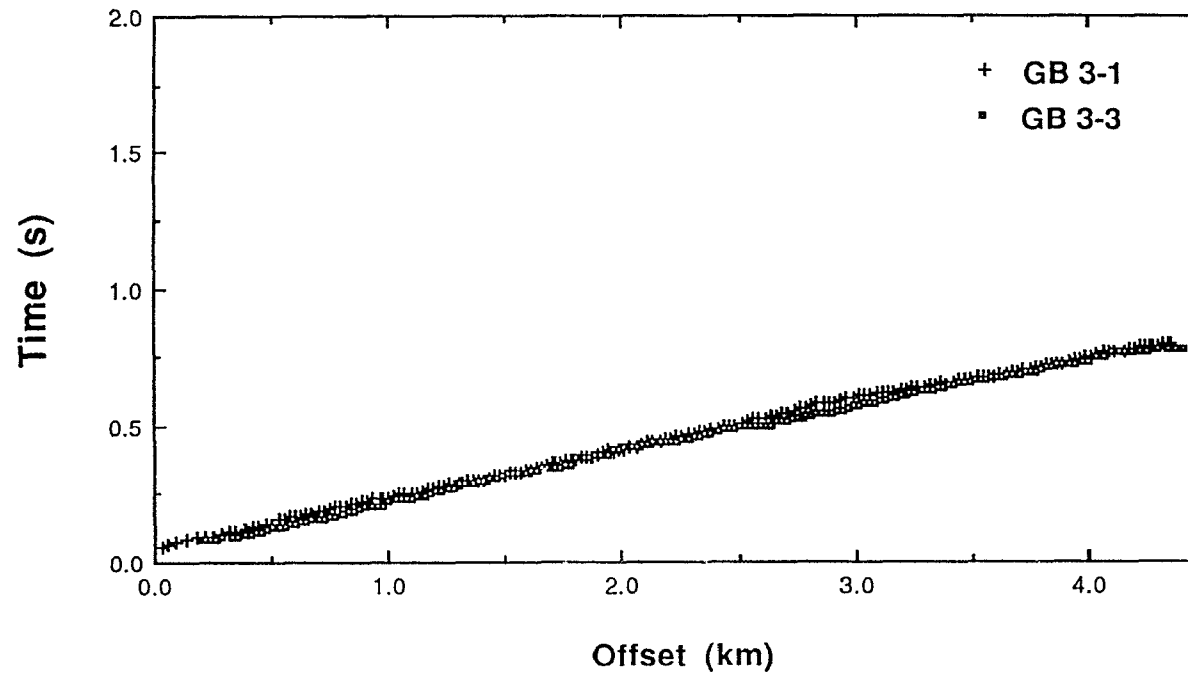


Figure 3.6. Superposition of the first arrivals recorded at sites GB 3-1 and GB 3-3. The curves are indistinguishable, confirming a one-dimensional structure across the boundary fault.

apparent velocities reported can be regarded as true in situ velocities (Telford et al., 1976).

Site GB 3-2 (in Appendix 1), near the midpoint of Line 3, provides shallow velocity information on the boundary fault rocks. The slopes of the best-fit lines to the first breaks (Table 3.2) are equal for this split-spread geometry, another indication that the velocities obtained by shooting up-dip are the same as those observed shooting down-dip. Therefore, a flat layer (i.e. one-dimensional) geometry can be successfully used to model the data. The compressional wave velocity measured at this site is 5.31 km/s for near offsets, and 5.86 km/s for offsets greater than 1.23 km. Shear wave velocities are reported in Table 3.3.

Line 4 Velocities

Despite the short length of Line 4, good quality data were obtained from the end of line sites of this profile (Figures 3.7 and 3.8). The water between sites GB 4-3 and GB 4-4 was too shallow for Neecho to sail through so the airgun was not fired between sites GB 4-3 and GB 4-4. Velocities from the end-of-line sites are equal at 5.78 km/s, within the error of the slope estimates (Table 3.2). The deepest ray penetration along Line 4 is less than 200 meters, due to the short profile length. The second

Figure 3.7. A) Seismic section and B) picked arrivals at site GB 4-1.

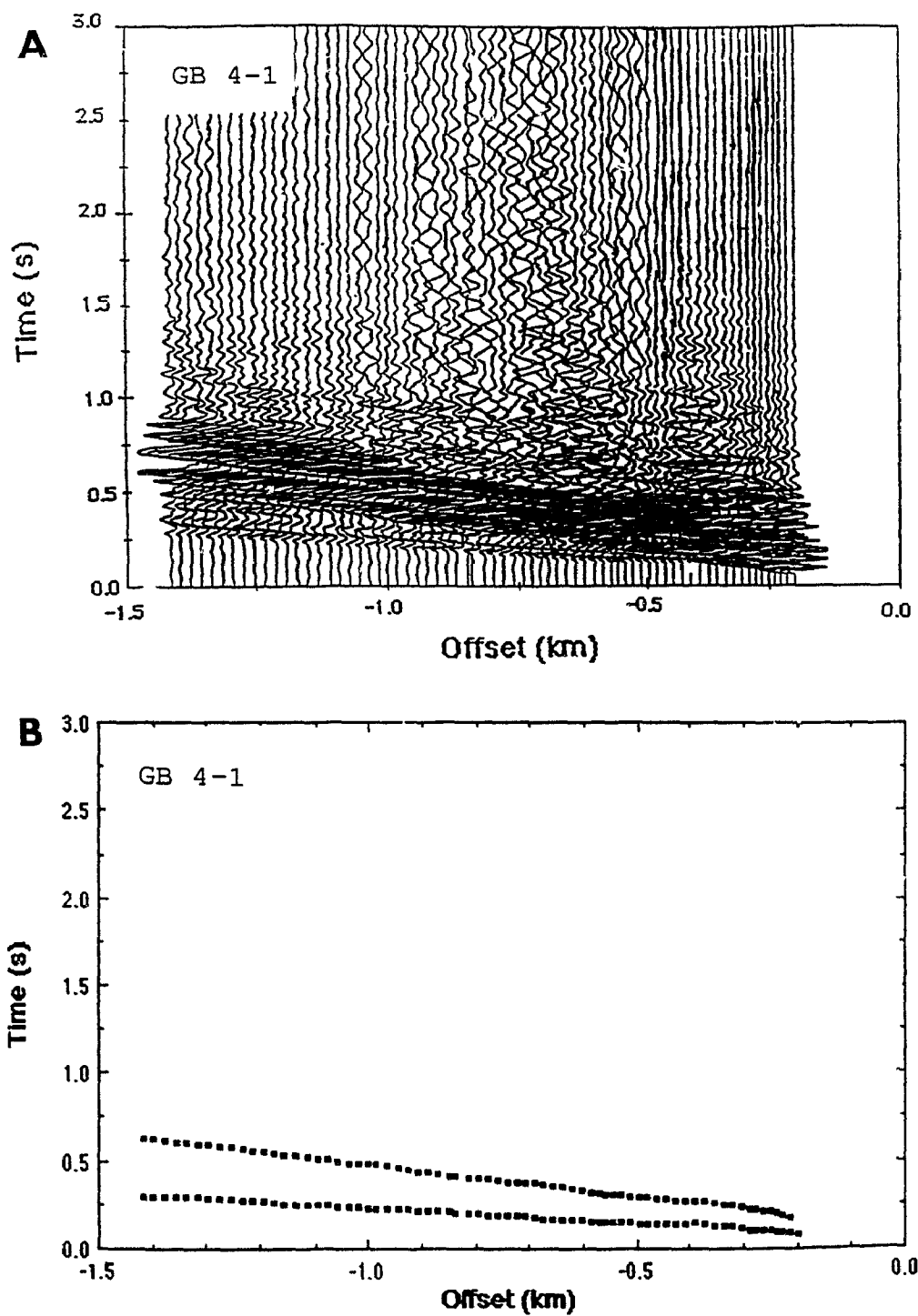


Figure 3.7

Figure 3.8. A) Seismic section and B) picked arrivals at site GB 4-4.

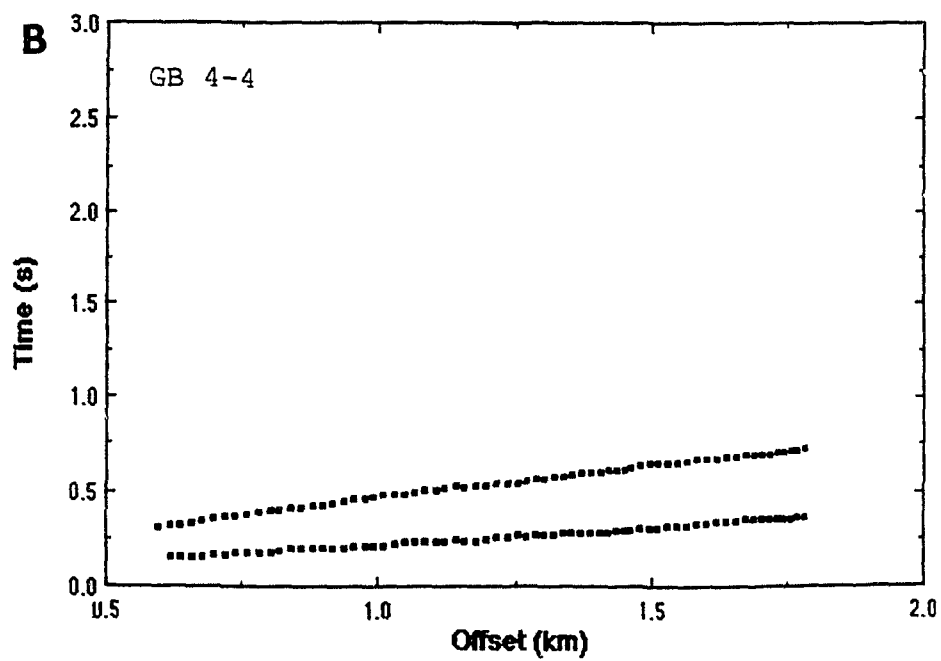
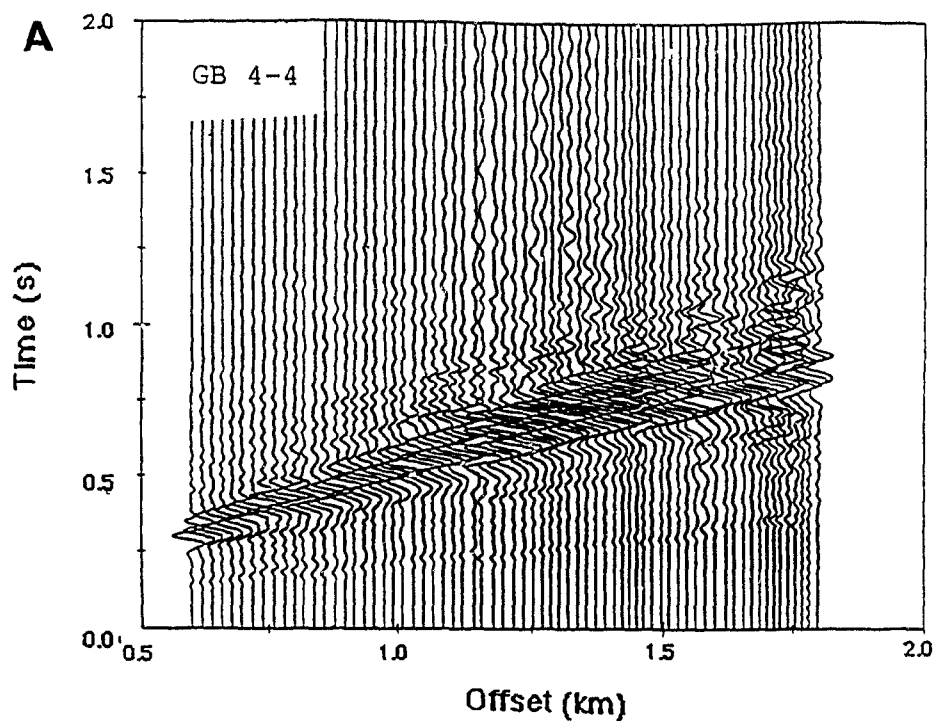


Figure 3.8

arrivals were also adequately fit by a single slope with a velocity of 2.78 km/s (see Table 3.3).

The data from site GB 4-2 (in Appendix 1) are of limited value as this site was not directly "in line" and resulted in a fan geometry for much of the section. Nonetheless, linear regression analysis results in the same velocities for compressional and shear waves (5.75 and 2.84 km/s, respectively) as at other sites along Line 4.

Anisotropy of the GFTZ Boundary Fault

The in situ compressional wave velocities measured normal and parallel to the mylonitic fabric in these rocks are identical to each other within the error of the fitting technique. This strong similarity in compressional wave velocities for orthogonal propagation directions supports the laboratory results which indicate the mylonites of the GFTZ boundary fault are nearly isotropic. The identical shear wave velocities measured by OGLE Lines 3 and 4 also support this conclusion.

Beaverstone Bay Profiles

The refraction profiles in Beaverstone Bay were designed to measure the velocities both normal and parallel to the foliation in this paragneiss assemblage. These rocks do not outcrop south of the mouth of Beaverstone Bay (Davidson and Bethune, 1988). The width of Beaverstone Bay

(Figure 3.1) was a critical parameter for Line 5, as this was the only location in the GFTZ that allowed cross-strike shooting of a paragneiss assemblage. Unfortunately, this location was not ideal, as discussed below.

Five sites were located along Line 5, two to the east of Burnt Island, and three to the west of it. Four sites were used along Line 6, which extended the length of Beaverstone Bay, parallel to the foliation of the paragneiss units exposed on shore.

Line 5 Velocities

The data collected at the sites along Line 5 cannot be adequately modelled by simple linear regression. The data from each site produce highly unstable velocities, with associated large error estimates (generally greater than 0.3 km/s). This non-linearity of first arrivals (Figure 3.9) is likely caused by the location of the line across Burnt Island (Figure 3.1), which consists largely of metagabbro. The downdip extent of this metagabbro body is unknown (Davidson, personal communication, 1989), and therefore its effect on the refraction arrivals is difficult to assess.

The location of the profile was constrained by the narrow width of Beaverstone Bay, the relatively shallow water and especially by the numerous small islands scattered throughout the bay. Line 5 was positioned to

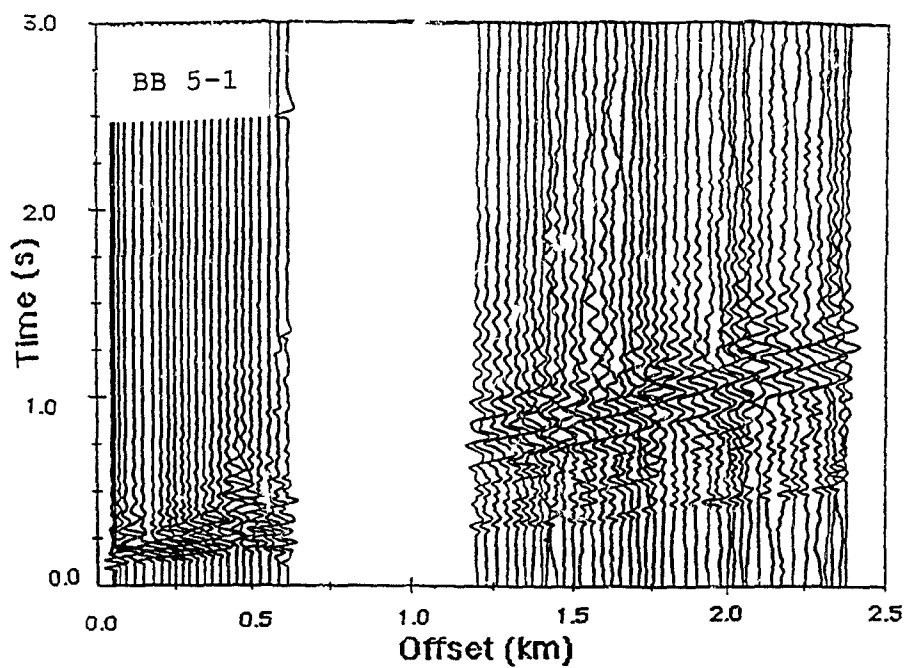


Figure 3.9 Seismic section recorded at site BB 5-1. Note the very complex pattern of first arrivals. The data from Line 5 were not used for linear regression analyses because of this non-linear behavior.

take advantage of the greatest width of the bay, while avoiding many of the islands. The complications make a simple interpretation of the Line 5 data impossible; more rigorous processing of these data will be conducted by OGLE at a later date.

Line 6 Velocities

The sites at the endpoints of Line 6 (Figures 3.10 and 3.11) have the largest offsets and thus the deepest ray penetration for Beaverstone Bay. Unfortunately, the wind noise at these sites was quite high and it was not possible to pick first arrivals for offsets greater than 4 kilometers at site BB 6-4. Although noise was high at site BB 6-1, first breaks are apparent on this profile to 4.5 km. However, it was impossible to differentiate the first break from the noise at high magnification for offsets greater than 3.5 km. Both sections show a gap of ca. 0.2 km width as the airgun was not shot when *Neecho* sailed around the island of site BB 6-3 (see Figure 3.1). Velocity data for these sites are given in Table 3.2.

Both sites BB 6-1 and BB 6-4 show a relatively low velocity (4.49 and 3.95 km/s, respectively) for near offsets. This layer has a thickness of $370 \text{ m} \pm 35 \text{ m}$, and is anomalous for having such low velocities. These low velocities may be indicators of; (1) fractures in paragneiss, (2) alteration or weathering of the paragneiss,

Figure 3.10. A) Seismic section and B) picked arrivals at site BB 6-1.

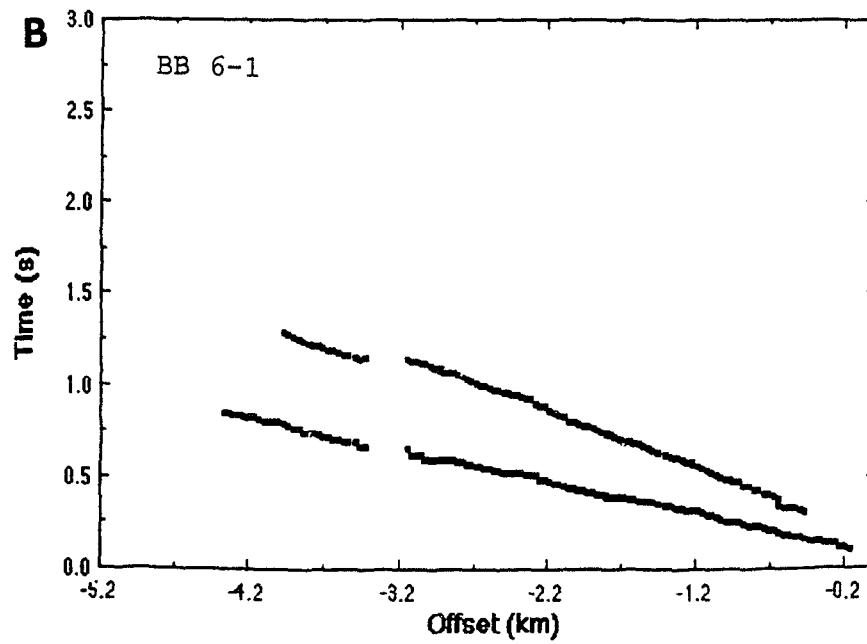
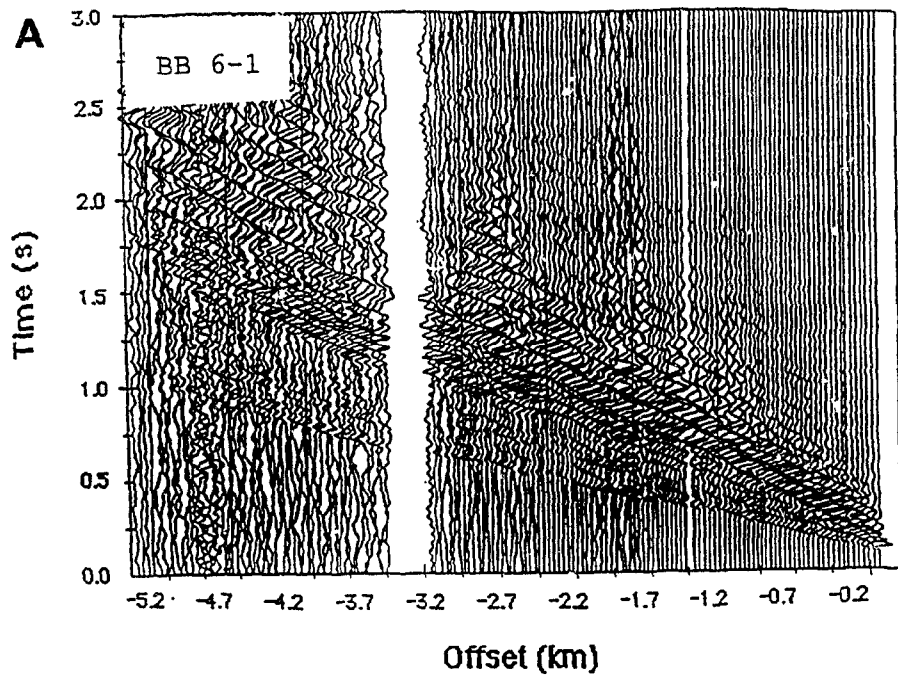


Figure 3.10

Figure 3.11. A) Seismic section and B) picked arrivals at site BB 6-4.

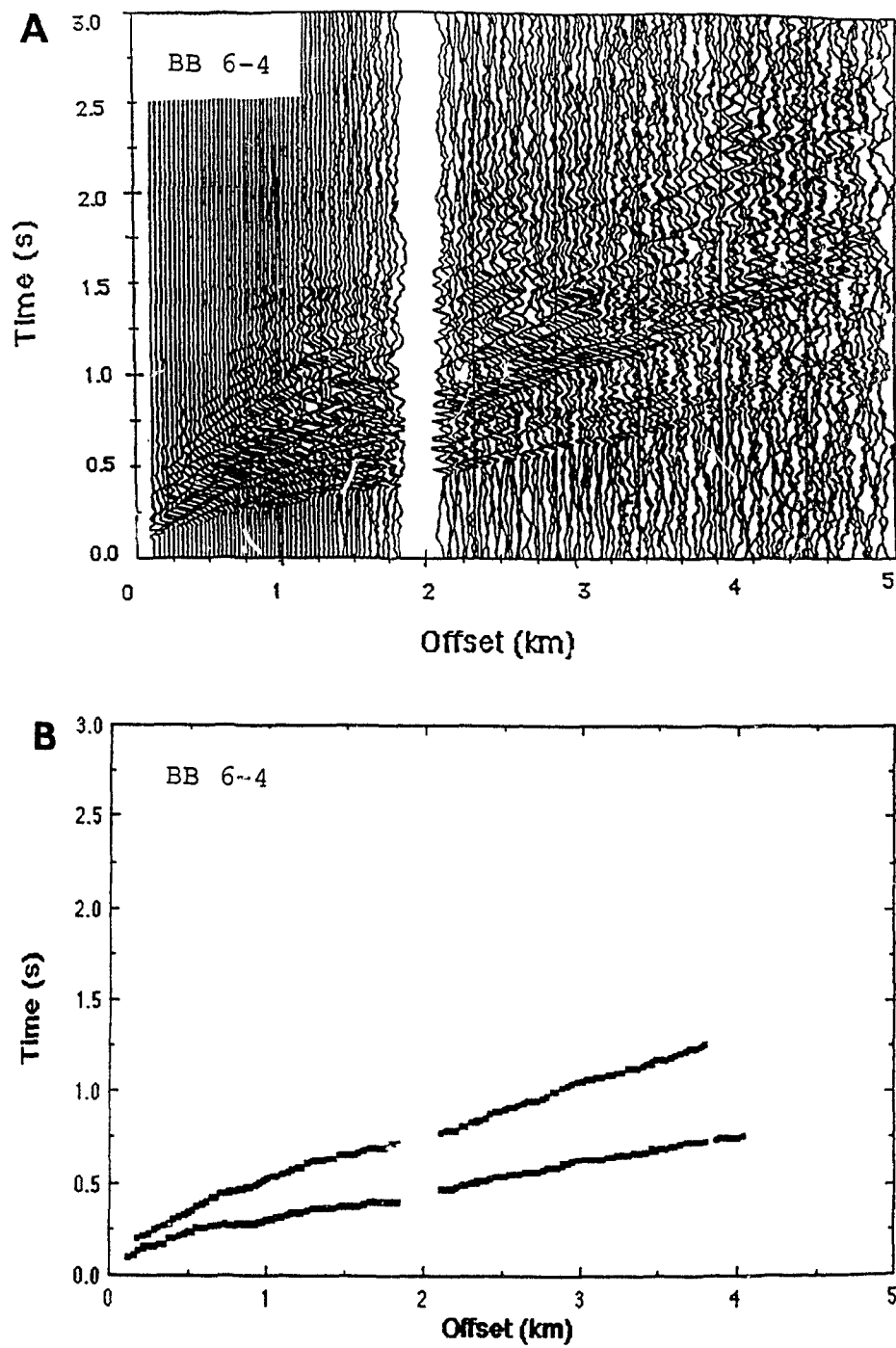


Figure 3.11

or (3) the presence of a different rock type under Beaverstone Bay.

The higher velocity segments of the first arrivals at both of the end-of-line sites produce the same velocity (6.30 km/s) within error, and likely represent "unaltered" paragneiss velocities. The similarity of the first arrivals (Figure 3.12) at these end-of-line sites indicates that, like Lines 3 and 4 south of Philip Edward Island, a one-dimensional geometry is adequate to model these data.

The second arrivals can also be treated as two segments. Both sites BB 6-1 and BB 6-4 have near offset arrivals (<1.3 km) with a velocity of 2.68 km/s. At greater offset the velocity of the second arrival at both sites is 3.41 km/s. The thickness of the shallow layer defined by shear wave velocities is the same as that for the compressional wave velocities layer (ca. 400 m), and it is clear that the shear waves are sampling the same layer.

The sites in the middle of Line 6 (Appendix 1) recorded split spread geometries, and do not have as great offsets as the end of line sites. Nonetheless, they provide additional information on the shallow velocity structure, as well as some confirmation of the deeper velocity information. Site BB 6-2 had a lunchbox recorder that malfunctioned, and thus there are several large data gaps in this profile where the instrument did not record.

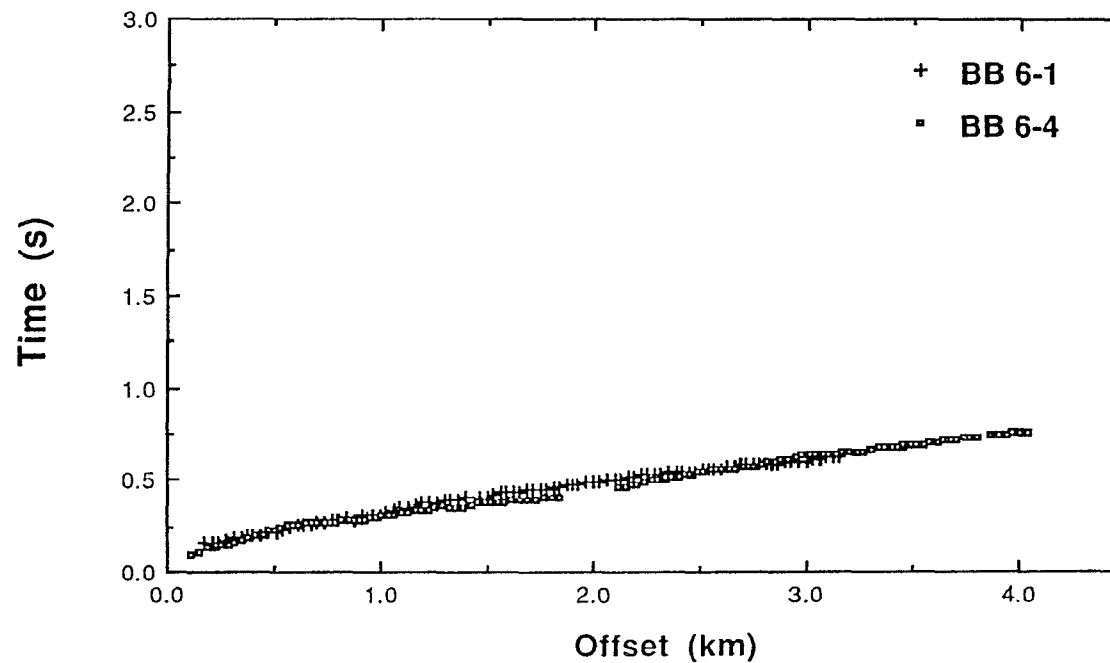


Figure 3.12. Superposition of the first arrivals recorded at sites BB 6-1 and BB 6-4. The curves are virtually indistinguishable, confirming a one-dimensional structure along the strike of the paragneisses in Beaverstone Bay.

Site BB 6-3 has the same data gap as sites BB 6-1 and BB 6-4 which resulted from the lack of shots around the island on which site BB 6-3 was located. The first break branches at site BB 6-2 are mirror images, again reinforcing the interpretation of this line as a one-dimensional structure. The data from site BB 6-3 also show mirror-image first arrivals very similar to those at the sites discussed previously.

Both the shallow and the deeper first and second arrivals at these mid-line sites confirm the data collected from sites BB 6-1 and 6-4. Line 6 can thus be adequately modelled as a one dimensional velocity structure with a shallow layer ($< 400\text{m}$) having a compressional wave velocity of ca. 4.40 km/s and shear wave velocity of 2.63 km/s underlain by a deeper layer with a compressional wave velocity of 6.30 km/s and a shear wave velocity of 3.4 km/s .

Mill Lake

Seven lunchbox sites were located along the length of Mill Lake (Figure 3.1) in order to provide very high resolution coverage of the paragneiss assemblage under the lake. Unfortunately, the lake was too narrow and shallow to conduct a cross strike profile (proposed Line 2). Therefore it is not possible to assess, using refraction

techniques alone, the seismic anisotropy of the rocks beneath Mill Lake. However, data from the Mill Lake sites can be compared to the results of Line 6 which crosses similar rocks in Beaverstone Bay.

Line 1 Velocities

There are three end-of-line sites on Line 1, as no shots were fired between ML 1-6 and ML 1-7. The data from sites ML 1-1 (Figure 3.13) and ML 1-6 (Figure 3.14) at opposite ends of the profile are very similar, reinforcing the one-dimensional velocity structure interpretation for along-strike profiles. As in Beaverstone Bay, the first arrivals have been broken into two segments. For near offsets the compressional wave velocity is 4.0 ± 0.25 km/s, and is similar to the zone of very low velocities discussed for Line 6. The thickness of this zone is 270 ± 50 m. For greater offsets, the compressional wave velocity is 6.05 ± 0.07 km/s, which probably corresponds to unaltered paragneiss.

The second arrivals for Line 1 can also be divided into two segments with different slopes. The first has a velocity of ca. 2.6-2.7 km/s, and a thickness of 300 m. The slope of the second branch has a velocity of 3.15 km/s.

Site ML 1-7 (Figure 3.15) does not have the same shallow level data as the previous sites, because the airgun was not fired at close offsets (few shots were fired

Figure 3.13. A) Seismic section and B) picked arrivals at site ML 1-1.

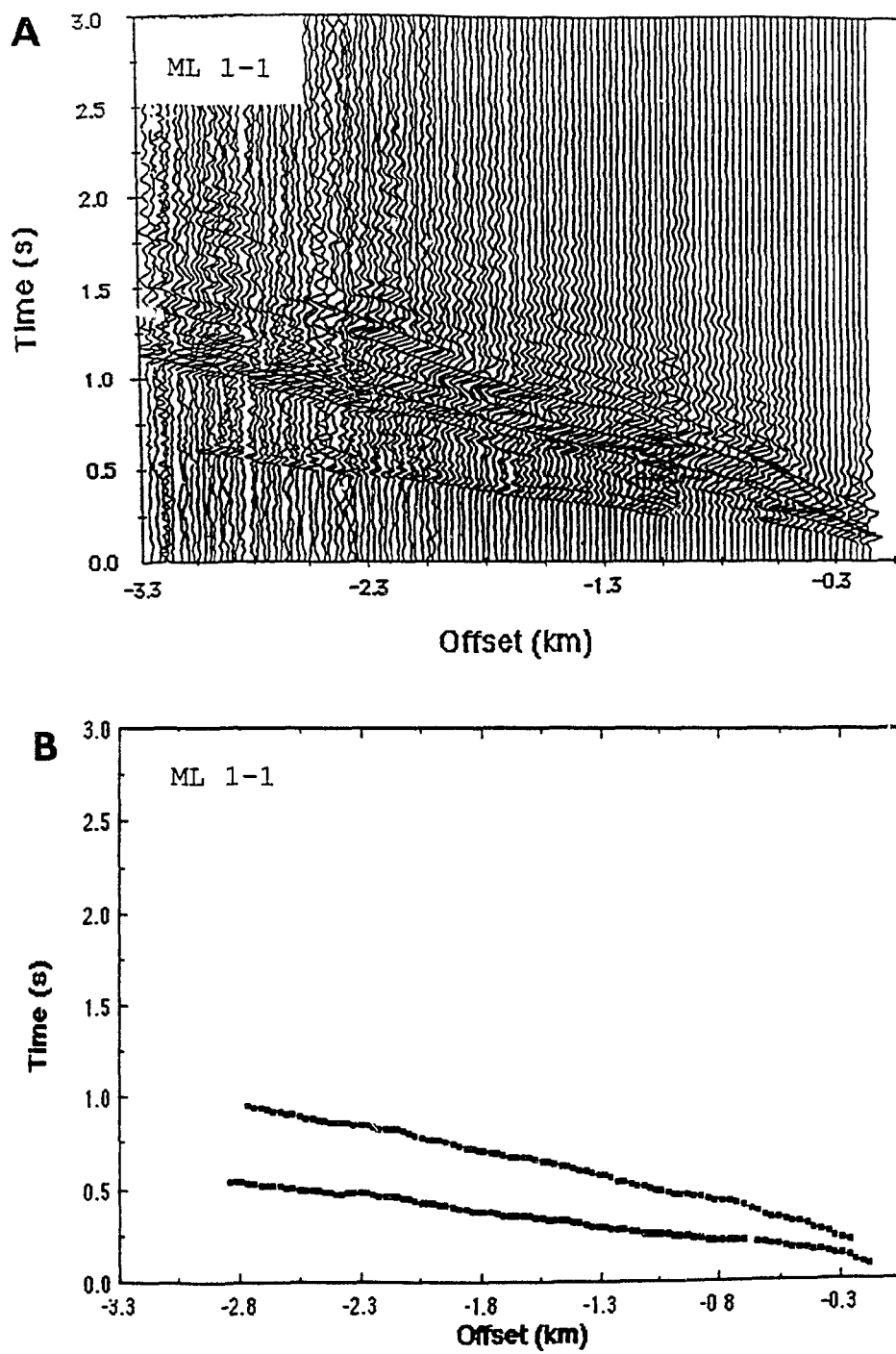


Figure 3.13

Figure 3.14. A) Seismic section and B) picked arrivals at site ML 1-6.

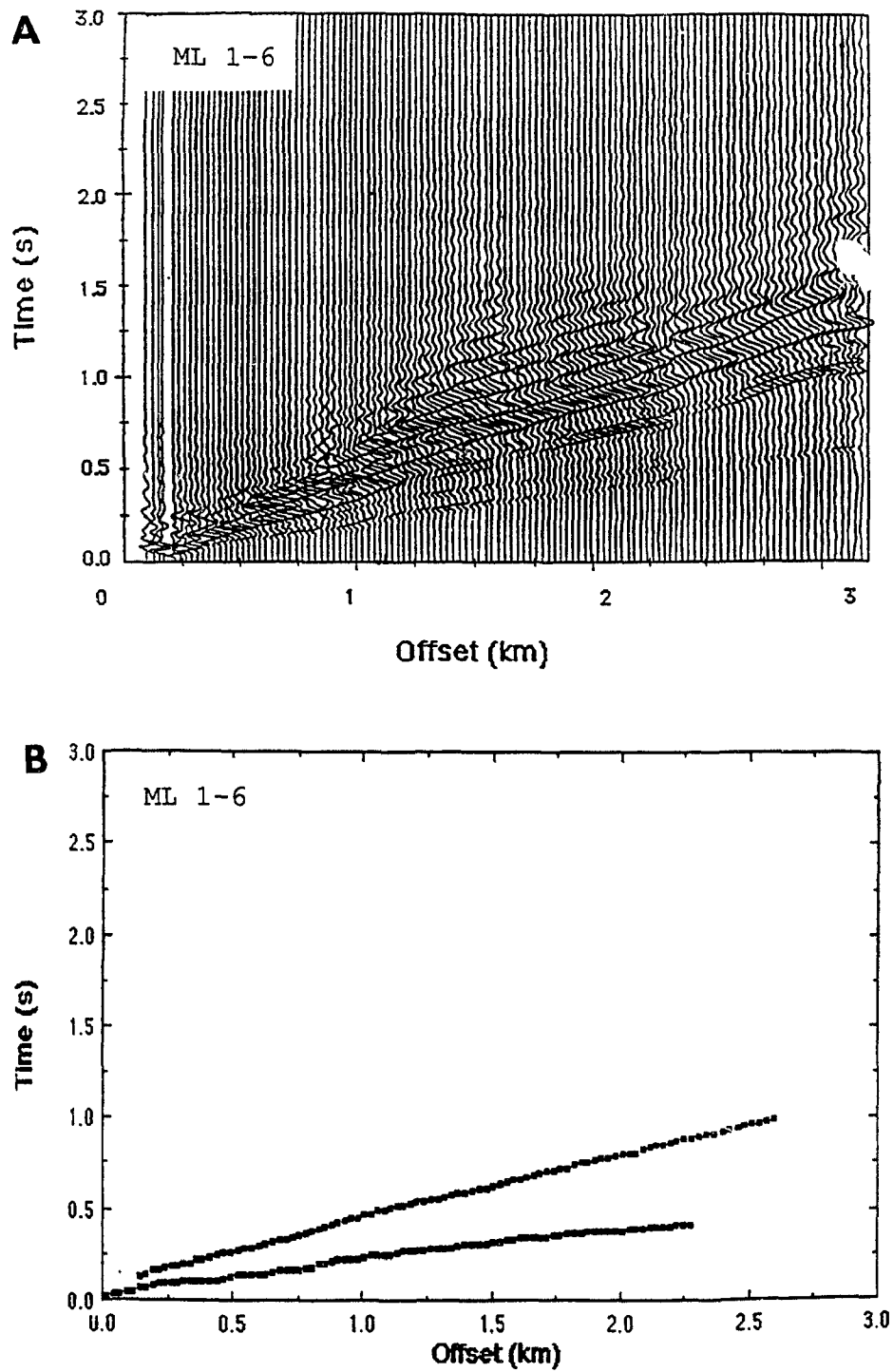


Figure 3.14

Figure 3.15. A) Seismic section and B) picked arrivals at site ML 1-7.

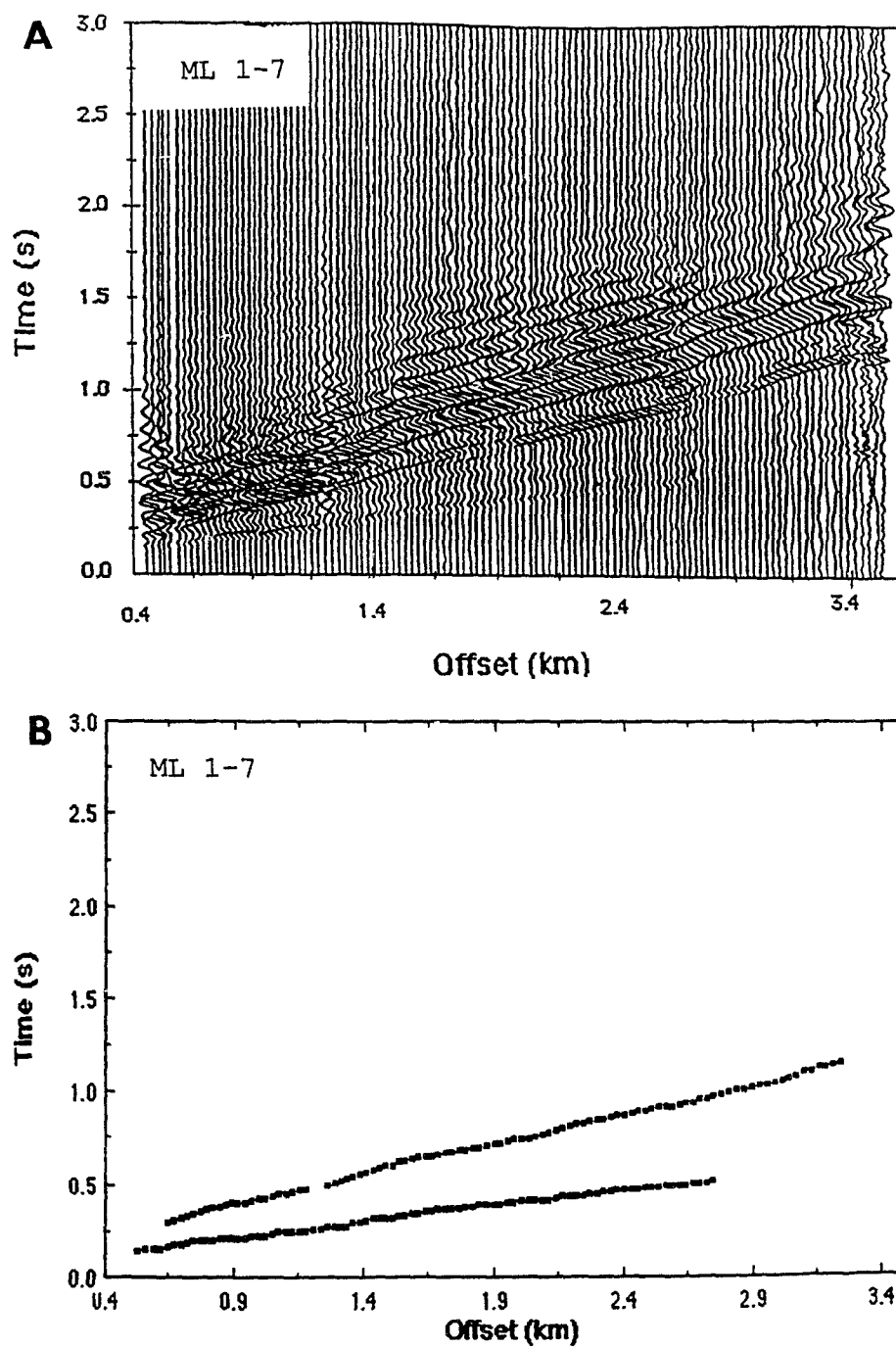


Figure 3.15

between ML 1-6 and ML 1-7). Therefore this profile can be fit with a single slope ($V_p=5.99$ km/s) for all offsets (Table 3.2). The second arrivals at this site can be fit by a single slope with a velocity of 3.17 km/s.

The data from the mid-line sites of Line 1 (in Appendix 1) do not provide as deep coverage as the end of line sites, but can be used to confirm the shallow level structure. Unfortunately, the errors associated with the shallow-level fits are quite high (generally 0.2 to 0.3 km/s) and therefore do not provide a tight constraint on the velocity. Nonetheless, the linear regression analyses for the data from these mid-line sites are identical, within the error of the fitting technique. The results are consistent with a one-dimensional structure with a shallow-level compressional wave velocity of 4.05 km/s and shear wave velocity of 2.7 km/s and a deeper layer with a compressional wave velocity of 6.05 km/s and a shear wave velocity of 3.15 km/s.

Velocities from Line 1 and Line 6

At first glance it appears that the results of lines 1 and 6 are contradictory. The Line 1 refraction data indicate a maximum velocity of 6.21 km/s along-strike for paragneiss, while Line 6 showed a maximum velocity of 6.34 km/s. However, the greatest offset for Line 1 was 2.84 km, corresponding to a maximum ray penetration depth of 550 m.

The data from Line 6 included offsets of 4.37 km, or a maximum penetration of 900 m. These data are modelled as layers with constant velocities, but the arrivals from both lines actually show curvature, indicating that velocities increase with depth. Thus the difference in velocity between these profiles can be easily explained by a velocity gradient of 0.2 km/s/km for each layer. This velocity-depth gradient is compatible with the velocity-pressure gradients measured in the laboratory.

Summary

OGLE provides in situ refraction velocities of both compressional and shear waves for the rocks of the GFTZ. The mylonitized orthogneisses of the GFTZ boundary fault are isotropic and have a one-dimensional structure with two layers. The shallow layer (< 400 m) has a compressional wave velocity of 5.3 km/s and a shear wave velocity of ca. 2.7 km/s, and corresponds to fractured mylonite-orthogneiss. The deeper layer has a compressional wave velocity of 5.9 km/s and a shear wave velocity of 3.2 km/s.

The parallel-to-strike paragneiss profiles also show a two-layer one-dimensional structure. Both display a shallow layer with low compressional wave velocities of ca. 3.9-4.4 km/s and a shear wave velocity of 2.7 km/s. The

deeper layer in Beaverstone Bay has a compressional wave velocity of 6.3 km/s and a shear wave velocity of 3.3 km/s. In Mill Lake, the velocities are slightly lower, 6.05 and 3.2 km/s respectively. The cross-strike profile (Line 5) needs more processing and will be the subject of further work.

CHAPTER 4

DATA INTERPRETATION

The comparison of the independent velocity data sets discussed in the previous chapters provides a means to assess the effect of large-scale features on the compressional wave velocity structure of the GFTZ. These large scale features could include fracture or cataclasis zones, medium-and large-scale inhomogeneity of lithologic units, or pore fluids. The OGLE data sets provide large-scale compressional and shear wave velocity and anisotropy information on both mylonitized orthogneiss and paragneiss units, while the laboratory data set provides intrinsic velocities for these lithologies.

Understanding the controls on compressional wave velocity is critical to understanding the reflection coefficients between different lithologies. Using the velocity information from the previous chapters, the possible ranges of reflection coefficients between different lithologic groups at varying confining pressures will be discussed. In addition, the effect of changing angles of incidence on reflection coefficients is investigated, and potential reflectors, based on the laboratory and in situ data sets are offered for GLIMPCE Profile J.

Mylonitized Orthogneiss

Velocities

OGLE Lines 3 and 4 (Figure 3.1) obtained normal-to-strike (A-direction) and parallel-to-strike (C-direction) velocity information on the mylonitized granitic orthogneiss rocks in the vicinity of the GFTZ boundary fault south of Philip Edward Island. Figure 4.1A is a schematic diagram of the one-dimensional (i.e., no lateral variation) velocity structure consistent with Lines 3 and 4. The upper layer of this simple two-layer model is characterized by a compressional wave velocity of 5.7 km/s, a shear wave velocity of 2.8 km/s, and a thickness of 300m. The underlying layer has a compressional wave velocity of 5.9 km/s and a shear wave velocity of 3.2 km/s. The thickness of the lower layer is undetermined by the Line 3 and 4 data, but it extends to a depth of at least 800 m. The data from Line 4 are insufficient to show the two-layer structure but the velocities of Line 4 agree with those of Line 3 at similar offsets.

Figure 4.1B shows the results of a single RAYAMP model that fit the data from site GB 3-1 on Line 3 (Figure 3.1). The velocity structure used is shown schematically in Figure 4.1C. Three layers were incorporated into the model below a layer of water assumed to be 3 m deep. Layer 1

A

South Shore Philip Edward Island Lines 3 and 4

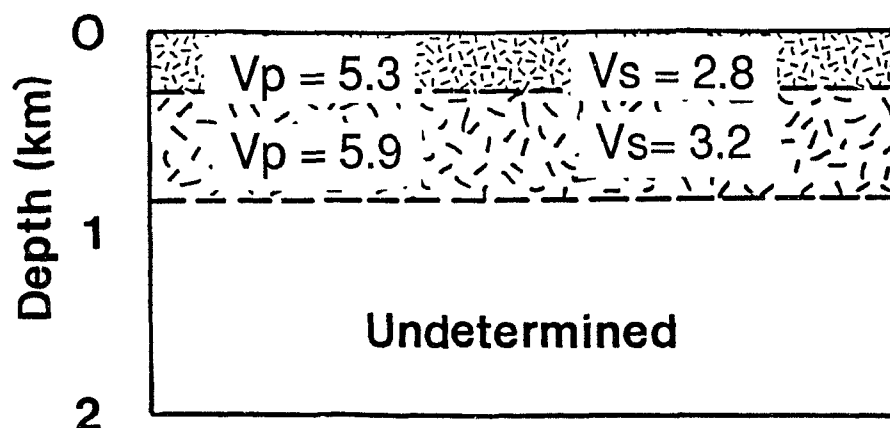


Figure 4.1. A) Simple one-dimensional velocity model for the mylonitized orthogneiss assemblage, OGLE Lines 3 and 4, near the GFTZ boundary fault south of Philip Edward Island.

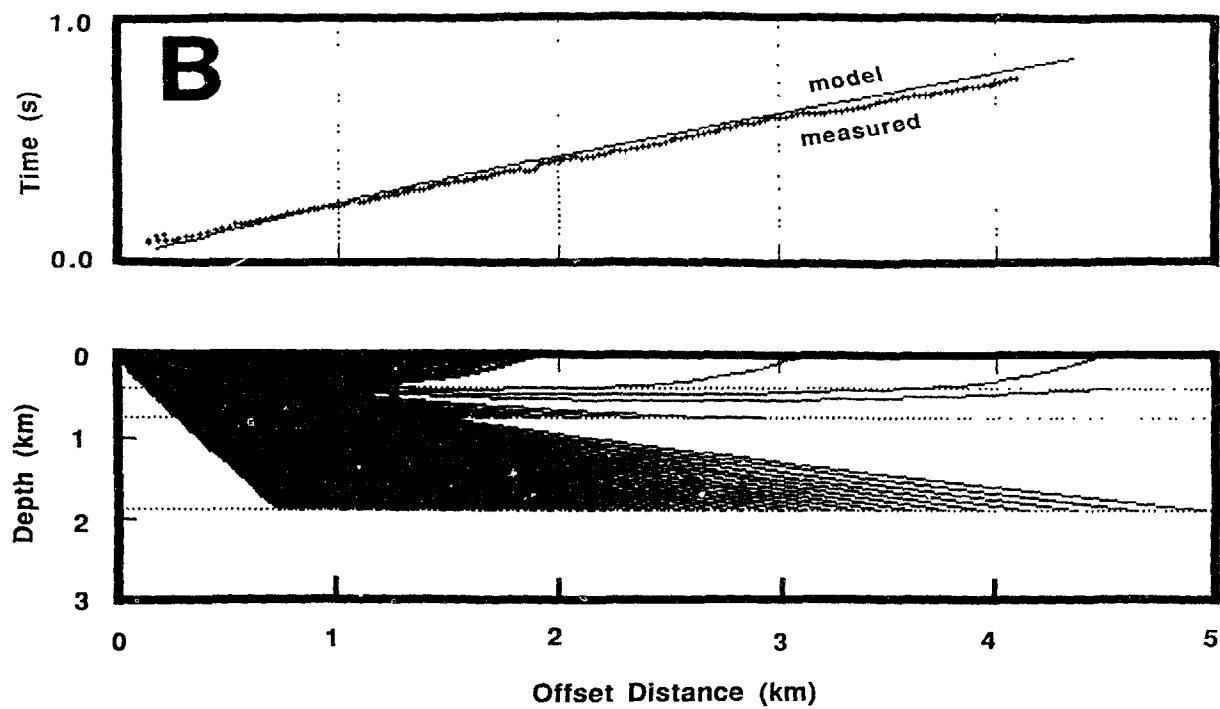


Figure 4.1. B) RAYAMP model of site GB 3-1 along Line 3. The top plot is a comparison between model and true arrival times; the bottom plot shows the ray paths for the model.

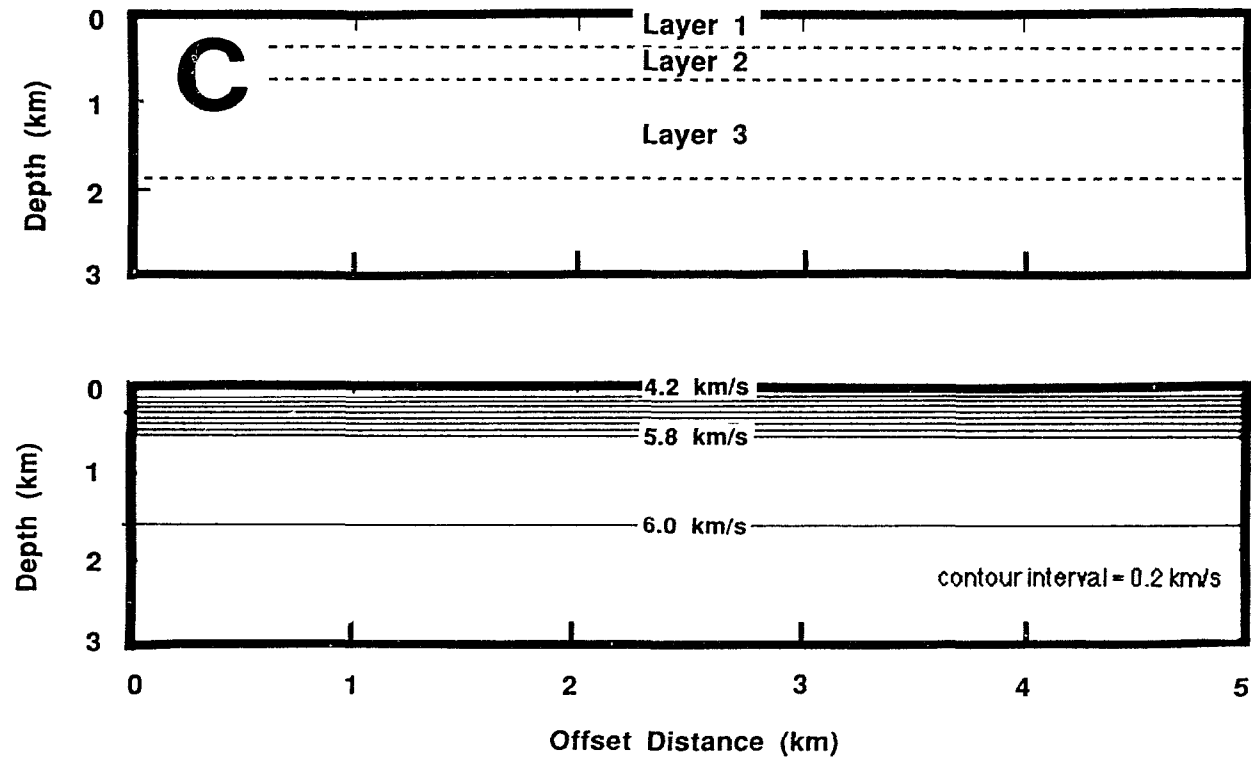


Figure 4.1. C) Velocity gradient layers and contours of compressional wave velocities for the RAYAMP model, site GB 3-1.

ranges in depth from 3–377 m, has a minimum compressional wave velocity of 4.20 km/s, and has a velocity gradient of 4.01 km/s/km. Layer 2 ranges in depth from 377–755 m, has a minimum compressional wave velocity of 5.70 km/s, and has a velocity gradient of 0.53 km/s/km. Layer 3 ranges in depth from 755–1887 m, has a minimum compressional wave velocity of 5.90 km/s, and has a velocity gradient of 0.11 km/s/km.

Figure 4.2 is a plot of the average compressional wave velocity versus confining pressure measured for mylonitic orthogneiss in the GFTZ boundary fault region (solid squares). Although the lower pressure data tend to be of poorer quality (note the larger error bars), the estimated compressional wave velocities at 0 MPa and 20 MPa are 5.70 km/s and 5.90 km/s, respectively (open squares). These pressures correspond to lake bottom and 755 m depth, respectively, for rocks with a mean density of 2.65 g/cm^3 . In the simple two-layer model, the in situ velocity of the lower layer at 755 m depth is in good agreement with the estimated laboratory velocity for this pressure. However, the velocity in the upper layer is significantly lower than the estimated laboratory velocity at 0 MPa suggesting either (a) the existence of a velocity gradient in this upper layer or (b) a poorly estimated laboratory velocity for 0 MPa confining pressure. The RAYAMP model gives

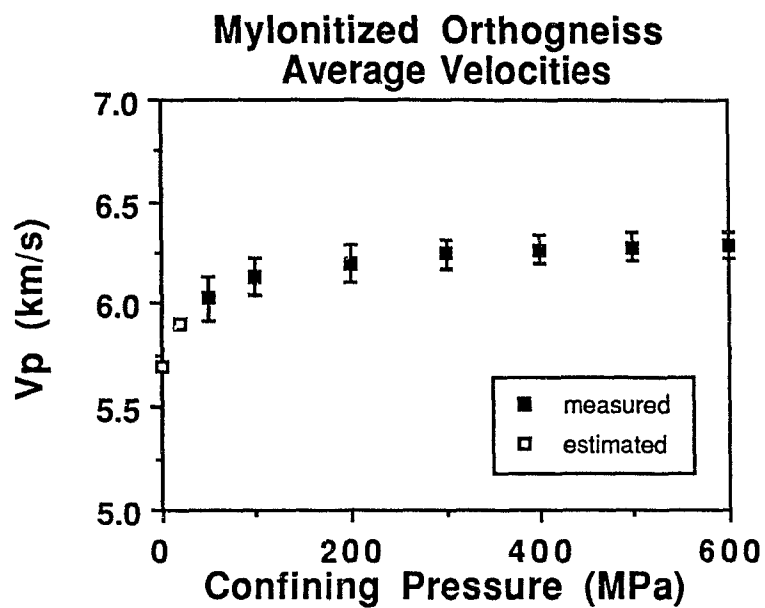


Figure 4.2. Average compressional wave velocities for mylonitized orthogneisses versus confining pressure. The solid squares are measured values (see Table 2.6); the open squares are estimates (compare to Figure 2.10); the error bars are one standard deviation.

approximately the same result as the simple two-layer model. In both models considered, the shallowest layer exhibits velocities that are considerably lower than those measured in the laboratory at the nearest confining pressure. This is probably due to open fractures near the surface in the vicinity of the boundary fault. The similarity of the laboratory and in situ measurements at deeper levels suggests that these open fractures cannot extend to depths greater than approximately 300 m.

The in situ velocities of the deeper layers in the area of the GFTZ boundary fault are approximately equal to the average of the laboratory-measured velocities in the same rocks at the nearest equivalent pressure, to within the precision of the different techniques. This similarity in compressional wave velocity is a strong indication that macroscopic fractures do not have a significant effect on velocity across this major mylonite zone except at very shallow depths. This is probably due to the saturation of the closed fractures with water, which boosts the compressional wave velocities to values that are nearly equal to those of unfractured samples (Simmons and Nur, 1968). This increase in fractured rock velocity holds as long as the water is at lithostatic pressure, and not overpressured.

One would expect the effect of large-scale fractures to be maximized at the shallow depths sampled by the in situ study, as closure of cracks and fractures by lithostatic loading occurs at greater depths (Moos and Zoback, 1983). Pore fluids at high confining pressures can hold fractures open at significant crustal depths, but are not likely to be present in this Proterozoic mylonite zone because of its great age. The time interval since movement along the GFTZ boundary fault has been long enough (van Breemen and Davidson, 1988) to allow any pore fluid under pressure to escape, even if one assumes extremely low permeabilities for the rocks (Jones and Nur, 1982).

Anisotropy

Both the laboratory and in situ studies confirm the lack of significant seismic anisotropy in the rocks of the GFTZ boundary fault zone (Burke et al., 1989). The laboratory results showed anisotropy values generally do not exceed 4 per cent, even at the lowest confining pressures. The in situ results obtained parallel and perpendicular to the strike of the mylonite zone are identical within the error of the fitting technique, and thus no significant anisotropy is observed in situ (Tables 3.2 and 3.3). This lack of seismic anisotropy is caused by the low mica content of the orthogneisses (Table 2.1),

which is the primary cause of anisotropy in granitoid mylonites (Fountain et al., 1984; Chroston and Max, 1988; Kern and Wenk, 1990). In addition, the negligible effect of macroscopic fractures on the in situ velocity of the boundary fault zone, except at very shallow levels, contributes to its seismically isotropic nature.

Paragneiss

Velocities

OGLE Lines 1 and 6 were shot parallel to the foliation (in the C-direction) of the paragneiss outcrops in Mill Lake and Beaverstone Bay. Unfortunately the data from Line 5, the only paragneiss cross-strike profile, do not lend themselves to a simple analysis, and no cross-strike in situ velocities are as yet available. This is not a serious problem, however, as several conclusions can be drawn about the behavior of the paragneiss units from the laboratory and in situ data at hand.

Figure 4.3A shows a simple two-layer model of the in situ velocity structure that is consistent with OGLE Line 1. The upper layer is characterized by a compressional wave velocity of 4.1 km/s, a shear wave velocity of 2.7 km/s, and a thickness of 300 m. The underlying layer has a

A

Mill Lake Line 1

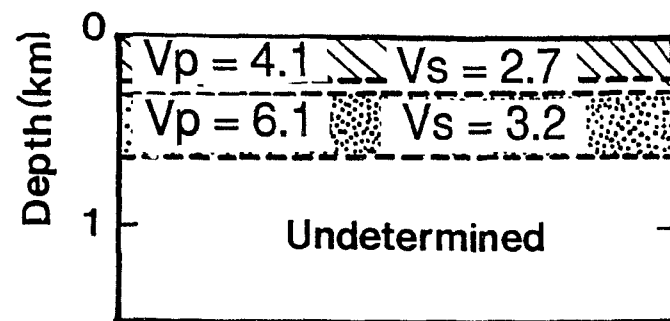


Figure 4.3. A) Simple one-dimensional velocity model for the paragneiss assemblage in Mill Lake, OGLE Line 1.

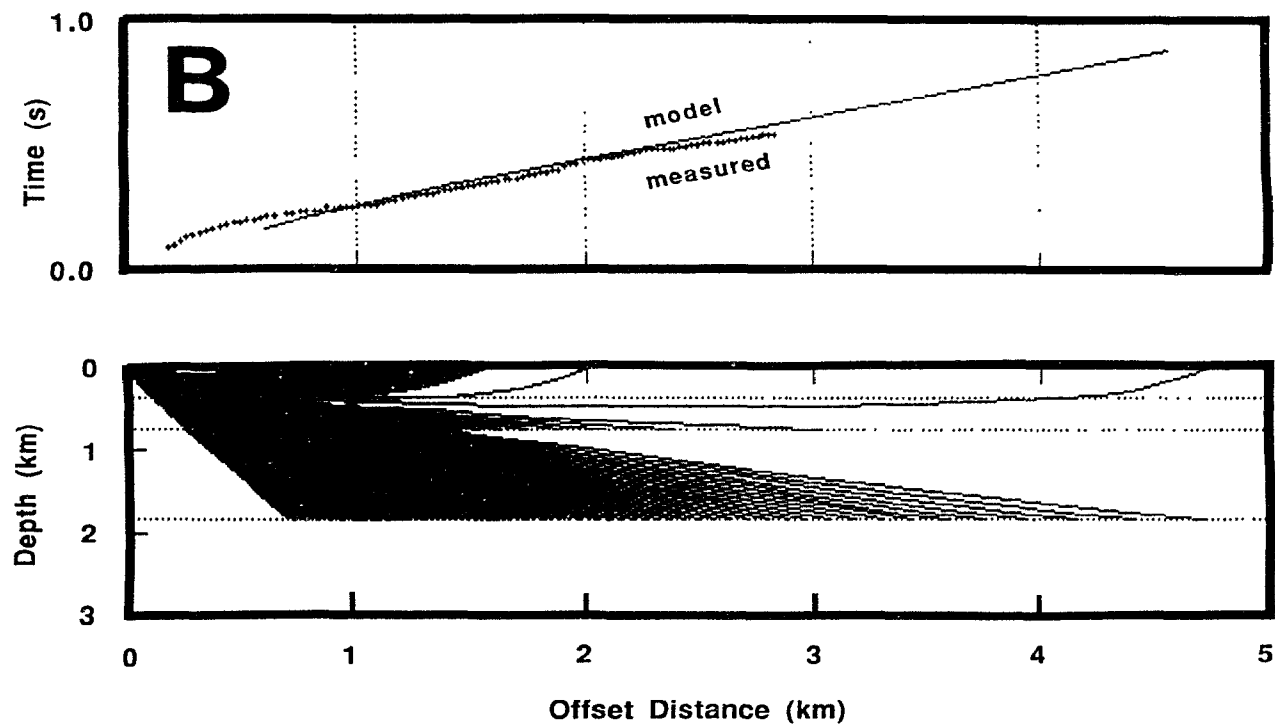


Figure 4.3. B) RAYAMP model of site ML 1-1 along Line 1. The top plot is a comparison between model and true arrival times; the bottom plot shows the ray paths for the model.

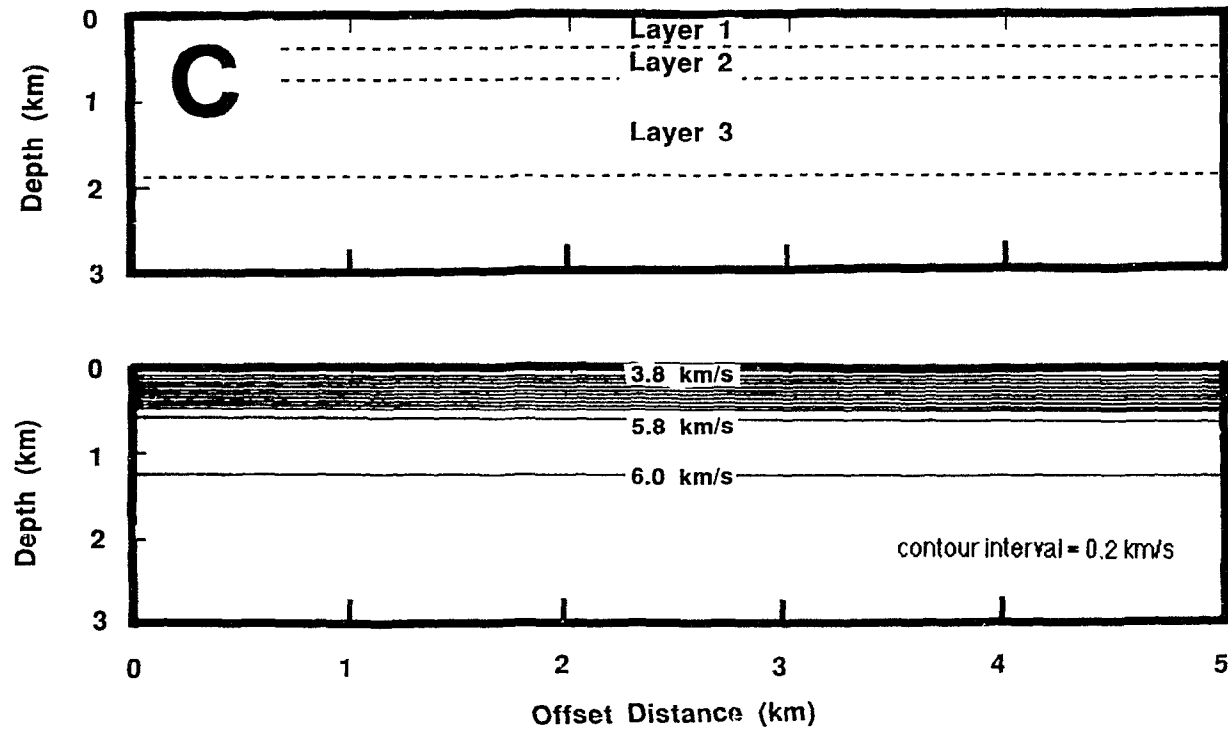


Figure 4.3. C) Velocity gradient layers and contours of compressional wave velocities for the RAYAMP model, site ML 1-1.

compressional wave velocity of 6.1 km/s and a shear wave velocity of 3.2 km/s.

Figure 4.3B shows the results of a single RAYAMP model that fit the data from site ML 1-1 along Line 1. The velocity structure used is shown in Figure 4.3C in the form of a contour plot. Three layers were incorporated into the model below a layer of water assumed to be 3 m deep. Layer 1 ranges in depth from 3-368 m, has a minimum compressional wave velocity of 3.75 km/s, and has a velocity gradient of 5.48 km/s/km. Layer 2 ranges in depth from 368-735 m, has a minimum compressional wave velocity of 5.75 km/s, and has a velocity gradient of 0.54 km/s/km. Layer 3 ranges in depth from 735-1838 m, has a minimum compressional wave velocity of 5.90 km/s, and has a velocity gradient of 0.14 km/s/km.

Line 6 was analyzed in a manner similar to Line 1. The simple two-layer model in Figure 4.4A of the in situ velocity structure for OGLE Line 6 is very similar to the results for Line 1 (compare to Figure 4.3A). Figure 4.4B shows the results of a single RAYAMP model that fit the data from site BB 6-1 along Line 6. This model is the same as that used to model site ML 1-1 in Figure 4.3B and it has the velocity structure detailed in Figure 4.3C.

Figure 4.5 is a plot of the C-direction compressional wave velocity versus confining pressure measured for

A Beaverstone Bay Line 6

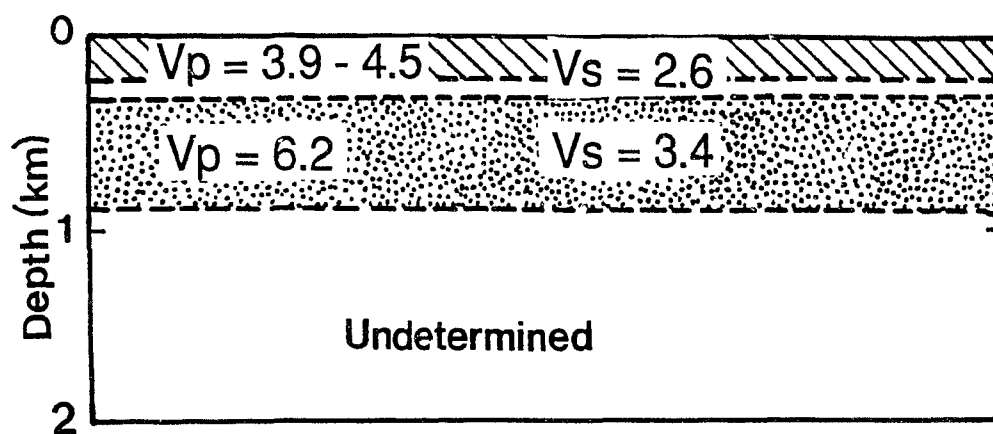


Figure 4.4. A) Simple one-dimensional velocity model for the paragneiss assemblage in Beaverstone Bay, OGLE Line 6.

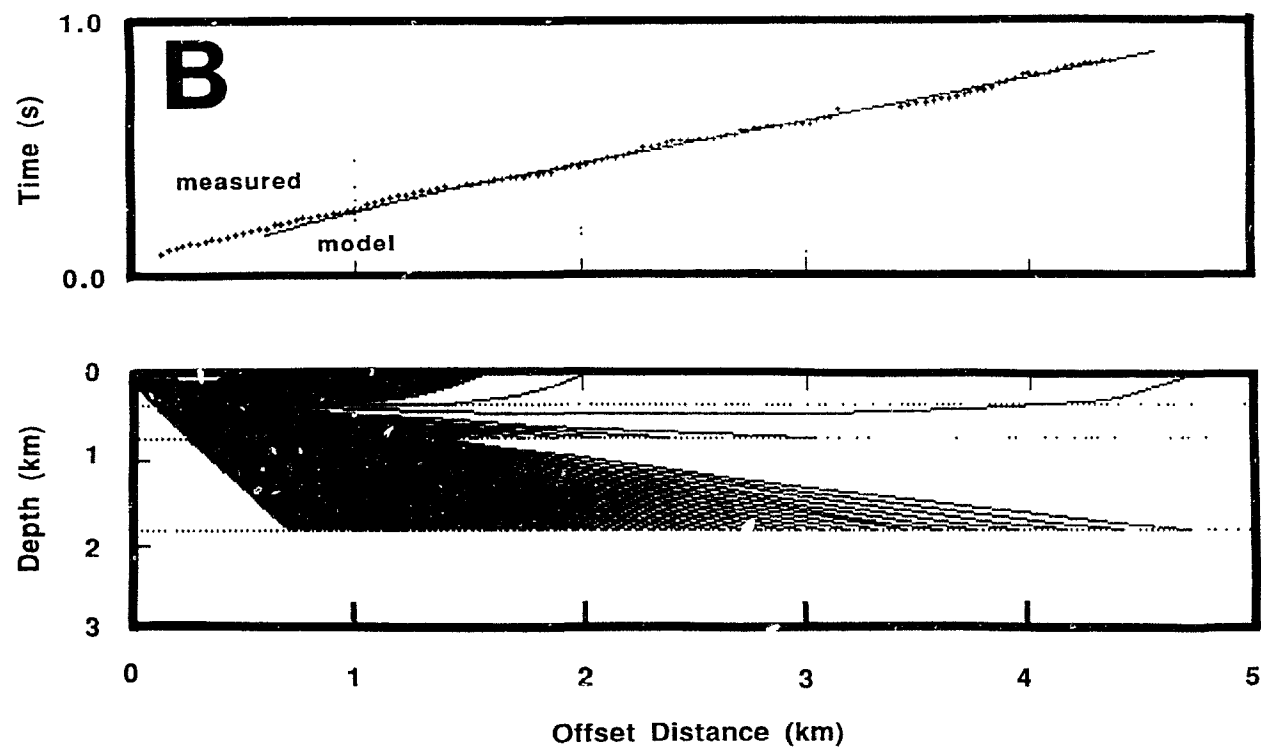


Figure 4.4. B) RAYAMP model of site BB 6-1 along Line 6. The top plot is a comparison between model and true arrival times; the bottom plot shows the ray paths for the model. Velocity gradient layers and contours of compressional wave velocities for the RAYAMP model are given in Figure 4.3C.

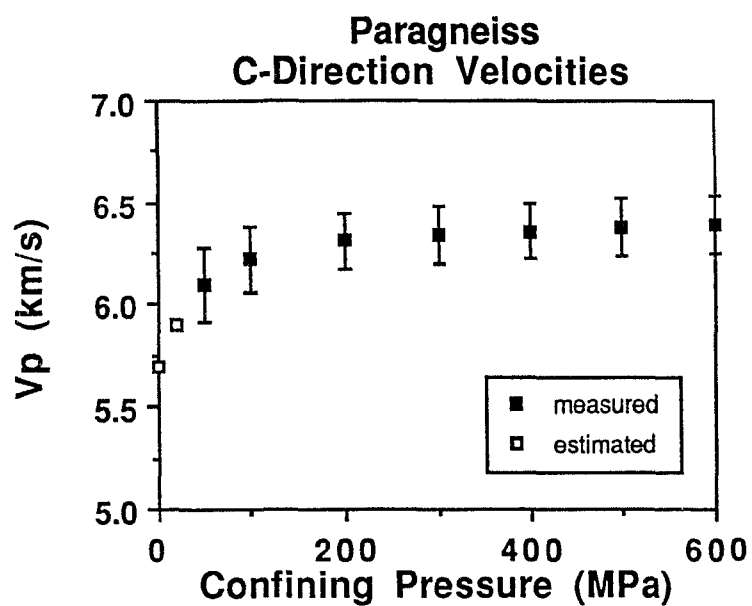


Figure 4.5. C-direction compressional wave velocities for paragneisses versus confining pressure. The solid squares are measured values (see Table 2.6); the open squares are estimates (compare to Figure 2.10); the error bars are one standard deviation.

paragneiss from the GFTZ (solid squares). The estimated compressional wave velocities at 0 MPa and 20 MPa are 5.70 km/s and 5.90 km/s, respectively (open squares). These pressures correspond to lake bottom and 735 m depth, respectively, for rocks with a mean density of 2.72 g/cm^3 . In the simple two-layer models, the in situ velocity of the lower layer at 735 m depth is in fairly good agreement with the estimated laboratory velocity for this pressure. However, the velocity in the upper layer is significantly lower than the estimated laboratory velocity at 0 MPa, again suggesting either (a) the existence of a velocity gradient in this upper layer or (b) a poorly estimated laboratory velocity for 0 MPa confining pressure. The RAYAMP models give approximately the same result as the simple two-layer models.

The very low velocity of the shallow layer in the paragneiss assemblages near Mill Lake and Beaverstone Bay has no correlative in the laboratory measurements. It is possible that these very low values are the result of (1) large scale, water-undersaturated fractures, (2) a shallow weathering zone, (3) a different lithology or (4) water at high pore pressure in the paragneiss at these shallow depths. Because the zone is shallow and very thin, these low velocities are not critical to the interpretation of Profile J.

The deeper raypaths which traveled along strike in OGLE Lines 1 and 6 most nearly follow the C-direction of these rocks (i.e., normal to lineation, but in the foliation plane). The average of the C-direction velocities determined in the laboratory at 50 MPa is 6.10 ± 0.10 km/s. This pressure corresponds to a depth of ca. 1.7 km, slightly deeper than the ray penetration in Beaverstone Bay. The first arrivals from the deeper layer in both Mill Lake and Beaverstone Bay show a velocity range from 5.99 to 6.34 km/s, with an average of 6.16 km/s. As in the profiles across the GFTZ boundary fault, the agreement between the in situ velocities of the deeper layer and the low pressure laboratory data is quite good.

The lack of cross-strike velocities from Line 5 precludes the calculation of in situ anisotropy at Beaverstone Bay. However, previous workers have observed that laboratory-measured compressional wave velocities form the upper limit for in situ velocities through the same rocks (Stierman and Kovach, 1979). The OGLE shallow-level refraction velocity data and laboratory compressional wave velocity data collected in the GFTZ for two propagation directions (A and C) through orthogneiss and one propagation direction (C) through paragneiss support this hypothesis. Therefore, if this relationship is extended to the cross-strike velocity through paragneisses, assessments

of the possible velocities and thus the reflectivity at both shallow and deeper levels of the GFTZ can be made.

Constraints on Reflection Coefficients

The velocity and density data presented in Chapters 2 and 3 are sufficient to constrain possible reflection coefficients for vertical angles of incidence between various lithologies present in the GFTZ. Table 4.1 shows the ranges of possible reflection coefficients between all possible combinations of the four major lithologies (orthogneiss, paragneiss, mafic gneiss and quartzite) in the GFTZ at confining pressures of 50, 200, and 600 MPa. The table includes reflection coefficients calculated from the mean velocity in each direction (i.e. A, B and C) for each lithology, and from the average of the mean velocities (see Table 2.6). Values for average quartzite ($V_p=5.92$ km/s, $\rho=2.59$) were taken from Christensen (1982). The effects of (1) varying confining pressure, (2) seismic anisotropy and (3) varying angle of incidence on reflection coefficients are discussed in the following sections.

Pressure Dependence

In most rocks, compressional wave velocities are highly dependent on confining pressure, and increase with

Table 4.1. Possible reflection coefficients for GFTZ rocks at various confining pressures.

50 MPa

Lithologies in Contact	Average Properties	A-A Boundary	B-B Boundary	C-C Boundary
Orthogneiss-Paragneiss	0.02	0.01	0.03	0.02
Orthogneiss-Mafic Gneiss	0.10	0.09	0.11	0.10
Orthogneiss-Quartzite	0.02	0.02	0.03	0.01
Paragneiss-Mafic Gneiss	0.08	0.07	0.09	0.08
Paragneiss-Quartzite	0.04	0.03	0.06	0.03
Mafic Gneiss-Quartzite	0.12	0.11	0.15	0.10

200 MPa

Lithologies in Contact	Average Properties	A-A Boundary	B-B Boundary	C-C Boundary
Orthogneiss-Paragneiss	0.01	0.00	0.02	0.01
Orthogneiss-Mafic Gneiss	0.09	0.08	0.11	0.09
Orthogneiss-Quartzite	0.02	0.02	0.03	0.01
Paragneiss-Mafic Gneiss	0.08	0.07	0.09	0.08
Paragneiss-Quartzite	0.04	0.03	0.05	0.03
Mafic Gneiss-Quartzite	0.11	0.10	0.14	0.10

600 MPa

Lithologies in Contact	Average Properties	A-A Boundary	B-B Boundary	C-C Boundary
Orthogneiss-Paragneiss	0.01	0.00	0.02	0.01
Orthogneiss-Mafic Gneiss	0.10	0.07	0.11	0.09
Orthogneiss-Quartzite	0.02	0.02	0.03	0.01
Paragneiss-Mafic Gneiss	0.08	0.07	0.08	0.08
Paragneiss-Quartzite	0.04	0.03	0.05	0.03
Mafic Gneiss-Quartzite	0.11	0.10	0.14	0.10

increasing pressure, as discussed in Chapter 2. However, the magnitude of this increase in velocity is very similar for all samples within a given lithologic group, and also for the various directions in each sample.

The reflection coefficients calculated at 50 MPa from the A, B, and C direction velocities and from the average velocities are slightly higher than those values calculated at 200 MPa. Given the very large increase in compressional wave velocities over this pressure range, this is not a surprising result. However, the magnitude of this change is only 0.01 for the contacts that show any variation, and many do not change. Because the in situ velocities agree so well with the laboratory velocity data at relatively shallow levels, these reflection coefficients can be considered valid to greater depths.

At pressures above 200 MPa, the reflection coefficients are constant for virtually all lithologic combinations. This result is consistent with the similarity of the velocity-pressure curves for different lithologies within this pressure range.

Effect of Seismic Anisotropy

The reflection coefficients tabulated in Table 4.1 include calculations based on the juxtaposition of isotropic rocks (average velocities) and anisotropic rocks

(A-A, B-B and C-C directions). Because surface exposures of rocks in the GFTZ have highly regular foliation planes (i.e. no A-B boundaries are seen), these calculations are appropriate.

Significant variations in directional reflection coefficients are apparent in Table 4.1. Reflection coefficients calculated for the A-A direction contacts are uniformly lower than those based on the average rock properties or the B and C direction reflection coefficients. At all three pressures, the reflection coefficients calculated from the averaged properties of each lithologic group are closely mimicked by the reflection coefficients calculated from the C direction velocities. The C propagation direction avoids the complications caused by foliation and lineations, and thus the resemblance to average rocks is expected. The highest reflection coefficients are calculated for B-B boundaries.

Variable Angles of Incidence

The structures imaged in GLIMPCE Profile J show a decrease in dip from west to east, and with increasing depth in the GFTZ (Figure 1.4). This requires that the rays recorded along the CDP Profile J reflected off the boundaries at varying angles of incidence. This is shown schematically in Figure 4.6. The discussion below attempts

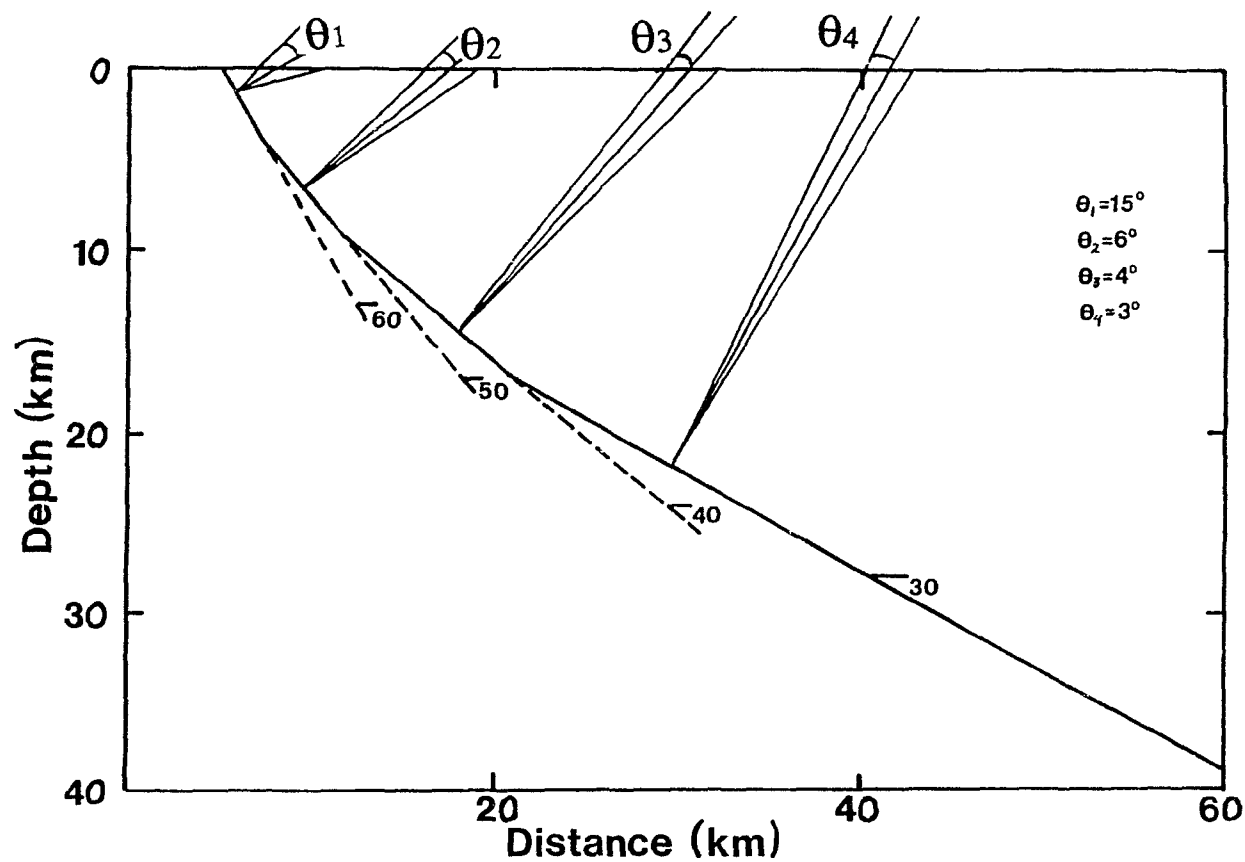


Figure 4.6. Schematic ray diagram for GLIMPCE Profile J, showing the decrease in dip of the GFTZ reflections, and the corresponding decrease in the angle ($2\theta_i$) subtended by the recording array which is 3 km long.

to quantify the effect of this variation in the angle of incidence on reflection coefficients.

Reflection coefficients are commonly calculated for vertical angles of incidence, where the form of the Zoeppritz equations is simplified to a single equation because of the lack of shear wave energy. For this case,

$$rc = (\rho_1 v_1 - \rho_2 v_2) / (\rho_1 v_1 + \rho_2 v_2) \quad (1)$$

where rc is the reflection coefficient, ρ_1 is the density and v_1 the compressional wave velocity, respectively, of the upper layer, and ρ_2 and v_2 are the density and compressional wave velocity of the lower layer (Zoeppritz, 1919). This simplification holds for angles of incidence up to ca. 15 degrees.

Because of the decrease in dip, and the increase in depth of the GFTZ reflections, the effective angle of incidence of reflected rays also changes (see Figure 4.6). For the case of the GFTZ, the angles of incidence are effectively greater for larger dips, but still do not exceed 15°. The results from the vertical incidence Zoeppritz relation are valid over this range, so the reduction in reflection coefficient due to variations in the angle of incidence will be minimal. Reflections off the steeply dipping portion of the boundary might be slightly

weaker than those off the more gently dipping portion, but the magnitude of this effect is very minor.

Summary

Laboratory and shallow in situ measurements of the compressional wave velocity of rocks from the GFTZ are similar. The in situ velocity of the shallow layer across the GFTZ boundary fault has no analog in the laboratory derived velocities. This relatively low velocity layer is probably caused by open, macroscopic fractures, which can effectively reduce compressional wave velocities. The similarity of laboratory and in situ compressional wave velocities measured by the different methods for the deeper layer in the mylonitized orthogneiss of the GFTZ boundary fault is probably due to either (1) the absence of significant fractures in situ, or (2) the complete saturation of closed fractures with water at hydrostatic pressure. In any case, the shallow level features cannot be responsible for the reflections at depth in the GFTZ.

The very low velocity shallow layer seen in both paragneiss profiles probably represents water undersaturated fractures or a weathering zone in Mill Lake and Beaverstone Bay. The velocities from the deeper layer in these profiles are, like the velocities from the

orthogneiss lines, consistent with the low pressure laboratory velocity data.

Contacts between mafic gneisses and orthogneiss have the largest reflections coefficients (ca. 0.10), and orthogneiss-paragneiss boundaries the lowest (ca. 0.01). Neither increasing confining pressure nor variation in the angle of incidence of reflected rays in the range recorded in the GLIMPCE Profile J experiment has a significant effect on the reflection coefficient for the rocks of the GFTZ. The anisotropy exhibited by some of the paragneiss and mafic rocks, however, did have an appreciable effect on the reflection coefficients. This amounts to a range of 0.03 in reflection coefficients between normal- and parallel-to-foliation direction boundaries. However, the CDP Profile J sampled the equivalent of A propagation direction velocities, so this range in coefficients is not likely to influence the reflection character of GLIMPCE Profile J.

CHAPTER 5

SYNTHETIC MODELS

Introduction .

Three methods are commonly employed to interpret and understand deep seismic profiles (Hurich (1988)). They are: 1) comparison of well logs and vertical seismic profiles (VSP) to large scale reflectivity, 2) extrapolation of surface geologic structures and 3) construction of synthetic models. Well logs and VSPs cannot be used in this region of the GFTZ because there are no suitable boreholes. Extrapolation of surface structures is of limited value because of the uncertainties inherent in projecting fine-scale features to significant depths. Synthetic models of seismic response, which are based on known geology and laboratory-derived rock properties, provide a means of assessing the seismic reflectivity of candidate structures and lithologic features. Although the construction of such synthetic models is non-unique, the models can be used as working analogs for comparison with GLIMPCE Profile J.

Two features of the geology of the GFTZ have been targeted for synthetic modelling in this work. They are the effect on seismic reflectivity of: 1) very thin

metamorphosed mafic dikes in the predominantly granitic orthogneiss sequence displayed in Collins Inlet and 2) lithologic-compositional variation as displayed in map-scale units in the Tyson Lake region. These problems will be discussed in detail in the following sections.

Thin Mafic Dikes

Resolution of Thin Beds

The problem of the resolution of thin beds by seismic techniques has been studied for a number of years, primarily by workers interested in characterizing sedimentary sequences for the oil industry. These studies focus on the problem of resolving a single thin bed in a homogeneous medium by altering input wavelet characteristics (e.g. Ricker, 1953; Schoenberger, 1974; Kallweit and Wood, 1982; De Voogd and Den Rooijen, 1983) or by altering the thickness of the thin layer itself (e.g. Widess, 1973; Tatalovic et al., 1988; Robertson and Nogami, 1984; Krollpfeifer et al., 1988). The results of the work of Ricker (1953) and Widess (1973) are now regarded as "common knowledge" in seismic reflection and are used to suggest that only features on the order of $1/4$ to $1/8$ of the wavelength (typically 15 meters and greater thickness)

of the seismic wavelet can be resolved by the seismic technique (Figure 5.1).

However, the problem of the response of a wavelet to a number of thin beds has not been addressed as thoroughly. Knapp (1990) has shown that in regularly spaced cyclothem, amplitudes will be double that of a single layer when the tuning frequency is matched, and that for all other frequencies the amplitudes go to zero. Hurich (1988) demonstrated that for a bimodal velocity distribution with an acoustic impedance of $+0.036$, the seismic response is maximized when most layers in the model are approximately $1/4$ wavelength in thickness, a result entirely consistent with the single-layer work of Widess (1973). Hurich's (1988) work also indicated that an array of these thin layers does not "sum up" to resemble a thicker layer with intermediate velocity or acoustic impedance characteristics. Hurich (1988) was challenged by Roy-Choudhury et al. (1988) who suggest that very thin layers can substantially contribute to large scale reflectivity and by Christensen and Szymanski (1988) and Christensen (1989) who show that very thin units (ca. 1 meter thick) might have a significant effect on seismic response.

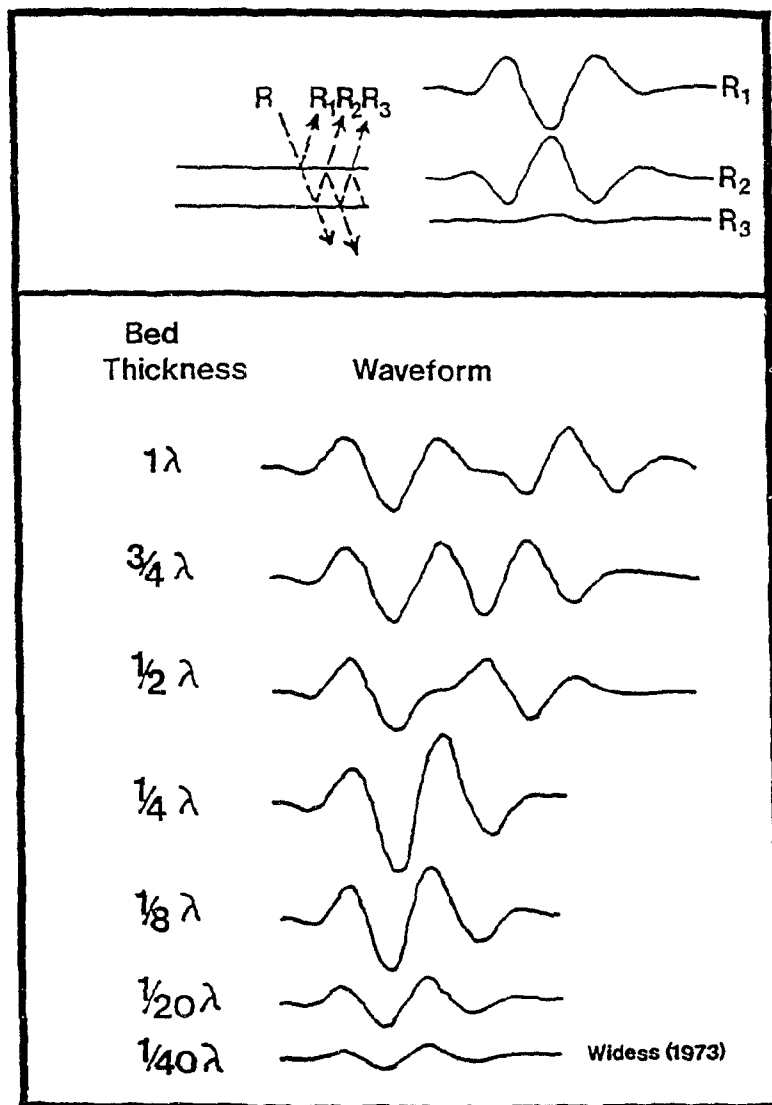


Figure 5.1. Adaptation from Widess (1973) showing constructive interference of reflections from a thin, high velocity layer embedded in a homogeneous medium of lower velocity. This shows the limit of vertical seismic resolution.

Modelling Technique

A simple FORTRAN program (NORMI) developed by Fuller (1988) at the University of Wyoming was used for the one-dimensional modelling of mafic dikes in granitic orthogneiss. Compressional wave velocity, density and the thickness of each layer (dike or orthogneiss) were used to construct a reflection coefficient series using the solution to the vertical-incidence Zoeppritz equation (see Chapter 4). A zero phase sinc function ($\sin(x)/x$) wavelet was bandpass filtered for the desired frequencies for each model run. This wavelet is similar in form and frequency content to the Ricker wavelet used for GLIMPCE Profile J (Green, personal communication, 1989; Milkereit et al., 1990)). Convolution of the wavelet with the reflection coefficient series resulted in a synthetic trace that was repeated 6 times to simulate a one-dimensional seismic section. This modelling technique does not incorporate the effects of various phenomena such as spherical divergence of energy or multiple reflections.

The synthetic sections are displayed at true amplitudes, i.e. no automatic gain control (AGC) was applied. In order to assess the relative strength of the complex events generated by thin layer models, each model has a 300 m thick "artificial dike" near the top of the section. For the wavelet frequencies used in this work,

this artificial dike thus is thick enough so that its top and bottom can easily be resolved, with no interference effects. This artificial dike provides a calibration for the complex events in the synthetic sections.

Collins Inlet

Collins Inlet displays a monotonous sequence of granitic orthogneiss from the western boundary fault of the GFTZ to Mill Lake (see Chapter 2). These granitic rocks are mineralogically very similar and have physical properties that are equally monotonous. However, a large number of metamorphosed mafic dikes occur in clusters along this portion of the GFTZ (Figure 5.2). The mineralogy and physical properties of these dikes are discussed in Chapter 2. The thicknesses of the dikes range from 0.10 to 3.5 m, with an average thickness of 0.30 m. Clusters of dikes, rather than individual dikes are shown in Figure 5.2 for ease of presentation, but the thickness of each dike and the intervening orthogneiss were noted. These complete dike data are presented in Table 5.1, with the cluster intervals noted.

The contrast in average velocity at 100 MPa and density between the granitic orthogneiss ($V_p = 6.09$ km/s, $\rho = 2.65$ g/cc) and the mafic dikes ($V_p = 6.78$ km/s, $\rho = 2.95$ g/cc) results in a high reflection coefficient of 0.10. The

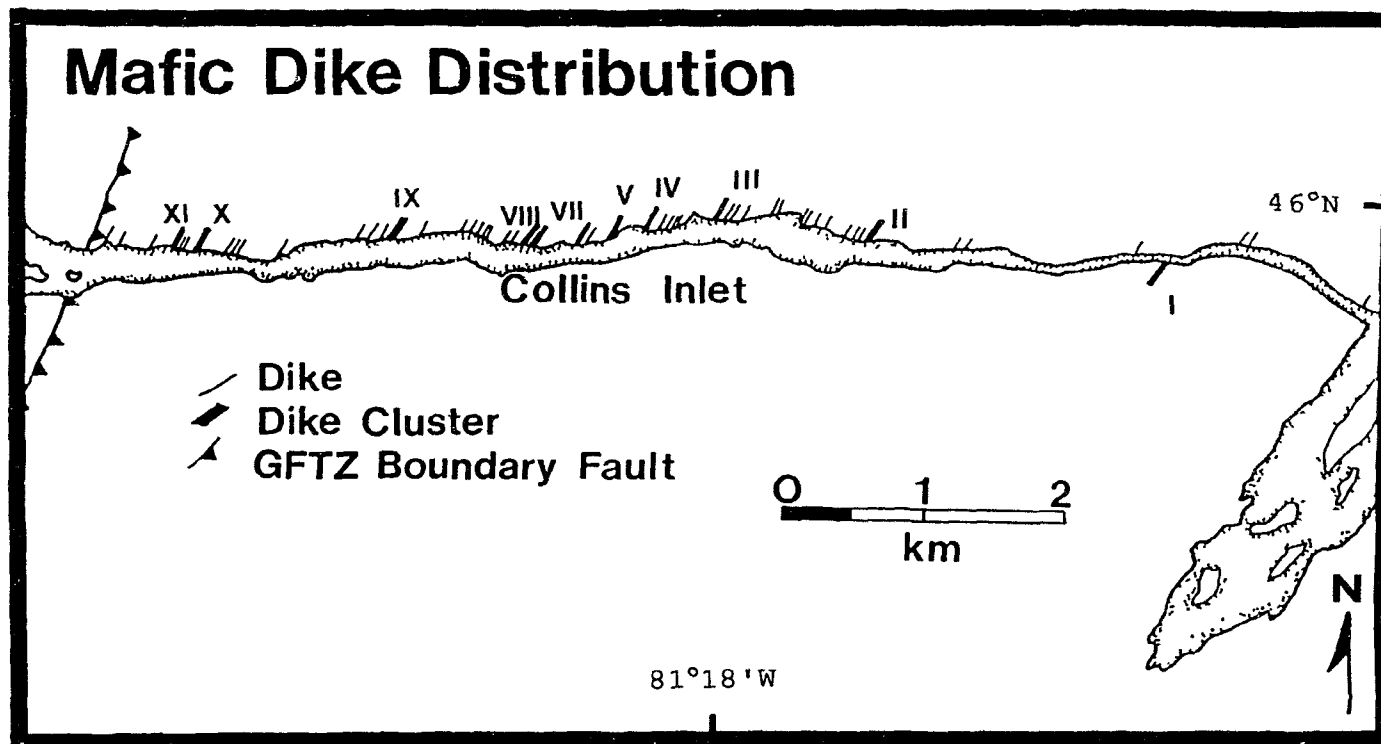


Figure 5.2 Distribution of dike clusters as mapped along Collins Inlet. Dikes are grouped into clusters for ease of presentation; individual dike data are given in Table 5.1.

Table 5.1
Detailed Mafic Dike Distribution

Thickness (m)	Lithology	Cluster
740.0	Granitic Orthogneiss	I
0.2	Mafic Dike	
60.0	Granitic Orthogneiss	
0.2	Mafic Dike	
280.0	Granitic Orthogneiss	
0.5	Mafic Dike	
0.3	Granitic Orthogneiss	
0.5	Mafic Dike	
6.5	Granitic Orthogneiss	
0.2	Mafic Dike	
1.0	Granitic Orthogneiss	
0.2	Mafic Dike	
0.6	Granitic Orthogneiss	
0.2	Mafic Dike	
0.3	Granitic Orthogneiss	
0.2	Mafic Dike	
0.3	Granitic Orthogneiss	
0.2	Mafic Dike	
5.0	Granitic Orthogneiss	
0.2	Mafic Dike	
1.0	Granitic Orthogneiss	
0.2	Mafic Dike	
210.0	Granitic Orthogneiss	
0.1	Mafic Dike	
25.0	Granitic Orthogneiss	
0.4	Mafic Dike	
1000.0	Granitic Orthogneiss	II
1.0	Mafic Dike	
75.0	Granitic Orthogneiss	
0.8	Mafic Dike	
480.0	Granitic Orthogneiss	
0.8	Mafic Dike	
1.0	Granitic Orthogneiss	
1.0	Mafic Dike	
3.5	Granitic Orthogneiss	
1.2	Mafic Dike	
4.8	Granitic Orthogneiss	
0.2	Mafic Dike	
0.1	Granitic Orthogneiss	
0.2	Mafic Dike	
0.4	Granitic Orthogneiss	
0.3	Mafic Dike	
0.1	Granitic Orthogneiss	
0.4	Mafic Dike	
4.8	Granitic Orthogneiss	
0.8	Mafic Dike	

Table 5.1 (cont)

40.0	Granitic Orthogneiss
1.5	Mafic Dike
23.0	Granitic Orthogneiss
1.0	Mafic Dike
1.0	Granitic Orthogneiss
2.0	Mafic Dike
20.0	Granitic Orthogneiss
0.6	Mafic Dike
21.0	Granitic Orthogneiss
0.8	Mafic Dike
35.0	Granitic Orthogneiss
0.3	Mafic Dike
19.0	Granitic Orthogneiss
0.3	Mafic Dike
159.0	Granitic Orthogneiss
0.2	Mafic Dike
40.0	Granitic Orthogneiss
0.6	Mafic Dike
24.0	Granitic Orthogneiss
0.2	Mafic Dike
22.0	Granitic Orthogneiss
0.6	Mafic Dike
15.0	Granitic Orthogneiss
0.7	Mafic Dike
200.0	Granitic Orthogneiss
1.0	Mafic Dike
26.0	Granitic Orthogneiss
0.8	Mafic Dike
175.0	Granitic Orthogneiss
1.0	Mafic Dike
160.0	Granitic Orthogneiss
0.2	Mafic Dike
25.0	Granitic Orthogneiss
1.0	Mafic Dike
155.0	Granitic Orthogneiss
0.8	Mafic Dike
2.1	Granitic Orthogneiss
1.4	Mafic Dike
3.6	Granitic Orthogneiss
0.8	Mafic Dike
2.9	Granitic Orthogneiss
0.8	Mafic Dike
3.1	Granitic Orthogneiss
1.7	Mafic Dike
7.0	Granitic Orthogneiss
1.5	Mafic Dike
0.2	Granitic Orthogneiss
1.0	Mafic Dike
1.9	Granitic Orthogneiss
0.8	Mafic Dike

III

Table 5.1 (cont)

2.0	Granitic Orthogneiss	I
1.8	Mafic Dike	
1.0	Granitic Orthogneiss	II
2.0	Mafic Dike	
24.0	Granitic Orthogneiss	III
0.2	Mafic Dike	
128.0	Granitic Orthogneiss	IV
0.3	Mafic Dike	
20.0	Granitic Orthogneiss	V
0.3	Mafic Dike	
10.0	Granitic Orthogneiss	VI
0.3	Mafic Dike	
25.0	Granitic Orthogneiss	VII
0.2	Mafic Dike	
55.0	Granitic Orthogneiss	VIII
1.0	Mafic Dike	
95.0	Granitic Orthogneiss	IX
0.6	Mafic Dike	
80.0	Granitic Orthogneiss	X
0.3	Mafic Dike	
1.9	Granitic Orthogneiss	XI
0.2	Mafic Dike	
6.3	Granitic Orthogneiss	XII
1.0	Mafic Dike	
2.5	Granitic Orthogneiss	XIII
0.1	Mafic Dike	
0.1	Granitic Orthogneiss	XIV
0.2	Mafic Dike	
1.5	Granitic Orthogneiss	XV
1.0	Mafic Dike	
25.0	Granitic Orthogneiss	XVI
0.3	Mafic Dike	
170.0	Granitic Orthogneiss	XVII
0.5	Mafic Dike	
3.5	Granitic Orthogneiss	XVIII
0.2	Mafic Dike	
15.0	Granitic Orthogneiss	XIX
0.2	Mafic Dike	
2.0	Granitic Orthogneiss	XX
0.4	Mafic Dike	
4.0	Granitic Orthogneiss	XXI
0.1	Mafic Dike	
75.0	Granitic Orthogneiss	XXII
0.5	Mafic Dike	
110.0	Granitic Orthogneiss	XXIII
1.2	Mafic Dike	
30.0	Granitic Orthogneiss	XXIV
1.0	Mafic Dike	
4.0	Granitic Orthogneiss	XXV
0.1	Mafic Dike	
4.0	Granitic Orthogneiss	XXVI

Table 5.1 (cont)

0.1	Mafic Dike	I
5.0	Granitic Orthogneiss	VI
0.4	Mafic Dike	
2.0	Granitic Orthogneiss	
0.2	Mafic Dike	
250.0	Granitic Orthogneiss	
0.2	Mafic Dike	
3.0	Granitic Orthogneiss	
0.8	Mafic Dike	
8.5	Granitic Orthogneiss	
1.0	Mafic Dike	
7.0	Granitic Orthogneiss	VII
0.1	Mafic Dike	
2.0	Granitic Orthogneiss	
0.2	Mafic Dike	
2.5	Granitic Orthogneiss	
0.2	Mafic Dike	
10.0	Granitic Orthogneiss	
1.5	Mafic Dike	
7.0	Granitic Orthogneiss	
0.8	Mafic Dike	
1.5	Granitic Orthogneiss	
0.1	Mafic Dike	
2.5	Granitic Orthogneiss	
0.3	Mafic Dike	
1.0	Granitic Orthogneiss	
1.5	Mafic Dike	
2.2	Granitic Orthogneiss	VIII
0.2	Mafic Dike	
1.0	Granitic Orthogneiss	
0.1	Mafic Dike	
4.0	Granitic Orthogneiss	
0.1	Mafic Dike	
0.9	Granitic Orthogneiss	
0.2	Mafic Dike	
45.0	Granitic Orthogneiss	
1.2	Mafic Dike	
62.0	Granitic Orthogneiss	
3.5	Mafic Dike	
80.0	Granitic Orthogneiss	
1.5	Mafic Dike	
40.0	Granitic Orthogneiss	
0.9	Mafic Dike	
45.0	Granitic Orthogneiss	
2.0	Mafic Dike	
31.0	Granitic Orthogneiss	
2.5	Mafic Dike	
120.0	Granitic Orthogneiss	
0.4	Mafic Dike	
86.0	Granitic Orthogneiss	
0.5	Mafic Dike	

Table 5 1 (cont)

365.0	Granitic Orthogneiss	IX
2.3	Mafic Dike	
7 1	Granitic Orthogneiss	
0.6	Mafic Dike	
2 0	Granitic Orthogneiss	
0.9	Mafic Dike	
5.1	Granitic Orthogneiss	
2.0	Mafic Dike	
38.0	Granitic Orthogneiss	
0 4	Mafic Dike	
12.0	Granitic Orthogneiss	
0.3	Mafic Dike	
14.2	Granitic Orthogneiss	
1 8	Mafic Dike	
66.0	Granitic Orthogneiss	
0.3	Mafic Dike	
78.0	Granitic Orthogneiss	
0.6	Mafic Dike	
8 5	Granitic Orthogneiss	
0 1	Mafic Dike	
420.0	Granitic Orthogneiss	
0.6	Mafic Dike	
10.9	Granitic Orthogneiss	
0 4	Mafic Dike	
385.0	Granitic Orthogneiss	
0.7	Mafic Dike	
75.0	Granitic Orthogneiss	
0.5	Mafic Dike	
45.0	Granitic Orthogneiss	
0 4	Mafic Dike	
12 1	Granitic Orthogneiss	
1 0	Mafic Dike	
4 0	Granitic Orthogneiss	
0 3	Mafic Dike	
35 0	Granitic Orthogneiss	
1 0	Mafic Dike	
260 0	Granitic Orthogneiss	
0 3	Mafic Dike	
6.3	Granitic Orthogneiss	
0 4	Mafic Dike	
4.0	Granitic Orthogneiss	X
0 4	Mafic Dike	
3.5	Granitic Orthogneiss	
0 2	Mafic Dike	
0.5	Granitic Orthogneiss	
0.2	Mafic Dike	
1.8	Granitic Orthogneiss	
0.4	Mafic Dike	
0.6	Granitic Orthogneiss	
0.1	Mafic Dike	
40.0	Granitic Orthogneiss	

Table 5.1 (cont)

0.5	Mafic Dike] XI]
60.0	Granitic Orthogneiss	
0.3	Mafic Dike	
2.0	Granitic Orthogneiss	
0.4	Mafic Dike	
1.6	Granitic Orthogneiss	
0.8	Mafic Dike	
4.3	Granitic Orthogneiss	
0.2	Mafic Dike	
3.9	Granitic Orthogneiss	
0.3	Mafic Dike	
0.6	Granitic Orthogneiss	
0.3	Mafic Dike	
180.0	Granitic Orthogneiss	
1.5	Mafic Dike	
160.0	Granitic Orthogneiss	
0.2	Mafic Dike	
180.0	Granitic Orthogneiss	
1.0	Mafic Dike	
130.0	Granitic Orthogneiss	

average velocity at 600 MPa of orthogneiss ($V_p=6.28$ km/s) and the mafic dikes ($V_p=6.98$ km/s) results in a reflection coefficient of 0.10, identical to the value at 100 MPa. Even though the average velocities are different at higher confining pressures, the impedance contrasts do not vary significantly with pressure. For this reason, thin dikes were modeled using only the 600 MPa velocities.

Two types of synthetic models of dikes in orthogneiss were constructed: 1) a highly detailed model that incorporated each individual dike and 2) a more generalized model that assigned an average velocity to each dike cluster shown in Figure 5.2, based on the ratio of dikes to orthogneiss for each cluster. Both the detailed and general models are one-dimensional to facilitate calculation of multilayer models, and because of the uncertainty of the lateral extent of the dikes.

Detailed model of mafic dikes

Figure 5.3 shows the result of the convolution of the spike reflection coefficient series derived from the detailed dike distribution with a sinc function wavelet with a maximum frequency of 35 Hz. The single trace generated by the convolution has been repeated six times to better simulate a seismic section. The vertical scale is two way travel time, in seconds. A one-dimensional strip-

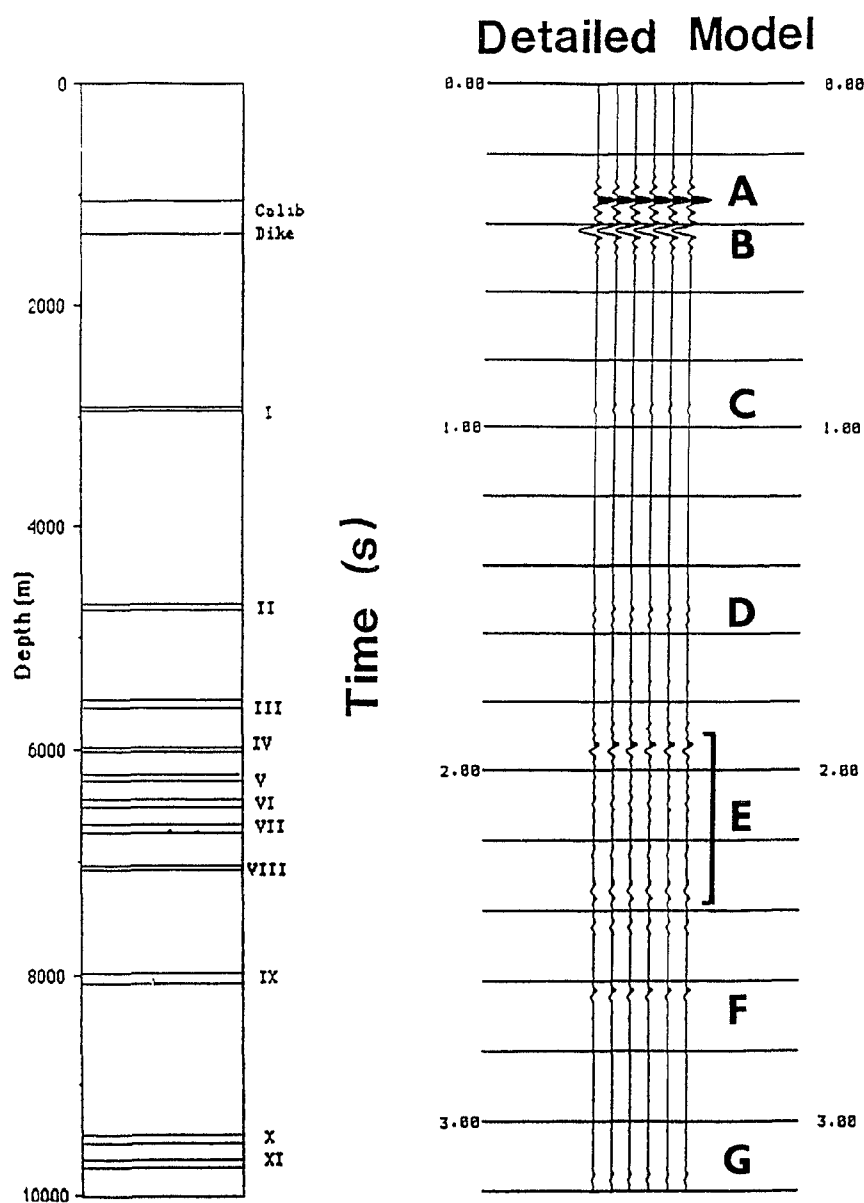


Figure 5.3. One-dimensional seismic section for the detailed dike distribution given in Table 5.1. Reflections annotated with letters are discussed in the text. The strip map shows the relative position of the dike clusters. Vertical axis is two-way travel time.

map of Collins Inlet, showing the relative positions of the dike clusters is also shown for comparison.

The high amplitude reflections labelled A and B near the top of the section result from the 300 meter thick "calibration dike" inserted in the model. The reflection coefficient at these boundaries is 0.10, and there is no interference between the top and bottom of this layer at this wavelet frequency.

Between 0.9 seconds and the base of the model a number of coherent reflections appear. The pattern of these reflections is consistent with the distribution of dike clusters along Collins Inlet (compare to strip-map). Reflections C and D seem to correlate with the dikes in clusters I and II, reflection F to the dikes in Cluster IX and reflection G to those in Clusters X and XI. The broad band of complex reflectivity labelled E is associated with the numerous dikes at Cluster III through Cluster VIII.

The amplitudes of the events generated by the finely layered dikes are considerably smaller than the amplitude of the reflections off the calibration dike. However, the amplitude of event F and one of the complex events in region E are $1/4$ to $1/3$ the amplitude of the calibration dike reflections. Recall that the coefficient of the calibration reflection is ± 0.10 , a value that is

considered very high in deep crustal reflection profiles (Warner, 1990; Burke and Fountain, 1990).

Contrary to the results of Hurich (1988), the individual thin dikes do seem to group into resolvable aggregate layers with intermediate physical properties. Hurich's results are related to the relatively low reflection coefficient (0.036) that he used in his bimodal velocity distribution. Figure 5.4 shows the result of the convolution of the same dike-orthogneiss distribution given in Table 5.1, but the input velocities for dikes and orthogneiss have been changed to the values used by Hurich (1988), 6.33 and 6.00 km/s, respectively.

Reflections A and B in Figure 5.4 are the reflections from the top and the bottom of the "calibration dike", with reflection coefficients at these boundaries of ± 0.037 . The rest of the section is notable for the lack of significant reflection energy. Very low amplitude reflections occur at locations marked C and D, but these are extremely weak events compared to those associated with the calibration dike.

These modelling results suggest that a relatively large velocity contrast between the thin layers and the surrounding medium is a necessary condition for significant reflections to be generated. In order to determine the contrast necessary to produce reflections, the detailed

Detailed Model, Hurich Velocities

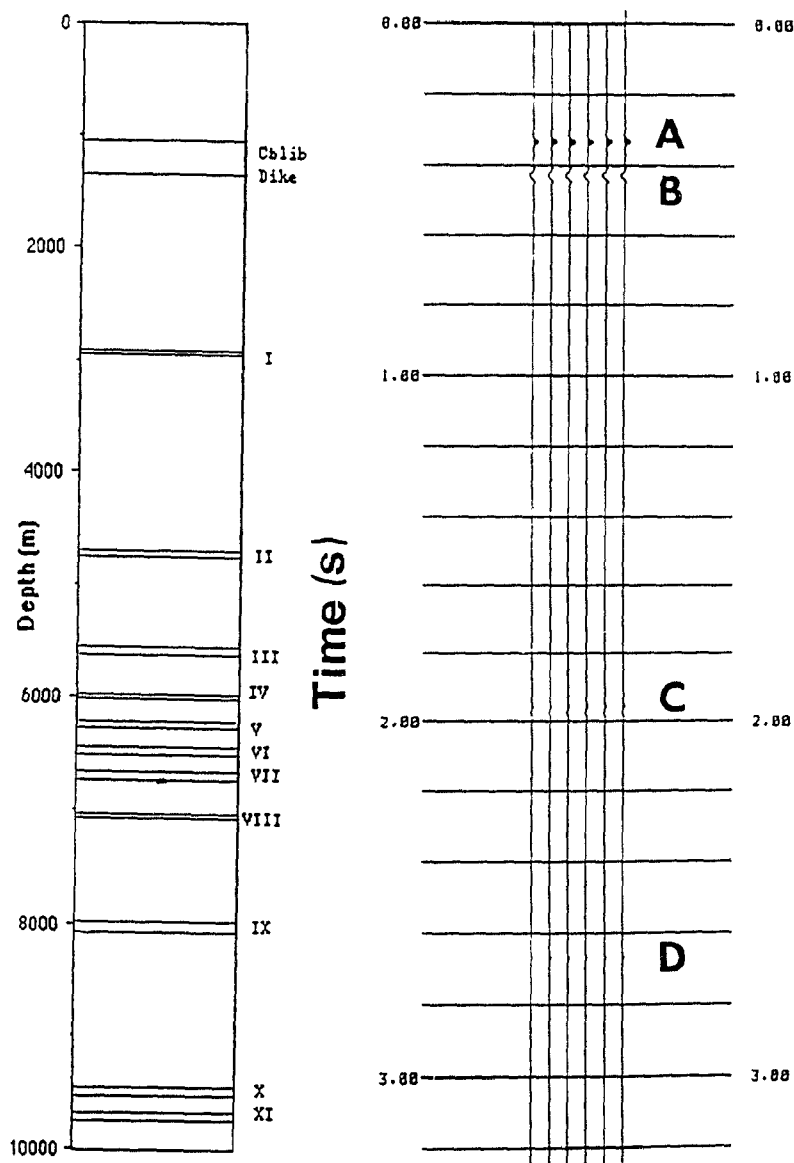


Figure 5.4 One-dimensional, synthetic seismic section for the same detailed dike distribution as in Figure 5.3, but with the velocities used by Hurich (1988). The strip map shows the relative position of the dike clusters. Note the extremely weak reflections as compared with Figure 5.3.

dike model was run repeatedly, each time increasing the velocity contrast (and hence the reflection coefficient) between the thin layers and the surrounding medium. Figures 5.5 through 5.10 show the result of step-wise increases of 0.01 in reflection coefficient between thin layers and surrounding rock from 0.03 to 0.08. There is clearly a continuum in the response as the reflection coefficients increase, the reflections in Figures 5.9 and 5.10 being much stronger than those in Figure 5.5 and 5.6. A reflection coefficient of 0.07 appears to be the minimum value necessary to produce significant reflection amplitudes. Hurich (1988) failed to observe this behavior simply because the velocity contrasts used were too small.

Generalized model of mafic dikes

The highly detailed data in Table 5.1 indicate that dikes along Collins Inlet occur in fairly discrete clusters, and that relatively few dikes occur outside these clusters. The results of the previous section indicate that the thin dikes group together to resemble thicker layers with intermediate velocities. A generalized model based on clustering of dikes was constructed to test whether the average physical properties of a dike cluster respond in the same manner as the individual dike model. The average physical properties of dike clusters are presented in Table 5.2. These data are means of densities and 600 MPa

Detailed Model, $rc = .03$

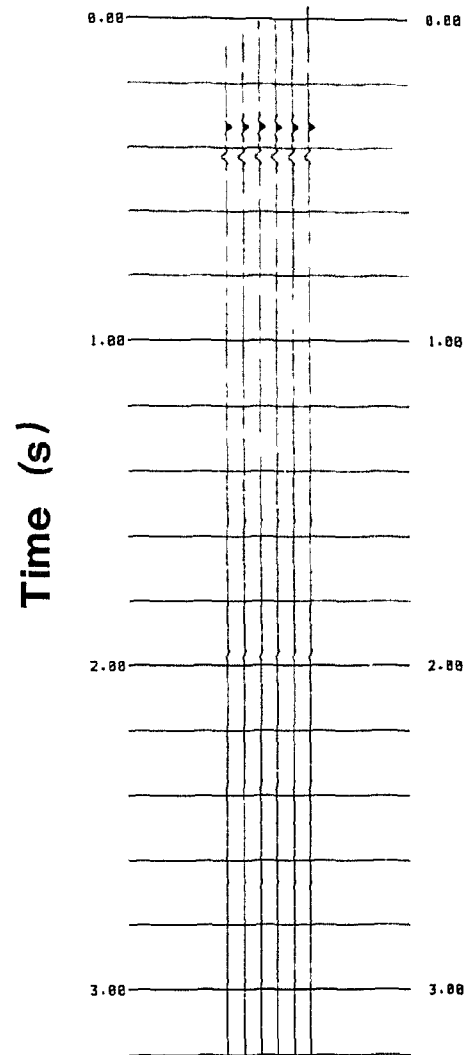


Figure 5.5 One-dimensional, synthetic seismic section of the detailed dike distribution given in Table 5.1, with reflection coefficients of ± 0.03 . All reflections are of very low amplitude.

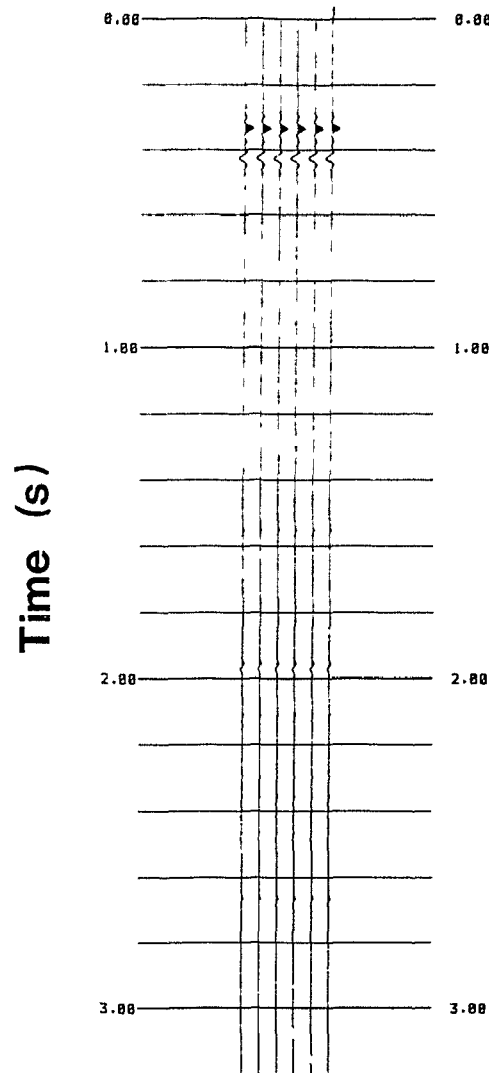
Detailed Model, $rc = .04$ 

Figure 5.6 One-dimensional, synthetic seismic section of the detailed dike distribution given in Table 5.1, with reflection coefficients of ± 0.04 . All reflections are of very low amplitude.

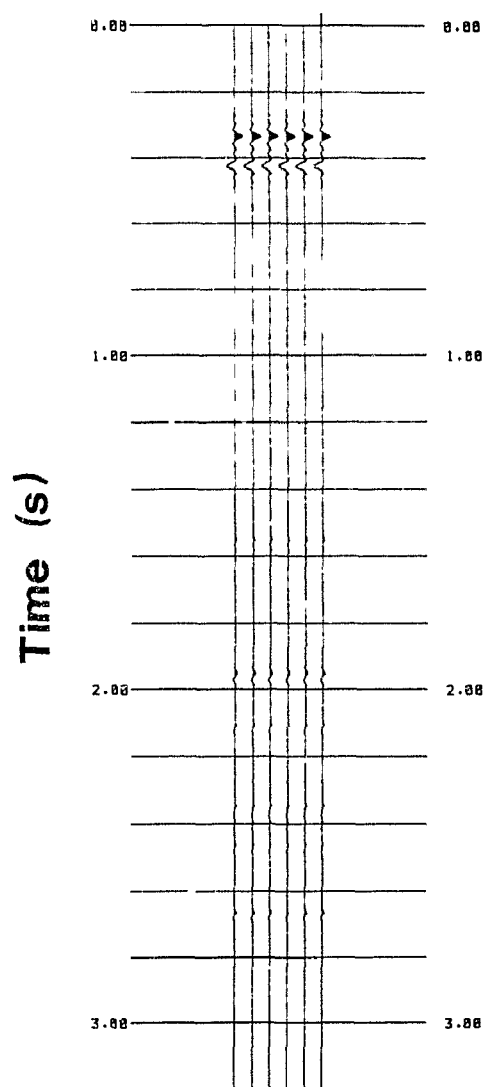
Detailed Model, $rc = .05$ 

Figure 5.7 One-dimensional, synthetic seismic section of the detailed dike distribution given in Table 5.1, with reflection coefficients of ± 0.05 . All reflections are of low amplitude.

Detailed Model, $rc = .06$

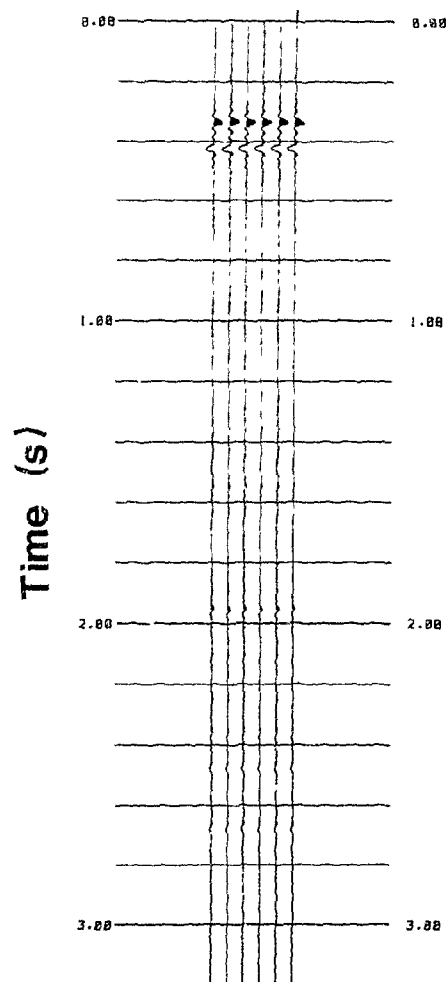


Figure 5.8 One-dimensional, synthetic seismic section of the detailed dike distribution given in Table 5.1, with reflection coefficients of ± 0.06 . All reflections are of low amplitude.

Detailed Model, $rc = .07$

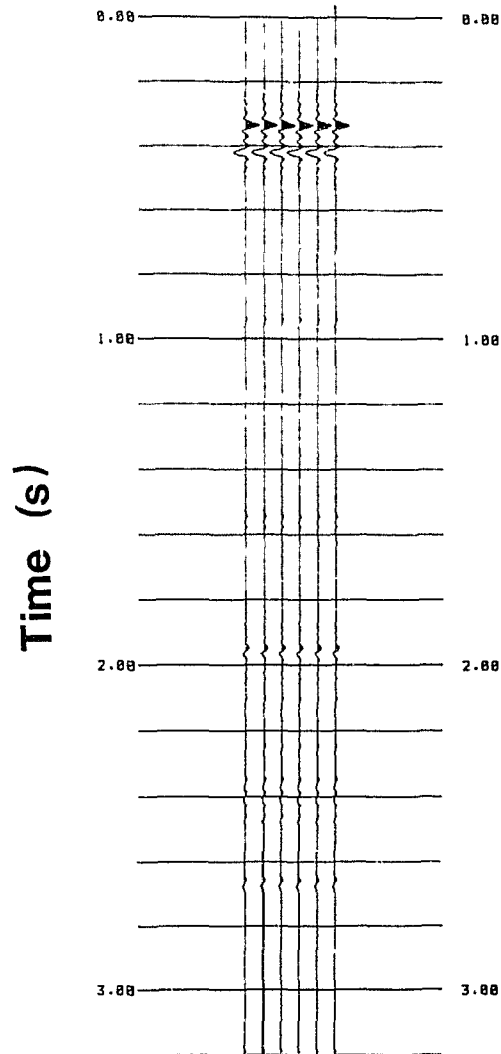


Figure 5.9 One-dimensional, synthetic seismic section of the detailed dike distribution given in Table 5.1, with reflection coefficients of ± 0.07 . Compare to the earlier figures, where the amplitudes are much lower. This reflection coefficient can be regarded as a threshold value for significant reflections.

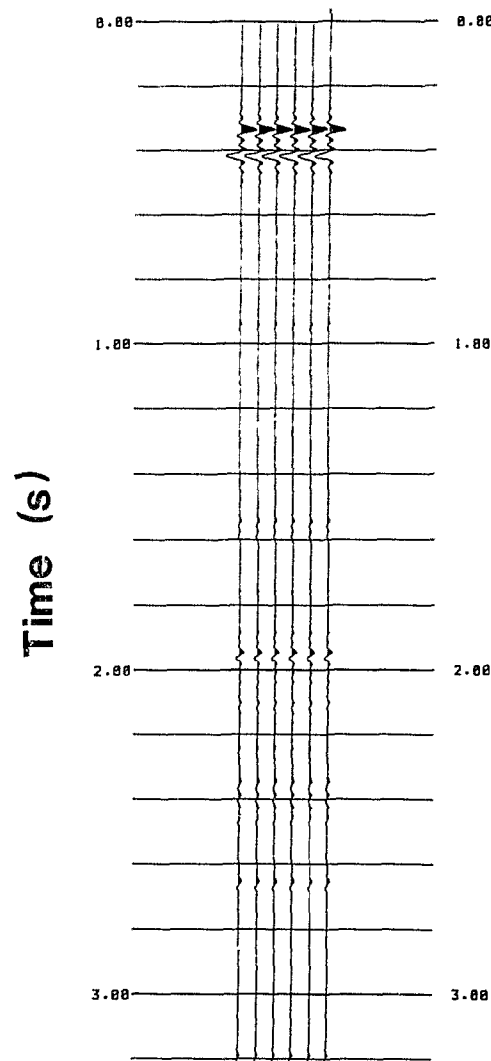
Detailed Model, $rc = .08$ 

Figure 5.10 One-dimensional, synthetic seismic section of the detailed dike distribution given in Table 5.1, with reflection coefficients of ± 0.08 .

Table 5.2. Dike cluster distribution and physical properties.

Thickness (m)	Cluster Number	Per Cent Dike	Velocity (km/s)	Density (g/cm ³)
1080.0			6.28	2.65
17.4	I	14	6.35	2.69
1792.3			6.28	2.65
19.6	II	25	6.42	2.73
1331.2			6.28	2.65
35.4	III	36	6.48	2.76
439.9			6.28	2.65
15.1	IV	19	6.39	2.71
195.3			6.28	2.65
25.9	V	5	6.29	2.65
216.7			6.28	2.65
16.8	VI	11	6.31	2.68
250.0			6.28	2.65
25.5	VII	10	6.31	2.68
18.5			6.28	2.65
16.4	VIII	20	6.39	2.71
886.5			6.28	2.65
22.0	IX	26	6.42	2.73
1472.1			6.28	2.65
18.6	X	11	6.31	2.68
100.5			6.28	2.65
14.7	XI	16	6.33	2.70
652.7			6.28	2.65

Cluster physical properties are calculated as volumetric weighted means (see text) using 600 MPa velocities of orthogneiss and metamorphosed mafic dikes. Calculations of average velocity based on time-averaged velocities are higher by 0.02 km/s.

velocities, dependent on the modal dike content in each cluster. For the areas outside the discrete clusters the scattered lone dikes were disregarded, and these regions were modelled as "pure" granitic orthogneiss.

Figure 5.11 shows the result of the convolution of the spike reflection coefficient series from the generalized cluster model with the same sinc function wavelet as used in the previous, more detailed models. As in the earlier examples, reflections A and B result from the top and bottom interfaces of the "calibration" dike (reflection coefficient of 0.10).

The rest of the wavefield generated by this composite model is strikingly similar to the result of the detailed model (compare Figure 5.11 to Figure 5.3). Reflections C, D, F and G occur at the same travel times in both models, with nearly identical amplitudes. The sole difference in the results of these model runs is in the highly reflective E section of the models. The generalized synthetic section has four significant reflections in this time interval, with virtually no signal between these events. The signal from the more detailed model has seven discrete events in the same time period, although only four have strong amplitudes.

Generalized Model

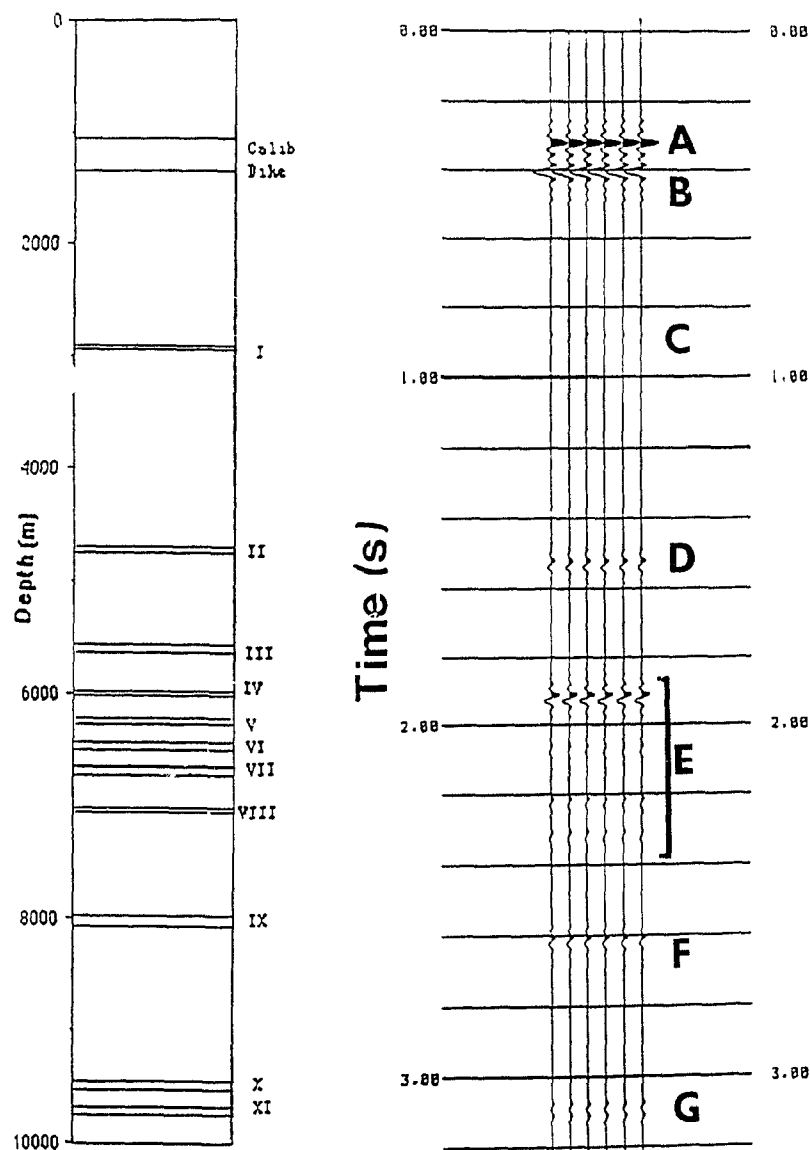


Figure 5.11 One-dimensional, synthetic seismic section derived from the generalized model of dike clusters given in Table 5.2. Note the very strong similarity to Figure 5.3. The strip map shows the relative position of the dike clusters.

Thin Layer Implications

The similarity between the synthetic seismograms generated from the highly detailed model of mafic dikes in granitic orthogneiss and the generalized model of the same features strongly indicates that these very thin mafic dikes do have a significant contribution to crustal scale seismic reflectivity of the region. The generalized model essentially duplicates the detailed model. This implies that one can assess the seismic response of complexly interlayered rocks by treating those rocks that occur in clusters as the primary contributors to the wavefield, disregarding the contribution of thin, isolated layers. This approach makes intuitive sense, if one considers that the wavelet is performing a running average of the physical properties of the rocks through which it passes. Thus thin layers, too thin to be independently resolved, can have a marked effect on seismic response by altering the bulk properties of the formation.

This result has important implications for deep reflection profiles which show strong reflections from lower crust with average (ca. 6.5 km/s) refraction velocities. Because refraction velocities for these regions are relatively low, large volumes of mafic rocks interlayered with other lithologies cannot adequately explain the reflectivity (Wever, 1990; Warner, 1990). The

thin layer modelling indicates that a small volume of mafic rock (< 5%) in a dominantly granitic crust can generate significant reflections if the mafic layers are clustered.

Thin mafic dikes or pods in granitoid rocks are ubiquitous in many exposed regions of middle to lower crustal rocks such as the Ivrea Zone, the Kapuskasing Uplift and the Britt Domain of the Grenville Province (Schmid, 1967; Percival and Card, 1983; Fountain and Salisbury, 1981).

Dikes are believed to be intruded parallel to the σ_3 stress direction (Hall, 1986). Thus any given suite of dikes intruded in a single episode is likely to have a similar orientation (e.g. the Sudbury Swarm, the Grenville Swarm). Random distributions commonly have empty regions interspersed with regions of greater complexity, so if dikes are randomly distributed in the granitic section it is likely they would have the necessary clustering characteristics to cause reflections.

Lithologic Variation

The geologic map of Frarey (1985) shows considerable lithologic variation in map scale units in the region surrounding Tyson Lake. Lithologic or compositional variation was shown in Chapter 2 to have a significant

effect on the physical properties of the rocks of the GFTZ. This is not a new concept, as others have documented similar behavior in various rock suites throughout the world (i.e. Birch, 1960; Christensen, 1965; Christensen and Fountain, 1975; Fountain et al., 1990). The effect of lithologic variation on seismic reflectivity in rocks from the Ivrea zone was addressed by Burke and Fountain (1990), using a one-dimensional model to show that high reflectivity could result from ca. 100 m thick units of contrasting lithologies. The following discussion addresses whether or not the lithologic variation seen in the GFTZ could also generate significant reflections.

Modelling Technique

The SIERRA MIMIC, QUIKRAY, and SLIPR software packages (Mellman et al., 1984) were used to model, in two dimensions, the reflectivity of a non-planar, complex geometry for rocks with contrasting physical properties. The MIMIC program is an interactive package that allows the user to construct a two dimensional geometry at user-specified distance scales, with user-defined layer properties. This input model is then used for subsequent modelling using the QUIKRAY program.

The QUIKRAY program allows the user to define a set of "working rays" to trace through the supplied geometry. For

this work, because GLIMPCE Profile J is a common depth point (CDP) profile, only half-raypaths were used to speed computation. These half-raypath rays originate at the reflecting boundary and propagate toward the surface. This method can be used because for a normally incident (i.e. CDP) geometry all raypaths are symmetric about the normal incident reflection point. Travel times are calculated for the captured rays using the equation:

$$t = (d_i/v_i) + \mathbf{p} \cdot \mathbf{x}$$

where d_i and v_i are the distance and the velocity of the i th leg of the ray, \mathbf{p} is the ray parameter vector at the receiver and \mathbf{x} is the vector describing the difference between the captured ray emergence point and the receiver location.

The effects of reflection-transmission coefficients and geometric spreading are calculated in this software package. The fully elastic, incident-angle-dependent, plane wave transmission and reflection coefficients are calculated at each interface using the four coupled Zoeppritz equations (Aki and Richards, 1980). The final contribution to the amplitude of a ray due to reflection-transmission effects is a product of all of the reflection and transmission coefficients calculated for that ray.

Geometric spreading is the decrease in amplitude related to the spreading of the wavefield, with

modifications caused by the focusing and defocusing effects of curved boundaries. A modification of the WKB method (Chapman, 1978) is used to calculate the effect of geometric spreading on amplitudes. This method replaces the single-point curvature calculation of dynamic ray theory (Cerveny, 1983) with an integral over the ray parameter, and thus not only the captured ray, but nearby rays contribute to the calculated amplitude. This method is more stable than dynamic ray tracing, and is valid in the vicinity of caustics (Frazer and Phinney, 1980). It is the default method of calculating amplitudes in SIERRA. The final results of the QUIKRAY program are travel times and complex, vector amplitudes for geometric rays propagated through the geologic model. These results are used in the final program SLIPR, which transforms them into synthetic seismic sections.

The SLIPR program first sorts the data generated by the QUIKRAY program into shot and group locations. These sorted time-amplitude files are then convolved with a user-specified wavelet. These synthetic sections can then be displayed in various formats, and with user-specified levels of random noise.

Simplified Model

One model, loosely based on the types of outcrops seen in the Tyson Lake region, was run using the SIERRA programs. The model is fairly simple, but shows some of the effects related to juxtaposition of different rock types, curved boundaries and discontinuous layers. This model, and synthetic sections based upon it, will be discussed in the following section.

Figure 5.12 shows the velocity-depth model tested. The compressional wave velocities used were based on the average laboratory-derived velocities at 600 MPa of the lithologic units discussed in Chapter 2. Appropriate shear wave velocities were taken from Christensen (1982) for rocks with similar compressional wave velocities and anisotropy values. The model shows lithologic contacts between: (1) the Killarney Complex (granite) and GFTZ granitic orthogneiss, (2) orthogneiss and paragneiss, (3) orthogneiss and amphibolite gneiss, (4) orthogneiss and quartzite and finally (5) paragneiss and quartzite. In the field these boundaries are mylonite zones of considerable thickness, but they have been assigned no intrinsic seismic properties in this model. Instead they are treated as simple contacts between different lithologic units, due to the lack of effect of mylonitization on the physical properties of the granitic rocks examined.

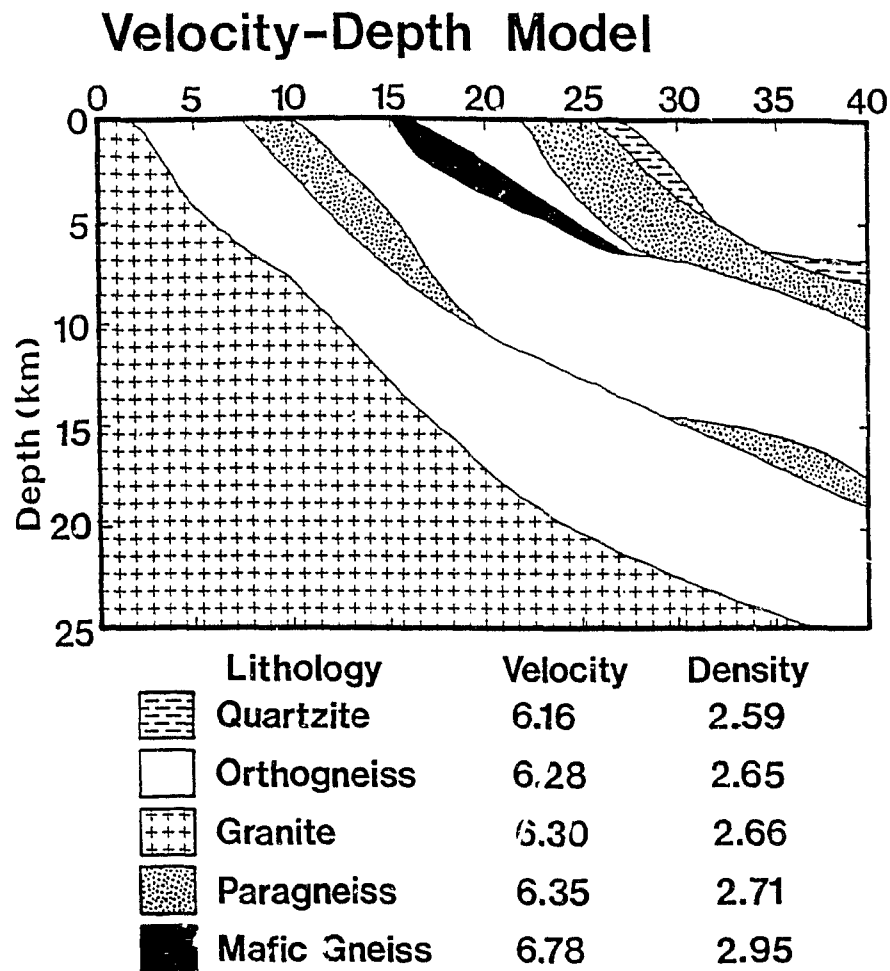


Figure 5.12. Simple, hypothetical, two-dimensional model of the lithologic and physical property variation seen near Tyson Lake. Compressional wave velocities are in km/s; densities are in g/cm³; horizontal scale in km.

Unit thicknesses in the model are based on outcrop thicknesses in the Tyson Lake region and the dips of contacts at the surface are based upon those measured by Frarey and Cannon (1969). The decrease of dip with increasing depth in the model is based on the decrease in reflection dip as seen in GLIMPCE Profile J (Green et al., 1988; Milkereit et al., 1989).

Milkereit and others (1990) present a model of the GFTZ that is, in many ways, similar to the one presented here (Figure 5.13). The primary difference between these two models is the number of layers included in the GFTZ. The number of layers that can be included in a SIERRA two-dimensional model was the limiting factor for this work. Although a greater number of layers would be preferred, the model presented here is meant to be an analog only, and not an exact solution of GFTZ reflection response. Keeping this in mind, the layer limitations imposed by SIERRA are not a critical problem.

Synthetic Sections

Figure 5.14 shows the synthetic seismic section generated by the convolution of a Ricker wavelet with a center frequency of 20 Hz with the travel time and amplitude information of CDP sorted traces. The results have been filtered with AGC over an 800 ms window. This

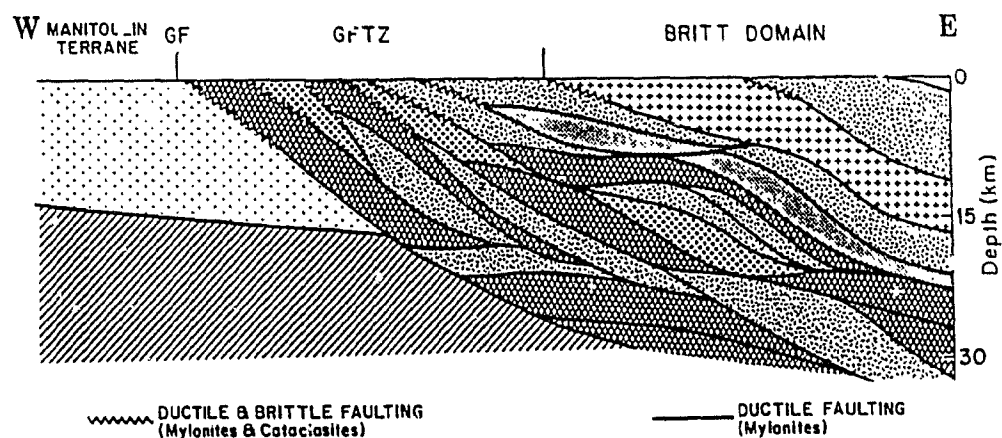


Figure 5.13 Two-dimensional model of the GFTZ from Milkereit et al. (1990). Although this diagram has many more layers than Figure 5.12, the thicknesses and attitudes of the units are very similar. Different patterns are meant to imply differing lithologies, but they are not identified by Milkereit et al. (1990).

Figure 5.14. Synthetic seismic section for the model shown in Figure 5.12. AGC has been applied. No noise has been added, and each boundary shown in Figure 5.12 produces a reflection.

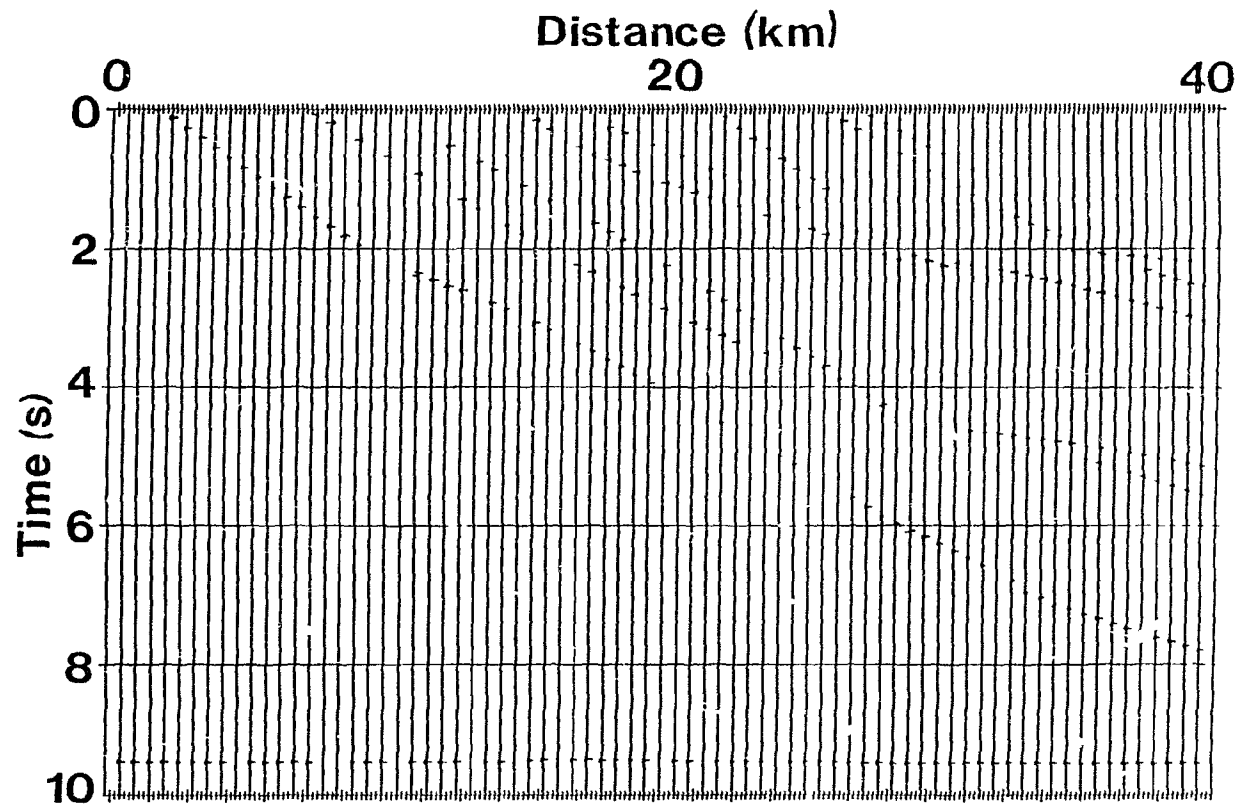


Figure 5.14

figure shows that each of the input boundaries generates a seismic response, and reflection amplitudes appear to be relatively strong. Figure 5.15 shows the same section with five per cent noise added to each trace prior to AGC over the same 800 ms window.

The differences between Figure 5.14 and 5.15 are instructive. The reflection associated with the contact between the Killarney Granite and the GFTZ orthogneisses virtually disappears when a small amount of noise is added to the traces. This is not surprising, as the velocity and density contrasts between these mineralogically similar rocks are very small. The laboratory data showed that mylonitization had no measurable effect on the seismic properties of these granitic rocks. Thus even if the boundary fault was included as a discrete zone, its effect on the reflectivity would be negligible.

The strongest reflections are caused by the quartzite-paragneiss contacts and the mafic gneiss-orthogneiss contacts. The reflection coefficients at these boundaries are 0.05 and 0.09 respectively. These reflections are well imaged over their entire extent in the model. They stand out prominently even in the section with added noise, where AGC was highly successful in bringing out these events. Paragneiss-mafic gneiss contacts (not shown in this model)

Figure 5.15. Synthetic seismic section for the model shown in Figure 5.12. AGC has been applied and five per cent noise added to each trace. Note how the weaker reflections are lost in noise but that reflections associated with mafic gneiss-orthogneiss and quartzite-paragneiss contacts are still visible.

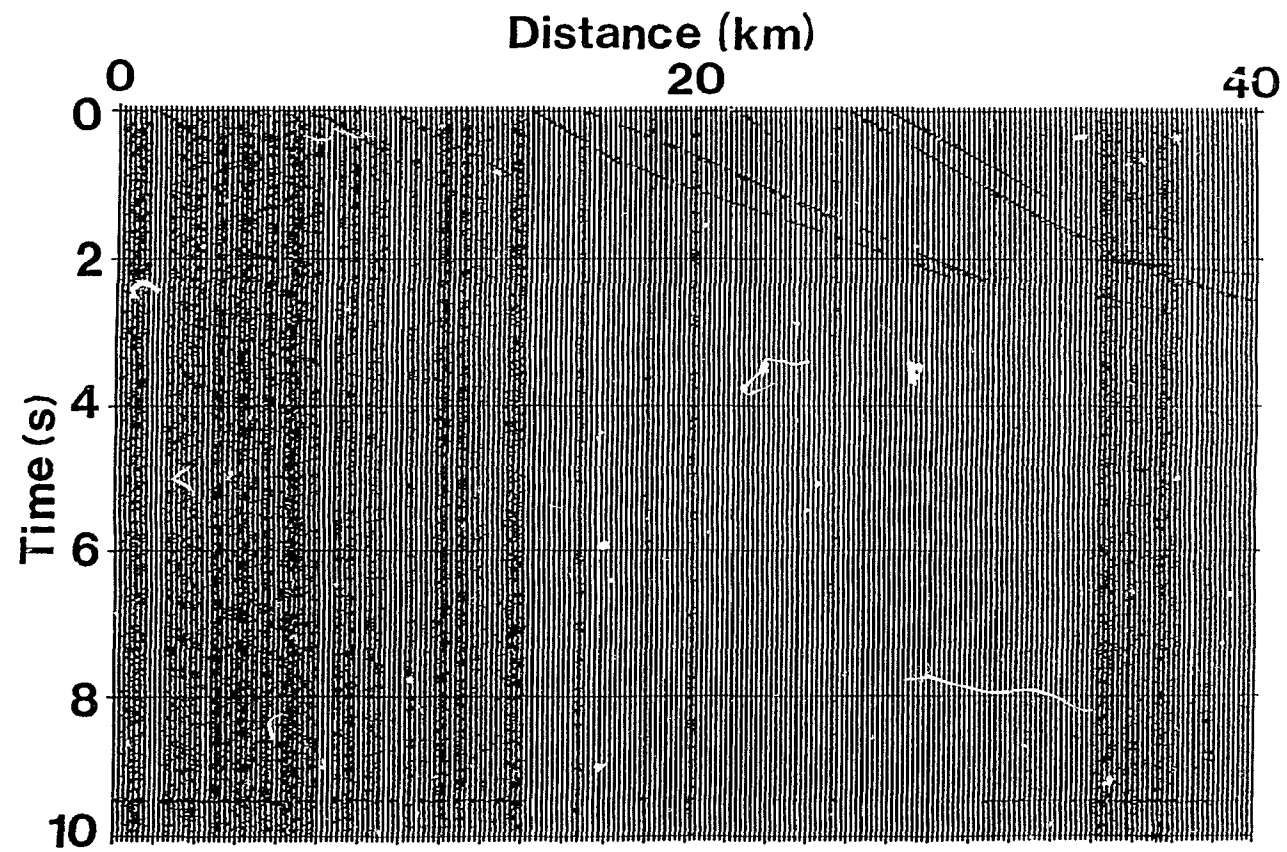


Figure 5.15

would have a reflection coefficient of 0.07, and would also produce strong reflections.

The quartzite-orthogneiss contacts have reflection coefficients of 0.02. Consequently, these events are much weaker than those of the quartzite-paragneiss and orthogneiss-mafic gneiss contacts in both Figure 5.14 and Figure 5.15. However, the reflections still have sufficient amplitude to allow the reflector geometry to be seen in both synthetic sections, including the section with added noise.

The boundaries between paragneiss and orthogneiss layers have reflection coefficients of 0.01. These reflectors are clear in the section without noise, but are almost completely overwhelmed by the added noise in Figure 5.15. At shallow depths, where geometric spreading is not large, the paragneiss-orthogneiss reflectors are visible, even though the amplitudes are low. However, deeper reflectors are entirely lost or barely visible through the noise. An interpretation based on these reflections alone could not correctly reconstruct the input model geometry.

Lithologic Variation Implications

These synthetic seismic sections, based upon a relatively simple input geometry, provide important constraints on the causes of reflections seen in GLIMPCE

Profile J. As can be seen in Figure 1.1, reflections on that profile extend to 11 seconds, with high amplitudes and complex geometries. The model presented in Figures 5.12, 5.14 and 5.15 shows that the contrast in physical properties between GFTZ orthogneiss and Killarney Complex rocks produces no reflections, due to the similarity in mineralogy of these rock suites. Differences in the average properties of orthogneiss and paragneiss are insufficient to generate strong reflections at great depths, although they could contribute to shallow-level reflectivity.

The most likely contributors to the strong reflections in GLIMPCE Profile J are the contacts between: mafic gneiss and granitic orthogneisses; mafic gneiss and paragneisses and between quartzites and paragneisses. These boundaries reflect energy well, and produce strong events, visible even through added noise on the synthetic traces. While mafic gneiss-quartzite boundaries would have high reflection coefficients, these rocks are never seen in contact, and therefore cannot be invoked to explain the GFTZ reflectivity.

The thickness of these units as mapped in the Tyson Lake region range from 100 m to 3 km, thicknesses that are generally well imaged by the seismic reflection technique. For a 35 Hz wavelet and velocities near those determined in

the laboratory, constructive interference will be maximized for 75 m thick layers, and still thicker layers will be well resolved in time (Widess, 1973).

The exposed units in the Tyson Lake area range from 1 km to greater than 15 km, with most longer than 2 km. The Fresnel zone radius $F(r)$ is an estimate of the spatial resolution of seismic data. For plane waves, Sheriff (1984) developed the equation:

$$F(r) = v/2 (2t/f)^{1/2}$$

where v is the average velocity, t is the two way travel time and f is the center frequency of the wavelet. For an average velocity of 6.3 km/s and a wavelet with a 20 Hz center frequency, the Fresnel zone radius is 1.4 km at 2 seconds, 2.2 km at 5 seconds and 3.2 km at 10 seconds. Thus, most of the units at Tyson Lake have lengths comparable to Fresnel zone diameters, and could be imaged. Hurich (1988) showed that short reflectors (as small as 18 per cent of the Fresnel zone diameter) produce coherent reflections, but with lower amplitudes than those caused by reflectors close to or greater than the Fresnel zone diameter.

Summary

This chapter discussed two modelling techniques and the results and implications of each. The results of both simple and very detailed one-dimensional modeling of thin mafic units in orthogneiss provides a new means of explaining high reflectivity of continental crust with average velocities. Minor quantities of mafic dikes in a dominantly granitic suite can produce numerous reflections as long as the dikes are clustered in some fashion. Pervasive deformation may be an effective means of enhancing such clustering.

Larger scale lithologic variations also have significant effects on the reflectivity of the crust. The contacts between mafic rocks and other lithologies produce the strongest reflection coefficients, and consequently the highest amplitude reflections for the type of geometry exposed in the Tyson Lake region. Contacts between paragneiss and quartzite also have relatively high reflection coefficients, but quartzite is considerably less abundant than the mafic rocks, and is therefore a less likely contributor to the reflectivity of Profile J. Orthogneiss-paragneiss boundaries do not have high reflection coefficients, and only produce reflections in the shallow crust where the effects of geometrical

spreading are minimal. It is also clear that variations in the deformation in the mylonitized orthogneisses of the GFTZ do not cause the reflectivity of GLIMPCE Profile J, because the properties of the highly deformed rocks are identical to the less deformed orthogneisses from which they were derived.

CHAPTER 6

CONCLUSIONS

This work provides laboratory values of compressional wave velocities in rocks of the Grenville Front Tectonic Zone (GFTZ), and provides in situ compressional and shear wave velocities, obtained from the OGLE refraction experiment, for the same rocks. These data are summarized below for the three main lithologic groups studied. Following this section, the origin of seismic wave reflections within the GFTZ, and within deep crustal sections in general, is revisited in light of the new data and ideas presented here.

Laboratory Velocity Measurements

Compressional wave velocities were measured on a total of 41 rocks from the Collins Inlet and Tyson Lake regions near the north shore of Georgian Bay. Three lithologic groups are represented: granitic orthogneiss, paragneiss, and mafic gneiss.

Granitic Orthogneiss

The granitic orthogneiss samples, including mylonitic samples, exhibit a narrow range in mineralogy (Table 2.1) and narrow ranges in compressional wave velocity and

density (Table 2.3). The average velocity at 600 MPa for this lithology is 6.29 km/s and the average bulk density is 2.65 g/cm³ (Table 2.6). These rocks have low seismic anisotropy (1-6%; Table 2.5) at this pressure. The apparent strain has no effect on either the average compressional wave velocity or on the seismic anisotropy for the mylonitic orthogneiss samples from the boundary fault traverse.

Paragneiss

The paragneiss samples have a wide range in modal mineralogy (Table 2.1) and, consequently, a large range of compressional wave velocity and seismic anisotropy (Table 2.3). The average velocity for these rocks at 600 MPa is 6.31 km/s and the average bulk density is 2.72 g/cm³. Seismic anisotropy is found to range from 0-5% for samples with relatively high total quartz+potassium feldspar and from 5-15% for samples with low quartz+potassium feldspar (Table 2.5). The latter may be explained by the occurrence of variable amounts of muscovite.

Mafic Gneiss

The average velocity of all mafic rocks studied is 6.88 km/s at 600 MPa and the average bulk density is 2.98 g/cm³. These rocks exhibit a wide range of both

compressional wave velocity (Table 2.3) and seismic anisotropy (Table 2.5), both values being somewhat dependent upon the percentage and degree of preferred orientation of anisotropic minerals (Table 2.1). Diabasic rocks of the Sudbury and Grenville Dike swarms are notable for complete seismic isotropy, interpreted as due to the preservation of ophitic textures.

OGLE Refraction Velocities

Five refraction profiles were conducted for the GFTZ in order to determine the shallow level compressional and shear wave velocity structure, and assess the effect of large scale fractures or lithologic variation on in situ velocities. The profiles crossed both mylonitized granitic orthogneiss and paragneiss assemblages.

Orthogneiss Profiles

The two refraction profiles conducted off the south shore of Philip Edward Island (OGLE Lines 3 and 4; Figure 3.1) cross the GFTZ boundary fault region within mylonitic orthogneiss. The orthogonal profiles produced identical average compressional wave velocities of 5.9 km/s and an average shear wave velocity of 3.2 km/s, both for a deeper layer in shallow crust (below ca. 300 m; Figure 4.1a).

Because the in situ compressional wave velocity for the orthogneiss is identical to the laboratory-measured velocity at equivalent pressures, the visible large scale fractures do not have a significant effect on compressional wave velocities in the GFTZ boundary fault region below ca. 300 m. There is, however, evidence for a significant velocity gradient in the upper 300 m in this region. This is consistent with other areas of the Shield and may indicate that fractures play an important near surface role in recently glaciated crystalline rocks.

The lack of in situ seismic anisotropy of the GFTZ boundary fault mylonite zone is consistent with the laboratory velocity results, and indicates that high strain zones are not necessarily seismic reflectors in the GFTZ.

Paragneiss Profiles

Two refraction profiles (OGLE Lines 1 and 6; Figure 3.1) were shot parallel to the foliation in paragneiss assemblages. Both show one-dimensional structures with a shallow layer of slow compressional and shear wave velocities (ca. 4.1 and 2.7 km/s respectively; Figure 4.3a and 4.4a) and a deeper layer of higher velocity rocks (ca. 6.2 and 3.3 km/s, respectively). These results match those obtained in the laboratory. The agreement between the laboratory and in situ values for the parallel-to-strike

direction suggests that the in situ velocity for the normal-to-strike direction will also be similar to the laboratory value. As with Lines 3 and 4 above, these lines possess evidence of significant near-surface velocity gradients.

Deep Crustal Reflections Revisited

As stated in Chapter 1, horizontal to sub-horizontal reflectors in deep crustal seismic profiles result from high reflection coefficients that may be due to some combination of primary depositional layering, primary intrusive layering, tectonic layering, metamorphic layering, and/or fluids. It is not possible to definitively identify the cause of high reflection coefficients in the highly deformed GFTZ but the data obtained in this study strongly suggest that lithologic layering, either primary intrusive and/or tectonic, is responsible.

The highest reflection coefficients in the GFTZ are determined to be on the order of 0.10 (Table 4.1) and occur when mafic rocks are in contact with other lithologies. All other reflection coefficients associated with the GFTZ are significantly lower. Of particular interest is the observation (both in the laboratory and in situ) that the

degree of strain (e.g., mylonitization) exhibited by orthogneisses from the GFTZ boundary fault has little effect on seismic anisotropy, and, consequently, reflection coefficients. Elsewhere, however, mylonites have been postulated to be responsible for deep crustal reflections where it has been demonstrated that increasing strain gives rise to an increase in the preferred orientation of anisotropic minerals, such as micas (e.g., Jones and Nur, 1984). The lack of significant seismic anisotropy in GFTZ orthogneisses precludes a significant correlation between degree of strain and reflection coefficient in these rocks, but does not necessarily preclude such a correlation elsewhere. GFTZ mylonites exhibit mineralogies dominated by quartz and feldspar, with mica virtually absent. Neither quartz nor feldspar typically impart significant seismic anisotropy to their host rock, the former because it exhibits low inherent seismic anisotropy and the latter because it is brittle and often fractures and rotates during deformation. Muscovite and biotite micas, however, are highly anisotropic to compressional waves and they often exhibit a preferred orientation of their c-axes normal to foliation planes.

Seismic anisotropy of the mafic rocks and some of the paragneiss samples has an effect on the calculated reflection coefficients for different wave propagation

directions, but the total range is only approximately 0.03. The reflection coefficients are lowest for A-A direction boundaries, and highest for B-B direction boundaries (Table 4.1). The A-A direction boundaries are most nearly applicable to the ray paths for GLIMPCE Profile J. Therefore, even though some GFTZ samples exhibit high degrees of seismic anisotropy, the effect is not pervasive and seismic anisotropy alone cannot be responsible for the reflectivity of the GFTZ.

The variation in the angle of incidence of rays to reflecting boundaries ranges from 3° to 15° for GLIMPCE Profile J (Figure 4.6). For the largest angles of incidence of Profile J, this variation amounts to a very slight reduction (ca. 0.01) in the effective reflection coefficient and constitutes a minor effect on reflection amplitudes.

The observation that the mafic rocks are associated with the highest reflection coefficients has interesting consequences. Unlike other lithologic contacts in the GFTZ, the contribution of mafic rocks to overall reflectivity should increase with depth in the continental crust. As mafic rocks progress from amphibolite to granulite to the eclogite facies, the relative per cent of garnet and pyroxene increases at the expense of biotite and amphibole. In contrast, the quartzo-feldspathic

orthogneisses do not experience such drastic changes in mineralogy. Because both pyroxenes and garnets are minerals with very high compressional wave velocities (Christensen, 1982), increasing the metamorphic grade accentuates the velocity difference between mafic rocks and the surrounding orthogneiss and increases the reflection coefficient. Therefore, thin mafic dikes, if they truly cluster to form reflectors, can serve as important contributors to deep crustal reflectivity in deformed zones like the GFTZ.

Synthetic Models

Both detailed one-dimensional models and more general two-dimensional models of the GFTZ are presented in order to determine the cause of the reflections in GLIMPCE Profile J. These are meant to be viewed as analogs to Profile J, not exact representations.

One-dimensional models of mafic dikes in granitic orthogneiss show that very thin layers (<30 cm) which occur in clusters can have a substantial effect on large scale seismic reflectivity (Table 5.1, Figures 5.3). This result provides a new mechanism, namely sub-parallel clusters of thin mafic dikes, to explain high reflectivity of deep continental crust characterized by average compressional

wave velocities. Only minor amounts of mafic rocks, comparable to those often observed in middle and lower crustal granitoid rocks, are required to produce reflections. Sub-parallel orientation of mafic rocks in a granite-dominated assemblage may result from a number of processes including: (1) original injection of a parallel dike or sill swarm, (2) alignment by deformation of initially "randomly" oriented mafic rocks in a high strain zone or (3) repeated faulting of a single mafic layer. Deep crustal reflectivity caused by sub-parallel clusters of thin layers with high velocity contrasts to the host medium can be applied to a number of different geologic environments, for example underplated continental crust (e.g., Warner, 1990) and orogenic belts that experience substantial lateral deformation (e.g., Jamieson and Beaumont, 1989).

The two-dimensional model shows that geometrical spreading of seismic energy causes the orthogneiss-paragneiss boundaries to become invisible at depths greater than 6 km (Figure 5.14). Mafic gneiss-orthogneiss boundaries and paragneiss-quartzite boundaries are still visible at the base of the model because of their higher reflection coefficients. Boundaries between mafic rocks and other lithologies are a more likely contributor to the reflectivity of Profile J than paragneiss-quartzite

boundaries because of their greater abundance in the GFTZ and their tendency to occur in clusters. Mereu et al. (1989) show a refraction velocity of 6.5 km/s for the part of GLIMPCE Profile J that crossed the GFTZ, another indication that large volumes of quartzite cannot explain the GFTZ reflectivity.

Figure 6.1 is a schematic representation of the factors that have been proposed as possible causes of the reflections in the portion of GLIMPCE Profile J that crosses the GFTZ. They are: (1) anisotropy or low compressional wave velocities related to mylonitization, (2) the presence of fracture or cataclasis zones, (3) lithologic contacts, (4) very thin, high velocity, mafic dikes and (5) high pore pressure zones.

The suggestion of Green et al. (1988) of reflectivity in the GFTZ related to anisotropy caused by mylonitization is not supported by the laboratory and in situ velocity data, because the boundary fault mylonites are essentially isotropic and have the same compressional wave velocity as the lesser deformed orthogneisses from which they were most likely derived. Likewise, the in situ experiments across the boundary fault region of the GFTZ nearly duplicated the low pressure laboratory velocity data which show very low reflection coefficients for the boundary fault rocks; and therefore cataclasis or large scale fractures are not

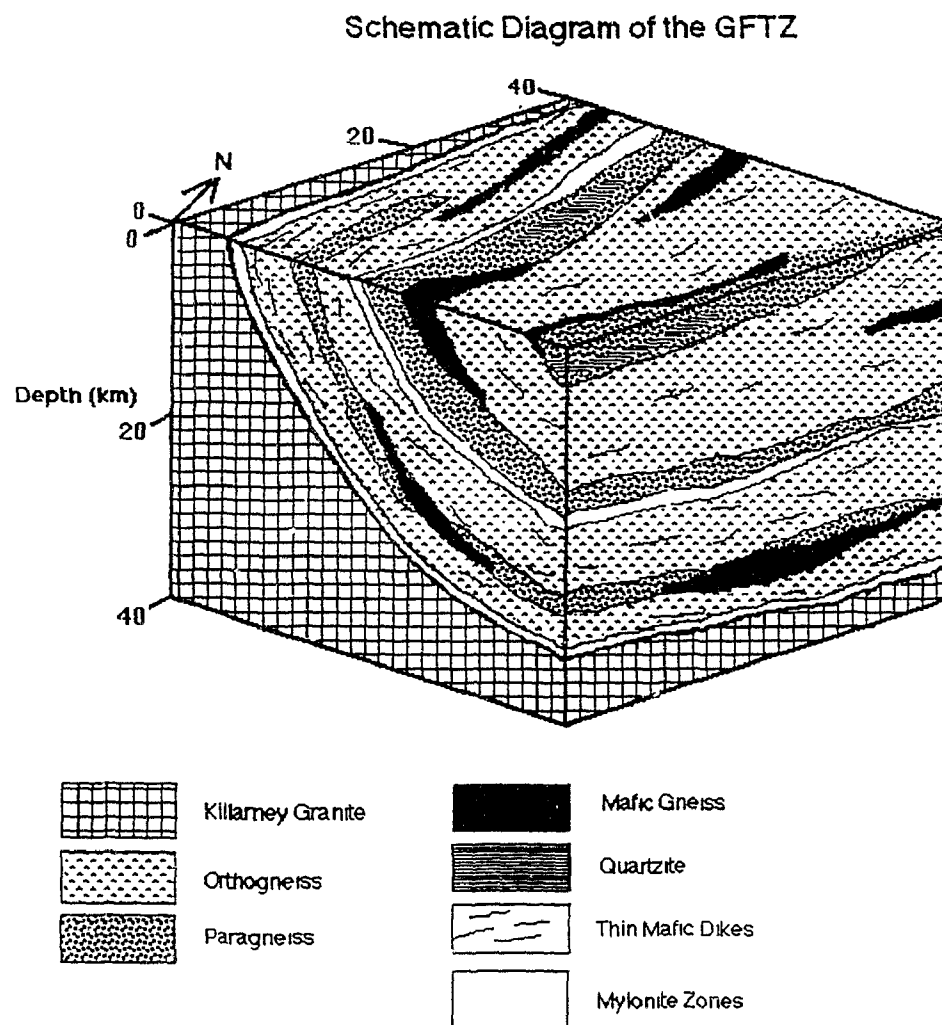


Figure 6.1 Schematic diagram of the GFTZ showing proposed reflectors.

likely contributors to the seismic reflectivity in this region, except, possibly, in the upper several hundred meters of the crust. Similarly, maintaining sufficiently high pore fluid pressures to cause high amplitude reflections seems unlikely for a Proterozoic tectonic zone (Jones and Nur, 1984; Warner, 1990).

The contacts between mafic gneisses and other lithologies have large reflection coefficients, and are likely candidates to explain the high reflectivity of Profile J. The diversity and intercalation of such outcrops near Tyson Lake are sufficient to cause high reflectivity if projected to greater depths. Additional reflectivity can be provided by very thin, sub-parallel mafic dike clusters in an orthogneiss-dominated assemblage.

Further Work

Considerably more work on the velocity structure of the GFTZ needs attention. Laboratory-measured shear wave velocities are needed to compare to the in situ values from OGLE, and to determine if shear wave anisotropy is present in the GFTZ rocks. Compositional data on the samples for which compressional wave velocities have already been measured will allow the calculation of velocity behavior as a function of grain density and chemical composition, and

could possibly be used for arguments regarding chemical evolution of the Canadian Shield, and other continents.

More OGLE work on the GFTZ profiles in progress. Digitization of a single channel reflection line off the south shore of Philip Edward Island is underway, and should confirm the results of this work. Three-component data were collected at all of the end-of-line sites for the refraction profiles, and await further analysis. Finally, the high shot density and data quality of all of the OGLE profiles make them ideal candidates for inversion analyses.

Appendix 1
OGLE Mid-Line Refraction Profiles

Figure A.1. A) Seismic section and B) picked arrivals at site GB 3-2.

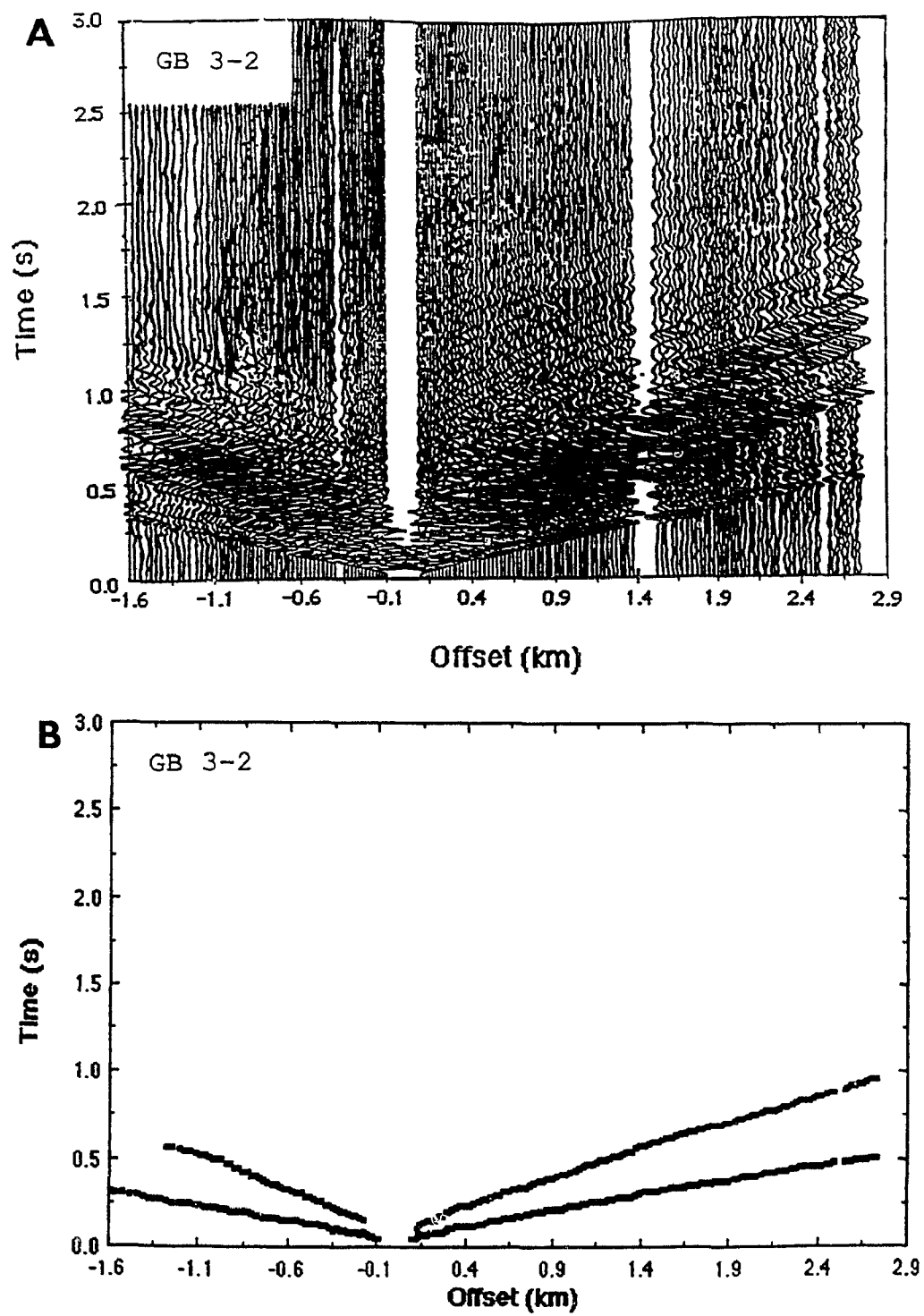


Figure A.1

Figure A.2. A) Seismic section and B) picked arrivals at site GB 4-2.

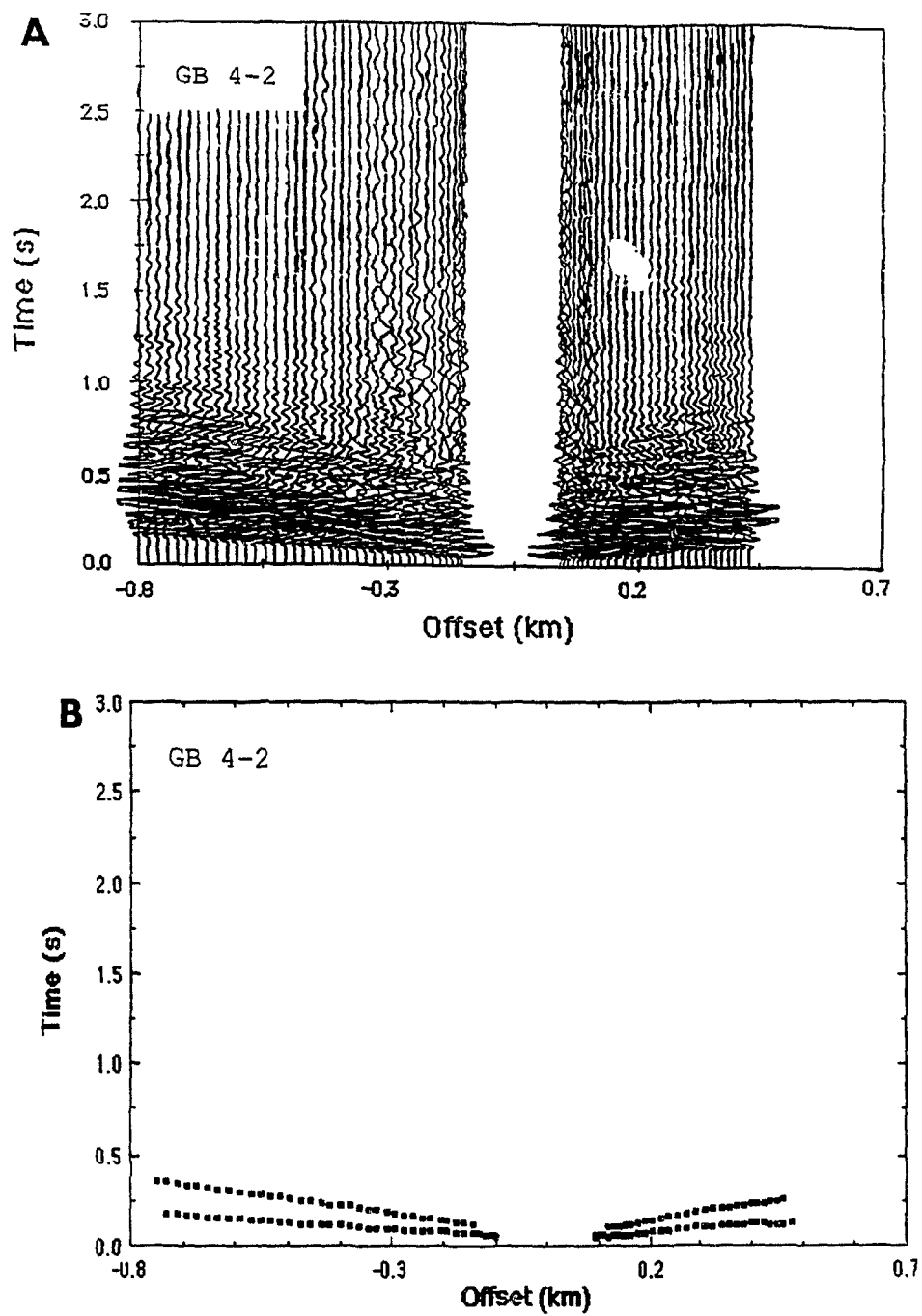


Figure A.2

Figure A.3. A) Seismic section and B) picked arrivals at site GB 4-3.

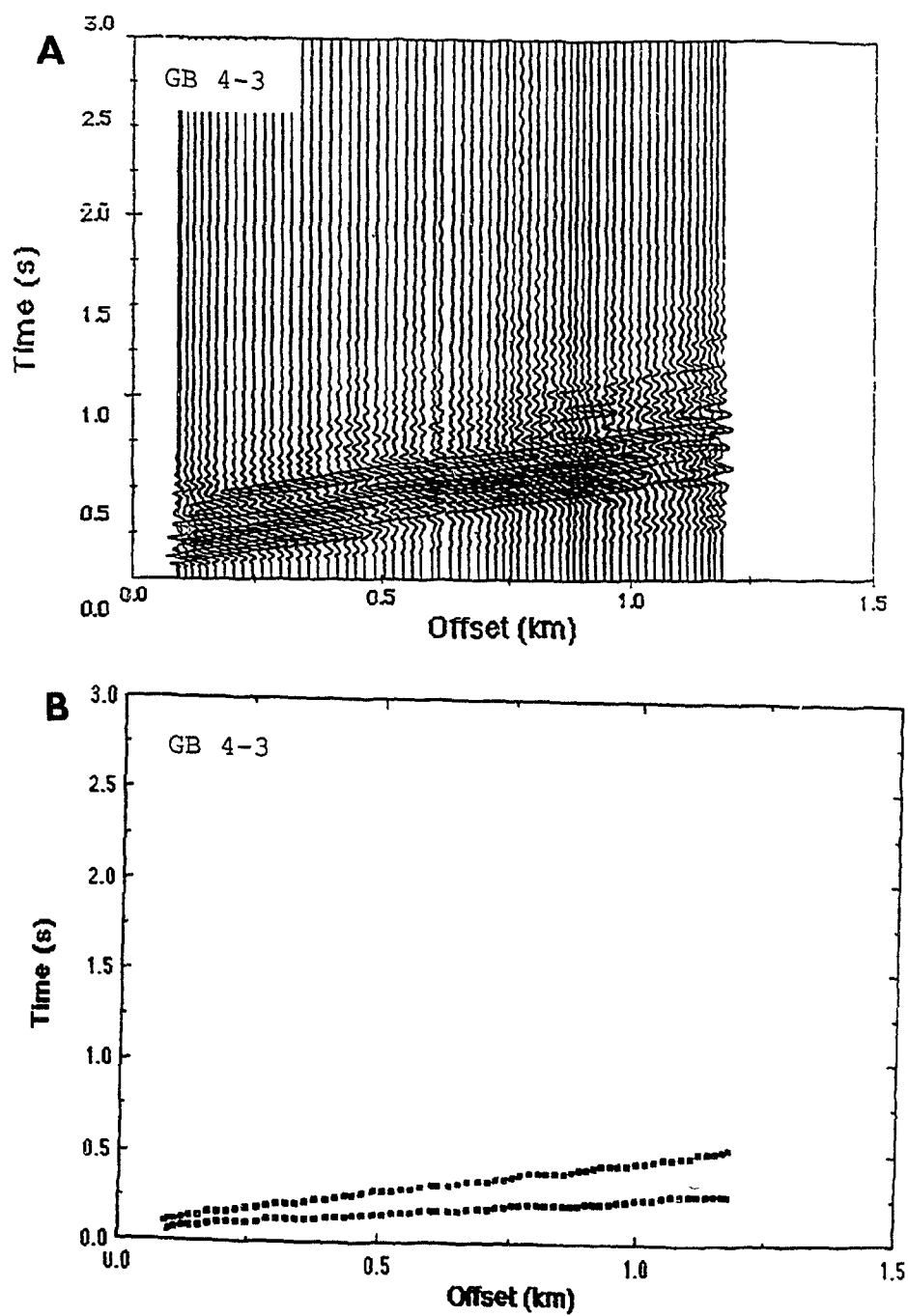


Figure A.3

Figure A.4. A) Seismic section and B) picked arrivals at site BB 6-2.

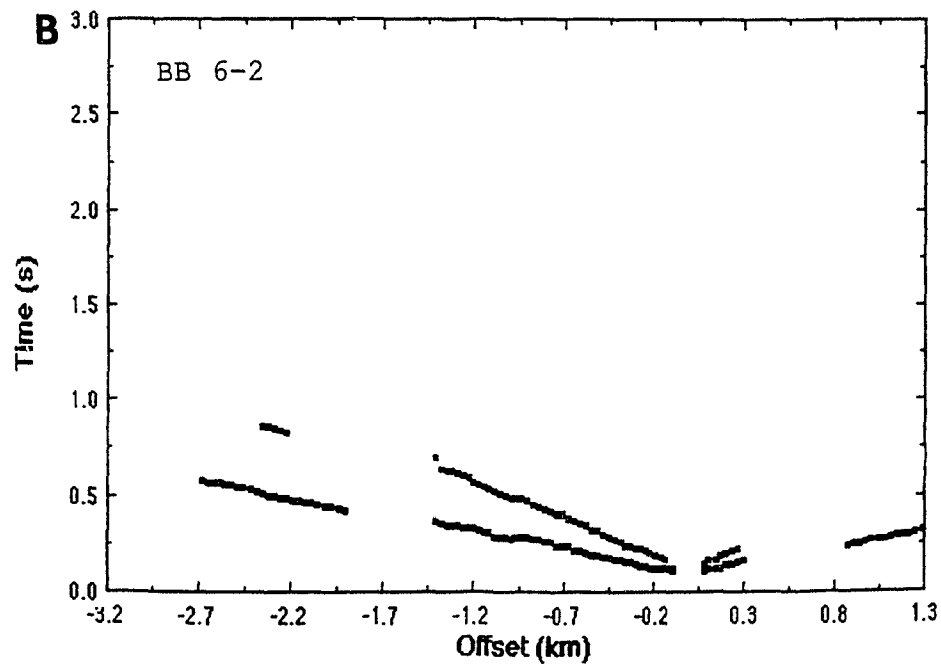
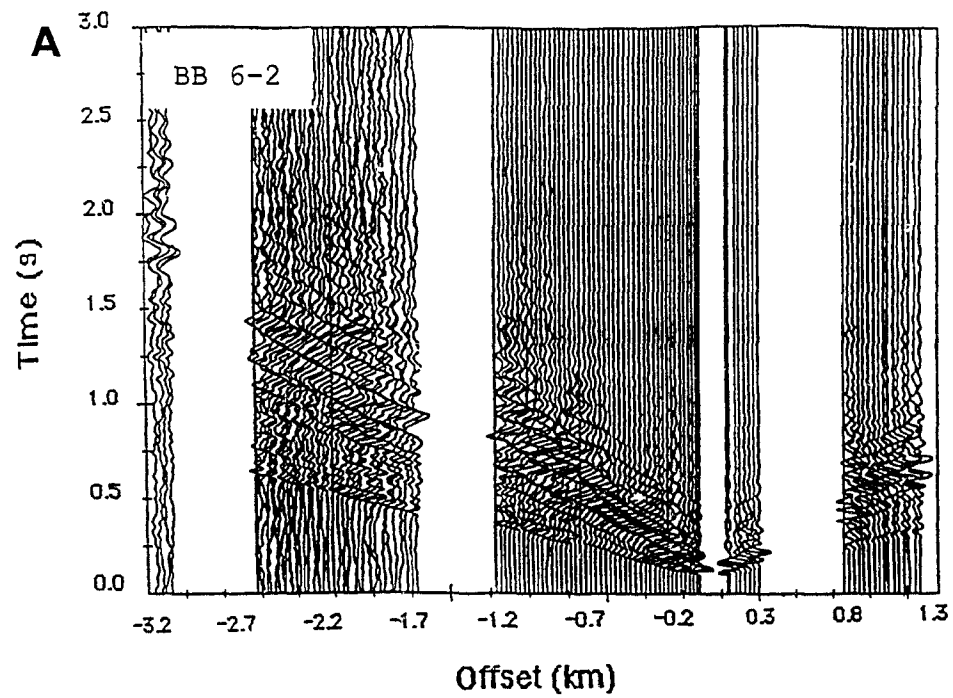


Figure A.4

Figure A.5. A) Seismic section and B) picked arrivals at site BB 6-3.

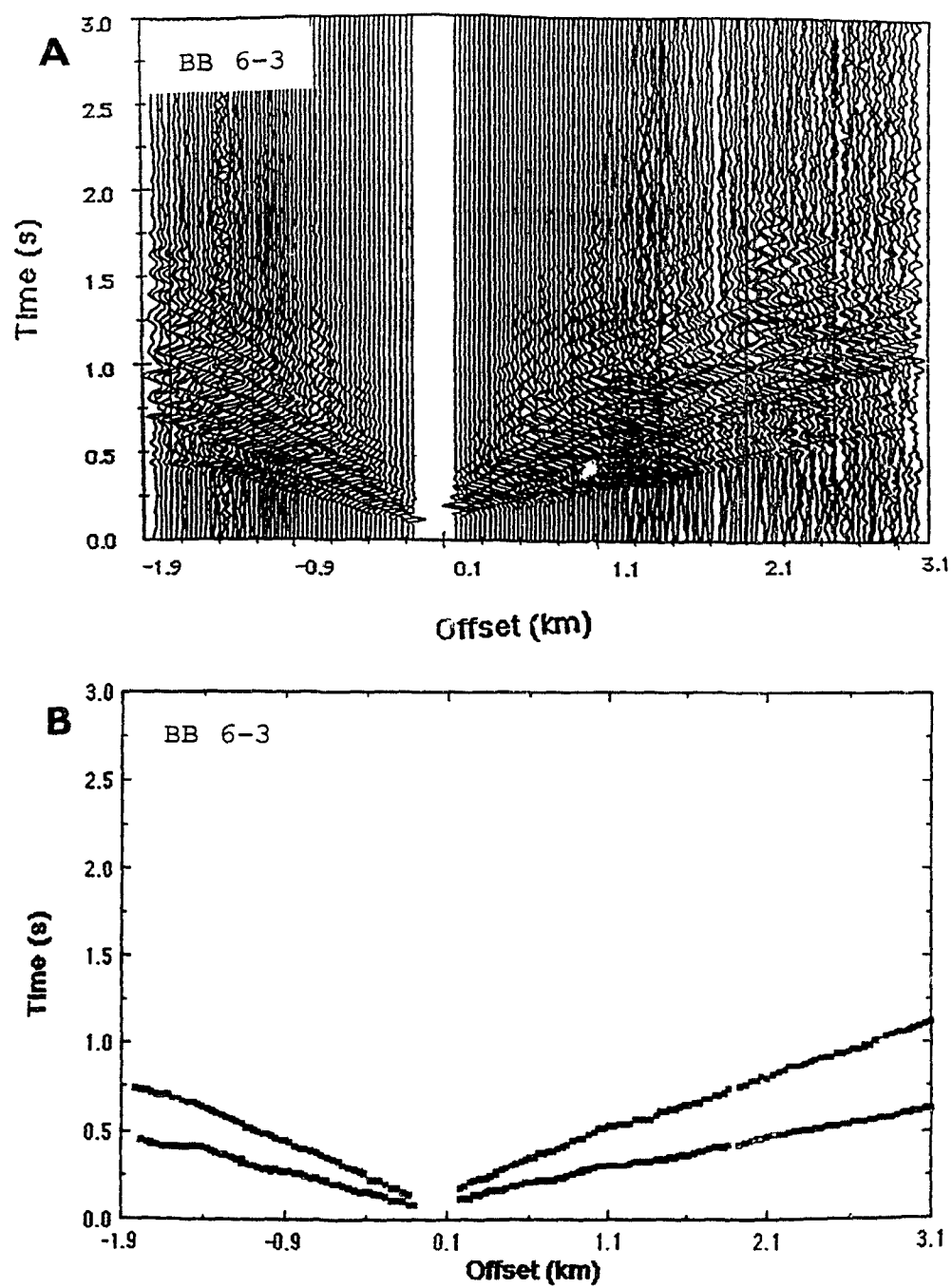


Figure A.5

Figure A.6. A) Seismic section and B) picked arrivals at site ML 1-2.

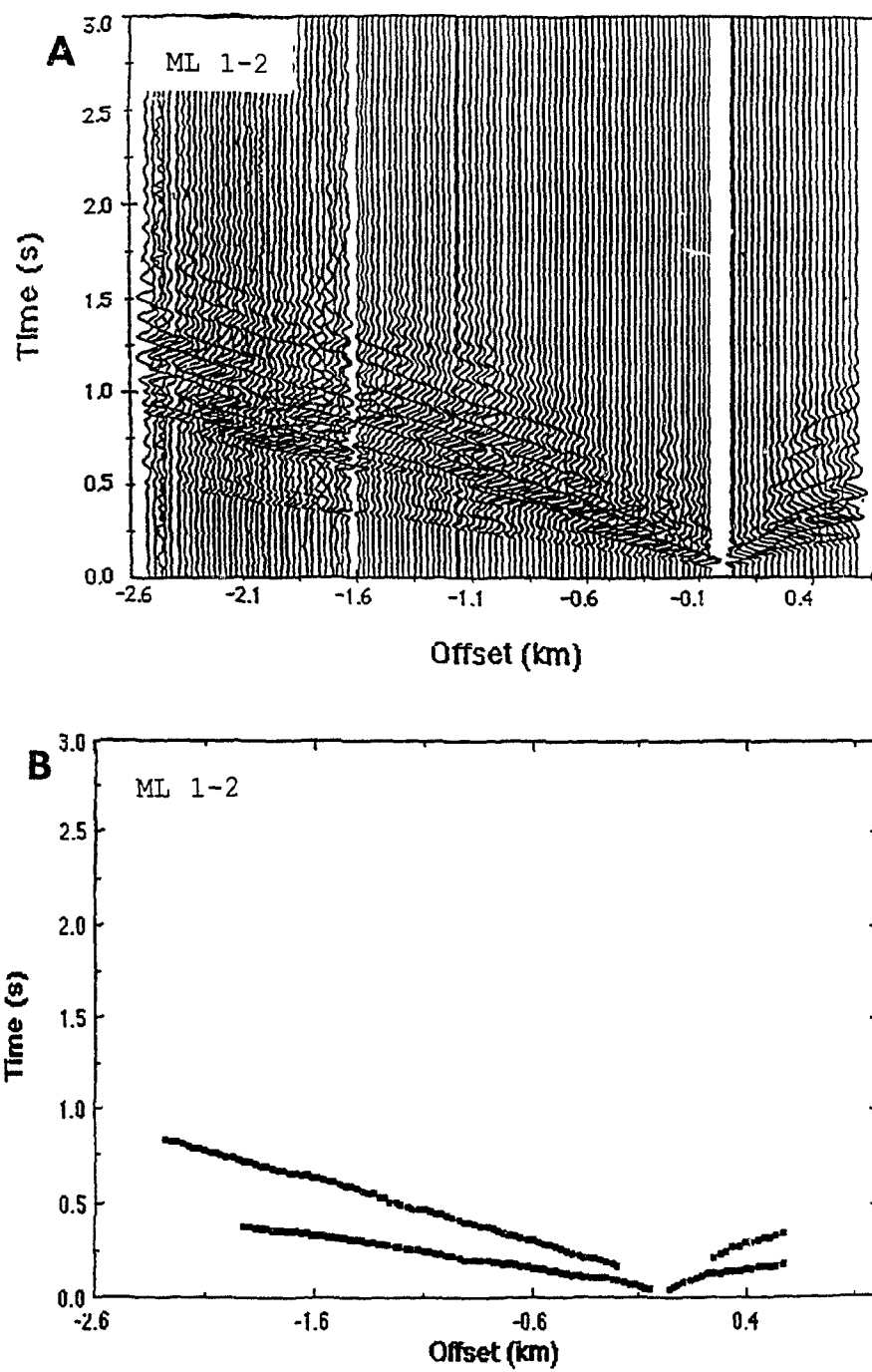


Figure A.6

Figure A.7. A) Seismic section and B) picked arrivals at site ML 1-3.

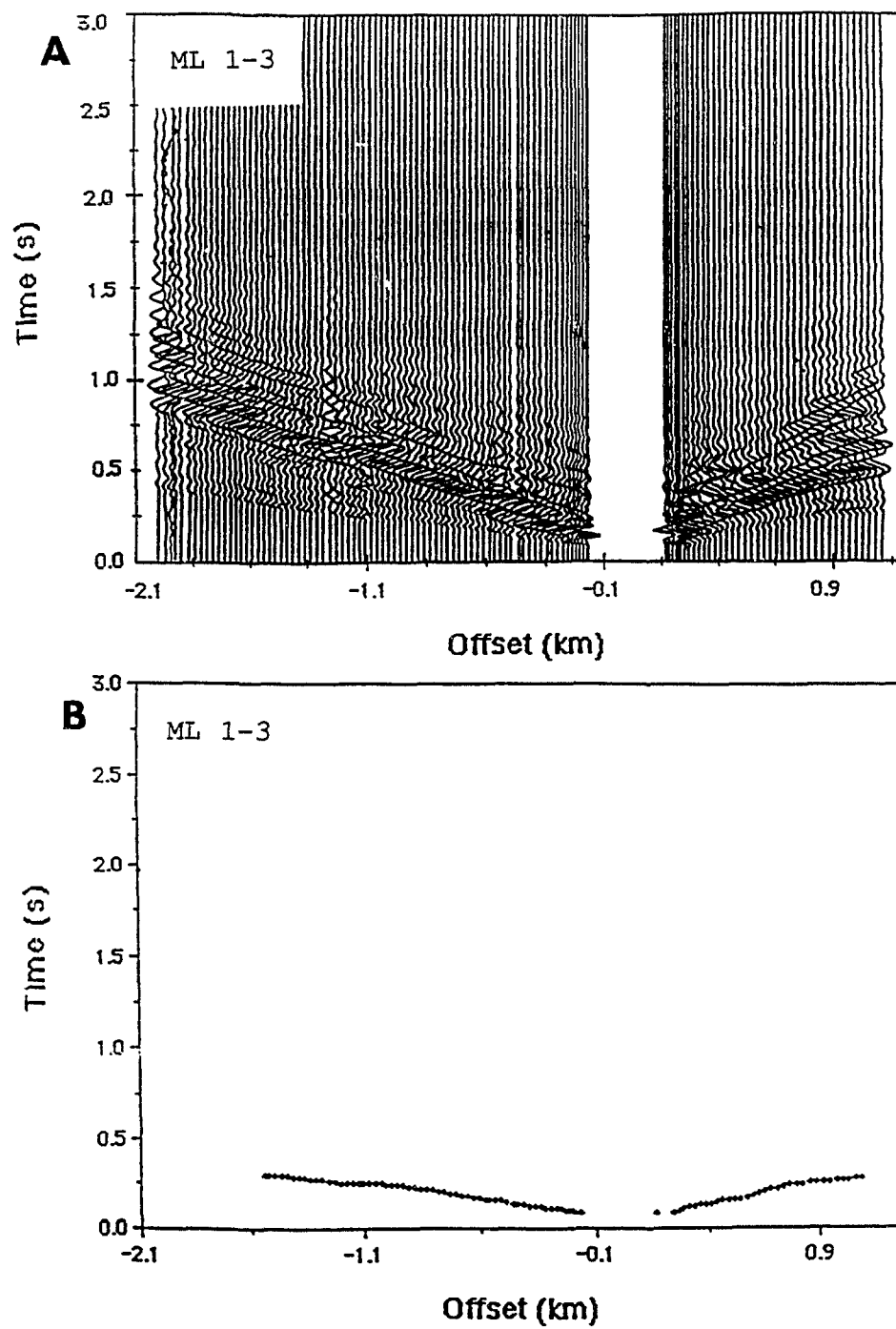


Figure A.7

Figure A.8. A) Seismic section and B) picked arrivals at site ML 1-4.

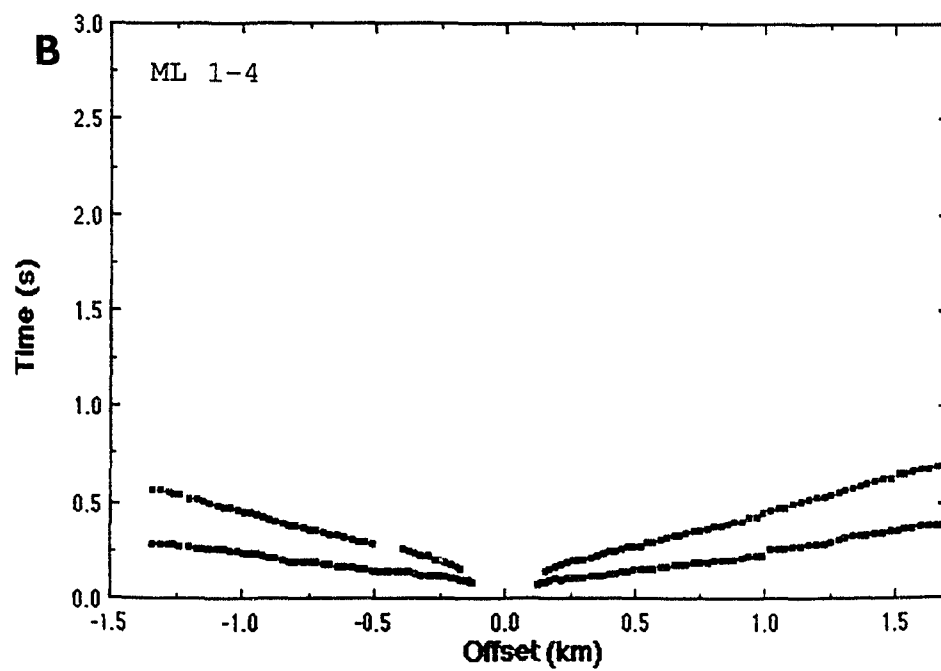
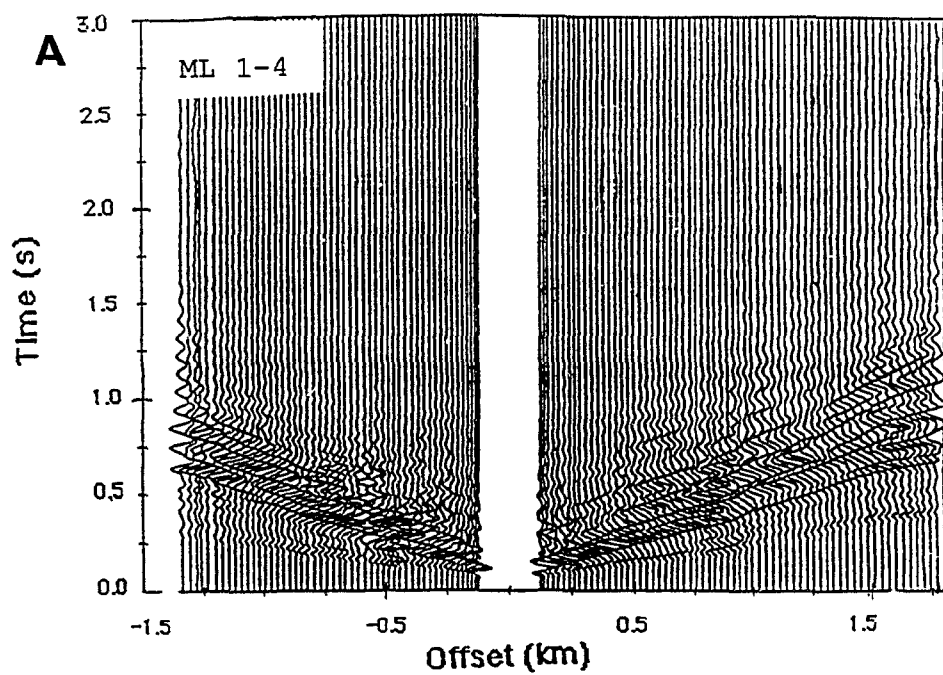


Figure A.8

Figure A.9. A) Seismic section and B) picked arrivals at site ML 1-5.

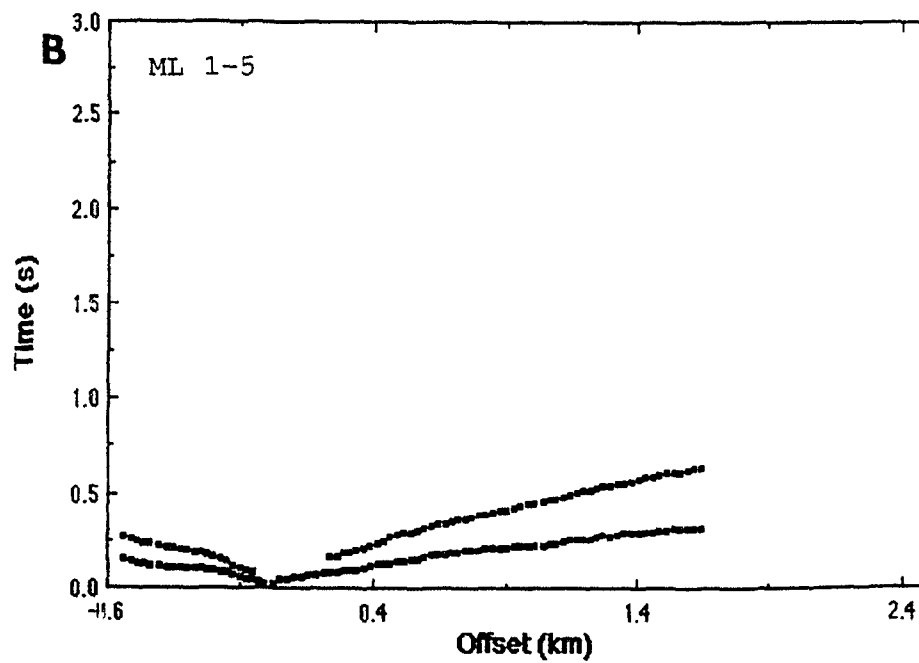
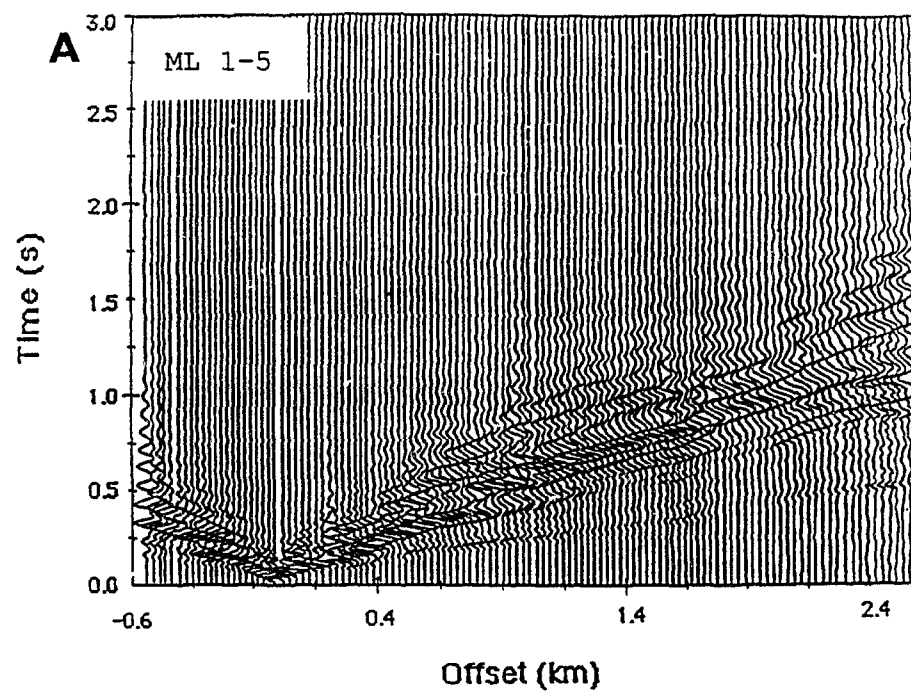


Figure A.9

References Cited

- Aki, K. and P. Richards, 1980, Quantitative Seismology, Theory and Methods, Vols. 1 and 2, W.H. Freeman and Co. San Francisco, 932 p.
- Alexandrov, K.S. and T.V. Ryzhova, 1961, Elastic properties of rock forming minerals, 1, pyroxenes and amphiboles, Bull. Acad. Sci. USSR Geophys. Ser., English Trans., **9**, 1165-1168.
- Alexandrov, K.S. and T.V. Ryzhova, 1961, Elastic properties of rock forming minerals, 2, layered silicates, Bull. Acad. Sci. USSR Geophys. Ser., English Trans., **11**, 871-875.
- Alexandrov, K.S. and T.V. Ryzhova, 1962, Elastic properties of rock forming minerals, 3, feldspars, Bull. Acad. Sci. USSR Geophys. Ser., English Trans., **2**, 129-131.
- Alexandrov, K.S. and T.V. Ryzhova, 1965, Elastic properties of potassium-sodium feldspars, Bull. Acad. Sci. USSR Geophys. Ser., English Trans., **1**, 53-55.
- Barazangi, M and L. Brown, (eds) 1986, Reflection Seismology: the Continental Crust, AGU Geodynamics Ser, **14**, 339 p.
- Bethune, K.M. and A. Davidson, 1988 Diabase dikes and the Grenville Front southwest of Sudbury, Ontario, in Current Research, Part C, GSC Paper 88-1C, 151-159.
- Bickford, M.E., W.R. Van Schmus and I. Zietz, 1986, Proterozoic history of the midcontinent region of North America, Geology, **14**, 492-296.
- Birch, F., 1960, The velocity of compressional wave in rocks to 10 kilobars, part 1, J. Geophys Res., **65**, 1083-1102.
- Birch, F., 1961, The velocity of compressional wave in rocks to 10 kilobars, part 2, J. Geophys Res., **66**, 2199-2224.
- Bois, C., M. Cazes, A. Hirn, P. Matte, A. Mascle, L. Montadert and B. Pinet, 1987, Crustal laminations in deep seismic profiles in France and neighboring areas, Geophys. J. R. astr. Soc., **89**, 297-304.

- Brace, W., 1965, Some new measurements of linear compressibility of rocks, *J. Geophys. Res.*, **70**, 391-398.
- Brewer, J.A., D.H. Matthews, M.R. Warner, J. Hall, D.K. Smythe and R.J. Whittington, 1983, BIRPS deep seismic reflection studies of the British Caledonides, *Nature*, **305**, 206-210.
- Burke, M., 1987, Compressional wave velocities in rocks from the Ivrea-Verbano and Strona-Ceneri Zones, Southern Alps, Northern Italy: implications for models of crustal structure, University of Wyoming M.Sc. Thesis, 78 p.
- Burke, M. and M.H. Salisbury, 1989, Preliminary velocity measurements in the Grenville Front; do mylonites cause high reflectivity in the Grenville Front Tectonic Zone?, *EOS Trans. AGU.*, **70**, 271.
- Burke, M., I. Asudeh and D.R. Hutchinson, 1989, Laboratory and in situ velocity measurements from the Grenville Front, *EOS Trans., AGU*, **70**, 493.
- Burke, M. and D.M. Fountain, 1990, Seismic properties of rocks from an exposure of extended continental crust-new measurements from the Ivrea zone, *Tectonophys.*, **182**, 149-162.
- Card, K.D., W.R. Church, J.M. Franklin, M.J. Frarey, J.A. Robertson, G. West and G.M. Young, 1972, in The Southern Province in R.A. Price and R.J. Douglass (eds) Variations in Tectonic Styles in Canada, *Geol. Assoc. Can. Special Paper* **11**, 335-379.
- Cerveny, V., 1893, Synthetic body wave seismograms for laterally varying structures by the Gaussian beam method, *Geophys. J.R. astr. Soc.*, **73**, 389-426.
- Choukroune, P., 1989, The ECORS Pyrenean deep seismic profile reflection data and the overall structure of an orogenic belt, *Tectonics*, **8**, 23-39.
- Christensen, N.I., 1965, Compressional wave velocities in metamorphic rocks to 10 kilobars, *J. Geophys. Res.*, **70**, 6147-6164.
- Christensen, N.I., 1982, Seismic Velocities, in R.S. Carmichael (ed.) Handbook of Physical Properties of Rocks, Vol. 2, CRC Press, 228 p.

- Christensen, N.I., 1989, Reflectivity and seismic properties of the deep continental crust, *J. Geophys. Res.*, **94**, 17793-17804.
- Christensen, N.I. and G. Shaw, 1970, Elasticity of mafic rocks from the Mid-Atlantic Ridge, *Geophys. J.*, **20**, 271-284.
- Christensen N.I. and D.M. Fountain, 1975, Constitution of the lower continental crust based on experimental studies of seismic velocities in granulite, *GSA Bull.*, **86**, 227-236.
- Christensen, N.I. and D. Szymanski, 1988, Origin of reflections from the Brevard Fault Zone, *J. Geophys. Res.*, **93**, 1087-1102.
- Chroston, P.N. and M.D. Max, 1988, Seismic anisotropy in mylonites; an example from the Mannin Thrust Zone, southwest Connemara, Ireland, *Tectonophys.*, **148**, 29-39.
- Crampin, S., 1989, Suggestions for a consistent terminology for seismic anisotropy, *Geophys. Prosp.*, **37**, 753-770.
- Davidson, A., 1985, Tectonic framework of the Grenville Province in Ontario and Western Quebec, Canada, in A.C. Tobi and J. Touret (eds.) The Deep Proterozoic Crust in North Atlantic Provinces, 133-149.
- Davidson, A., 1986, New interpretations in the southwestern Grenville Province, in Moore, J.M., A. Davidson and A. Baer (eds.) The Grenville Province, GAC Special Paper **31**, 61-74.
- Davidson, A. and K. Bethune, 1988, Geology of the north shore of Georgian Bay, Grenville Province of Ontario, in Current Research, Part C, GSC Paper 88-1C, 135-144.
- Davidson, A. and W. Morgan, 1980, Preliminary notes on the geology east of Georgian Bay, Grenville Structural Province, Ontario, in Current Research, Part A, GSC Paper 81-1a, 291-298.
- DeVoogd, N. and H. Den Rooijen, 1983, Thin layer response and spectral bandwidth, *Geophysics*, **48**, 12-18.

- Epilli, D., and R. Mereu, 1989, The crustal structure beneath Lake Huron and Georgian Bay as revealed from GLIMPCE refraction and wide angle reflection data, EOS Trans. AGU., **70**, 271.
- Finlayson, D. and S. Mathur, 1984, Seismic reflection and refraction features of the lithosphere in northern and eastern Australia, and continental growth, Ann. Geophys., **2**, 711-722.
- Fountain, D.M., 1986, Implications of deep crustal evolution for seismic reflection in Baranganzi, M. and L. Brown (eds.) Reflection Seismology: The Continental Crust, AGU Geodynamic Series, **14**, 1-7.
- Fountain, D.M. and F.H. Salisbury, 1981, Exposed cross sections through the continental crust: implications for crustal structure, petrology and evolution, Earth Planet. Sci. Lett., **56**, 263-277.
- Fountain, D.M., C.A. Hurich and S.B. Smithson, 1984, Seismic **12**, 195-198.
- Fountain, D.M., D.T. McDonough and J.M. Gorham, 1987, Seismic reflection models of continental crust based on metamorphic terranes, Geophys. J. R. astr. Soc., **89**, 61-66.
- Fountain, D.M., M.H. Salisbury and J. Percival, 1990, Seismic structure of the continental crust based on rock velocity measurements from the Kapuskasing Uplift, J. Geophys. Res., **95**, 1167-1186.
- Frarey, M.J., 1985, Proterozoic geology of the Lake Panache-Collins Inlet area, Ontario, GSC Paper 83-22, 61 p.
- Frarey, M.J. and R.T. Cannon. 1969, Notes to accompan a map of the geology of the Lake Panache-Collins Inlet area, Ontario, GSC Paper 68-63, 5 p.
- Frazer, N., 1990, Dynamic elasticity of microbedded and fractured rocks, J. Geophys. Res., **95**, 4821-4831.
- Frazer, N. and R. Phinney, 1980, The theory of finite frequency body wave synthetic seismograms in inhomogeneous media, Geophys. J. R. astr. Soc., **63**, 691-717.
- Fuchs, K., 1969, On the properties of deep crustal reflections, J. Geophys., **35**, 133-149.

- Fuchs, K. and G. Muller, 1971, Computation of synthetic seismograms with the reflectivity method and comparisons with observations, *Geophys. J.*, 23, 417-433.
- Fuller, B., 1988, Seismic detection of Upper Cretaceous stratigraphic oil traps in the Powder River Basin, Wyoming, University of Wyoming Ph. D. Thesis, 107 p.
- Gardner, G., M. Wyllie and D. Droschak, 1965, Hysteresis in the velocity-pressure characteristics of rocks, *Geophys.*, 30, 111-134.
- Geological Survey of Canada, 1987, 41H Georgian Bay, Ontario, Total Magnetic Field Map, open file map # 1417.
- Green, A.G., B. Milkereit, A. Davidson, C. Spencer, D. Hutchinson, W.F. Cannon, M. Lee, W. Agena, J.C. Behrendt and W.J. Hinze, 1988, Crustal structure of the Grenville front and adjacent terranes, *Geology*, 16, 788-792.
- Green, A.G., B. Milkereit, J. Percival, A. Davidson, R. Parrish, F. Cook, W. Geis, W.F. Cannon, D. Hutchinson, G. West and R. Clowes, 1990, Origin of deep crustal reflections: seismic profiling across high grade metamorphic terranes in Canada, *Tectonophysics*.
- Holbrook, W.S., D. Gajewski, A. Krammer and C. Prodehl, 1988, An interpretation of wide-angle compressional and shear wave data in southwest Germany: Poisson's ratio and petrological implications, *J. Geophys. Res.*, 93, 12081-12106.
- Hurich, C.A., 1988, Investigations of mylonite reflectivity and reflections in deep crustal reflection profiles, University of Wyoming Ph.D. Thesis, 120 p.
- Hurich, C.A. and S.B. Smithson, Compositional variation and the origin of deep crustal reflections, *Earth Planet. Sci. Lett.*, 85, 416-426.
- Jamieson, R.A. and Beaumont, C., 1989, Deformation and metamorphism in convergent orogens: a model for uplift and exhumation of metamorphic terranes. in Daly, J.S. et al., (eds.), Evolution of Metamorphic Belts, Geological Society Special Publication No. 43, 117-129.

- Jones, E., R.S. White, V. Hughes, D.M. Matthews and B. Clayton, 1984, Crustal structure of the continental shelf off northwest Britain from two-ship seismic experiments, *Geophys.*, **49**, 1605-1621.
- Jones, T. and A. Nur, 1982, Seismic velocity and anisotropy in mylonites and the reflectivity of deep crustal fault zones, *Geology*, **10**, 260-263.
- Jones, T. and A. Nur, 1984, The nature of seismic reflections from deep crustal fault zones, *J. Geophys Res.*, **89**, 3153-3171.
- Kallweit, R.S. and L.C. Wood, 1982, The limits of resolution of zero-phase wavelets, *Geophysics*, **47**, 1035-1046.
- Kern, H., 1978, The effect of high temperature and high confining pressure on compressional wave velocities in quartz bearing and quartz free igneous and metamorphic rocks, *Tectonophys.*, **44**, 185-302.
- Kern, H. and V. Schenk, 1985, Elastic wave velocities in rocks from a lower crustal section in southern Calabria, Italy, *Phys. Earth Planet. Int.*, **40**, 147-160.
- Kern, H. and H.-R. Wenk, 1990, Fabric related velocity anisotropy and shear wave splitting in rocks from the Santa Rosa Mylonite Zone, California, *J. Geophys. Res.*, **95**, 11213-11223.
- Klemperer, S., L.D. Brown, J. Oliver, C. Ando, B. Czuchra and S. Kaufman, 1985, Some results of COCORP seismic reflection profiling in the Grenville aged Adirondack Mountains, New York State, *Can. J. Earth Sci.*, **22**, 141-153.
- Klemperer, S. and BIRPS Group, 1987, Reflectivity of the crystalline crust: hypotheses and tests, *Geophys. J. R. astr. Soc.*, **89**, 217-222.
- Knapp, R.W., 1990, Vertical resolution of thick beds, thin beds and thin bed cyclothems, *Geophys.*, **55**, 1183-1190.
- Koefoed, O. and N. De Voogd, 1980, The linear properties of thin layers, with an application to synthetic seismograms over coal seams, *Geophysics*, **45**, 1254-1268.

- Krollpfiefer, D., L. Dresen, C. Hsieh and C. Chern, 1988,²³⁴
Detection and resolution of thin layers; a model
eismic study, *Geophysical Prosp.*, **36**, 244-264.
- Krogh, T. and G.L.Davis, 1971, The Grenville Front
interpreted as an ancient plate boundary, Carnegie
Institution of Washington, Yearbook, **70**, 239-240.
- Lister, G.S. and A.W. Snoke, 1984, S-C Mylonites, *J.*
structural Geol., 617-638.
- Levin, F.K., 1990, Reflection from a dipping plane-
transversely isotropic solid, *Geophys.*, **55**, 851-855.
- Mathur, S., 1983, Deep reflection probes in Eastern
Australia reveal differences in nature of the crust,
First Break, **1**, 9- 16.
- Matthews, D.H. and C. Smith, (eds) 1987, Deep Seismic
Profiling of the Continental Lithosphere, *Geophys. J.*
R. astr. Soc. Special Issue, **89**, 447 p.
- McDonough, D., and D.M. Fountain, 1988, Reflection
characteristics of a mylonite zone based on
compressional wave velocities of rock samples,
Geophys. R. astron. Soc., **93**, 547-558.
- McSkimin, H. and P. Andreatch, Analysis of the pulse
superposition method for measuring ultrasonic wave
velocities as a function of temperature and pressure,
J. Acoust. Soc. Amer., **34**, 609-637.
- Meissner, R., 1986, The Continental Crust: a Geophysical
Approach, Volume 34 in the International Geophysics
Series, Academic Press, Orlando, FL, 426 p.
- Mellman, G., K. Kaufman and G. Lundquist, 1984, Some
theoretical aspects of the QUIK three dimensional
raytracing software, *Sierra Report R-84-115*.
- Mereu, R.F., D. Epili and A.G. Green, 1990, Pg shingles:
preliminary results from the onshore GLIMPCE
refraction experiment, *Tectonophys.*, **173**, 617-626.
- Milkereit, B., A.Green, M. Lee, W. Agena and C. Spencer,
1989, Pre- and post- stack migration of GLIMPCE
reflection data, *Tectonophys.*, **173**, 1-13.

- 235
- Milkereit, B., D. Epilli, A. Green, R. Mereu, and P. Morel-a-l-Hussier, 1990, Migration of wide angle seismic reflection data from the Grenville Front in Lake Huron, *J. Geophys. Res.*, **95**, 10987-10998.
- Moos, D. and M.D. Zoback, 1983, In situ studies of velocity in fractured crystalline rocks, *J. Geophys. Res.*, **88**, 2345-2358.
- Mueller, St., J. Ansorge, N. Sierro, P. Finckh and D. Emter, 1987, Synoptic interpretation of seismic reflection and refraction data, *Geophys. J. R. astr. Soc.*, **89**, 345-352.
- Pant, D.R. and S.A. Greenhalgh, 1989, Lateral resolution in seismic reflection - a physical model study, *Geophysical J.*, **97**, 187-198.
- Patterson, S.R., R.H. Vernon and O.T. Tobisch, 1989, A review of criteria for the identification of magmatic and tectonic foliations in granitoids, *J. Structural Geo.*, **11**, 349-363.
- Percival, J.A. and K.D. Card, 1983, The Archaen crust as revealed in the Kapuskasing Uplift, Superior Province, Canada, *Geology*, **11**, 323-326.
- Potter, C., C. Liu, J. Huang, L. Zheng, T. Hauge, E. Hauser, R. Allmendinger, J. Oliver, S. Kaufman and L. Brown, 1987, Crustal structure of north central Nevada; results from COCORP deep seismic profiling, *Geol. Soc. Amer. Bull.*, **98**, 330-337.
- Press, W.H., B.P. Flannery, S.A. Teukolsky and W.T. Vetterling, 1986, Numerical Recipes: The Art of Scientific Computing, Cambridge University Press, 818.
- Pyrak-Nolte, L.J., L.R. Myer and N. Cook, 1990, Anisotropy in seismic velocities and amplitudes from multiple parallel fractures, *J. Geophys. Res.*, **95**, 11345-11358.
- Quirke, T.T. and W.H. Collins, 1930, The disappearance of the Huronian, *GSC Memoir*, **160**, 112 p.
- Ricker, N., 1953, Wavelet contraction, wavelet expansion and the control of seismic resolution, *Geophysics*, **18**, 769-792.
- Robertson, J. and H. Nogami, 1984, Complex seismic trace analysis of thin beds, *Geophysics*, **49**, 344-354.

- Roy-Chowdhury, K., R.A. Phinney and J. Pan, 1988, Consequences of multiple scales of layering for the crustal seismic response, (Abstract) in J.C. Dooley, (ed) International Workshop and Symposium: Seismic Profiles of the Continents and Their Margins, Bureau of Mineral Resources, Geology and Geophysics Record 1988/21, p. 130.
- Ryzhova, T.V., 1964, Elastic properties of plagioclases, Izv. Acad. Sci. USSR, Geophys. Ser., **7**, 1049-1051.
- Sandmeier, K.-J. and F. Wenzel, 1990, Lower crustal petrology from wide angle P- and S- wave measurements in the Black Forest, Tectonophys., **173**, 495-505.
- Schmid, R., 1967, Zur Petrographie und Struktur der Zone Ivrea-Verbano zwischen Valle D'Ossoloa und Val Grande (Prov. Novara, Italien), Schweiz. Min. Petr. Mitt., **47**, 935-1117.
- Sheriff, R.E., 1984, Encyclopic Dictonary of Exploration Geophysics, 2nd Edition. Society of Exploration Geophysicists, Tulsa.
- Sibson, R.H., 1977, Fault rocks and fault mechanisms, J. Geol. Soc. London, **13**, 191-213.
- Siegesmund, S., T. Takeshita and H. Kern, 1988, Anisotropy of Vp and Vs in an amphibolite of the deeper crust and its relationship to the mineralogical, microstructural and textural characteristics of the rock, Tectonophys., **157**, 25-38.
- Simmons, G. and A. Nur, 1968, Granites: relations of properties in situ to laboratory measurements, Science, **162**, 789-791.
- Simpson, C., 1985, Deformation of granitic rocks across the brittle-ductile transition, J. Structural Geol., **7**, 503-511.
- Smithson, S.B., 1978, Modelling continental crust: structural and chemical constraints, Geophys. Res. Lett., **5**, 749-752.
- Smithson, S.B., 1986, A physical model of the lower crust from North America based on seismic reflection data, in Dawson, J., D. Carswell, J. Hall and K. Wedepohl (eds.) The Nature of the Lower Continental Crust, Geological Soc. Special Publication, **24**, 23-34.

- Smithson, S.B., R.A. Johnson, C.A. Hurich, P. Valasek and C. Branch, 1987, Deep crustal structure and genesis from contrasting reflection patterns; an integrated approach, *Geophys. J. R. astr. Soc.*, **89**, 67-72.
- Spencer, C., A. Green, P. Morel-a-l'Hussier, B. Milkereit, J. Luetgert, D. Stewart, J. Unger and J. Phillips, 1989, The extension of Grenville basement beneath the northern Appalachians; results from the Quebec-Maine seismic reflection and refraction surveys, *Tectonics*, **8**, 677-696.
- Stierman, D.J. and R.L. Kovach, 1979, An in situ velocity study; the Stone Canyon well, *J. Geophys. Res.*, **84**, 672-678.
- Stockwell, C.H., 1982, Proposals for time classification and correlation of Precambrian rocks and events in Canada and adjacent areas of the Canadian Shield; Part 1, A time classification of Precambrian rocks and events, GSC Paper 80-19, 135 p.
- Streckeisen, A., 1976, To each plutonic rock its proper name. *Earth. Sci. Rev.*, **12**, 1-33.
- Tatalovic, R., J.A. McDonald and G. Gardner, 1988, Modelling study of tuning effects for the calculation of the thickness and areal extent of thin beds, *First Break*, **6**, 395-404.
- Telford, W.M., L.D. Geldart, R.E. Sheriff and D.A. Keys, 1976, Applied Geophysics, Cambridge University Press, 860 p.
- Van Breemen, O. and A. Davidson, 1988, Northeast extension of Proterozoic terranes of mid-continental North America, *Geol. Soc. Amer. Bull.*, **100**, 630-638.
- Walsh, J.B., 1965, The effect of cracks on the compressibility of rocks, *J. Geophys. Res.*, **70**, 381-390.
- Wang, C.-Y., D.A. Okaya, C. Ruppert, G.A. Davis, T.S. Guo, Z. Zhong and H.R. Wenk, 1989, Seismic reflectivity of the Whipple Mountain Shear Zone, Southern California, *J. Geophys. Res.*, **94**, 2989-30005.
- Warner, M., 1990, Basalts, water, or shear zones in the lower continental crust? *Tectonophysics*, **173**, 163-174.

- White, S., 1979, Grain and sub-grain size variations across a mylonite zone, *Contrib. Min. Petrol.*, **70**, 193-202.
- Whittall, K.P. and R. Clowes, 1979, A simple, efficient method for the calculation of traveltimes and raypaths in laterally inhomogeneous media, *J. Can. Expl. Geophys.*, **15**, 21-29.
- Widess, M.B., 1973, How thin is a thin bed?, *Geophysics*, **38**, 1176-1180.
- Wynne-Edwards, H.R., 1972, The Grenville Province, in R.A. Price, and R.J.W. Douglass (eds) Variations in Tectonic Styles in Canada, Geol. Assoc. Can. Special Paper 11, 264-334.
- Young, G.M., 1968, Sedimentary structures in Huronian rocks of Ontario, *Paleogeography, Paleoclimatology, Paleocology*, **4**, 125-153.
- Zoeppritz, K. 1919, *Über reflexion und durchgang seismischer wellen durch Unsteigkerlsflaschen. Über Erdbebenwellen VII B*, Nachrichten der Koniglichen Gesellschaft der Wissenschaften zu Gottingen, math-phys., Berlin, p 57-84.
- Zolnai, A.I., R.A. Price and H. Helmstaedt, 1984, Regional cross section of the Southern Province adjacent to Lake Huron, Ontario: implications for the tectonic significance of the Murray Fault Zone, *Can. J. Earth Sci.*, **21**, 447-456.